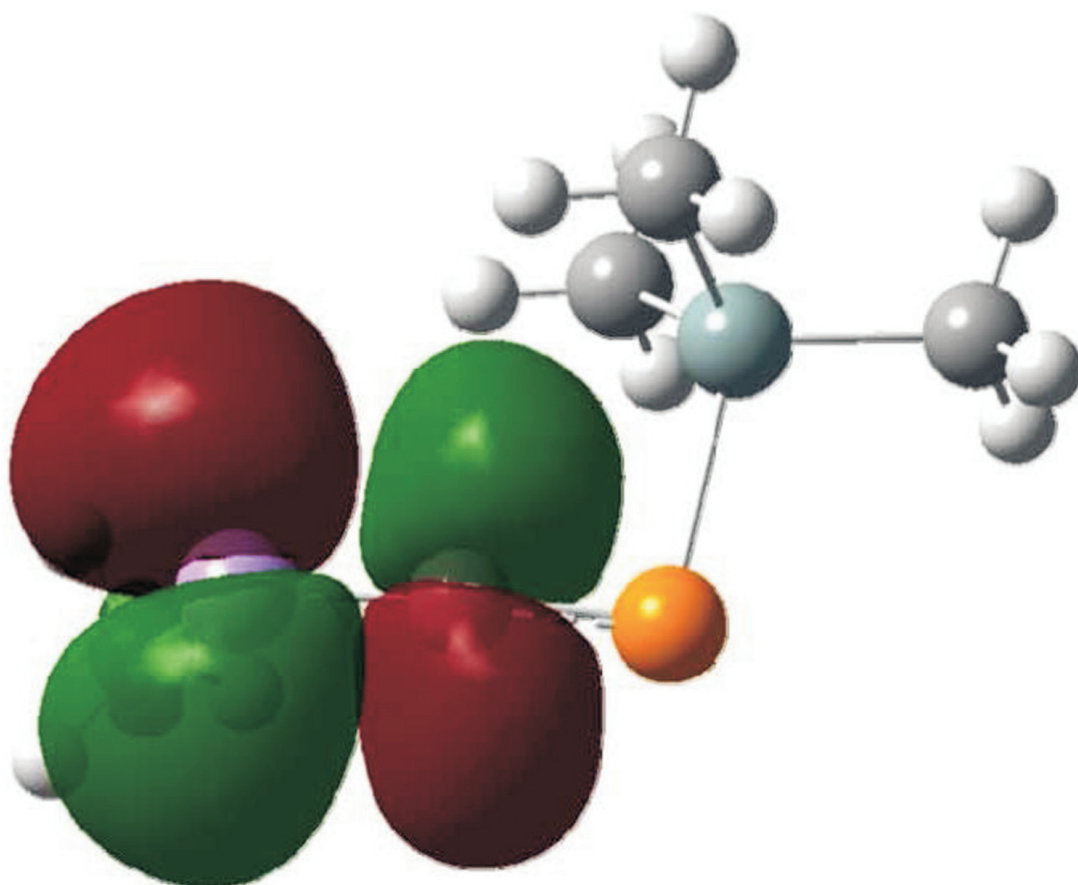




STUDIA UNIVERSITATIS
BABEŞ-BOLYAI



CHEMIA

2/2010
tom II

STUDIA

UNIVERSITATIS BABEȘ-BOLYAI

CHEMIA

2

tom II

Desktop Editing Office: 51ST B.P. Hasdeu Street, Cluj-Napoca, Romania, Phone + 40 264-405352

CONTENT – SOMMAIRE – INHALT – CUPRINS

M.L. POP, M.V. DIUDEA, Topology of a New Lattice Containing Pentagon Triples	199
C. COMSA, R.A. VARGA, C. SILVESTRU, Methyltin(IV) Trichloride Complexes of β -Ketimine, $\text{MeSnCl}_3[\text{OC}(\text{Me})\text{CHC}(\text{Me})\text{NH}(\text{C}_6\text{H}_3\text{Pr}_2\text{-}2',6')\text{-}4]_n$ ($n = 1,2$). Solution Behavior and Solid State Structure.....	207
M.M. VENTER, V.N. BERCEAN, R.A. VARGA, V. SASCA, T. PETRIȘOR Jr., L. CIONTEA, Solid State Structure of a New Nickel(II) (3 <i>H</i> -2-thioxo-1,3,4-thiadiazol-2-yl) Thioacetato Complex.....	217
S.C. COBZAC, D. CASONI, C. SÂRBU, An Improved Sample Preparation of Starch-Based Foods for Synthetic Dyes Analysis.....	227
A.M. PREDA, M. KULCSAR, R.A. VARGA, D. MARGINEANU, A. SILVESTRU, Ammonium Salts of Organophosphorus Acids. Crystal and Molecular Structure of $[\text{Et}_3\text{NH}]^+[(\text{SPMe}_2)(\text{SPPH}_2)\text{N}]^-$ and $[2\text{-}\{\text{O}(\text{CH}_2\text{CH}_2)_2\text{N}(\text{H})\text{CH}_2\}\text{C}_6\text{H}_4]^+[\text{S}_2\text{P}(\text{OPr}^i)_2]^-$	237
D. BRĂTFĂLEAN, V.M. CRISTEA, P.Ș. AGACHI, Artificial Neural Networks Used for Investigation of Fatty Acid Content of Romanian Sunflower Oilseeds Genotypes.....	245

L.E. MURESAN, E.-J. POPOVICI, E. BICA, A.-I. CADIŞ, M. MORAR, E. INDREA, Spectroscopic and Structural Characterisation of SiO ₂ -Y ₂ O ₃ Based Materials with Luminescent Properties	255
A.-I. CADIŞ, E.-J. POPOVICI, E. BICA, L. BARBU-TUDORAN, Studies on the Synthesis of Manganese Doped Zinc Sulphide Nanocrystalline Powders	265
A. FALAMAS, S. CINTA PINZARU, C.A. DEHELEAN, M.M. VENTER, Raman Imaging of In Vivo Damaged Skin Tissues from Mice Specimens	273
S. DRĂGAN, A. GHIRIŞAN, Kinetic Study of Flue Gas Desulphurization with Sodium Carbonate at Low Temperature.....	283
D. GLIGOR, C. VARODI, A. MĂICĂNEANU, L.M. MUREŞAN, Carbon Nanotubes-Graphite Paste Electrode Modified with Cu(II)-Exchanged Zeolite for H ₂ O ₂ Detection	293
A. MOCANU, R.-D. PAŞCA, O. HOROVITZ, M. TOMOAIACOTISEL, Behavior of Mixed DMPC-Cholesterol Monolayers at the Air/Water Interface	303
M. TOMOAIACOTISEL, N. CIOICA, C. COTA, CS. RACZ, I. PETEAN, L.D. BOBOS, A. MOCANU, O. HOROVITZ, Structure of Starch Granules Revealed by Atomic Force Microscopy	313
D. RUSU, O. BABAN, S. DREVE, M. PUIA, M. RUSU, Synthesis and Spectroscopic Investigations of New UO ₂ ²⁺ - Polyoxometalate Complexes	327
L.-I. CSEPEI, CS. BOLLA, The Thermodynamics and Kinetics of Saturated Hydrocarbon Separation on a DB-1 Column.....	337
N.-K. OLAH, D. HANGANU, L. VLASE, C. COBZAC, The Study of Polyphenols from <i>Trifolium Pratense</i> L. and <i>Medicago Sativa</i> L. Hydroalcoholic Extracts by HPLC-UV-MS	353
E.-S. BOGYA, I. BÂLDEA, R. BARABÁS, A. CSAVDÁRI, G. TURDEAN, V.-R. DEJEU, Kinetic Studies of Sorption of Copper(II) Ions onto Different Calcium-Hydroxyapatite Materials	363
A. CREŢU, D.-I. CREŢU, The Values of Biochemical Indicators in People who Practice 'Maintenance' Aerobics.....	375
R. GRECU, V. COMAN, O. COZAR, Intermolecular Interactions of 1- and 2-Bromopropane with Solvent Mixtures Studied by Infrared Spectroscopy.....	381
OVIDIU NEMES, Adhesive Influence on Double-Lap Bonded-Joints Assemblies	389

Studia Universitatis Babes-Bolyai Chemia has been selected for coverage in Thomson Reuters products and custom information services. Beginning with V. 53 (1) 2008, this publication is indexed and abstracted in the following:

- Science Citation Index Expanded (also known as SciSearch®)
- Chemistry Citation Index®
- Journal Citation Reports/Science Edition

Dedicated to the memory of Prof. dr. Ioan Silaghi-Dumitrescu marking 60 years from his birth

TOPOLOGY OF A NEW LATTICE CONTAINING PENTAGON TRIPLES

MONICA L. POP AND MIRCEA V. DIUDEA^a

ABSTRACT. A new crystal-like network is designed by using some net operations. The topology of this hypothetical lattice is characterized by Omega polynomial and Cluj-Ilmenau CI index.

Keywords: map operations, Omega polynomial, Cluj-Ilmenau index

INTRODUCTION

In the nano-era, several new carbon structures: fullerenes (zero-dimensional), nanotubes (one dimensional), graphene (two dimensional), spongy carbon (three dimensional) and nano-diamond (three dimensional) [1,2] have been discovered. Inorganic clusters, like zeolites, also attracted the attention of scientists.

Zeolites are natural or synthetic aluminosilicates with an open three-dimensional crystal structure. Zeolites are members of the family of microporous solids known as "molecular sieves." This term refers to the property of these materials to selectively sort molecules based primarily on a size exclusion process. This is due to a regular structure of pores, of molecular dimensions, forming channels. The maximum size of the molecular or ionic species that can enter the pores of a zeolite is controlled by the dimensions of the channels [3-7].

Recent articles in crystallography promoted the idea of topological description and classification of crystal structures [8-13].

The present study presents a hypothetical crystal-like nano-carbon structure, with the topological description in terms of Omega counting polynomial.

OPERATIONS ON MAPS

Several operations on maps are known and used for various purposes.

Dualization *Du* of a map is achieved as follows: locate a point in the center of each face. Join two such points if their corresponding faces share

^a Faculty of Chemistry and Chemical Engineering, "Babes-Bolyai" University, Arany Janos Str. 11, 400084, Cluj, Romania

a common edge. The transformed map is called the (Poincaré) *dual* $Du(M)$. The vertices of $Du(M)$ represent the faces of M and *vice-versa* [14]. Thus the following relations exist between the parent map parameters (denoted by subscript zero) and those of the transformed map:

$$Du(M): v=f_0; e=e_0; f=v_0 \quad (1)$$

Dual of the dual recovers the original map: $Du(Du(M)) = M$. Tetrahedron is self dual while the other Platonic polyhedra form pairs: $Du(\text{Cube}) = \text{Octahedron}$; $Du(\text{Dodecahedron}) = \text{Icosahedron}$ (see Figure 1 for symbols hereafter used). It is also known the Petrie dual.

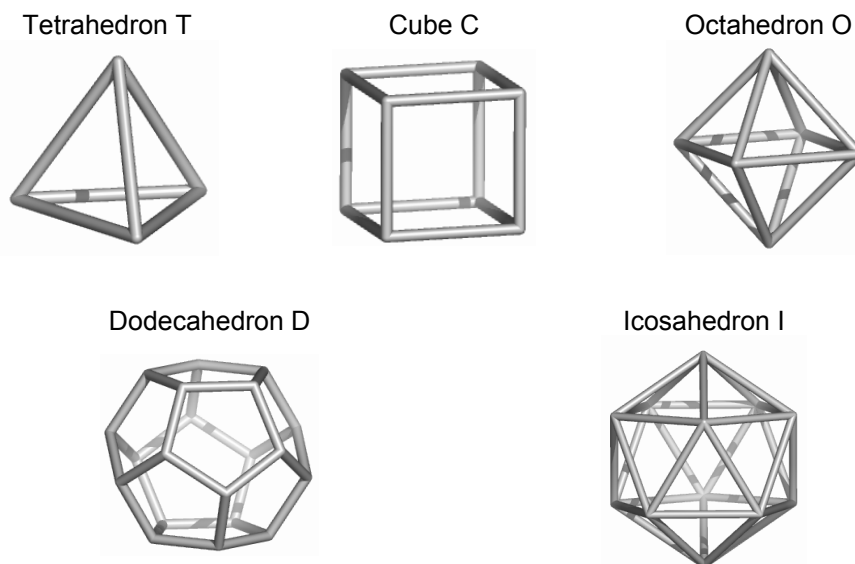


Figure 1. The five Platonic polyhedra.

Medial *Med* is another important operation on maps [15-17]. It is constructed as follows: put the new vertices as the midpoints of the original edges. Join two vertices if and only if the original edges span an angle (more exactly, the two edges must be incident and consecutive within a rotation path around their common vertex in the original map).

The medial graph is a subgraph of the line-graph [18]. In the line-graph each original vertex gives rise to a complete graph while in the medial graph only a cycle C_d (*i.e.*, a d -fold cycle, d being the vertex degree/valence) is formed.

The medial of a map is a 4-valent graph and $Med(M) = Med(Du(M))$. The transformed parameters are:

$$Me(M): v=e_0; e=2e_0; f=f_0 + v_0 \quad (2)$$

The medial operation rotates parent s -gonal faces by π/s . Points in the medial represent original edges, thus this property can be used for topological analysis of edges in the parent polyhedron. Similarly, the points in dual give information on the topology of parent faces.

Cuboctahedron = $Med(C)$

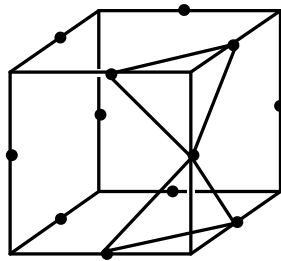
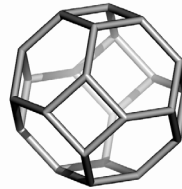
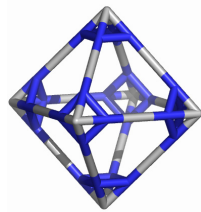


Figure 2. Medial operation; construction (left) and realization (right).

Truncation Tr is achieved by cutting of the neighborhood of each vertex by a plane close to the vertex, such that it intersects each edge incident to the vertex. Truncation is similar to the medial, with the main difference that each old edge will generate three new edges in the truncated map. The transformed parameters are:

$$Tr(M): v = 2e_0 = d_0v_0; e = 3e_0; f = f_0 + v_0 \quad (3)$$

This was the main operation used by Archimedes in building his well-known 13 solids [3]. Note that truncation always provides a trivalent net. Figure 3 illustrates this operation.



$Tr(O) =$ Truncated Octahedron

Figure 3. Truncation; construction (left) and realization (right).

Leapfrog Le is a composite operation [16,17-24] that can be written as:

$$Le(M): Tr(Du(M))=Du \tag{4}$$

This operation rotates parent s -gonal faces by π/s . Note that the vertex degree in $Le(M)$ is *always* 3. Leapfrog operation is illustrated, for a tetragonal face, in Figure 4.

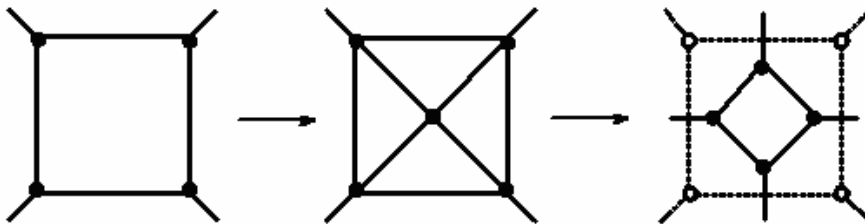


Figure 4. Leapfrogging a tetragonal face of a trivalent map; the white circles are the new vertices of $Le(M)$.

A bounding polygon, of size $2d_0$, is formed around each original vertex. In the most frequent cases of 4- and 3-valent maps, the bounding polygon is an octagon and a hexagon, respectively (Figure 5).

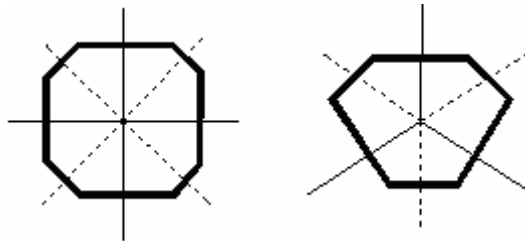


Figure 5. The bounding polygon around a 4-degree (left) and 3-degree (right) vertex.

In trivalent maps, $Le(M)$ is the *tripling* operation. The complete transformed parameters are:

$$Le(M): v = s_0 f_0 = d_0 v_0; e = 3e_0; f = v_0 + f_0 \tag{5}$$

being the same as for $Tr(M)$, eq 3.

A nice example of Le operation realization is: $Le(D) = \text{Fullerene } C_{60}$ (Figure 6). The leapfrog operation can be used to insulate the parent faces by surrounding bounding polygons (see above).

TOPOLOGY OF A NEW LATTICE CONTAINING PENTAGON TRIPLES

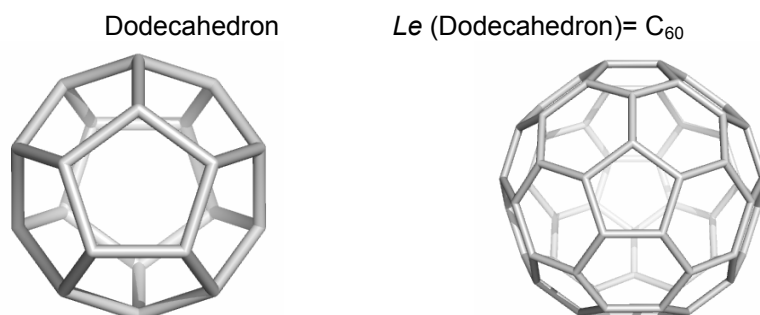


Figure 6. Leapfrog operation – molecular realization.

LATTICE BUILDING

The lattice under study (Figure 7), named S_2CL , was designed by the sequence: $Trs(Du(Med(Le(Oct))))$ and is a triple periodic network. In the above sequence, Trs means the truncation of some selected vertices. This sequence of operations introduces pentagon triples in a polygonal covering, which apparently violate the IPR (Isolated Pentagon Rule) condition in fullerene stability [25,26].

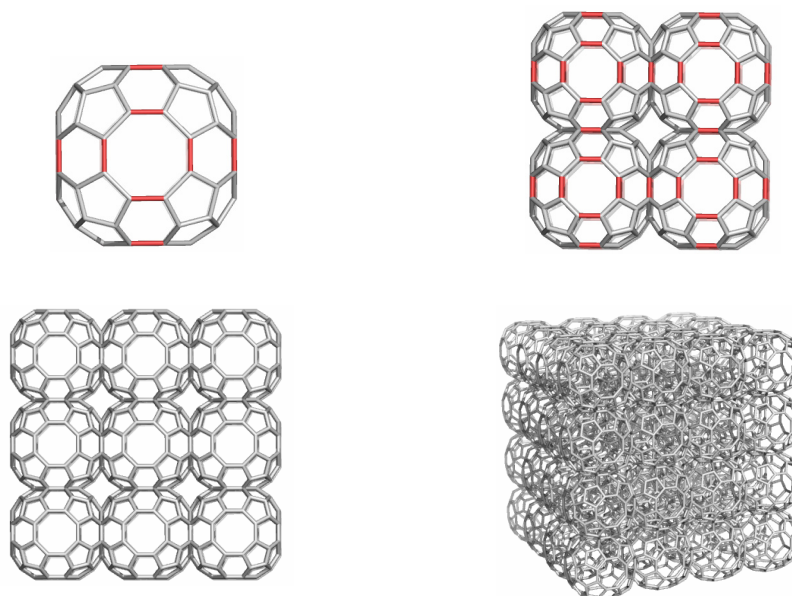


Figure 7. Lattice S_2CL ; unit designed by $Trs(Du(Med(Le(Oct))))$; the red bonds mark the octagonal faces to be identified in construction of the network.

However, fullerenes which tessellation included pentagon triples have been obtained as real molecules. Calculation of stability of cages bearing pentagon triples [27] makes the subject of another article.

Network was performed by identifying the octagons in two neighbor units (Figure 7, left top corner). In this way, ordered channels appear, like those in zeolites.

For the topological characterization, cubic domains were constructed (Figure 7, right, bottom, corner). Formulas for Omega polynomial and examples are given in the next section.

OMEGA POLYNOMIAL IN CRYSTAL LATTICE

Two edges e and f of a plane graph G are in relation *opposite*, $e \text{ op } f$, if they are opposite edges of an inner face of G . Then $e \text{ co } f$ holds by assuming the faces are isometric. Note that relation *co* involves distances in the whole graph while *op* is defined only locally (it relates face-opposite edges).

Using the relation *op* we can partition the edge set of G into *opposite edge strips*, *ops*: any two subsequent edges of an *ops* are in *op* relation and any three subsequent edges of such a strip belong to adjacent faces.

Note that John *et al.* [28,29] implicitly used the “*op*” relation in defining the Cluj-Ilmenau index CI .

Denote by $m(s)$ or simply m the number of *ops* of length $s=|s_k|$ and define the Omega polynomial as [30-32]:

$$\Omega(x) = \sum_s m(s) \cdot x^s \quad (6)$$

The exponent counts just the *ops* of length s ; the coefficients m are easily counted from the symmetry of G . The first derivative (in $x=1$) provides the number of edges in G :

$$\Omega'(1) = \sum_s m \cdot s = e = |E(G)| \quad (7)$$

On Omega polynomial, the Cluj-Ilmenau index [33], $CI=CI(G)$, was defined:

$$CI(G) = \{[\Omega'(1)]^2 - [\Omega'(1) + \Omega''(1)]\} \quad (8)$$

We used here the topological description by Omega polynomial because this polynomial was created to describe the covering in polyhedral nanostructures and because it is the best in describing the constitutive parts of nanostructures, particularly for large structures, with a minimal computational cost [34].

Formulas for Omega polynomial in S_2CL network and examples are given in Table 1.

Table 1. Omega polynomial in S_2CL ; $R_{max}[8]$.

Formulas		
$\Omega(S_2CL, x) = 24a^3 \cdot x^1 + 6a(a^2 + 9a - 4) \cdot x^2 + 12a(a - 1)^2 \cdot x^4 + 3a \cdot x^{a(8+4(a-1))}$		
$\Omega'(S_2CL, 1) = 24a^2(4a + 1)$		
$\Omega''(S_2CL, 1) = 48a(a^4 + 2a^3 + 4a^2 - 4a + 2)$		
$CI(S_2CL) = 24a(384a^5 + 190a^4 + 20a^3 - 12a^2 + 7a - 4)$		
Examples		
Net	Omega	CI
111	$24x+36x^2+3x^8$	14040
222	$192x+216x^2+24x^4+6x^{24}$	741600
333	$648x+576x^2+144x^4+9x^{48}$	7858872
777	$8232x+4536x^2+3024x^4+21x^{224}$	1161954360
888	$12288+6336x^2+4704x^4+24x^{288}$	2567169792

Data were calculated by the original software Nano-Studio, developed at TOPO Group Cluj, Romania.

CONCLUSIONS

Design of S_2CL hypothetical crystal structure was performed by using some operations on maps. This network is aimed to simulate the ordered channels existing in some zeolites. The topology of the proposed network was described in terms of Omega polynomial.

ACKNOWLEDGMENTS

The authors wish to thank for the financial support provided from programs co-financed by The SECTORAL OPERATIONAL PROGRAMME HUMAN RESOURCES DEVELOPMENT, Contract **POS DRU 6/1.5/S/3** – „Doctoral studies: through science towards society”.

REFERENCES

1. M. V. Diudea, *Ed., Nanostructures, novel architecture*, NOVA, **2005**.
2. M. V. Diudea and Cs. L. Nagy, *Periodic Nanostructures*, Springer, **2007**.
3. R. W. Thompson and A. Dyer, *Zeolites*, **1985**, 5, 292.
4. Zh. Liu, T. Ohsuna, O. Terasaki, M. A. Camblor, M.-J. Diaz- Cabañas and K. Hiraga, *J. Am. Chem. Soc.*, **2001**, 123, 5370.

5. Zh. Yang, Y. Xia and R. Mokaya, *J. Am. Chem. Soc.*, **2007**, *129*, 1673.
6. G. O. Brunner, *Zeolites*, **1993**, *13*, 88.
7. E. H. Ellison, *J. Phys. Chem.*, **2006**, *110*, 11406.
8. L. Carlucci, G. Ciani and D. Proserpio, *Coord. Chem. Rev.*, **2003**, *246*, 247.
9. L. Carlucci, G. Ciani and D. Proserpio, *Cryst. Eng. Comm.*, **2003**, *5*, 269.
10. V. A. Blatov, L. Carlucci, G. Ciani and D. Proserpio, *Cryst. Eng. Comm.*, **2004**, *6*, 377.
11. I. A. Baburin, V. A. Blatov, L. Carlucci, G. Ciani and D. Proserpio, *J. Solid State Chem.*, **2005**, *178*, 2452.
12. O. Delgado-Friedrichs and M. O'Keeffe, *J. Solid State Chem.*, **2005**, *178*, 2480.
13. V. A. Blatov, O. Delgado-Friedrichs, M. O'Keeffe and D. Proserpio, *Acta Cryst.*, **2007**, *A63*, 418.
14. T. Pisanski and M. Randić, in *Geometry at Work*, M. A. A. Notes, **2000**, *53*, 174.
15. P. W. Fowler and T. Pisanski, *J. Chem. Soc. Faraday Trans.* **1994**, *90*, 2865.
16. M. V. Diudea, and P. E. John, *Commun. Math. Comput. Chem. (MATCH)*, **2001**, *44*, 103.
17. F. Harary, *Graph Theory*. Addison-Wesley, Reading, MA, **1969**.
18. M. V. Diudea, *Forma (Tokyo)*, **2004**, *19* (3), 131.
19. P. W. Fowler, *Phys. Lett.*, **1986**, *131*, 444.
20. P. W. Fowler and J. I. Steer, *J. Chem. Soc., Chem. Commun.*, **1987**, 1403.
21. P. W. Fowler and K.M.Rogers, *J. Chem. Soc., Faraday Trans.*, **1998**, *94*, 1019.
22. P. W. Fowler and K.M.Rogers, *J. Chem. Soc., Faraday Trans.*, **1998**, *94*, 2509.
23. M. V. Diudea, P. E. John, A. Graovac, M. Primorac, and T. Pisanski, *Croat. Chem. Acta*, **2003**, *76*, 153.
24. G. Brinkmann, P. W. Fowler, and M. Yoshida, *MATCH Commun. Math. Comput. Chem.*, **1998**, *38*, 7.
25. H. W. Kroto, *Nature*, **1987**, *329*, 529.
26. X. Han, S. J. Zhou, Y. Z. Tan, X. Wu, F. Gao, Z. J. Liao, R. B. Huang, Y. Q. Feng, X. Lu, S. Y. Xie, and L. S. Zheng, *Angew. Chem. Int. Ed.*, **2008**, *47*, 5340.
27. C. R. Wang, Z. Q. Shi, L. J. Wan, X. Lu, L. Dunsch, C. Y. Shu, Y. L. Tang, H. Shinohara, *J. Am. Chem. Soc.*, **2006**, *128*, 11352.
28. P. E. John, A. E. Vizitiu, S. Cigher, and M. V. Diudea, *MATCH Commun. Math. Comput. Chem.*, **2007**, *57*, 479.
29. P. E. John, P. V. Khadikar, and J. Singh, *J. Math. Chem.*, **2007**, *42*, 37-45.
30. A. R. Ashrafi, M. Ghorbani, and M. Jalali, *Indian J. Chem.*, **2008**, *47A*, 535.
31. P. V. Khadikar, V. K. Agrawal, S. Karmarkar, *Bioorg. Med. Chem.*, **2002**, *10*, 3499.
32. Cs. L. Nagy and M. V. Diudea, *Nano Studio*, "Babes-Bolyai" Univ., 2009.
33. A. R. Ashrafi, M. Jalali, M. Ghorbani, and M. V. Diudea, *MATCH Commun. Math. Comput. Chem.*, **2008**, *60*, 905.
34. M. V. Diudea, K. Nagy, M. L. Pop, F. Gholami-Nezhaad, and A.R. Ashrafi, *Int. J. Nanosci. Nanotechnol.*, **2010**, submitted.

Dedicated to the memory of Prof. dr. Ioan Silaghi-Dumitrescu marking 60 years from his birth

**METHYLTIN(IV) TRICHLORIDE COMPLEXES OF β -KETIMINE,
MeSnCl₃[OC(Me)CHC(Me)NH(C₆H₃ⁱPr₂-2',6')-4]_n (n = 1,2).
SOLUTION BEHAVIOR AND SOLID STATE STRUCTURE**

CARMEN COMSA, RICHARD A. VARGA, CRISTIAN SILVESTRU^{a,*}

ABSTRACT. Reaction of MeSnCl₃ with the β -ketimine OC(Me)CHC(Me)NH(C₆H₃ⁱPr₂-2',6')-4, in 1:1 and 1:2 molar ratio, gave the new methyltin(IV) trichloride adducts MeSnCl₃[OC(Me)CHC(Me)NH(C₆H₃ⁱPr₂-2',6')-4]_n [n = 1 (**1**), n = 2 (**2**)]. The compounds were characterized by multinuclear NMR studies in solution. The crystal and molecular structure of **1** and **2** was established by single-crystal X-ray diffraction. The crystals contain discrete molecules in which the β -ketimine ligand is coordinated to a metal center through its oxygen atom. This results in trigonal bipyramidal CSnCl₃O and octahedral CSnCl₃O₂ cores in **1** and **2**, respectively. In the crystals intermolecular Cl...H contacts result in supramolecular architectures.

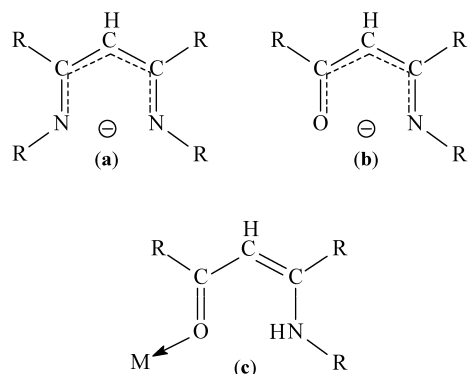
Keywords: methyltin(IV), trichloride complexes, β -ketimine, solution NMR studies, single-crystal X-ray diffraction.

INTRODUCTION

The β -diketiminato ligands [Scheme 1 (a)] were widely used to stabilize unusual species and coordination numbers in metal complexes which can show interesting catalytic effects [1]. In contrast to the β -diketiminato ligands [1-6], the coordination potential of the β -ketiminato ligands [Scheme 1 (b)] in tin(II) and tin(IV) chemistry is much less investigated. Some three, four and six-coordinate, monomeric Sn(II) and Sn(IV) derivatives containing the chelated β -ketiminato [OC(Me)CHC(Me)N(C₆H₃ⁱPr₂-2',6')-4]⁻ ligand, *i.e.* SnCl(L), Sn(L)₂ and SnX₂(L)₂, were reported only recently [7]. The β -diketiminates and β -ketiminates can also be used as neutral ligands. We have previously reported on some di- and triorganotin(IV) chloride adducts containing OC(Me)CHC(Me)NH(C₆H₃ⁱPr₂-2',6')-4 [8,9] and the molecular structures, established by single-crystal X-ray diffraction, were also described for some few other complexes of Ti [10], Zr [12], Mo [12], W [13], Al [14] and Sb [15].

^a Babeș-Bolyai University, Faculty of Chemistry and Chemical Engineering, Arany Janos 11, 400028 Cluj-Napoca, Romania; * cristi@chem.ubbcluj.ro

In all these complexes the β -ketimine ligand is coordinated to the metal centre through its oxygen atom in a monometallic monoconnective fashion [Scheme 1 (c)].

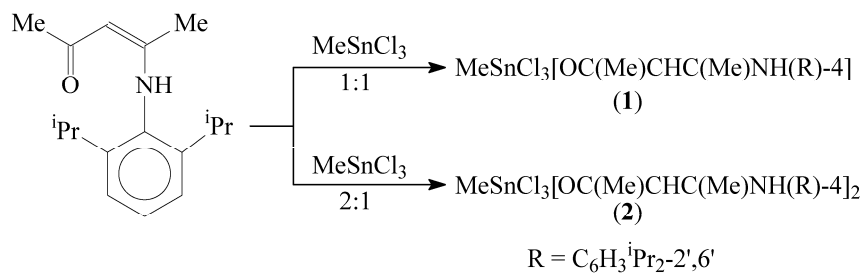


Scheme 1

We report here on the synthesis, solution behavior and solid state molecular structure of 1:1 and 1:2 adducts of methyltin(IV) trichloride, $\text{MeSnCl}_3[\text{OC}(\text{Me})\text{CHC}(\text{Me})\text{NH}(\text{C}_6\text{H}_3^i\text{Pr}_2\text{-}2',6')\text{-}4]_n$ [$n = 1$ (**1**), $n = 2$ (**2**)].

RESULTS AND DISCUSSION

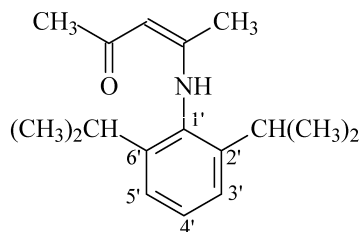
The new complexes **1** and **2** were obtained by reacting MeSnCl_3 with the β -ketimine in 1:1 and 1:2 molar ratio, respectively, in diethyl ether, at room temperature (Scheme 2).



Scheme 2

The new adducts were isolated in very good yields (ca. 90%) as white-yellow powders. They are air-stable and soluble in common organic solvents. The compounds were investigated by multinuclear NMR spectroscopy (^1H , ^{13}C , ^{119}Sn) in solution and their molecular structures were established by single-crystal X-ray diffraction.

The NMR spectra were recorded in CDCl_3 , at room temperature. The assignment of the ^1H and ^{13}C chemical shifts was made according to the numbering scheme shown in Scheme 3, based on 2D experiments.



Scheme 3

The NMR (^1H , ^{13}C) spectra of compounds **1** and **2** are very similar. They exhibit in the alkyl and aryl regions the expected resonances for the β -ketimine ligand. In addition, a singlet resonance is observed for the protons of methyl group attached to tin. In the ^1H spectra for both compounds these resonances are surrounded by ^{117}Sn / ^{119}Sn satellites due to tin-proton couplings. The integral ratio between ^1H resonances for the protons in the β -ketimine ligand and CH_3Sn is consistent with the formation of 1:1 and 1:2 adducts, respectively. The presence of a resonance for the hydrogen attached to nitrogen of the β -ketimine ligand is indicative of its coordination to the metal centre in the protonated form.

For both compounds the ^{119}Sn NMR spectra exhibit only one resonance, indicative for the presence of only one tin-containing species in solution, with very likely a similar structure as found in solid state.

Single-crystals suitable for X-ray diffraction studies were obtained by slow diffusion of *n*-hexane into a solution of **1** or **2** in CH_2Cl_2 . In both cases the crystals contain discrete monomers separated by distances between heavy atoms larger than the sum of the van der Waals radii for the corresponding atoms. The ORTEP diagrams of the molecular structures of **1** and **2**, with the atom numbering scheme, are shown in Figures 1 and 2. Selected interatomic distances and angles are listed in Tables 1 and 2.

A common structural feature for both adducts is the coordination of the β -ketimine ligand through its oxygen atom to tin. As in the free ligand, the acidic hydrogen of the β -ketimine is attached to the nitrogen atom and is involved in an intramolecular hydrogen bonding to the oxygen atom. A similar coordination pattern was observed in all the organotin(IV) complexes of the same β -ketimine described so far [8,9].

In the molecule of the 1:1 adduct **1** the oxygen atom is placed almost *trans* to a halogen atom [$\text{Cl}(1)\text{--Sn}(1)\text{--O}(1)$ $169.12(12)^\circ$], thus resulting in a distorted trigonal bipyramidal CSnCl_3O core.

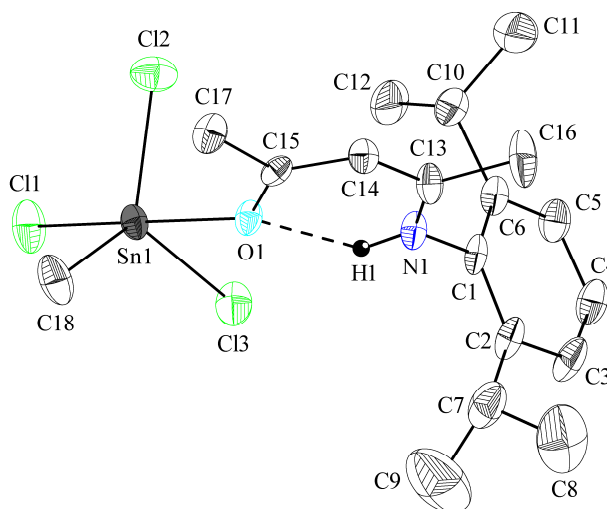


Figure 1. ORTEP representation at 20% probability and atom numbering scheme for **1**. Hydrogen atoms, except H(1) attached to nitrogen, are omitted for clarity.

Table 1. Interatomic bond distances (Å) and angles (°) for compound **1**.

Sn(1)–C(18)	2.099(7)	O(1)–C(15)	1.291(7)
Sn(1)–Cl(1)	2.408(2)	C(15)–C(17)	1.505(9)
Sn(1)–Cl(2)	2.312(2)	C(15)–C(14)	1.359(9)
Sn(1)–Cl(3)	2.335(2)	C(13)–C(16)	1.504(10)
Sn(1)–O(1)	2.191(4)	C(13)–C(14)	1.395(9)
Cl(1)–Sn(1)–O(1)	169.12(12)	N(1)–C(13)	1.306(9)
C(18)–Sn(1)–Cl(2)	123.9(3)	N(1)–C(1)	1.448(8)
C(18)–Sn(1)–Cl(3)	121.5(3)	N(1)–H(1)	0.856(19)
Cl(2)–Sn(1)–Cl(3)	113.36(10)	O(1)···H(1)	2.01(4)
Cl(1)–Sn(1)–C(18)	97.4(3)	O(1)–C(15)–C(14)	121.5(6)
Cl(1)–Sn(1)–Cl(2)	92.42(9)	O(1)–C(15)–C(17)	118.2(6)
Cl(1)–Sn(1)–Cl(3)	91.06(8)	C(14)–C(15)–C(17)	120.3(6)
O(1)–Sn(1)–C(18)	92.5(3)	C(13)–C(14)–C(15)	124.6(6)
O(1)–Sn(1)–Cl(2)	85.74(14)	N(1)–C(13)–C(14)	122.4(6)
O(1)–Sn(1)–Cl(3)	79.89(12)	N(1)–C(13)–C(16)	118.8(7)
Sn(1)–O(1)–C(15)	137.6(4)	C(14)–C(13)–C(16)	118.9(7)
		C(1)–N(1)–C(13)	126.5(6)
		C(1)–N(1)–H(1)	113(4)
		C(13)–N(1)–H(1)	120(4)
		C(15)–O(1)···H(1)	101(1)
		N(1)–H(1)···O(1)	129(3)

The length of the Sn(1)–O(1) bond [2.191(4) Å] suggests a stronger coordination [cf. the sums of the covalent and van der Waals radii are $\Sigma r_{\text{cov}}(\text{Sn},\text{O})$ ca. 2.06 Å and $\Sigma r_{\text{vdW}}(\text{Sn},\text{O})$ ca. 3.60 Å] [16]. As expected, the tin-oxygen distance in **1** is shorter than in the 1:1 adduct $\text{Me}_2\text{SnCl}_2[\text{OC}(\text{Me})\text{CHC}(\text{Me})\text{N}(\text{C}_6\text{H}_3^i\text{Pr}_{2-2',6'})-4]$ [Sn–O 2.375(3) Å] [8], the presence of three chlorine atoms attached to tin increasing the acidity of the metal centre. The Sn(1) atom is displaced only 0.147 Å from the CCl_2 equatorial plane on the side of the axial Cl(1) atom and the Sn(1)–Cl(1) bond is slightly elongated [2.408(2) Å] in comparison with the equatorial Sn–Cl bonds [Sn(1)–Cl(2) 2.312(2), Sn(1)–Cl(3) 2.335(2) Å] due to the *trans* effect of the oxygen.

The molecule of **2** is centrosymmetric and features a distorted octahedral CSnCl_3O_2 core achieved due to almost *trans* coordination of two β -ketimine ligands [O(1)–Sn(1)–O(1')] 170.9(2)°, which forces a square planar geometry of the covalent CSnCl_3 fragment. The strength of the tin-oxygen bonds in **2** is similar to that observed for **1**. In the equatorial plane, a difference in the length of the tin-chlorine bonds should be noted, *i.e.* those placed *trans* to each other are significantly elongated [Sn(1)–Cl(1) 2.462(2) Å] compared to Sn(1)–Cl(2) [2.386(3) Å], which is *trans* to the carbon atom attached to tin.

In both compounds, regardless the coordination geometry achieved around tin, the planar $\text{OC}_3\text{N}(\text{H})$ core of the β -ketimine ligands is twisted to allow intramolecular interaction between an equatorial chlorine and the NH proton [Cl(3)⋯H(1) 2.70 Å in **1**, and Cl(1)⋯H(1) 2.73 Å in **2**].

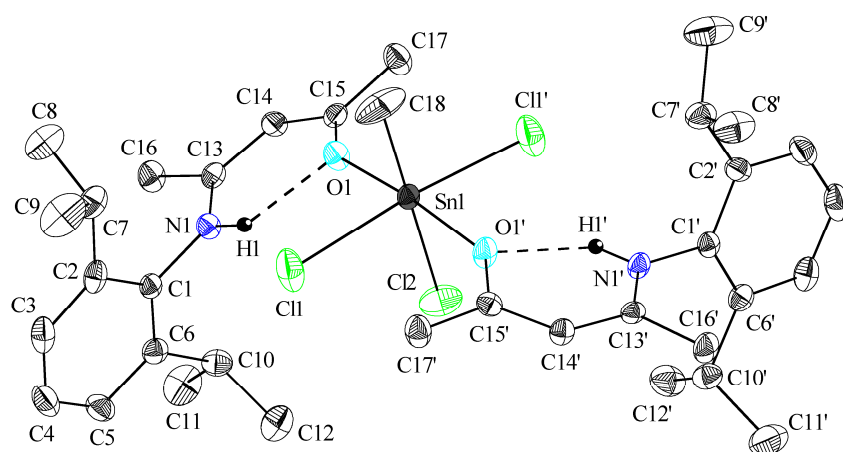


Figure 2. ORTEP representation at 20% probability and atom numbering scheme for **2**. Hydrogen atoms, except H(1) attached to nitrogen, are omitted for clarity [symmetry equivalent atoms (1 – x, y, 1.5 – z) are given by “prime”].

A closer check of the crystal structures of **1** and **2** revealed some supramolecular associations based on intermolecular Cl...H contacts between the molecular units [cf. $\Sigma r_{\text{vdW}}(\text{Cl},\text{H})$ ca. 3.0 Å] [16]. Thus, the molecules of **1** are associated into parallel polymeric chains through weak contacts which involve the axial chlorine atom [Cl(1)...H(17Ca)_{ketimine-methyl} 2.93 Å] (Figure 3) and further weaker inter-chain contacts between the equatorial chlorine atoms from one chain and an aromatic proton from the neighbouring chain [Cl(3)...H(5')_{aryl} 2.93 Å] led to a 3D architecture.

Table 2. Interatomic bond distances (Å) and angles (°) for compound **2**.

Sn(1)–C(18)	2.094(9)	O(1)–C(15)	1.287(6)
Sn(1)–Cl(1)	2.4620(19)	C(15)–C(17)	1.476(8)
Sn(1)–Cl(2)	2.386(3)	C(15)–C(14)	1.389(7)
Sn(1)–O(1)	2.158(4)	C(13)–C(16)	1.501(7)
		C(13)–C(14)	1.384(7)
Cl(1)–Sn(1)–Cl(1')	173.42(13)	N(1)–C(13)	1.321(7)
C(18)–Sn(1)–Cl(2)	180.000(1)	N(1)–C(1)	1.443(7)
O(1)–Sn(1)–O(1')	170.9(2)	N(1)–H(1)	0.848(19)
		O(1)...H(1)	2.01(4)
O(1)–Sn(1)–C(18)	94.56(11)		
O(1)–Sn(1)–Cl(1)	82.73(11)	O(1)–C(15)–C(14)	119.6(5)
O(1)–Sn(1)–Cl(2)	85.44(11)	O(1)–C(15)–C(17)	120.2(5)
O(1)–Sn(1)–Cl(1')	96.74(11)	C(14)–C(15)–C(17)	120.3(5)
		C(13)–C(14)–C(15)	126.1(5)
O(1')–Sn(1)–C(18)	94.56(11)	N(1)–C(13)–C(14)	122.5(5)
O(1')–Sn(1)–Cl(1)	96.74(11)	N(1)–C(13)–C(16)	118.3(5)
O(1')–Sn(1)–Cl(2)	85.44(11)	C(14)–C(13)–C(16)	119.1(5)
O(1')–Sn(1)–Cl(1')	82.73(11)	C(1)–N(1)–C(13)	127.5(4)
		C(1)–N(1)–H(1)	117(3)
Cl(1)–Sn(1)–C(18)	93.29(6)	C(13)–N(1)–H(1)	116(3)
Cl(1)–Sn(1)–Cl(2)	86.71(6)	C(15)–O(1)...H(1)	101(1)
Cl(1')–Sn(1)–C(18)	93.29(6)	N(1)–H(1)...O(1)	134(3)
Cl(1')–Sn(1)–Cl(2)	86.71(6)		
Sn(1)–O(1)–C(15)	144.8(4)		

By contrast, in the crystal of **2** the molecular units are doubly connected (Figure 4) through intermolecular interactions based on the *trans* chlorine atoms [Cl(1)...H(16Ab)_{ketimine-methyl} 2.81 Å], while the third halogen is not involved in any Cl...H contact. No further inter-chain contacts are established in the crystal of **2**.

METHYLTIN(IV) TRICHLORIDE COMPLEXES OF β -KETIMINE...

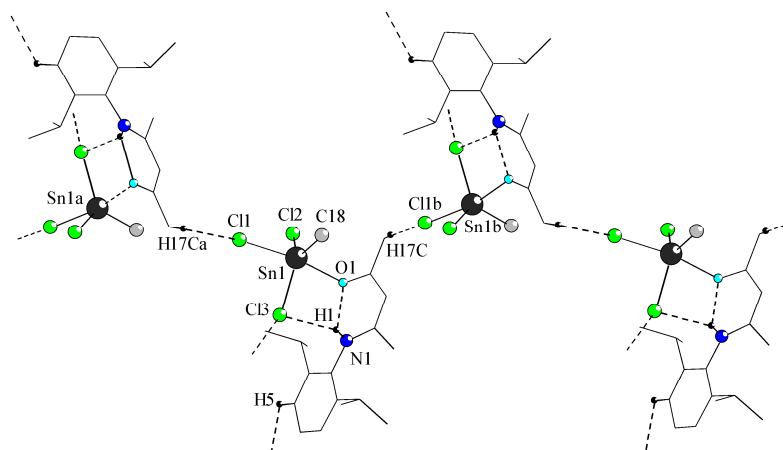


Figure 3. View of a chain polymer based on Cl...H contacts in the crystal of **1** (only H1 attached to nitrogen and hydrogens involved in intermolecular interactions are shown) [symmetry equivalent atoms: Sn1a ($-x, 0.5+y, 1.5-z$) and Sn1b ($-x, -0.5+y, 1.5-z$)].

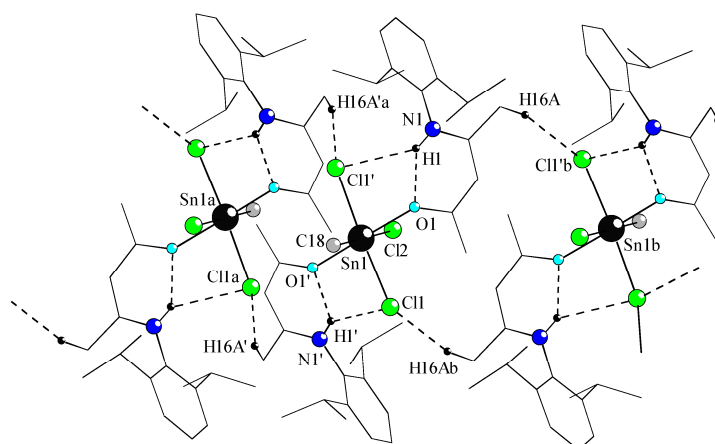


Figure 4. View of a polymeric ribbon-like association based on Cl...H contacts in the crystal of **2** (only H1 attached to nitrogen and hydrogens involved in intermolecular interactions are shown) [symmetry equivalent atoms: Sn1a ($1-x, 1-y, 2-z$); H16A'a ($x, 1-y, 0.5+z$); Sn1b ($1-x, 1-y, 1-z$) and Cl1b' ($x, 1-y, -0.5+z$)].

CONCLUSION

The first 1:1 and 1:2 adducts of an organotin(IV) trihalide with β -ketimine as neutral ligand, *i.e.* $\text{MeSnCl}_3[\text{OC}(\text{Me})\text{CHC}(\text{Me})\text{NH}(\text{C}_6\text{H}_3^i\text{Pr}_{2-2',6'})-4]_n$ [$n = 1$ (**1**), $n = 2$ (**2**)], were isolated as stable, crystalline solids. They were characterized in solution using multinuclear and 2D NMR spectroscopy, the data being

consistent with the proposed formulation. The solid-state molecular structure, as established by single-crystal X-ray diffraction, revealed the monometallic monoconnective nature of the β -ketimine, resulting in distorted trigonal bipyramidal CSnCl_3O (oxygen and chlorine in axial positions) and octahedral CSnCl_3O_2 (*trans* O–Sn–O fragment) for **1** and **2**, respectively.

EXPERIMENTAL SECTION

Solvents were dried and distilled prior to use. MeSnCl_3 was commercially available. The β -ketimine, $\text{OC}(\text{Me})\text{CHC}(\text{Me})\text{NH}(\text{C}_6\text{H}_3^i\text{Pr}_2\text{-}2',6')\text{-}4$, was prepared according to a published procedure [9]. ^1H , ^{13}C and ^{119}Sn NMR spectra, including 2D experiments, were recorded on Bruker Avance 300 instrument using solutions in CDCl_3 . The chemical shifts are reported in δ units (ppm) relative to the residual peak of the deuterated solvent (ref. CHCl_3 : ^1H 7.26, ^{13}C 77.0 ppm) for ^1H and ^{13}C NMR spectra and neat SnMe_4 for and ^{119}Sn NMR spectra. The NMR spectra were processed using the *MestReC* and *MestReNova* software [17].

Preparation of $\text{MeSnCl}_3[\text{OC}(\text{Me})\text{CHC}(\text{Me})\text{NH}(\text{C}_6\text{H}_3^i\text{Pr}_2\text{-}2',6')\text{-}4]$ (1**)**

A solution of MeSnCl_3 in Et_2O (1.85 g, 7.70 mmol) was added to a stirred solution of $\text{OC}(\text{Me})\text{CHC}(\text{Me})\text{NH}(\text{C}_6\text{H}_3^i\text{Pr}_2\text{-}2',6')\text{-}4$ (2 g, 7.71 mmol) in 50 mL Et_2O , at room temperature, and the reaction mixture was stirred for 24 h. Then the solvent was removed in vacuum to give the title compound as a white-yellow powder. Yield: 3.5 g (91%), m.p. 124-125 °C. ^1H NMR (300 MHz, 20 °C): δ 1.19d [6H_A, $-\text{CH}(\text{CH}_3)_2$, $^3J_{\text{HH}}$ 7.2 Hz], 1.21d [6H_B, $-\text{CH}(\text{CH}_3)_2$, $^3J_{\text{HH}}$ 7.4 Hz], 1.54s (3H, SnCH_3 , $^2J_{^{117}\text{SnH}}$ 106.0, $^2J_{^{119}\text{SnH}}$ 110.8 Hz), 1.76s [3H, $\text{CH}_3\text{C}(\text{N})$], 2.25s [3H, $\text{CH}_3\text{C}(\text{O})$], 2.88hept [2H, $-\text{CH}(\text{CH}_3)_2$, $^3J_{\text{HH}}$ 6.8 Hz], 5.29s (1H, $-\text{CH}=\text{}$), 7.21d (2H, $H_{3,5}$, $^3J_{\text{HH}}$ 7.7 Hz), 7.36t (1H, H_4 , $^3J_{\text{HH}}$ 7.7 Hz), 11.85s (1H, $-\text{NH}$). ^{13}C NMR (75.4 MHz, 20 °C): δ 16.47s (SnCH_3), 20.03s [$\text{CH}_3\text{C}(\text{N})$], 22.67s [$-\text{CH}(\text{CH}_3)_2$, (B)], 24.46s [$-\text{CH}(\text{CH}_3)_2$, (A)], 27.23s [$\text{CH}_3\text{C}(\text{O})$], 28.62s [$-\text{CH}(\text{CH}_3)_2$], 97.76s ($-\text{CH}=\text{}$), 123.99s ($\text{C}_{3,5}$), 129.44s (C_4), 131.61s (C_1), 145.15s ($\text{C}_{2,6}$), 170.15s [$\text{CH}_3\text{C}(\text{N})$], 191.61s [$\text{CH}_3\text{C}(\text{O})$]. ^{119}Sn NMR (111.9 MHz): -210.4s.

Preparation of $\text{MeSnCl}_3[\text{OC}(\text{Me})\text{CHC}(\text{Me})\text{NH}(\text{C}_6\text{H}_3^i\text{Pr}_2\text{-}2',6')\text{-}4]_2$ (2**)**

A solution of MeSnCl_3 in Et_2O (0.46 g, 1.92 mmol) was added to a stirred solution of $\text{OC}(\text{Me})\text{CHC}(\text{Me})\text{NH}(\text{C}_6\text{H}_3^i\text{Pr}_2\text{-}2',6')\text{-}4$ (1 g, 3.85 mmol) in 50 mL Et_2O , at room temperature. The reaction mixture was stirred for 24 h and then the solvent was removed in vacuum to give the title compound as a white-yellow powder. Yield: 1.3 g (89%), m.p. 134-135 °C. ^1H NMR (300 MHz, 20 °C): δ 1.17d [12H_A, $-\text{CH}(\text{CH}_3)_2$, $^3J_{\text{HH}}$ 6.8 Hz], 1.21d [12H_B, $-\text{CH}(\text{CH}_3)_2$, $^3J_{\text{HH}}$ 6.9 Hz], 1.53s (3H, SnCH_3 , $^2J_{^{117}\text{SnH}}$ 107.4, $^2J_{^{119}\text{SnH}}$ 112.1 Hz), 1.70s [6H, $\text{CH}_3\text{C}(\text{N})$], 2.19s [6H, $\text{CH}_3\text{C}(\text{O})$], 2.95hept [4H, $-\text{CH}(\text{CH}_3)_2$, $^3J_{\text{HH}}$ 6.8 Hz], 5.25s (2H, $-\text{CH}=\text{}$), 7.20d (4H, $H_{3,5}$, $^3J_{\text{HH}}$ 7.6 Hz), 7.33t (2H, H_4 , $^3J_{\text{HH}}$ 7.7 Hz), 11.94s (2H, $-\text{NH}$). ^{13}C NMR (75.4 MHz, 20 °C): δ 17.07s (SnCH_3), 19.65s [$\text{CH}_3\text{C}(\text{N})$], 22.69s [$-\text{CH}(\text{CH}_3)_2$, (B)],

24.52s [-CH(CH₃)₂, (A)], 28.10s [CH₃C(O)], 28.55s [-CH(CH₃)₂], 96.75s (-CH=), 123.78s (C_{3,5}), 128.89s (C₄), 132.46s (C₁), 145.67s (C_{2,6}), 166.99s [CH₃C(N)], 193.63s [CH₃C(O)]. ¹¹⁹Sn NMR (111.9 MHz): -238.3s.

X-ray Crystallographic Study

Data were collected with a SMART APEX diffractometer (*National Center for X-Ray Diffractometry*, "Babes-Boyai" University, Cluj-Napoca, Romania) at 297 K, using a graphite monochromator to produce a wavelength (Mo-K α) of 0.71073 Å. The crystal structure measurement and refinement data for compounds **1** and **2** are given in Table 3. Absorption correction was applied for both compounds (semi-empirical from equivalents). The structure was solved by direct methods (full-matrix least-squares on F²). All non hydrogen atoms were refined with anisotropic thermal parameters. For structure solving and refinement a software package SHELX-97 was used [18]. The drawings were created with the Diamond program [19].

CCDC-770827 (**1**) and -770826 (**2**) contains the supplementary crystallographic data for this paper. These data can be obtained free of charge at www.ccdc.cam.ac.uk/conts/retrieving.html [or from the Cambridge Crystallographic Data Centre, 12, Union Road, Cambridge CB2 1EZ, UK; fax: (internat.) +44-1223/336-033; E-mail: deposit@ccdc.cam.ac.uk].

Table 3. Crystallographic data for compounds **1** and **2**.

	1	2
chemical formula	C ₁₈ H ₂₈ Cl ₃ NOS	C ₃₅ H ₅₃ Cl ₃ N ₂ O ₂ S
crystal habit	colorless block	colorless block
crystal size [mm]	0.40 x 0.28 x 0.23	0.31 x 0.28 x 0.2
crystal system	orthorhombic	monoclinic
space group	<i>Pbca</i>	<i>C2/c</i>
<i>a</i> [Å]	13.995(3)	15.575(5)
<i>b</i> [Å]	14.977(3)	18.136(6)
<i>c</i> [Å]	22.255(4)	14.000(5)
α [deg]	90	90
β [deg]	90	100.651(6)
γ [deg]	90	90
<i>U</i> [Å ³]	4664.9(15)	3886(2)
<i>Z</i>	8	4
<i>D_c</i> [g cm ⁻³]	1.422	1.297
<i>M</i>	499.45	758.83
<i>F</i> (000)	2016	1576
θ range [deg]	2.19 – 25.00	2.12 – 25.00
μ (Mo K α) [mm ⁻¹]	1.444	0.894
no. of reflections collected	32026	13862
no. of independent reflections	4102 (<i>R</i> _{int} = 0.0648)	3436 (<i>R</i> _{int} = 0.0548)
<i>R</i> ₁ [<i>I</i> > 2 σ (<i>I</i>)]	0.0745	0.0651
<i>wR</i> ₂	0.1373	0.1412
no. of parameters	228	206
no. of restraints	1	1
GOF on <i>F</i> ²	1.327	1.139
largest difference electron density [e Å ⁻³]	0.617, -0.940	0.755, -1.465

ACKNOWLEDGEMENTS

This work was supported by the National University Research Council of Romania (CNCSIS, Research Project Nos. A-709/2006 and TD-340/2007). We also thank the NATIONAL CENTER FOR X-RAY DIFFRACTION ("Babes-Bolyai" University, Cluj-Napoca, Romania) for the support in the solid state structure determinations.

REFERENCES

1. L. Bourget-Merle, M. F. Lappert, J. R. Severn, *Chem. Rev.*, **2002**, *102*, 3031.
2. I. Saur, G. Rima, K. Miqueu, H. Gornitzka, J. Barrau, *J. Organomet. Chem.*, **2003**, *672*, 77.
3. L. W. Pineda, V. Jancik, K. Starke, R. B. Oswald, H. W. Roesky, *Angew. Chem., Int. Ed. Engl.*, **2006**, *45*, 2602.
4. A. P. Dove, V. C. Gibson, E. L. Marshall, H. S. Rzepa, A. J. P. White, D. J. Williams, *J. Am. Chem. Soc.*, **2006**, *128*, 9834.
5. A. Jana, H. W. Roesky, C. Schulzke, A. Doring, T. Beck, A. Pal, R. Herbst-Irmer, *Inorg. Chem.*, **2009**, *48*, 193.
6. A. Jana, H. W. Roesky, C. Schulzke, A. Doering, *Angew. Chem., Int. Ed. Engl.*, **2009**, *48*, 1106.
7. H.-M. Kao, S.-M. Ho, I.-C. Chen, P.-C. Kuo, C.-Y. Lin, C.-Y. Tu, C.-H. Hu, J.-H. Huang, G.-H. Lee, *Inorg. Chim. Acta*, **2008**, *361*, 2792.
8. C. I. Raț, C. Comșa, C. Silvestru, *Acta Crystallogr.*, **2010**, *E66*, m130.
9. C. Comșa, A. Cristea, R. A. Varga, C. Silvestru, *Rev. Roum. Chim.*, **2010**, *in press*.
10. L. Kakaliou, W. J. Scanlon IV, B. Qian, S. W. Baek, M. R. Smith III, D. H. Motry, *Inorg. Chem.*, **1999**, *38*, 5964.
11. J. Kim, J.-W. Hwang, Y. Kim, M. H. Lee, Y. Han, Y. Do, *J. Organomet. Chem.*, **2001**, *620*, 1.
12. V. S. Sergienko, A. D. Garnovskii, M. A. Porai-Koshits, V. L. Abramenko, *Koord. Khim.*, **1985**, *11*, 1407.
13. V. S. Sergienko, V. L. Abramenko, A. B. Ilyukhin, *Zh. Neorg. Khim.*, **1997**, *42*, 945.
14. P. Shukla, J. C. Gordon, A. H. Cowley, J. N. Jones, *J. Organomet. Chem.*, **2005**, *690*, 1366.
15. L. A. Lesikar, A. F. Gushwa, A. F. Richards, *J. Organomet. Chem.*, **2008**, *693*, 3245.
16. J. Emsley, *Die Elemente*, Walter de Gruyter: Berlin, **1994**.
17. *MestReC and MestReNova*, Mestrelab Research S.L., A Coruña 15706, Santiago de Compostela.
18. G. M. Sheldrick, *Acta Crystallogr., Sect. A* **2008**, *64*, 112.
19. *DIAMOND – Visual Crystal Structure Information System*, Crystal Impact, Postfach 1251, 53002 Bonn, Germany, **2001**.

Dedicated to the memory of Prof. dr. Ioan Silaghi-Dumitrescu marking 60 years from his birth

SOLID STATE STRUCTURE OF A NEW NICKEL(II) (3*H*-2-THIOXO-1,3,4-THIADIAZOL-2-YL) THIOACETATO COMPLEX

MONICA M. VENTER^{a,*}, VASILE N. BERCEAN^b, RICHARD A. VARGA^a,
VIOREL SASCA^c, TRAIAN PETRIȘOR JR.^d AND LELIA CIONTEA^d

ABSTRACT. Reaction of the monosodium salt of (3*H*-2-thioxo-1,3,4-thiadiazol-2-yl) thioacetic acid, Na(C₂HN₂S₃CH₂COO)·H₂O (**1**) with NiSO₄·7H₂O produced the corresponding nickel(II) complex, Ni(C₂HN₂S₃CH₂COO)₂·nH₂O where n = 4 (**2**) and 6 (**3**). The product was characterized by means of microanalysis and thermal analysis. The crystal structure of **3** was determined by single-crystal X-ray diffraction. The molecular structure consists of discrete molecular units: one octahedral [Ni(H₂O)₆]²⁺ cation and two organic anions, (C₂HN₂S₃CH₂COO)⁻. The supramolecular structure of **3** is discussed by comparison with that of **1** in its decahydrate, dinuclear form, [Na(C₂HN₂S₃CH₂COO)(H₂O)₄]₂·2H₂O (**1'**), and reveals the self-assembly of the ionic units into alternating columns through N-H···O, O-H···O/S and S···S interactions.

Keywords: mercapto-1,3,4-thiadiazole derivatives; nickel(II) complex; thermal decomposition; crystal structure.

INTRODUCTION

We have an on-going interest in the chemistry of mercapto-aza type heterocyclic compounds (i.e. trithiocyanuric acid, *Bismuthiol I* and *II*), which have been proved valuable candidates for coordination and supramolecular chemistry.¹⁻³ 2,5-Dimercapto-1,3,4-thiadiazole (*Bismuthiol I*, Fig. 1a) displays a flat, rigid molecule with an extensive number of donor atoms which may generate a large variety of coordination and supramolecular patterns, leading in many cases to metallamacrocycles⁴ and metal-organic frameworks (MOFs).^{5,6} In order to improve the flexibility and to increase the coordination versatility

^{a,*} "Babeș-Bolyai" University, Faculty of Chemistry and Chemical Engineering, 400028 Cluj-Napoca, Romania; * monica@chem.ubbcluj.ro

^b "Politehnica" University, Faculty of Industrial Chemistry and Environment Engineering, 300001 Timișoara, Romania

^c Institute of Chemistry of the Romanian Academy, 300223 Timișoara, Romania

^d Technical University, Materials Science Laboratory - Thin Films, 400020 Cluj-Napoca, Romania

of the ligand, the *Bismuthiol I* skeleton was symmetrically extended with two carboxylic pedant arms. The resulting (1,3,4-thiadiazole-2,5-diylthio)diacetic acid, $C_2N_2S_3(CH_2COOH)_2$ (Fig. 1b) was successfully used in its di-anionic form to build new coordination polymers with transition and rare earth metals.⁷⁻¹⁵

Concomitantly, we have initiated structural investigations on the asymmetric homologue, the (3*H*-2-thioxo-1,3,4-thiadiazol-2-yl)thioacetic acid, $C_2HN_2S_3CH_2COOH$ (Fig. 1c) and a large range of coordination and organic derivatives.¹⁶⁻¹⁸

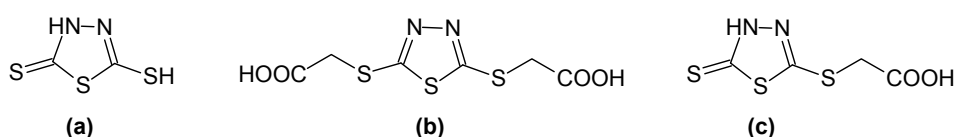


Figure 1. Schematic drawing of *Bismuthiol I* (a), (1,3,4-thiadiazole-2,5-diylthio)diacetic acid (b) and (3*H*-2-thioxo-1,3,4-thiadiazole-2-yl)thioacetic acid (c).

Our choice for asymmetrically substituted *Bismuthiol I* skeleton targets the following objectives: (i) Selective deprotonation of the ligand due to the presence of different acidic groups in the molecule (Fig. 2); (ii) The use of mono-anionic molecule as coordination ligand and/or hydrogen bond donor, which might diversify the self-assembly pattern in solid state; (iii) The use of di-anionic molecule as selective ligand due to the different affinity of the thioamido and carboxylato groups towards metal cations.

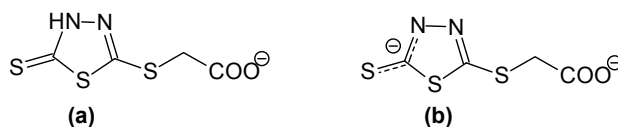


Figure 2. Schematic drawing of the mono- (a) and di-anionic (b) forms of (3*H*-2-thioxo-1,3,4-thiadiazole-2-yl)thioacetic acid.

In the view of the first two objectives, we have reported the general preparative procedure and the vibrational investigation of new metal complexes: $M(C_2HN_2S_3CH_2COO)_n$, $n = 1$, $M = Na$ and K ; $n = 2$, $M =$ group 2 metals, Mn , Co , Ni , Cu and Zn , along with the structural characterization of $[Na(C_2HN_2S_3CH_2COO)(H_2O)_4] \cdot H_2O$.¹⁶⁻¹⁸ The aim of this work is to complete the characterization of the nickel(II) homologue, $Ni(C_2HN_2S_3CH_2COO)_2 \cdot nH_2O$ by means of microanalysis and thermal analysis, as well as single-crystal X-ray diffraction. The supramolecular structure of the title compound is discussed by comparison with that of the starting material in its decahydrate, dinuclear form, $[Na(C_2HN_2S_3CH_2COO)(H_2O)_4]_2 \cdot 2H_2O$ (**1'**). It must be mentioned that the supramolecular structure of **1'** has not been reported previously, along with the molecular structure.¹⁸

RESULTS AND DISCUSSION

The reaction of the monosodium salt of (3*H*-2-thioxo-1,3,4-thiadiazol-2-yl)thioacetic acid, $\text{Na}(\text{C}_2\text{HN}_2\text{S}_3\text{CH}_2\text{COO})\cdot\text{H}_2\text{O}$ (**1**) with $\text{NiSO}_4\cdot 7\text{H}_2\text{O}$ produced the corresponding nickel(II) complex described by the general empirical formula $\text{Ni}(\text{C}_2\text{HN}_2\text{S}_3\text{CH}_2\text{COO})_2\cdot n\text{H}_2\text{O}$ where $n = 4$ (**2**) and 6 (**3**). The hexahydrate product (**3**) is stable only as freshly crystallized solid and turns into the tetrahydrate homologue (**2**) during drying at room temperature. The tetrahydrate product (**2**) shows a much higher stability under ambient conditions, preserving the crystal water.

Thermal analysis: The thermal stability of **2** was checked by thermogravimetric analysis. The simultaneous TG/DTA/DTG curves recorded in N_2 atmosphere are presented in Figure 3.

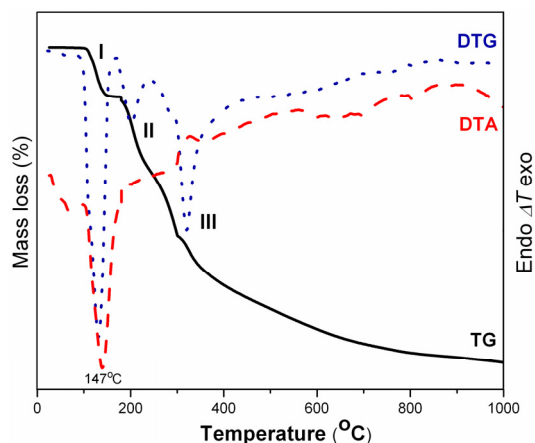


Figure 3. Simultaneous TG/DTA/DTG curves of **2** recorded in N_2 at $10^\circ\text{C}/\text{min}$.

The TG curve shows an initial weight loss (**I**) of -13.03% in the 100–160°C temperature range, which corresponds to the removal of four water molecules per formula unit (Calc. 13.21%). The DTA peak centred at 147°C reveals the most explicit endothermic process assigned to the dehydration step. Above 180°C the anhydrous complex undergoes a continuous mass loss caused by the decomposition of the organic part, and does not end before 1000°C. The major mass loss occurs in the 200–500°C temperature range revealed by the 205°C (**II**) and 318°C (**III**) peaks of the DTG curve. This thermal behaviour is in good agreement with the thermogravimetric analysis reported for Mn(II), Co(II) and rare earth complexes of (1,3,4-thiadiazole-2,5-diylthio)diacetic acid.^{9,10}

For a better elucidation of the decomposition process, the thermogravimetric measurements were repeated in air, coupled with QMS investigation of the evolved gas. The simultaneous TG/DTA and TG-QMS

curves are presented in Figures 4 and 5. Due to the unexpected foaming produced by the energetic decomposition of the complex, the temperature rate was reduced twice, from 10°C to 7.5°C and 5°C, respectively.

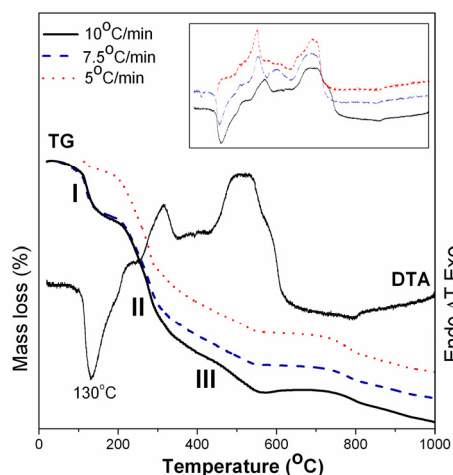


Figure 4. Simultaneous TG/DTA curves of **2** recorded in air at 10, 7.5 and 5°C/min.

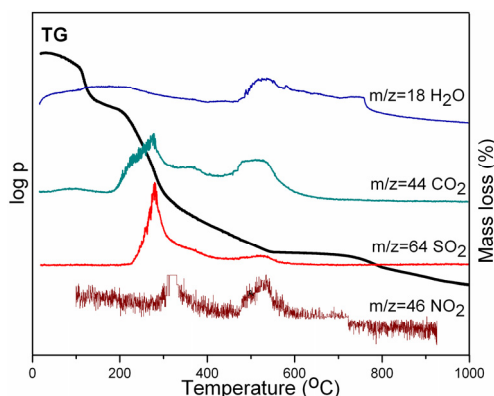


Figure 5. TG-QMS analysis of **2** recorded in air at 7.5°C/min.

The TG/DTA curves recorded at different temperature rates are comparable. However, a slightly decrease in temperature of the DTA peaks can be observed as the temperature rate is reduced.

Similarly to the thermal behaviour in N_2 atmosphere, the first decomposition step in air (I) takes place in the 100–160°C temperature range and corresponds to the complete dehydration of **2** ($4H_2O$, Exp. 13.1–13.3%, Calc. 13.21%) accompanied by an endothermic effect centred at 126–130°C in the DTA plot. The water elimination is confirmed by the broad band of the QMS spectrum located in the mentioned thermal range.

Above 200°C, the anhydrous complex undergoes a complex and continuous mass loss which reveals two major exothermic processes at 281–315 and 509–511°C, respectively in the DTA plots and ends at 550–560°C. The QMS plots reveal the evolution of NO_2 , SO_2 , CO_2 and H_2O , suggesting the combustion of the organic molecules in the 200–550°C range. The overall mass loss of 55% recorded for this temperature range is consistent with the removal of the heterocyclic fragments $C_2HN_2S_2$ (Calc. 42.9%) and part of the pendant chain, C_2H_2 (Calc. 9.5%). The remaining 28.6% solid residue remains stable in the 560–750°C temperature range and may be assigned to $NiSO_4$ (Calc. 28.4%) as a result of the rapid oxidation of the NiS intermediate. Such an oxidation process was proved by running TG/DTA/MS measurements on NiS in O_2 flow.¹⁹

SOLID STATE STRUCTURE OF A NEW NICKEL(II)

Above 750°C the decomposition continues and does not end before 1000°C. The lack of SO₂ evolution beyond 800°C questions the previous formation of NiSO₄. As a consequence, FT-IR and XRD investigations on the solid residue are in progress and will be published elsewhere.

Structural analysis: The crystal structure of the hexahydrate complex, [Ni(H₂O)₆](C₂HN₂S₃CH₂COO)₂ (**3**) was determined by single-crystal X-ray diffraction. Suitable crystals were freshly crystallized from hot water. The molecular structure is presented in Figure 6 and selected metric data are given in Table 1.

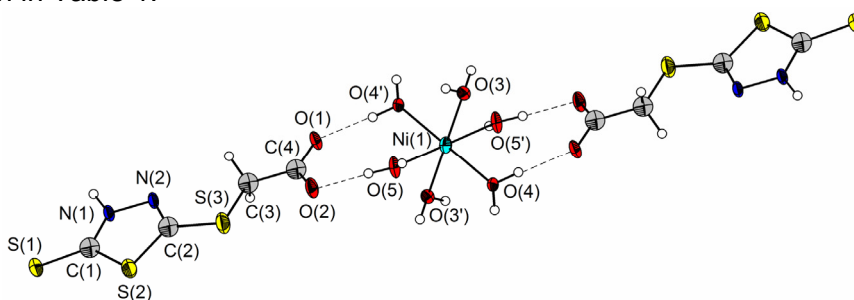


Figure 6. Ortep plot of **3**, showing the labeling used in the text.

Table 1. Selected metric data for **3**.

Bond lengths	[Å]	Bond angles	[deg]
Ni(1)-O(3)	2.054(3)	O(3)-Ni(1)-O(4)	86.37(13)
Ni(1)-O(4)	2.076(3)	O(3)-Ni(1)-O(5)	93.43(14)
Ni(1)-O(5)	2.021(3)	O(4)-Ni(1)-O(5)	90.36(14)
C(1)-N(1)	1.318(6)	C(1)-N(1)-N(2)	118.5(4)
C(2)-N(2)	1.274(6)	C(2)-N(2)-N(1)	109.5(4)
C(1)-S(2)	1.735(5)	C(1)-S(2)-C(2)	88.9(2)
C(2)-S(2)	1.743(4)	N(1)-C(1)-S(2)	108.2(3)
C(1)-S(1)	1.680(4)	N(2)-C(2)-S(2)	114.9(3)
C(2)-S(3)	1.745(4)	C(2)-S(3)-C(3)	98.1(2)
C(4)-O(1)	1.262(6)	O(1)-C(4)-O(2)	126.8(4)
C(4)-O(2)	1.230(6)		

The crystal structure of **3** will be discussed by comparison with that of [Na(C₂HN₂S₃CH₂COO)(H₂O)₄]₂·2H₂O (**1'**), the later being – to the best of our knowledge – the only crystallographic evidence for the (3*H*-2-thioxo-1,3,4-thiadiazol-2-yl)thioacetic moiety.¹⁸ Moreover, the supramolecular structure of **1'** has not been reported previously.

The molecular structure of **3** reveals the presence of three ionic units, a $[\text{Ni}(\text{H}_2\text{O})_6]^{2+}$ cation and two $(\text{C}_2\text{HN}_2\text{S}_3\text{CH}_2\text{COO})^-$ anions, associated only through O-H \cdots O hydrogen bonding (O \cdots O 2.608 – 2.629 Å, O-H \cdots O 177.29 – 177.39°) designated $R_2^2(7)$. The asymmetric unit of **3** consists of one half of the inorganic complex cation and one organic anion, the remainder being generated by an inversion center located at the metal atom. The structure of the $[\text{Ni}(\text{H}_2\text{O})_6]^{2+}$ unit is largely unexceptional. The nickel(II) cation lays in an octahedral environment described by six water molecules. The very narrow range of the Ni-O bond lengths [2.021(3) – 2.076(3) Å], as well as the almost ideal O-Ni-O bond angles [86.37(13) – 93.43(14)°] support the proposed coordination geometry.

The structure of $(\text{C}_2\text{HN}_2\text{S}_3\text{CH}_2\text{COO})^-$ is comparable with that of the corresponding ligand coordinated to sodium through the S(3) atom in **1'**. Thus, the structure of the heterocyclic unit is governed by the planarity of the dimercapto-thiadiazole skeleton, $\text{C}_2\text{N}_2\text{S}_3$ [Ex. C(1)-N(1)-N(2)-C(2) 1.5(6)°; N(1)-C(1)-S(2)-C(2) -0.2(3)°; S(1)-C(1)-N(1)-N(2) 179.1(3)°; S(3)-C(2)-N(2)-N(1) 179.9(3)°] and the thione tautomeric form of the thiocyanate fragment [C(1)-S(1) 1.680(4) Å]. The later structural feature is supported by comparison with similar CS thione groups in **1'** [1.667(3) Å] and related *Bismuthiol II* complexes [1.653(3) – 1.668(3) Å].² The pendant arm of the organic anion displays an uncoordinated and strongly delocalized carboxylato group [C-O 1.230(6) – 1.262(6) Å]. Despite the expected flexibility, the acetato chain is almost co-planar with the heterocycle [N(2)-C(2)-S(3)-C(3) -11.3(4)°; S(3)-C(3)-C(4)-O(2) 4.5(6)°].

The formation of the 3D supramolecular structure of **3** can be described by three association tendencies: the self-assembly of the organic anions, the self-assembly of the hydrated nickel cations, and the self assembly of the organic / inorganic parts.

The self-assembly of the $(\text{C}_2\text{HN}_2\text{S}_3\text{CH}_2\text{COO})^-$ anions is driven by two distinctive interactions. First, the N(1)-H(1) \cdots O(1) hydrogen bonding [N(1) \cdots O(1) 2.721 Å; N(1)-H(1) \cdots O(1) 170.07°] generates dimer aggregates describing ring patterns which contain a total of 16 atoms, two of them donors and two acceptors, and hence designated $R_2^2(16)$ (Fig. 7a).²⁰ The same motif can be identify in the crystal structure of **1'** [N(1) \cdots O(1) 2.715 Å; N(1)-H(1) \cdots O(1) 178.59°] (Fig. 7b). The dimer aggregates further associate through short S \cdots S interactions, involving the thione S(1) atom in the case of **3** [S(1) \cdots S(1) 3.458 Å] and the S(2)/S(3) atoms in the case of **1'** [S(2) \cdots S(3) 3.420 Å]. Similar S \cdots S interactions (3.45 – 3.71 Å) have been reported for related *Bismuthiol II* complexes.²

The self-assembly of the $[\text{Ni}(\text{H}_2\text{O})_6]^{2+}$ cations in **3** is driven exclusively by water directed hydrogen bonding, leading to columns which run parallel to each other along the a axis (Fig. 8a). The inorganic and organic aggregates are alternatively linked through O-H \cdots O and O-H \cdots S interactions, producing a

SOLID STATE STRUCTURE OF A NEW NICKEL(II)

three dimensional supramolecular structure. Similarly, the 3D supramolecular structure of **1'** (Fig. 8b) shows hydrated, dinuclear sodium cation columns along the b axis, alternating with the organic aggregates.

Only in this case, the connection between the organic and inorganic parts consists of both O-H \cdots O hydrogen bonding and S \rightarrow Na coordination.

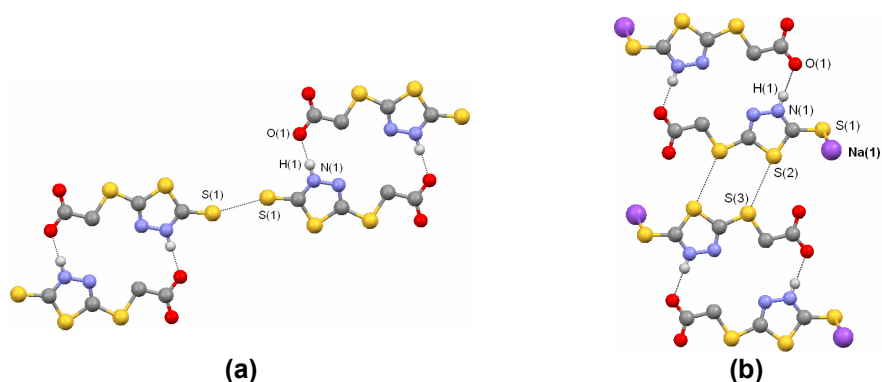


Figure 7. Self-assembly pattern of organic anions in **3** (a) and **1'** (b). Some of the hydrogen atoms were omitted for clarity.

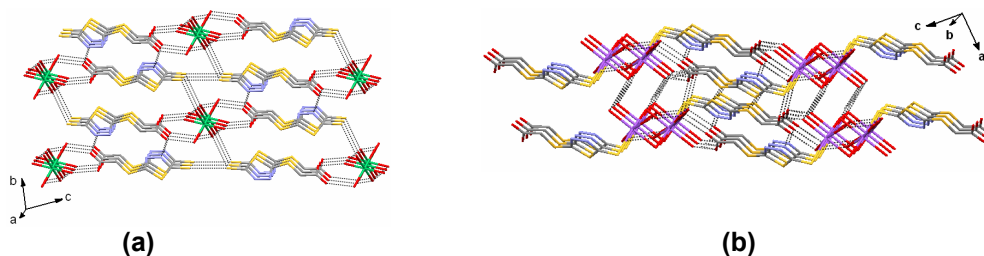


Figure 8. The 3D supramolecular structure of **3** (a) and **1'** (b). Hydrogen atoms were omitted for clarity.

CONCLUSIONS

One new nickel complex of the mono-deprotonated (3H-2-thioxo-1,3,4-thiadiazol-2-yl)thioacetic acid was prepared and characterized in solid state by thermal analysis and single-crystal X-ray diffraction. The thermal decomposition of the tetrahydrate complex was carried out both in N₂ and air atmosphere and revealed the water content, as well as the organic unit combustion. However, none of these measurements were able to prove the formation of nickel chalcogenides below 1000°C. The crystal structure of the hexahydrate complex shows uncoordinated anionic ligands and [Ni(H₂O)₆]²⁺

cations which self-assemble through hydrogen bonding and S...S interactions, generating a 3D supramolecular structure. A similar structural behaviour was evidenced in the crystal structure of the starting material.

EXPERIMENTAL SECTION

Methods and materials

Elemental analyses were obtained on a VarioEL apparatus from Elementar Analysensysteme GmbH. Melting points (uncorrected) were measured in the 30-360°C range using a KRUSS KSPI digital apparatus. Thermal decompositions (TG/DTA/DTG) were carried out using a TGA/SDTA 851-LF 1100 Mettler apparatus. The samples with mass of about 30 mg were placed in alumina crucible of 150 µl and heated non-isothermally from 25°C to 1000°C with a heating rate of 10°C·min⁻¹, under a nitrogen flow of 50 ml·min⁻¹, with the exception of a short isothermal period of 5 min. at 180°C necessary for a better delimitation of decomposition processes. Alternatively, TG/DTA analysis was carried out in air, in the temperature range 20-1000°C, at rates of 5, 7.5 and 10°C/min, coupled with a quadrupole mass spectrometer (QMS) using an atmospheric sampling residual gas analyzer 200 QMS Stanford Research System. Drawings were created with the ORIGIN graphing and data analysis software package.²¹

The inorganic salts were purchased from commercial sources (Merck) as analytical pure substances and were used with no further purification. The preparation of (3*H*-2-thioxo-1,3,4-thiadiazol-5-yl)thioacetic acid was reported elsewhere.²²

Synthesis

Sodium (3H-2-thioxo-1,3,4-thiadiazol-2-yl)thioacetate monohydrate (1). Solid (3*H*-2-thioxo-1,3,4-thiadiazol-2-yl)thioacetic acid (50 g, 0.24 mol) was added in small portions, under continuous stirring, to a clear solution of NaHCO₃ (20.2 g, 0.24 mol / 220 mL H₂O). After the fizzing stopped, the reaction mixture was heated slowly below boiling point to complete the reaction and dissolve the solid material. The resulting hot solution was filtered and cooled to deposit the product as colourless microcrystalline solid, which was further recrystallized from hot distilled water as colourless plates. The product is relatively stable in open atmosphere, at room temperature, as dry solid. In these conditions, it dehydrates continuously until the water content drops to monohydrate. It is soluble in hot water as well as alcohols and dmsO. Yield: 47.8 g, 80%; mp: 234-6°C (dec). Microanalysis: found (calc. for C₄H₅N₂S₃O₃Na, MW 248.283) C 19.29 (19.35), H 1.76 (2.03), N 11.09 (11.28).

Nickel(II) (3H-2-thioxo-1,3,4-thiadiazol-2-yl)thioacetate tetrahydrate (2). Aqueous solutions of NiSO₄·7H₂O (0.56 g, 2 mmol / 10 mL H₂O) and Na(C₂N₂HS₃CH₂COO)·H₂O (1 g, 4 mmol / 10 mL H₂O) were stirred at room temperature for 30 minutes. The green precipitate was filtered and further

recrystallized from hot distilled water as green plates. Some of the crystals were suitable for X-ray diffraction analysis. The product is stable in open atmosphere, at room temperature, soluble in hot water and insoluble in common organic solvents. Yield: 0.49 g, 49%; mp: 97-9°C (dec). Microanalysis: found (calc. for $C_8H_{14}N_4S_6O_8Ni$, MW 545,306) C 17.63 (17.62), H 2.23 (2.58), N 9.82 (10.27).

Crystallography

Crystallographic data for $[Ni(H_2O)_6](C_2HN_2S_3CH_2COO)_2$ (**3**) are summarized in Table 2. The single-crystal X-ray diffraction analysis was performed on a Bruker SMART APEX system (Babes-Bolyai University of Cluj-Napoca, Romania) using graphite monochromated Mo-K α radiation ($\lambda = 0.71073$ Å). The software package SHELX-97 was used for structure solving and refinement.²³ Non-hydrogen atoms were refined anisotropically without exception. The hydrogen atoms were refined with a riding model and a mutual isotropic thermal parameter, except the hydrogen atom of the heterocycle which was found in a difference map and refined with a N–H distance of 0.95(6) Å. Drawings were created with the MERCURY and DIAMOND graphic visualization softwares.^{24,25} **Supplementary material:** CCDC reference number 775075. Free information and copies: The Director, CCDC, 12 Union Road, Cambridge CB2 1EZ, UK (fax: +44-1223-336033; email: deposit@ccdc.cam.ac.uk or www: <http://www.ccdc.cam.ac.uk>).

Table 2. Crystal data and structure refinement for **3**.

Empirical formula	$C_8H_{18}N_4O_{10}S_6Ni$
Formula weight	581.33
Temperature / K	297(2)
Crystal system; Space group	Triclinic; P-1
a / Å	4.8707(6)
b / Å	8.2334(10)
c / Å	14.1470(17)
α / °	98.622(2)
β / °	99.405(2)
γ / °	104.016(2)
Volume / Å ³	532.29(11)
Z	1
Absorption coefficient / mm ⁻¹	1.553
Reflections collected / unique	5496 / 2159 [R(int) = 0.0308]
Refinement method	Full-matrix least-squares on F ²
Final R indices [$I > 2\sigma(I)$]	R1 = 0.0589, wR2 = 0.1165
R indices (all data)	R1 = 0.0671, wR2 = 0.1198
Goodness-of-fit on F ²	1.260

ACKNOWLEDGMENTS

The authors thank The National University Research Council Romania for financial support during the course of this work (Grant CNCSIS-A/2007-2008, 14-25/1449).

REFERENCES

1. I. Haiduc, M.F. Mahon, K.C. Molloy, M.M. Venter, *J. Organomet. Chem.*, **2001**, 627, 6.
2. V. Bercean, C. Crainic, I. Haiduc, M.F. Mahon, K.C. Molloy, M.M. Venter, P.J. Wilson, *J. Chem. Soc., Dalton Trans.*, **2002**, 1036.
3. M.F. Mahon, K.C. Molloy, M.M. Venter, I. Haiduc, *Inorg. Chim. Acta*, **2003**, 348, 75.
4. C. Ma, F. Li, D. Wang, H. Yin, *J. Organomet. Chem.*, **2003**, 667, 5.
5. J.D.E.T. Wilton-Ely, A. Schier, H. Schmidbauer, *Organomet*, **2001**, 20(10), 1895.
6. J.D.E.T. Wilton-Ely, A. Schier, M.W. Mitzel, H. Schmidbauer, *Inorg. Chem*, **2001**, 40, 6266.
7. Y.T. Wang, Y.T. Fan, Y.L. Wang, Y.H. Li, H.W. Hou, H.Y. Zhang, *Synth. React. Inorg. Met.-Org. Nano-Metal Chem.*, **2007**, 37(1), 7.
8. Y.T. Wang, Y.L. Wang, Y.T. Fan, H.W. Hou, H.Y. Zhang, *Synth. React. Inorg. Met.-Org. Nano-Metal Chem.*, **2007**, 37(4), 241.
9. Y.T. Wang, L.P. Zhang, Y.T. Fan, H.W. Hou, X.Q. Shen, *Inorg. Chim. Acta*, **2007**, 360, 2958.
10. D.X. Xue, W.X. Zhang, X.M. Chen, *J. Mol. Struct.*, **2008**, 877, 36.
11. Y.T. Wang, X.Q. Shen, Y.T. Fan, H.C. Yao, H.W. Hou, *Supramol. Chem.*, **2008**, 20(5), 501.
12. Y.T. Wang, M.C. YIN, Y.T. Fan, H.W. Hou, *J. Coord. Chem.*, **2008**, 61(6), 907.
13. Y.H. Yu, C. He, G.F. Hou, J.S. Gao, H.K. Zhang, *Acta Cryst.*, **2008**, E64, m794.
14. Y.T. Wang, Y. Xu, *J. Solid State Chem.*, **2009**, 182, 2707.
15. X.M. Yang, M.C. Yin, D.G. Ding, Y.T. Fan, *Synth. React. Inorg. Met.-Org. Nano-Metal Chem.*, **2009**, 39(1), 36.
16. M.M. Venter, V. Chis, S. Cinta Pinzaru, V.N. Bercean, M. Ilici, I. Haiduc, *Studia Univ. Babeș-Bolyai, Ser. Chem.*, **2006**, LI(2), 65.
17. M.M. Venter, A. Pascui, V.N. Bercean, S. Cinta Pinzaru, *Studia Univ. Babeș-Bolyai, Ser. Chem.*, **2007**, LII(1), 55.
18. M.M. Venter, V.N. Bercean, M. Ilici, S. Cinta Pinzaru, *Rev. Roum. Chim.*, **2007**, 52(1-2), 75.
19. J.G. Dunn, C.E. Kelly, *J. Therm. Anal. Calorim.*, **1977**, 12(1), 43.
20. J. Bernstein, R.E. Davis, L. Shimoni, N.L. Chang, *Angew. Chem. Int. Ed. Engl.*, **1995**, 34, 1555.
21. *ORIGIN – Graphing and Data Analysis Software Package*, OriginLab Corporation, One Roundhouse Plaza, Northampton, MA 01060 USA, **2008**.
22. M.M. Venter, S. Cinta Pinzaru, I. Haiduc, V. Bercean, *Studia Univ. Babeș-Bolyai, Physica*, **2004**, XLIX(3), 285.
23. G. M. Sheldrick, *Acta Crystallogr., Sect. A*, **2008**, 64, 112.
24. C.F. Macrae, P.R. Edgington, P. McCabe, E. Pidcock, G.P. Shields, R. Taylor, M. Towler, J. van de Streek, *J. Appl. Cryst.*, **2006**, 39, 453.
25. *DIAMOND – Visual Crystal Structure Information System*, Crystal Impact, Postfach 1251, 53002 Bonn, Germany, **2001**.

Dedicated to the memory of Prof. dr. Ioan Silaghi-Dumitrescu marking 60 years from his birth

AN IMPROVED SAMPLE PREPARATION OF STARCH-BASED FOODS FOR SYNTHETIC DYES ANALYSIS

SIMONA CODRUȚA COBZAC^{*}, DORINA CASONI, COSTEL SÂRBU

ABSTRACT. The purpose of this study is to develop a simple and fast sample preparation method for synthetic dyes determination from starch-based foods (puddings). Because at sample preparation stage the main problem is to extract quantitatively the dye unchanged, seven different extraction systems were tested. The extractions were carried out using two different techniques: magnetic stirring and sonication. Quantitative determinations were performed using molecular absorption spectrometry and standard calibration method. The efficiency of extraction of eight synthetic food dyes from spiked corn starch samples was evaluated in terms of recovery. The most efficient extraction solvent proved to be ammonia 25%, the recoveries for all dyes (exception for brilliant blue FCF dye) being higher than 92%. Ultrasounds assisted solvent extraction proved to be more efficient than magnetic stirring, leading to a recovery improvement up to 5% in most cases. Finally, commercial pudding samples were analyzed to assess applicability of this extraction procedure. The results obtained for determination of tartrazine in six identical samples showed no significant difference in terms of extracted amount of dye.

Keywords: *food dyes; starch-based foods; solvents extraction; extraction efficiency; ultrasounds assisted extraction; molecular absorption spectrophotometry*

INTRODUCTION

Foods additives have been used for centuries to enhance the quality of food products despite they are increasingly viewed as compounds with toxicological risk [1]. Synthetic dyes, a very important class of food additive, are commonly used in processed foodstuff to compensate the loss of natural colour which is destroyed during processing and storage or to provide the desired colored appearance. By comparing with natural dyes, synthetic dyes have several advantages such as high stability to oxygen, pH and light, great colors variety and color uniformity, low microbiological contamination

^{*} *Universitatea Babeș-Bolyai, Facultatea de Chimie și Inginerie Chimică, Str. Kogălniceanu, Nr. 1, RO-400084 Cluj-Napoca, Romania, codruta.cobzac@yahoo.com*

and relatively lower production costs. The use of food dyes is at least controversial because they are added only for esthetical role and some of these substances pose a potential risk to human health, especially to children that are considered a very vulnerable consumer group [2]. Specific directives in each country strictly regulate the use of synthetic food dyes, and safety data such as the acceptable daily intake have been repeatedly determined and evaluated by Food and Agricultural Organization (FAO) and World Health Organization (WHO) [3]. Consequently, accurate and reliable methods for the determination of synthetic dyes are required for assurance of food safety. While titrimetric and gravimetric methods are allowed for determining pure dyes content of color additives, spectrophotometric methods have been listed in the AOAC Official Methods of analysis since 1960 [4]. The speed, ease and efficacy of the spectrophotometric methods make them of particular value. Spectrophotometric methods often prove inadequate, in the analysis of real samples due to the overlapping of spectral absorption maxima. This drawback can be overpassed using complex spectrophotometric methods with chemometric data interpretation [5-7]. Another approach for food colorants determination can be solid-phase spectrometry when the dyes are adsorbed on Sephadex DEAE A-25 or C18 silica gel and the absorbance can be directly measured [8, 9]. Due to their properties, synthetic food colorants can be analyzed also by electrochemical techniques like absorbtive voltametry [10, 11] and polarography [12].

Chromatographic methods are playing an important role in dyes analysis [13]. The advantage of this technique consists in separation of colorant one from each other, followed by spectrophotometric VIS detection [14]. Generally RP [15, 16] ion-pair [17] and ion-chromatography [18] are used. Electrophoretic techniques are also used on large scale [19-21]

Due to the complexity of food matrices the isolation of dyes from sample is more problematic to the chemist than the determination step. Dyes isolation techniques have typically depended upon one of three general methodologies: leaching, liquid-liquid extraction, or active substrate absorption. As Marmion notes [22], there is no technique that can be used to all types of sample matrices, thus the chemist requires comprehensive knowledge to choose the technique and to optimize the extraction conditions. For example, the presence of high affinity binding agents such proteins, demand removal of the interfering matrix [23]. Various methods are used for the extraction of dyes from different foodstuff matrices [14, 24]. Given most analytical instruments handle liquid samples, attention is being paid to improving solids sample preparation. If the sample is water soluble, simple dissolution is carried out by manual or mechanical stirring, either with heating or at room temperature. Usually solid-phase extraction is used for purification [20, 25-27]. If the sample is insoluble (e.g., puddings, powder for ice-cream) quantitative extraction of dyes must be performed. Besides the simple liquid-solid extraction,

also more complex extraction techniques are available [28]. In recent decades ultrasound has established an important place in different field (industrial, environmental, medical) and its applications has a growing trend in analytical chemistry [29].

Taking in account these considerations, the aim of this study was to find the optimum solvent system and the best technique that ensure the quantitative extraction of dyes from starch-based foods. A detailed study concerning synthetic food dyes extraction from starch was not yet performed.

RESULTS AND DISCUSSION

Absorption spectra of dyes

The analyzed food synthetic dyes are organic substances with high solubility in water conferred by the presence of at least one sulfonic group (salt forming moiety). They can be classified by the nature of chromophoric group in quinoline, azo, and triarylmethane. Depending on the pH values they can be more or less ionized. By careful visual examination of the VIS spectra it is apparent that they presenting isosbestic points, and changes of the wavelength (λ_{\max}) and absorbance (A_{\max}) induced by the some of pH value. In alkaline extreme environment it can be observed a decreasing of absorbance (A_{\max}) for all colorants. There is although a pH range in which A_{\max} and λ_{\max} do not vary with pH value (Table 1). For good experimental results it is important that the absorbance measurements to be performed within this range. As was pointed out in the experimental part the residuum was dissolved in water, the pH of resulted solution being adjusted in this range.

Table 1. The stability range and specific wavelength λ_{\max} for studied dyes.

No.	Compounds	Stability pH range	λ_{\max} (nm)
1	Quinoline Yellow WS (E104)	1-9	415
2	Tartrazine (E102)	2-8	425
3	Sunset Yellow FCF (E110)	1-9	480
4	Azorubine (E122)	1-7	515
5	Ponceau 4R (E124)	1-9	507
6	Amaranth (Dye) (E123)	1-9	520
7	Brilliant Blue FCF (E133)	3-11	630
8	Patent Blue V (E131)	5-7	640

Recovery experiments and analysis of spiked samples

The extraction efficiency was evaluated in terms of recovery, calculated as ratio of the determined quantity to that used for preparing the spiked

sample. The extracted quantity was calculated on the basis of the sample absorbance and calibration equation (Table 2) at the maximum wavelength that corresponds to each dye.

The efficiency of extraction solvents was tested on the synthetic spiked samples processed as mentioned above. There were used seven different extraction systems, chosen on the basis of dyes solubility, ionic force and pH value.

Table 2. The linear range and calibration equations for studied dyes.

No	Compounds	Linear range (ppm)	Calibration equations	R ²
1	Quinoline Yellow E104)	2-20	$y = 0.0670x + 0.0304$	0.9985
2	Tartrazine (E102)	2-40	$y = 0.0349x + 0.0085$	0.9999
3	Sunset Yellow (E110)	3-20	$y = 0.0543x - 0.0077$	0.9991
4	Azorubine (E122)	2-15	$y = 0.0380x - 0.0473$	0.9981
5	Ponceau 4R (E124)	4-15	$y = 0.0374x - 0.0032$	0.9985
6	Amaranth (Dye) (E123)	4-15	$y = 0.0393x - 0.0119$	0.9987
7	Brilliant Blue (E133)	1-8	$y = 0.1359x + 0.0181$	0.9997
8	Patent Blue V (E131)	1-10	$y = 0.1679x + 0.0559$	0.9985

The obtained results and expanded uncertainty U ($\pm 2s$) for 95% are presented in Table 3. The profiles of recovery (Figure 1) illustrate that the high solubility of food dyes in water is not the most important parameter concerning the efficiency of extraction. This behaviour might be attributed to the specific interaction with starch. When pH was modified and ionic strength increased (extraction system 2 and 6) no improving of recovery was observed. Also, using methanol as extraction system, the extraction efficiency has not significantly increased. All these findings indicate that the interactions between starch and dyes are complex and extraction procedure is very difficult to be optimized. The best results obtained using ammonia 25% could be explained by a strong desorption effect generated by the resulted ammonium salts or by blocking the adsorption sites. Much more, the effect of ammonia is very similar in all cases and this fact is well illustrated in Fig. 1. In addition, as we can observe in Table 3, the best recoveries (higher than 92% for all studied dyes exception for brilliant blue) were obtained by using ammonia 25% as extraction solvent. For azorubine and ponceau 4R good recoveries (92.54% respectively 96.05%) were also obtained with methanol-ammonia 25% (9:1, v/v) mixture.

Table 3. Dyes recovery and expanded uncertainty U for 95% (n=6).

Compounds (Abbr.)	Recovery(%) ± U						
	Solvents extraction Systems						
	Water	Acetic buffer (pH=4)	MeOH	MeOH-HCl (9:1, v/v)	MeOH-NH ₃ (9:1, v/v)	Ammonia buffer (pH=10)	Ammonia (25%)
Quinoline (E104)	3.3±0.6	2.5±0.3	5.3±0.7	4.0±0.8	2.6±0.6	54.8±5.0	95.5±9.2
Tartrazine (E102)	71.9±10.0	28.4±3.8	10.2±5.7	6.9±1.4	9.0±1.7	13.6±3.4	92.2±10.8
Sunset Yellow (E110)	31.5±5.3	12.9±2.2	12.9±1.7	14.5±2.5	14.8±1.7	20.± 3.3	93.5±12.1
Azorubine (E122)	23.9±4.1	2.6±0.5	5.6±0.6	6.1±1.2	92.5±9.6	10.1±1.4	96.1±6.2
Ponceau 4R (E124)	44.4±7.0	2.3±0.4	7.3±1.4	5.9±1.4	96.0±11.6	69.6±12.7	97.8±6.3
Amaranth (E123)	64.9±9.5	78.7±9.4	49.6±10.6	53.7±10.3	55.2±8.9	65.1±7.3	91.2±6.9
Brilliant Blue (E133)	36.9±6.3	46.3±4.6	30.6±6.0	35.9±6.4	36.0±8.4	37.40±9.9	84.9±4.3
Patent Blue V (E131)	78.7±12.0	81.2±0.5	55.1±9.5	46.5±10.0	54.3±10.0	68.5±15.2	92.2±3.2

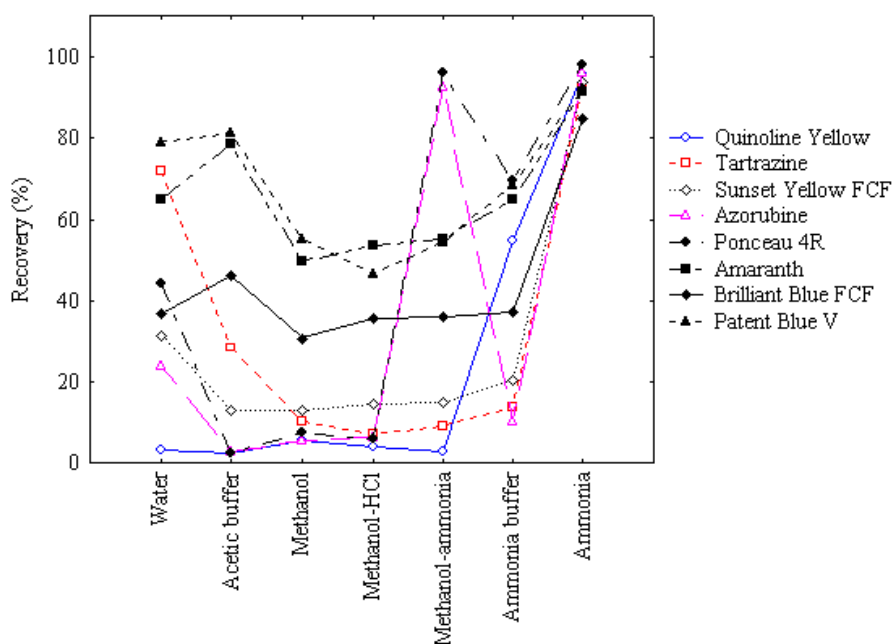


Figure 1. The influence of extraction system on the dyes recovery.

Dyes ultrasounds assisted extraction from spiked samples and puddings

The ultrasounds extraction efficiency of each colorant was tested using only ammonia 25% as extraction solvent. Absorption spectra of all extracts do not show degradation or displacement of maximum absorption wavelength. The obtained recovery data are presented in Table 4.

Table 4. Levels of dyes recovery obtained by ultrasounds assisted extraction using ammonia (25%) as solvent system.

No.	Name of compounds	Recovery(%) \pm U
1	Quinoline Yellow WS	98.50 \pm 2.1
2	Tartrazine	99.25 \pm 2.0
3	Sunset Yellow FCF	98.63 \pm 3.2
4	Azorubine	99.62 \pm 1.7
5	Ponceau 4R	99.63 \pm 1.3
6	Amaranth Dye	98.12 \pm 2.0
7	Brilliant Blue FCF	85.23 \pm 3.6
8	Patent Blue V	93.39 \pm 2.2

By comparing the efficiency of assisted ultrasounds extraction (Table 3) with that obtained by mechanical stirring (Table 2), it can be observe that by applying ultrasounds assisted extraction, the recovery is significantly improved, more than 5% in most cases. The low "s" values illustrate a good precision of determinations.

In order to assess reliability of this extraction procedure to the food dyes analysis from real samples, determination of tartrazine from vanilla pudding was performed. Six identical samples (0.5000 g) were processed by the protocol described above using ammonia 25% as extraction solvent. Tartrazine was identified from the absorption spectra and its amount was calculated on the basis of the sample absorbance and calibration equation at the specific wavelength. The average concentration of tartrazine for six identical commercially vanilla pudding samples was 144.84 \pm 0.05 mg/kg.

CONCLUSIONS

The results obtained in this study concerning the extraction of dyes from starch-based foods demonstrated that the most efficient system is ammonia 25%, in this case the recovery being higher than 92% for all studied food dyes (exception for brilliant blue FCF dye); for azorubine and ponceau 4R good recoveries (92.54% respectively 96.05%) were obtained also by using methanol-ammonia 25% (9:1,v/v) mixture as extraction system.

Ultrasounds assisted extraction proved to be a technique more efficient than simple mechanical stirring extraction, leading to a recovery improvement up to 5% in most cases. The technique developed in this paper was successfully applied for tartrazine determination from commercially pudding. The proposed method was found to be relative simple, precise, sensitive and accurate and might be efficiently applied for the determination of tartrazine and other food dyes in commercial available puddings.

EXPERIMENTAL SECTION

Chemicals

Methanol and Titrisol buffer solutions having pH from 1 to 12 and an error $\Delta\text{pH} = \pm 0.01$ were acquired from Merck (Darmstad, Germany). Acetic acid (glacial), ammonia 25% and hydrochloric acid fuming (37%) were from Chemical Company (Iasi, Romania). Natrium acetate and ammonium chloride solid salts used for preparation of buffer solutions were purchased from Chimopar (Bucuresti, Romania). Solid dyes standards (Quinoline Yellow WS, Tartrazine, Sunset Yellow FCF, Ponceau 4R, Azorubine, Erythrosine, Amaranth, Brilliant Blue FCF, and Patent Blue V) were purchased from Merck or Fluka. Standard stock solutions of all dyes (100 mg/mL) were prepared by weighting appropriate amounts of solid colorant and dissolving them in deionized water. Working solutions of individual dyes were prepared by dilution of aliquots of stock solutions. Corn starch and vanilla pudding were purchased from local market.

Methods

VIS spectra and calibration curve determination

The absorbance spectra in VIS for each colorant was plotted for different pH values : 1 ; 2; 3; 4; 5; 6,86; 8; 9; 10; 11, and 12, at a concentration of $2 \times 10^{-5} \text{M}$. The solution for calibration curves were prepared for each dye by successive dilution of stock aqua solution within the range 1-40 ppm. The absorbance was measured at specific λ_{max} of each compound.

Instrumentation

Ultrasound extractions were performed using a Transsonic T310 bath at 35 kHz. Spectrophotometric measurements were performed using a Jasco, V-550, UV/VIS spectrophotometer.

Extraction procedures

Eight different synthetic samples (0.1 mg/g), one for each of the studied dyes, were prepared by mixing of 30 g starch powder with 30 mL of aqueous dye solution (0.1mg/mL). After the evaporation of water at room temperature,

the powders were homogenized and portions of 0.5000 g from each were precisely weighted. Each sample was mixed with 10 mL of extraction solvent and homogenized by magnetic stirring for 15 min. There were used seven extraction systems: 1-water; 2-acetic buffer (pH = 4); 3-methanol; 4-methanol-hydrochloric acid (6M) (9:1, v/v); 5-methanol-ammonia 25% (9:1, v/v), 6-ammonia buffer (pH = 10) and 7-ammonia 25%. In each case the slurry was passed through an inert filtering cartridge - like that used in solid phase extraction but filled with very fine particle of powder glass as stationary phase. The cartridge was previously washed with 3 mL of methanol and 5 mL of extraction solvent in each case. After filtration, the cartridge was washed with extraction solvent (5 mL). The effluent was evaporated to dryness at 40 °C in a stove and the residuum was dissolved in 5 mL water. The maximum absorbance was measured at specific wavelength for each dye, the extracted quantity being determined using standard calibration method. For all of the studied dyes, six identical synthetic samples were processed like described above. The protocol for ultrasounds assisted extraction was similar as specified above. The extraction was performed in 25% ammonia in an ultrasonic bath for 15 minutes.

ACKNOWLEDGMENTS

The financial support of the Ministry of Education and Research of Romania (CNCSIS, IDEI 560/2007) is gratefully acknowledged.

REFERENCES

1. V. M. Ghorpade, S. S. Deshpande, D. K. Salunkhe, Maga JA, Tu AT, *Food colours: Food additives and toxicology*, Marcel Dekker, New York, **1995**.
2. F. M. Clydesdale, *Food Sci. Nutr.*, **1993**, 33, 83.
3. A. Downham, P. Collins, *Int. J. Food Sci. Technol.*, **2000**, 35, 5.
4. S. Bell, *Official Methods of Analysis: Food Compositions, Additives, Natural Contaminants*, Vol. 2, K. Helrich (Ed), Association of Official Analytical Chemists, Arlington, VA., **2002**.
5. K. Hofer, D. Jenewein, *Eur. Food Res.*, **1997**, 204, 32.
6. J. J. Berzas Nevado, J. Rodríguez Flores, M.J. Villaseñor Llerena, N. Rodríguez Fariñas, *Fresenius J. Anal. Chem.*, **1999**, 365, 383.
7. A. C. Moț, F. Saponar, D. Casoni, C. Cobzac, C. Sârbu, *Rev. Chim.*, **2009**, 60, 647.
8. L. F. Capitán-Vallvey, M. D. Fernández, I. de Orbe, J. L. Vilchez, R. Avidad, *Analyst*, **1997**, 122, 351.
9. F. Capitán, L. F. Capitán-Vallvey, M. D. Fernández, I. de Orbe, R. Avidad, *Anal. Chim. Acta*, **1996**, 331, 141.

10. Y. Ni, J. Bai, L. Jin, *Anal. Chim. Acta*, **1996**, 329, 65.
11. J. J. Berzas Nevado, J. Rodríguez Flores, M. J. Villaseñor, L. Lerena, *Talanta*, **1997**, 44, 467.
12. S. Chanlon, L. Joly-Pottuz, M. Chatelut, O. Vittori, J. L. Cretier, *J. Food Compos. Anal.*, **2005**, 18, 503.
13. M. Kucharska, J. Grabka, *Talanta*, **2010**, 80, 1045.
14. K. S. Minioti, C. F. Sakellariou, N. S. Thomaidis, *Anal. Chim. Acta*, **2007**, 583, 103.
15. M. S. Garcia-Falcon, J. Simal Gandara, *Food Control*, **2005**, 16, 293.
16. E. C. Vidotti, W. F. Costa, C. C. Oliveira, *Talanta*, **2006**, 68, 516.
17. M. G. Kiseleva, V. V. Pimenova, K. I. Eller, *J. Anal. Chem.*, **2003**, 58, 685.
18. Q. Chen, S. Mou, X. Hou, J. M. Riviello, Z. Ni, *J. Chromatogr. A*, **1998**, 827, 73.
19. A. De Villiers, F. Alberts, F. Lynen, A. Crouch, P. Sra, *Chromatographia*, **2003**, 58, 393.
20. H.-Ya Huang, Y.-Chieh Shih, Y.-Chieh Chen, *J. Chromatogr. A*, **2002**, 959, 317.
21. L. De Giovine, A. Piccioli Bocca, *Food Control*, **2003**, 14, 131.
22. D. M. Marmion, Handbook of U. S. Colorants for Foods, Drugs, and Cosmetics. 2nd ed, John Wiley & Sons, New York, **1979**.
23. M. Tripathi, S. K. Khanna, M. Das, *J. AOAC Int.*, **2004**, 87, 657.
24. M. D. Luque de Castro, J. L. Luque-García, Acceleration and Automation of Solid Sample Treatment, Elsevier, Amsterdam, **2002**.
25. C. Van Peteghem, J. Bijl, *J. Chromatogr. A*, **1981**, 210, 113.
26. J. F. Lawrence, F. E. Lancaster, H. B. S. Conacher, *J. Chromatogr.*, **1981**, 210, 168.
27. N. P. Boley, N. T. Crosby, P. Roper, L. Somers, *Analyst*, **1981**, 106, 710.
28. E. Wisher, R. König, W. Feldheim, *Eur. Food Res. Technol.*, **1980**, 170, 267.
29. F. Priego-Capote, M. D. Luque de Castro, *Trends Anal. Chem.*, **2004**, 23, 644.

Dedicated to the memory of Prof. dr. Ioan Silaghi-Dumitrescu marking 60 years from his birth

AMMONIUM SALTS OF ORGANOPHOSPHORUS ACIDS. CRYSTAL AND MOLECULAR STRUCTURE OF $[\text{Et}_3\text{NH}]^+[(\text{SPMe}_2)(\text{SPh}_2)\text{N}]^-$ AND $[2-\{\text{O}(\text{CH}_2\text{CH}_2)_2\text{N}(\text{H})\text{CH}_2\}\text{C}_6\text{H}_4]^+[\text{S}_2\text{P}(\text{OPr}^i)_2]^-$

ANA MARIA PEDA^a, MONIKA KULCSAR^b, RICHARD A. VARGA^a, DRAGOS MARGINEANU^a, ANCA SILVESTRU^{a,*}

ABSTRACT. The ammonium salts $[\text{Et}_3\text{NH}]^+\text{L}^-$ $\{\text{L}^- = [(\text{SPMe}_2)(\text{SPh}_2)\text{N}]^-$ (**1**), Ph_2PS_2^- (**2**) $\}$ were obtained in the reaction between triethylamine and the corresponding organophosphorus acid in a 1:1 molar ratio, while $[2-\{\text{O}(\text{CH}_2\text{CH}_2)_2\text{N}(\text{H})\text{CH}_2\}\text{C}_6\text{H}_4]^+[\text{S}_2\text{P}(\text{OPr}^i)_2]^-$ (**3**) resulted as hydrolysis product in the process of growing crystals of $[2-\{\text{O}(\text{CH}_2\text{CH}_2)_2\text{N}(\text{H})\text{CH}_2\}\text{C}_6\text{H}_4\text{SeS}_2\text{P}(\text{OPr}^i)_2]$. Compounds **1** and **2** were characterized by ^1H and ^{31}P NMR spectroscopy. Single-crystal X-ray diffraction studies revealed the presence of short intermolecular S...H contacts which result in the formation of dimeric units in **1** and of a layered supramolecular structure in **3**.

Keywords: *onium salts, intermolecular interactions, supramolecular network, dimeric units*

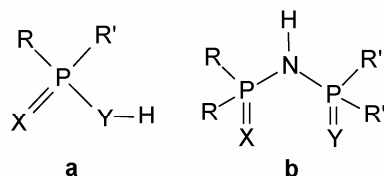
INTRODUCTION

Organophosphorus acids of type **a** (diorganodichalcogeno-phosphinic acids, diorganodichalcogenophosphonic acids and diorgano-dichalcogeno-phosphoric acids) or of type **b** (tetraorganodichalcogeno-imidodiphosphinic acids) (Scheme 1) have attracted a considerable interest in last three decades. They proved a high capacity to build metal complexes both with main group or transition metals by displaying a large variety of coordination patterns and their metal complexes found applications in biology, catalysis or electronics.[1-12]

On the other hand, onium salts melting at low temperatures was observed to be suitable as ionic liquids.[13,14]

^a Babeș-Bolyai University, Faculty of Chemistry and Chemical Engineering, Arany Janos 11, 400028 Cluj-Napoca, Romania; * ancas@chem.ubbcluj.ro

^b Departamento de Química Inorgánica, Instituto de Ciencia de Materiales de Aragón, Universidad de Zaragoza-C.S.I.C., E-50009 Zaragoza, Spain



R = alkyl, aryl, alkoxy, aryloxy; X, Y = O, S.

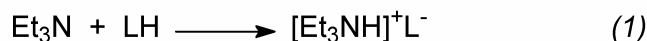
Scheme 1

We report here about the new ammonium salts

$[\text{Et}_3\text{NH}]^+\text{L}^-$ $\{\text{L}^- = [(\text{SPMe}_2)(\text{SPPH}_2)\text{N}]^-$ (**1**), $[\text{Ph}_2\text{PS}_2]^-$ (**2**) $\}$ and
 $[2-\{\text{O}(\text{CH}_2\text{CH}_2)_2\text{N}(\text{H})\text{CH}_2\}\text{C}_6\text{H}_4]^+[\text{S}_2\text{P}(\text{OPr}^i)_2]^-$ (**3**).

RESULTS AND DISCUSSION

The ionic compounds $[\text{Et}_3\text{NH}]^+[(\text{SPMe}_2)(\text{SPPH}_2)\text{N}]^-$ (**1**) and $[\text{Et}_3\text{NH}]^+[\text{S}_2\text{PPh}_2]^-$ (**2**) were prepared according to eq. (1), by reacting triethylamine either with the dimethyldiphenyldithioimidodiphosphinic acid or the diphenyldithiophosphinic acid, in a 1:1 molar ratio, in benzene, at room temperature.



$[2-\{\text{O}(\text{CH}_2\text{CH}_2)_2\text{N}(\text{H})\text{CH}_2\}\text{C}_6\text{H}_4]^+[\text{S}_2\text{P}(\text{OPr}^i)_2]^-$ (**3**) resulted as a hydrolysis product in the attempts to grow crystals of

$[2-\{\text{O}(\text{CH}_2\text{CH}_2)_2\text{N}(\text{H})\text{CH}_2\}\text{C}_6\text{H}_4\text{SeS}_2\text{P}(\text{OPr}^i)_2]$.

Compounds **1** and **2** were isolated in quantitative yields as microcrystalline solid species and were characterized by ^1H and ^{31}P NMR spectroscopy.

The ^1H NMR spectra display the expected resonances for the organic groups attached to phosphorus and nitrogen, respectively. The multiplicity of the ^1H resonances is determined by proton–proton and phosphorus–proton couplings. The *NH* protons in the triethylammonium cation give large singlet resonances at δ 10.02 and 10.22 ppm for **1** and **2**, respectively. The ^{31}P NMR spectra of the two compounds display two resonances in a 1:1 ratio for **1** and only one resonance for **2**, shifted in comparison with the corresponding free acids, due to the interaction with the cationic species.

Single-crystals suitable for X-ray diffraction studies were obtained for compounds **1** and **3** by slow diffusion from a mixture of CH_2Cl_2 and n-hexane (1:4, v/v). The ORTEP diagrams of the molecular structures of **1** and **3** with the atom numbering schemes are depicted in Figures 1 and 2, respectively, while selected interatomic distances and angles are listed in Table 1.

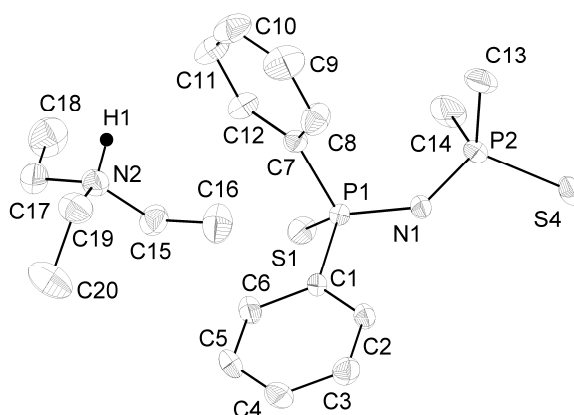


Figure 1. ORTEP plot of $[\text{Et}_3\text{NH}]^+ [(\text{SPMe}_2)(\text{SPPH}_2)\text{N}]^-$ (**1**). The atoms are drawn with 30% probability ellipsoids. Hydrogen atoms, except the one attached to nitrogen, are omitted for clarity.

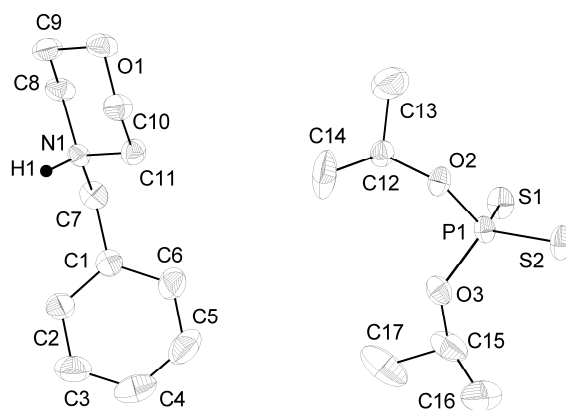


Figure 2. ORTEP plot of $[2\text{-}(\text{O}(\text{CH}_2\text{CH}_2)_2\text{N}(\text{H})\text{CH}_2)\text{C}_6\text{H}_4]^+ [\text{S}_2\text{P}(\text{OPr})_2]^-$ (**3**). The atoms are drawn with 30% probability ellipsoids. Hydrogen atoms, except the one attached to nitrogen, are omitted for clarity.

Both compounds are ionic species in which the ammonium cations and the organophosphorus anions are held together by electrostatic interactions. The central atoms N2 and N1, respectively, in the ammonium

cations in compounds **1** and **3** have a distorted tetrahedral coordination geometry, with angles ranging between 104(2) and 114.8(3) $^{\circ}$ in **1** and 107.1(2) and 112.9(2) $^{\circ}$ in **3**, respectively. The N–H distance is similar with those found in other ionic species containing [Et₃NH]⁺ or [Bu₃NH]⁺ cations.[15,16]

The organophosphorus ligands display almost equal P–S [1.971(1) and 1.985(1) Å in **1** and 1.968(1) and 1.980(2) Å in **3**] and P–N interatomic distances [1.594(3) and 1.596(3) Å in **1**], thus suggesting a symmetrical delocalization of the π electrons over the SPNPS system in **1** and the PS₂ system in **3**, respectively. However, these values are intermediate between those observed for single P–E and double P=E (E = S, N) bonds in the free acid Ph₂P(S)SH: P–S 2.077(1) and P=S 1.954(1) Å [17] and Ph₂P(=S)–N=PPh₂(–SMe): P=S 1.954(1), P–S 2.071(1), P=N 1.562(2) and P–N 1.610(2) Å [18].

Table 1. Interatomic bond distances (Å) and angles ($^{\circ}$) for compounds **1** and **3**

1		3	
N(1)–P(1)	1.594(3)	P(1)–S(1)	1.968(1)
N(1)–P(2)	1.596(3)	P(2)–S(2)	1.980(2)
P(1)–S(1)	1.971(1)	N(2)–H(1)	0.87(3)
P(2)–S(2)	1.985(1)	N(1)–C(7)	1.514(6)
N(2)–H(1)	0.87(2)	N(1)–C(8)	1.496(5)
N(2)–C(15)	1.488(4)	N(1)–C(5)	1.497(11)
N(2)–C(17)	1.501(5)		
N(2)–C(19)	1.489(5)		
P(1)–N(1)–P(2)	132.94(17)	S(1)–P(1)–S(2)	116.69(5)
C(15)–N(2)–C(19)	114.8(3)	C(7)–N(1)–C(8)	110.5(2)
C(15)–N(2)–C(17)	111.6(3)	C(7)–N(1)–C(11)	112.9(2)
C(19)–N(2)–C(17)	112.0(3)	C(8)–N(1)–C(11)	109.3(2)
C(15)–N(2)–H(1)	110(2)	C(7)–N(1)–H(1)	109.2(2)
C(17)–N(2)–H(1)	104(2)	C(8)–N(1)–H(1)	107.1(2)
C(19)–N(2)–H(1)	104(2)	C(11)–N(1)–H(1)	107.7(2)

A closer check of the crystal structures of **1** and **3** revealed intermolecular S...H contacts between cations and anions [cf. $\sum r_{vdw}(S,H)$ ca. 3.05 Å [19]. In compound **1** dimeric associations are formed both by strong cation – anion hydrogen bonding [H1...S2''' 2.351(3) Å] and weak inter-anions interactions [H13B''...S2''' 2.967(3) Å] (Figure 3).

By contrast, in the crystal of **3** a layered network is formed both by cation – anion hydrogen bonding [H1...S2'' 2.53(3), H8A...S1' 2.901(7) and S2'...H7B 2.981(2) Å] and inter-anions H...S interactions [H14B...S2' 2.984(1) Å] (Figure 4). While in compound **1** only one sulfur atom is involved

in hydrogen bonding, in compound **3** both sulfur atoms are involved, probably due to the small bite of the dithiophosphinato group in comparison with the highly flexible tetraorganoimidodiphosphinato moiety.

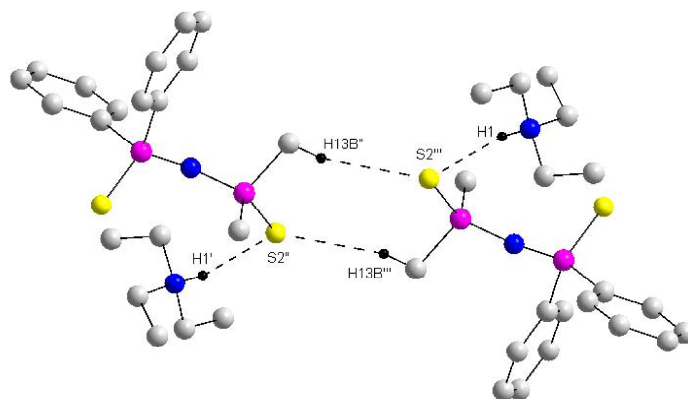


Figure 3. Dimeric association in the crystal of compound **1**. [symmetry equivalent atoms $(-x, 1 - y, 1 - z)$ are given by "prime"].

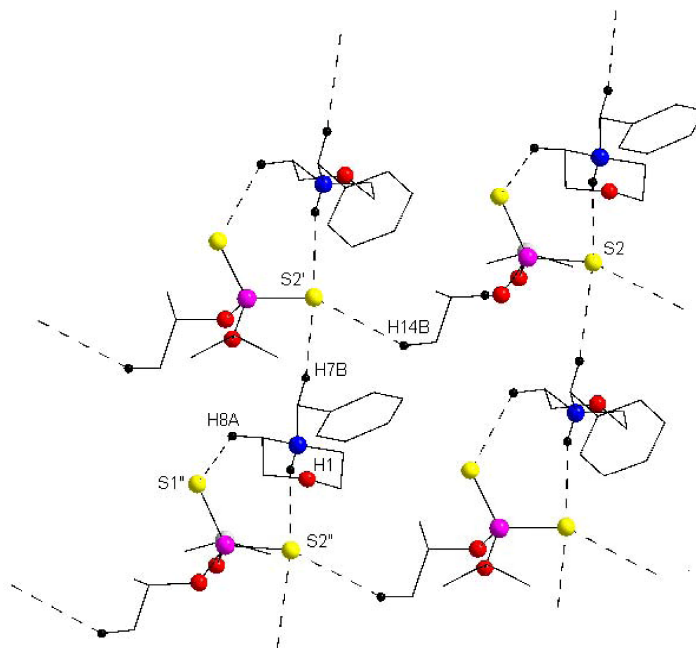


Figure 4. Polymeric association in the crystal of compound **3**. [symmetry equivalent atoms $(-0.5 + x, -0.5 + y, 0.5 + z)$ and $(x, y, 1 + z)$ are given by "prime" and "second", respectively].

The conformation of the S-P-N-P-S skeleton in compound **1** can be described as *syn* [S1-P1...P2-S2 torsion angle 89.2(8)^o] [12], with both phosphorus-sulfur bonds oriented on the same side of the PNP plane at 1.54 and 0.85 Å, respectively.

CONCLUSIONS

New ammonium salts of organophosphorus ligands, e.g. [Et₃NH]⁺[(SPMe₂)(SPPPh₂)N]⁻ and [Et₃NH]⁺[S₂PPh₂]⁻ were isolated as colorless, microcrystalline solids and were characterized in solution by ¹H and ³¹P NMR. X-Ray diffraction studies on [Et₃NH]⁺[(SPMe₂)(SPPPh₂)N]⁻ and the ammonium salt [2-{O(CH₂CH₂)₂N(H)CH₂}C₆H₄]⁺[S₂P(OPrⁱ)₂]⁻ revealed different association patterns in the crystals of the two compounds, e.g. dimeric units in the case of the tetraorganodithioimidodiphosphinato species and a polymeric layered structure in the case of the dithiophosphato derivative.

EXPERIMENTAL SECTION

Starting materials were commercially available (Fluka), or prepared following a published procedure: Ph₂PS₂H [17], (Me₂PS)(Ph₂PS)NH [20]. ¹H and ³¹P NMR spectra were recorded on a Bruker Avance 500 instrument using CDCl₃ solutions. The chemical shifts are reported in δ units (ppm) relative to the residual peak of the deuterated solvent (ref. CHCl₃: ¹H 7.26 ppm) for ¹H NMR and H₃PO₄ 85% for ³¹P NMR.

Preparation of [Et₃NH]⁺[(SPMe₂)(SPPPh₂)N]⁻ (1**)**

A mixture of triethylamine (0.14 mL, 1 mmol) and [(Me₂PS)(Ph₂PS)N]H (0.325 g, 0.1 mmol) in benzene (30 mL) was stirred for 12 h at room temperature. Then the solvent was removed in vacuum to give the title compound as a colorless powder. Yield: 0.4 g (94%), m.p. 172°C. ¹H NMR: δ 1.31t [9H, CH₂CH₃, ³J_{HH} 7.4 Hz], 1.64d (6H, PCH₃, ²J_{PH} 13.2 Hz), 3.29q (6H, CH₂CH₃, ³J_{HH} 7.4 Hz), 7.24m (6H P-C₆H₅-*meta+para*), 8.02ddd (4H, P-C₆H₅-*ortho*, ³J_{HH} 7.6, ⁴J_{HH} 1.8, ³J_{PH} 12.8 Hz), 10.02s (br., 1H, NH). ³¹P NMR (121.4 MHz): 37.1s, br., Ph₂PS, 45.3s, br., Me₂PS.

[Et₃NH]⁺[S₂PPh₂]⁻ (**2**) was similarly obtained from triethylamine (0.14 mL, 1 mmol) and Ph₂PS₂H (0.375 g, 0.1 mmol). Yield: 0.44 g (92%), m.p. 81°C. ¹H NMR: δ 1.32t [9H, CH₂CH₃, ³J_{HH} 7.3 Hz], 3.26q (6H, CH₂CH₃, ³J_{HH} 7.3 Hz), 7.30 – 7.36m (6H P-C₆H₅-*meta+para*), 8.15ddd (4H, P-C₆H₅-*ortho*, ³J_{HH} 7.9, ⁴J_{HH} 1.6, ³J_{PH} 13.9 Hz), 10.22s (br., 1H, NH). ³¹P NMR (121.4 MHz): 61.4s.

X-ray Crystallographic Study

Block crystals of $[\text{Et}_3\text{NH}]^+[(\text{SPMe}_2)(\text{SPPH}_2)\text{N}]^-$ (**1**) and $[2\text{-}\{\text{O}(\text{CH}_2\text{CH}_2)_2\text{N}(\text{H})\text{CH}_2\}\text{C}_6\text{H}_4]^+[\text{S}_2\text{P}(\text{OPr}^i)_2]^-$ (**3**) were attached with Paratone N oil on cryoloops. The data were collected at room temperature on a Bruker SMART APEX CCD diffractometer using graphite-monochromated Mo-K α radiation ($\lambda = 0.71073 \text{ \AA}$). The details of the crystal structure determination and refinement are given in Table 2.

The structures were refined with anisotropic thermal parameters. The hydrogen atoms were refined with a riding model and a mutual isotropic thermal parameter. The hydrogen atoms bonded to the nitrogen in compounds **1** and **3** were found in a difference map and refined with a restrained N–H distance of 0.87(2) \AA for **1** and 0.87(3) \AA for **3**, respectively. For structure solving and refinement the software package SHELX-97 was used [21]. The drawings were created with the Diamond program [22].

Table 2. Crystallographic data for compounds **1** and **2**.

	1	3
chemical formula	$\text{C}_{20}\text{H}_{32}\text{N}_2\text{P}_2\text{S}_2$	$\text{C}_{17}\text{H}_{30}\text{NO}_3\text{PS}_2$
crystal habit	colorless block	colorless block
crystal size [mm]	0.25 x 0.22 x 0.2	0.38 x 0.33 x 0.18
crystal system	triclinic	monoclinic
space group	<i>P</i> -1	<i>P</i> 2(1)/ <i>n</i>
<i>a</i> [\AA]	9.7823(11)	10.048(10)
<i>b</i> [\AA]	10.7488(12)	17.246(17)
<i>c</i> [\AA]	11.3737(13)	12.500(12)
α [deg]	91.951(2)	90
β [deg]	95.651(2)	92.469(17)
γ [deg]	93.647(2)	90
<i>U</i> [\AA^3]	1186.7(2)	2164(4)
<i>Z</i>	2	4
<i>D_c</i> [g cm^{-3}]	1.194	1.202
<i>M</i>	426.54	391.53
<i>F</i> (000)	456	840
θ range [deg]	1.90 to 25.00	2.35 to 25.00
μ (Mo K α) [mm^{-1}]	0.366	0.334
no. of reflections collected	11545	20438
no. of independent reflections	4177 ($R_{\text{int}} = 0.0470$)	3816 ($R_{\text{int}} = 0.0491$)
R_1 [$I > 2\sigma(I)$]	0.0616,	0.0611
wR_2	0.1270	0.1416
no. of parameters	244	225
no. of restraints	1	0
GOF on F^2	1.093	1.167
largest difference electron density [e \AA^{-3}]	0.418 and -0.262	0.413 and -0.296

ACKNOWLEDGEMENTS

This work was supported by the National University Research Council of Romania (CNCSIS, Research Project No. ID-2404/2008). A. M. P. thanks the European Social Fund for a Scholarship (Education and Training Program 2008-2013, POSDRU/6/1.5/S/3).

SUPPLEMENTARY MATERIAL

CCDC 753670 and 753671 contain the supplementary crystallographic data for compounds **1** and **3**. These data can be obtained free of charge from The Cambridge Crystallographic Data Centre via www.ccdc.cam.ac.uk/data_request/cif.

REFERENCES

1. I. Haiduc, *Rev. Inorg. Chem.*, **1981**, *3*, 353.
2. R.C. Mehrotra, G. Srivastava, B.P.S. Chauhan, *Coord. Chem. Rev.*, **1984**, *55*, 207.
3. E.R.T. Tiekink, *Main Group Metal Chem.*, **1992**, *15*, 161.
4. V.K. Jain, *Coord. Chem. Rev.*, **1994**, *135/136*, 809.
5. I. Haiduc, *Phosphorus, Sulfur Silicon*, **1994**, *93–94*, 345.
6. I. Haiduc, D.B. Sowerby, S.-F. Lu., *Polyhedron*, **1995**, *14*, 3389.
7. I. Haiduc, D.B. Sowerby, *Polyhedron*, **1996**, *15*, 2469.
8. C. Silvestru, I. Haiduc, *Coord. Chem. Rev.*, **1996**, *147*, 117.
9. I. Haiduc, *Coord. Chem. Rev.*, **1997**, *158*, 325.
10. T.Q. Ly, J.D. Woollins., *Coord. Chem. Rev.*, **1998**, *176*, 451.
11. R. Cea-Olivares, V. Garcia-Montalvo, J. Novosad, J.D. Woollins, R.A. Toscano, G. Espinosa-Perez, *Chem. Ber.*, **1996**, *129*, 919.
13. C. Silvestru, J. E. Drake, *Coord. Chem. Rev.*, **2001**, *223*, 117.
14. P. Wasserscheid, W. Keim, *Angew. Chem., Int. Ed.*, **2000**, *39*, 3772.
15. H. J. Breunig, T. Koehne, O. Moldovan, A. M. Preda, A. Silvestru, C. Silvestru,
16. R. A. Varga, L. F. Piedra-Garza, U. Kortz, *J. Organomet. Chem.*, **2010**, *695*, 1307.
17. R. Tacke, C. Burschka, I. Richter, B. Wagner, R. Willeke, *J. Am. Chem. Soc.*, **2000**, *122*, 8480.
18. E. J. Brown, A. C. Whitwood, P. H. Walton, A.-K. Duhme-Klair, *J. Chem. Soc. Dalton Trans.*, **2004**, 2458.
19. B. Krebs and G. Henkel, *Z. Anorg. Allg. Chem.* 1981, *475*, 143.
20. I. Ghesner, A. Soran, C. Silvestru, J.E. Drake, *Polyhedron*, **2003**, *22*, 3395.
21. J. Emsley, *Die Elemente*, Walter de Gruyter: Berlin, **1994**.
22. R. Roesler, J.E. Drake, C. Silvestru, J. Yang, I. Haiduc, G. Espinosa-Perez, *J. Chem. Soc. Dalton Trans.*, **1998**, 73.
23. G. M. Sheldrick, *Acta Crystallogr., Sect. A*, **2008**, *64*, 112.
24. DIAMOND – *Visual Crystal Structure Information System*, Crystal Impact, Postfach 1251, 53002 Bonn, Germany, **2001**.

Dedicated to the memory of Prof. dr. Ioan Silaghi-Dumitrescu marking 60 years from his birth

ARTIFICIAL NEURAL NETWORKS USED FOR INVESTIGATION OF FATTY ACID CONTENT OF ROMANIAN SUNFLOWER OILSEEDS GENOTYPES

**DORINA BRĂTFĂLEAN, VASILE MIRCEA CRISTEA*,
PAUL ȘERBAN AGACHI**

ABSTRACT. The objective of this study was to investigate the efficiency of Artificial Neural Networks (ANNs) in classifying and predicting the fatty acid content from Romanian sunflower oilseeds genotypes, as solutions of computational engineering problems. The two-layer probabilistic ANN, using a radial basis layer and a competitive layer, has been used for classification. There were two criteria of classification, the degree of polyunsaturation and the linoleic/oleic acid ratio, which allowed the defining of two categories. The first ANN has been designed for classifying the first category into three groups defined by the polyunsaturated fatty acid content: group 1 of less than 40% polyunsaturated fatty acid, group 2 of 40%-50% polyunsaturated fatty acid, and group 3 of higher than 50% polyunsaturated fatty acid. The classification was based on the following acids in the samples: C14:00, C15:00, C16:00, C16:01, C17:00, C18:00, C18:01, C18:02, C18:03, C20:00, C20:01 and C22:00. The second designed ANN has been used for classifying the category of linoleic/oleic acid ratio into three groups: group 1 of linoleic/oleic acid ratio higher than 2, group 2 of linoleic/oleic acid ratio between 1 and 2 and group 3 of linoleic/oleic acid ratio less than 1. The results of both classifications revealed a good accuracy of the trained ANNs for classifying the sunflower oilseeds. The numerical tests demonstrated the computational advantages of the prediction methodology.

Keywords: ANN, fatty acids, oilseeds, polyunsaturated fatty acid, sunflower genotypes.

INTRODUCTION

Fats are a subclass of lipids, but the term “fat” is often used instead of the term denoting “lipid”. For nutrition labeling purposes, fat has been defined as triglycerides (substances extracted with organic solvent) or total lipids. Triglycerides are the building blocks of fats and oils, such as sunflower oil, which is extracted from sunflower seeds and is the most common vegetable fat.

* Babeș-Bolyai University, Faculty of Chemistry and Chemical Engineering, 11. Arany Janos, RO-400028 Cluj-Napoca, Romania, mcristea@chem.ubbcluj.ro

From the economical point of view sunflower oil is a very good source for valorisation due to the variety of fatty esters contained. Fatty acids are differentiated by their molecular composition [1]. One differentiating characteristic is the degree of saturation, according to which they are: saturated, monounsaturated or polyunsaturated. Other differentiating characteristics are the chain length and the number of carbon atoms in the fatty acid molecule. Fatty acids represent 95 of every 100 grams of fat or oil. Fatty acid variability and profile in the sunflower oil depend on the sunflower genotype. They found numerous applications as food (human and animal feeds), and non-food products (pharmaceutical field, cosmetics, bio-detergents, biodiesel, etc).

Due to their many applications, it is important to be able to assess the quality of different oilseeds. This may be performed on the basis of the fatty acids content. This is an important reason for searching and developing new methodologies that allow more flexible and better-controlled means for the classification of fatty acid content of fats.

The quality of food or other products is monitored based on their composition through laboratory analyses, while computational screening may be used for prediction and simulation, thus offering economic benefits [2]. Methodologies based on Artificial Neural Networks (ANNs) have become an efficient tool in many studies involving property classification and prediction.

Modelling and data mining methodologies based on ANNs are able to represent information on complex systems [3]. ANNs are adaptive systems that change their structure based on external or internal information that flows through the network. Neural networks are non-linear statistical data modelling tools [4]. They can be used to model complex relationships between inputs and outputs or to find patterns in data.

The aim of the present work has been the comparative investigation of fatty acid content for different Romanian sunflower genotypes, based on ANNs classification aptitude. Several genotypes of Romanian sunflower oilseeds have been considered in the investigation of the fatty acid content, using laboratory analytical techniques. The fatty acid methyl esters (FAMES) were analyzed by gas-chromatography, and the results were used to test the ability of the specially trained ANNs for predicting the classis of genotypes, according to the type of their fatty acid contained.

Samples

The Romanian National Agricultural Research and Development Institute Fundulea provided the sunflower seeds used in this study. Before they were analyzed, the sunflower seeds were stored at a temperature of 5°C and low humidity [5]. First, the dry weight determination of each sample was performed in the laboratory. Around 10g of sunflower seeds at harvesting

maturity were sampled for each sunflower genotype [6]. Ten inbred lines and five Romanian hybrids have been considered in this study. The genotypes are presented in Table 1.

Table 1. Investigated inbred lines and Romanian sunflower hybrids

Genotype	LC-L1	LC-L2	LC-L3	LC-L4	LC-L5	LC-L6	LC-L7	
Type of variety	Semi-precocious	Semi-precocious	Precocious	Tardif	Semi-precocious	Semi-Tardif	Semi-Tardif	
enotype	LC-L8	LC-L9	LC-L10	R-H1	R-H2	R-H3	R-H4	R-H5
Type of variety	Semi-precocious	Precocious	Tardif	Alex	Favorit	Rapid	Top75	Turbo

The samples were collected for two types of laboratory analysis, qualitative and quantitative, and one computational method. The first method (quantitative) was the detection of the percent of fat from oilseeds by Accelerated Solvent Extractor (ASE) method, and the second method (qualitative) was gas chromatography analysis. The computational method was based on the ANNs classification capacity, using the Matlab software environment and its accompanying Neural Network Toolbox.

Procedure of total lipids extraction

Extraction of the total lipids from the sunflower seeds has been the initial step of this study. The ASE method was used according to Official Method of Analysis, 1999 [6]. This method has a similar operating principle as the Soxhlet Extraction method used for lipids extraction. ASE method involves the gravimetric determination of the oil using the light petroleum extract from sunflower seeds. The equipment consists in a metallic cell having six communique broiler based extractors. The petroleum extract is called "oil content". Following the weighting step, the seed material was placed in a cellulose extraction cartridge and then introduced into the extractor. The parameters of the extraction process and the number of cycles were programmed by means of an electronic interface [7]. The advantage of the ASE method consists in the relatively high number of samples which can be investigated and the reduced time of extraction (6 samples and 30 min of extraction for one sample). The fat content has been computed by the direct expression:

$$Fat\ content[\%] = \frac{Mass\ of\ the\ extract}{Mass\ of\ the\ sample} \cdot 100 \quad (1)$$

The ASE method was used to determine quantitatively the fat from the sunflower oilseed.

Fatty acid methyl esters (FAMES) preparation

FAMES were produced in order to determine the content of total fatty acids in the extracted oils [6]. The first step for FAMES preparation consists in the saponification procedure [2]. Two samples of 0.1g lipid extracted from each sunflower genotype were treated with 1 mL NaOH solution (1M) in methanol by refluxing for 1h at 100°C. After free fatty acid removal, the samples were esterified in the presence of H₂SO₄ as catalyst. The FAMES were extracted with petroleum ether from the salt saturated mixture. After FAMES drying, the Na₂SO₄ anhydride was added and the supernatant was poured in the specific cell.

Gas chromatography system

The fatty acids have been analyzed by gas chromatography (GC) according to the published methods [6]. The esters were separated by gas chromatograph (Carlo Erba model equipped with FID type FRATOVAP 300, and split/splitless injector and associated column (L=2m, d=3mm), containing 10% diethylene glycol succinat on Chromosorb W, AW). The temperature of the injection port was maintained at constant value of 190°C and the detector temperature at 225°C. The oven temperature was programmed to increase from 80°C to 200°C at a rate of 5°C /min using Argon as carrier gas, fed with a reference flow rate of 24mL/min. The peaks were identified based on their retention times using standard fatty acids methyl esters. All samples were run in duplicate.

Identification of FAMES

The total amount of Miristic acid-C14:00, Pentadecanoic acid-C15:00, Palmitic acid-C16:00, Palmitoleic acid-C16:01, Heptadecanoic-C17:00, Stearic acid-C18:00, Oleic acid-C18:01, Linoleic acid-C18:02, Linolenic C18:03, Arachidic acid-C20:00, Behenic acid-C22:00, Gadoleic acid-C20:01 was computed from the GC peak area of each FAME. No correction factors or internal standards were used. The average values for the two replicates were accepted as the concentrations of the sunflower oil samples. The precision of the results is given in the description of ISO 5508/9 standard method.

ANN Classification

Probabilistic ANNs have been used for classification [8]. The designed ANN is a two-layer probabilistic neural network consisting in a radial basis layer and a competitive layer. The radial basis layer computes distances from the input vector to the training input vectors and produces a vector whose elements measure how close the particular input is to a training input. The competitive layer cumulates these contributions for each class of inputs to produce, as its net output, a vector of probabilities. The layer uses a compete

transfer function for selecting the maximum of these probabilities and generates a vector having as elements a 1 (one) for the particular class and 0 (zero) for the other classes. The probabilistic ANN is guaranteed to converge to a Bayesian classifier. Artificial Neural Network Toolbox of Matlab software was used to build the present application [8, 9]. The input and hidden layer consist of fifteen neurons and the output layer includes three neurons. Output values of the network are rounded to the nearest integer to obtain the classes.

RESULTS AND DISCUSSION

Degree of fat extraction

First, the set of 15 sunflower seeds genotypes considered in the study (ten inbred lines and five hybrids) have been submitted to the investigations of fats and fatty acid content. The laboratory investigation determined the quantity of fat extracted by ASE method, as presented in Fig. 1.

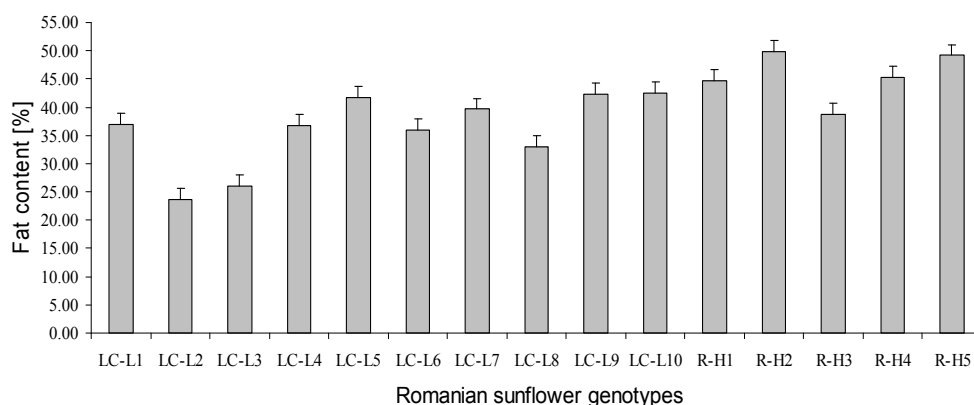


Figure 1. Fat content in the sunflower seeds of the investigated Romanian genotypes

For the case of the inbred lines the fat content ranges from 24.01% for the LC-L2 line to 42.49% for the LC-L10 line, while for the hybrids the fat content varies between 38.75% for the R-H3 line and 49.15% for the R-H2 line. Results confirm the large variability of fat content characterizing the Romanian sunflower seeds genotypes. The experimental results are show in Supporting Information.

Second, the profile of fatty acid analyzed thought GC-FID methods show that twelve types of fatty acids were determined [10]. The degree of saturation for the investigated inbred lines and Romanian sunflower hybrids are presented in Table 2.

Table 2. The degree of saturation results for the investigated inbred lines and Romanian sunflower hybrids.

Inbred lines and hybrids	Total Saturated fatty acids [%]	Total Monounsaturated fatty acids [%]	Total Polyunsaturated fatty acids [%]	Total Unsaturated fatty acids [%]	Saturated/unsaturated acid ratio	Linoleic /oleic acid ratio
LC-L1	11.441	31.719	56.840	88.559	0.129	1.787
LC-L2	13.291	48.724	37.985	86.709	0.153	0.772
LC-L3	10.652	42.144	47.204	89.348	0.119	1.116
LC-L4	12.765	40.528	46.707	87.235	0.146	1.149
LC-L5	10.704	39.015	50.281	89.296	0.120	1.291
LC-L6	10.007	41.716	48.277	89.993	0.111	1.153
LC-L7	13.994	39.865	46.141	86.006	0.163	1.153
LC-L8	12.432	47.099	40.469	87.568	0.142	0.852
LC-L9	13.957	43.345	42.698	86.043	0.162	0.973
LC-L10	10.545	35.731	53.724	89.455	0.118	1.502
R-H1	12.081	29.138	58.781	87.919	0.137	2.014
R-H2	13.275	25.369	61.356	86.725	0.153	2.429
R-H3	14.060	27.330	58.610	85.940	0.164	2.149
R-H4	13.470	26.010	60.520	86.530	0.156	2.344
R-H5	13.836	26.548	59.616	86.164	0.161	2.256

ANN screening data

The classification of the samples according to the fatty acid content into three groups has been performed using ANNs. There were two criteria of classification, the degree of polyunsaturation and the linoleic/oleic acid ratio, which allowed the defining of two *categories*. As a result, the two considered categories are: the category of polyunsaturated fatty acids and the category of linoleic/oleic acid ratio. For each of the two considered categories, ANNs were used for classifying the samples into three *groups*.

The first classification, of polyunsaturated fatty acid category, was performed by the ANNs for dividing the samples into three groups according to the percentage of polyunsaturated fatty acid content. The ANN was trained using a set of input-output literature data [11-16]. Inputs of the ANN have been considered the contents of: Miristic acid-C14:00, Pentadecanoic acid-C15:00, Palmitic acid-C16:00, Palmitoleic acid-C16:01, Heptadecanoic-C17:00, Stearic acid-C18:00, Oleic acid-C18:01, Linoleic acid-C18:02, Linolenic C18:03, Arachidic acid-C20:00, Behenic acid-C22:00, Gadoleic acid-C20:01. The outputs of the ANN are: *group 1* of samples having the polyunsaturated fatty acid content less than 40%, *group 2* of samples having the polyunsaturated fatty acid content between 40%-50% and *group 3* of samples with the polyunsaturated fatty acid content higher than 50%. The ANN testing step followed the training procedure. A randomly selected testing set of 15 experimental samples obtained from the Romanian inbred line genotypes (not yet seen by the ANN) was given to the previously trained ANN in order to test its ability to properly perform the classification. The investigated sunflower genotypes have the polyunsaturated fatty acids content higher than 40%,

except one inbred line having less than 40% polyunsaturated fatty acids (LC-L2 with 37.985%). The classification results for this testing set of samples are presented in Fig. 2, where the ANN predicted data are compared to the experimental results.

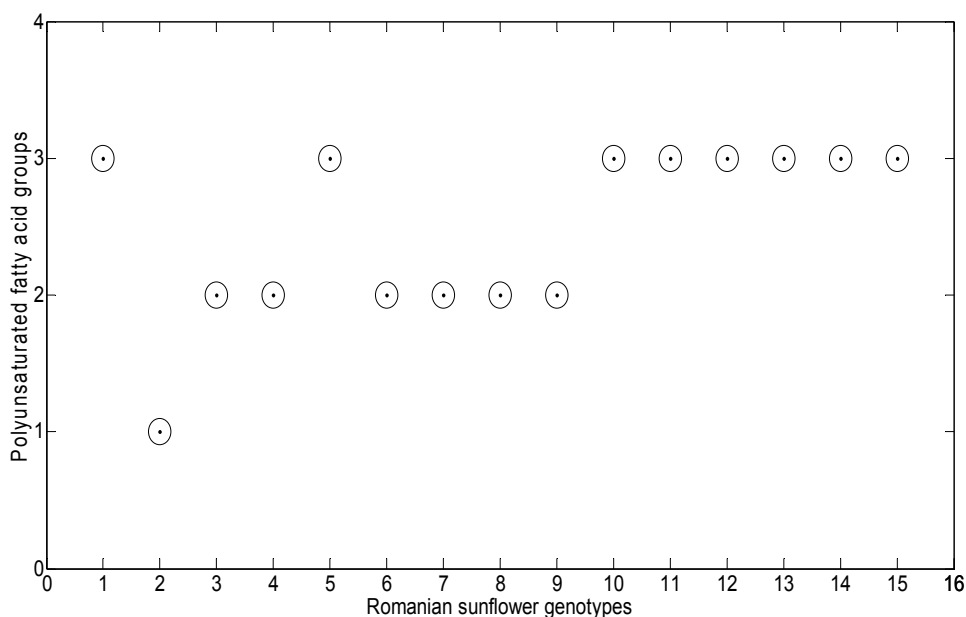


Figure 2. Classification results of polyunsaturated fatty acid groups, for the testing set of data; Group 1 of polyunsaturated fatty acid $\leq 40\%$, Group 2 of polyunsaturated fatty acid $40\% - 50\%$, Group 3 of polyunsaturated fatty acid $\geq 50\%$; the ANN groups predictions, marked by “○”, and the desired polyunsaturated fatty acid groups (experimental results), marked by “•”.

The three groups predicted by ANN simulation for the classification of the polyunsaturated fatty acid reveal a very good fit between the classification groups performed by the ANN and the groups obtained by the ASE method.

The second ANN classification of the experimental data, according to the linolenic/oleic acid ratio criterion, was also based on a previous step of ANN training. Again, literature data was used to train the ANN [11-16]. Values of the linoleic/oleic acid ratio reveal which fatty acid is predominant in the oilseed, i.e. either the monounsaturated fatty acid (oleic acid) or the polyunsaturated fatty acid (linoleic acid). In order to test the ability of the trained ANN for classifying the data, the testing was performed on the set of 15 experimental samples obtained from the Romanian inbred lines genotypes. Classification results are presented in Fig. 3.

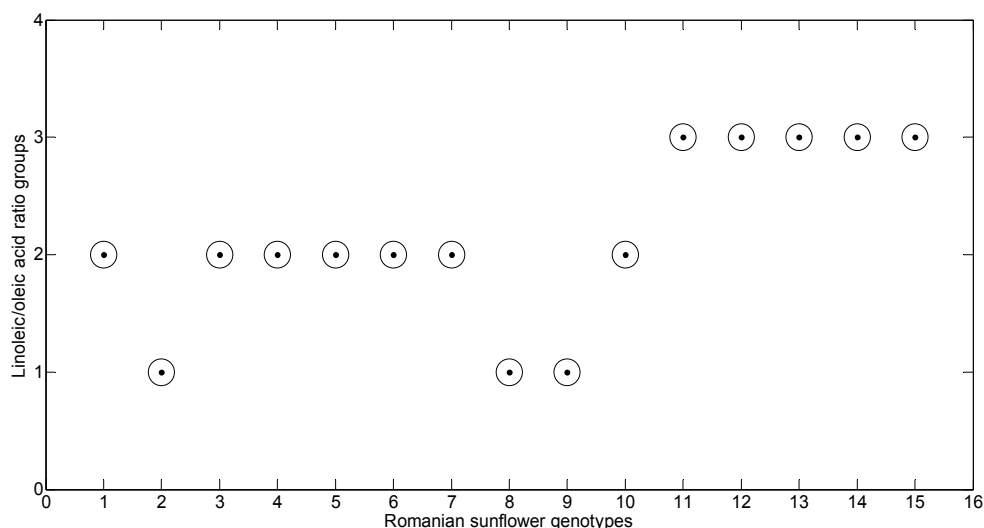


Figure 3. Classification results of linoleic/oleic acid ratio groups, for the testing set of data; Group 1 of linoleic/oleic acid ratio ≥ 2 , Group 2 of linoleic/oleic acid ratio between 1-2, Group 3 of linoleic/oleic acid ratio ≤ 1 ; the ANN groups predictions, marked by “○”, and the desired linoleic/oleic acid ratio groups (experimental results), marked by “•”.

Again, the classification reveals a perfect fit between the groups obtained by the experimental investigations and the results predicted by the ANN.

The obtained results prove the capacity of the trained ANNs for making exact sunflower oil seed group classifications in the cases of samples of unknown group membership.

Prediction of determined classes

Furthermore, by merging the two categories presented in Fig. 2 and Fig. 3 the combined results presented in Fig. 4 have been obtained.

Results presented in Fig. 4 reveal the prediction of three *classes* of the Romanian sunflower seeds genotypes. The first class consists of ten investigated sunflower oilseed genotypes with a high content of polyunsaturated fatty acids and a linoleic/oleic acid ratio less than 1. The second class consists of two sunflower inbred lines (LC-L8 and LC-L9), where the linoleic acid is dominant and the polyunsaturated fatty acid content places it into group 2 of the first classification category. The third class is composed of three sunflower lines (LC-L1, LC-L5 and LC-L10) where the oleic acid is dominant and the polyunsaturated fatty acid content is higher than 50%, corresponding to group 3 of the first classification category. It may be also noticed that all five considered hybrid lines are oleic hybrids, as they predominantly contain the oleic acid.

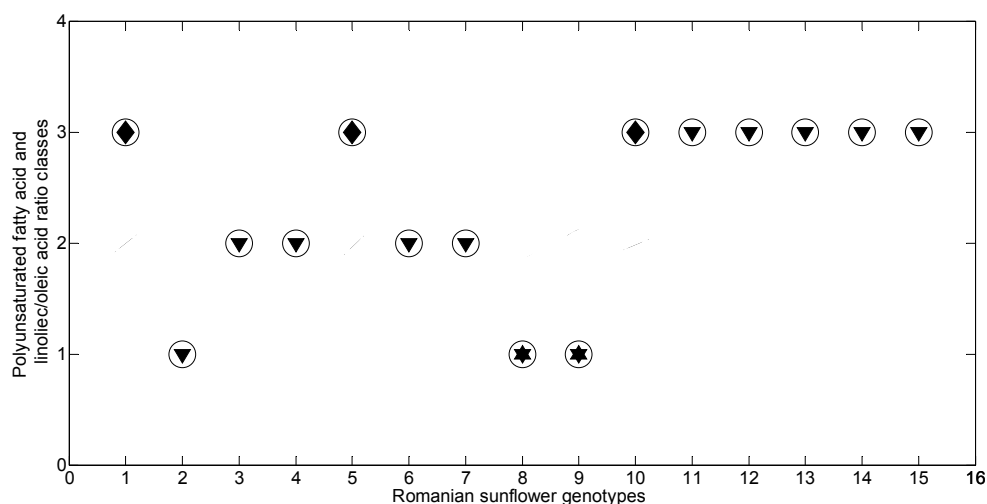


Figure 4. Classes of investigated Romanian sunflower genotypes; the ANN predicted classes are marked by “○” and the classes obtained from experimental data are: class 1 marked by “▼”, class 2 marked by “★” and class 3 marked by “◆”.

It may be concluded that the investigated lines may be used in crossed hybridization in order to obtain new hybrids with high content of either oleic or linoleic acid. The investigated hybrid lines may be appreciated for their nutritional potential, due to their high polyunsaturated fatty acid content.

CONCLUSIONS

Several genotypes of Romanian sunflower oilseeds have been considered in the investigation of the fatty acid content, using laboratory analytical techniques. Methodologies based on the two layer probabilistic ANNs, consisting in a radial basis layer and a competitive layer, have been used for classification of sunflower oilseed genotypes according to fatty acid content. The ANNs were trained with experimental data from the literature. Two classifications (categories) were obtained, function of (1) the degree of polyunsaturation and (2) the linoleic/oleic acid ratio. Three groups have been considered for each investigated category. Three classes have been also predicted by the investigation of the Romanian sunflower oilseeds genotypes.

The classification aptitude of the designed ANNs proved to be very good, as the group classification has been performed with no error, for both categories. Moreover, the advantages of the classification based on ANNs are significant when taking into consideration the limited number of parameters required as ANN inputs and the number of samples needed for the training set. Further improvement may be obtained by extending the number of input parameters and by carefully filtering the training set of data.

Starting from the methodology of designing ANNs, aimed to predict and classify the sunflower seeds, further classification procedures may be developed for similar applications. ANNs incentives consist in the help they bring for characterizing the sunflower oils with economical implication as oil composition assessment is an essential feature to provide its potential use in different fields, such as: nutrition, pharmacy, health care or other nonfood applications.

ACKNOWLEDGMENTS

The authors would like to acknowledge the support for providing the sunflower seeds genotypes to the Agricultural Research and Development Institute Fundulea, and to the Romania-Slovenia bilateral cooperation project.

REFERENCES

1. L. D. Villamide, *British Poultry Science*, **2000**, *41*, 182.
2. D. Brodnjak-Voncina, Z. C. Kodbab, M. Novic, *Chemometrics and Intelligent Laboratory Systems*, **2005**, *75*, 31.
3. Y. Tsompanakis, N. D. Lagaros, G. E. Stavroulakis, *Advances in Engineering Software*, **2008**, *39*, 612.
4. L. Fengjun, X. Zongben, *Chaos, Solitons and Fractals*, **2008**, *36*, 572.
5. D. Bratfalean, V. M. Cristea, P. S. Agachi, D. F. Irimie, *Revue Roumanie de Chimie*, **2008**, *53*, 881.
6. AOAC, "Official Method of Analysis" Association of Official Analytical Cereal Chemists, Washington, DC, USA, **1999**.
7. B. Matthaüs, L. Brühl, *Journal of the American Oil Chemist's Society*, **2001**, *78*, 95.
8. D. Bratfalean, M. V. Cristea, P. S. Agachi, D. F. Irimie, A. Sarrafi, M. Petitprez, *Proceedings of the 17th European Symposium on Computer Aided Process Engineering – ESCAPE17*, May, Bucharest, **2007**, 1.
9. M. V. Cristea, S. Varvara, L. Muresan, I. C. Popescu, *Indian Journal of Chemistry*, **2003**, *42A*, 764.
10. D. Bratfalean, D. F. Irimie, P. S. Agachi, *Studia Universitatis Babes-Bolyai, Chemia*, **2007**, *LII 2*, 47.
11. B. Perez-Vich, L. Velasco, J. M. Fernandez-Martinez, *Journal of the American Oil Chemist's Society*, **1998**, *75*, 547.
12. B. Perez-Vich, R. Garces, J. M. Fernandez-Martinez, *Heli*, **2000**, *23*, 77.
13. A. V. Vrânceanu, "Floarea-soarelui Hibridă", Ceres Press, Bucharest, **2000**, p.15-25, p. 650-720.
14. G. J. Seiler, "Potential Source of Reduced Palmitic and Stearic Fatty Acids in Sunflower Oil From a Population of Wild Helianthus Annuus", *ASHS Press, Alexandria VA*, **2002**, p.150-154.
15. N. Izquierdo, L. A. F. Andrade, V. Pereyra, *Field Crops Research*, **2002**, *77*, 115.
16. K. Warner, B. Vick, L.K. Leingrtner, R. Isaak, K. Doroff, *Proceedings from the 18th session of the CCFO – Report of the eighteenth session of the codex committee on fats and oil, U.K.*, **2003**.

Dedicated to the memory of Prof. dr. Ioan Silaghi-Dumitrescu marking 60 years from his birth

SPECTROSCOPIC AND STRUCTURAL CHARACTERISATION OF $\text{SiO}_2\text{-Y}_2\text{O}_3$ BASED MATERIALS WITH LUMINESCENT PROPERTIES

LAURA ELENA MURESAN^{a,*}, ELISABETH-JEANNE POPOVICI^a,
ECATERINA BICA^a, ADRIAN-IONUȚ CADIȘ^a,
MARIUS MORAR^a AND EMIL INDREA^b

ABSTRACT. Cerium activated yttrium silicate phosphors show blue luminescence under UV excitation. Phosphor utilisation depends on powder characteristics and luminescence properties that are regulated during the synthesis stage. In this paper yttrium silicate based phosphors were prepared by solid state reaction using different molar ratio between SiO_2 and Y_2O_3 . The effect of chemical composition and structure on luminescent properties of phosphors were investigated and discussed.

Keywords: *yttrium silicate, luminescence, solid state reaction*

INTRODUCTION

Yttrium silicate phosphors (Y_2SiO_5) doped with Eu^{3+} , Ce^{3+} , Pr^{3+} , Tb^{3+} or Yb^{3+} are well known luminescent materials due to their luminescent characteristics [1]. Under UV excitation $\text{Y}_2\text{SiO}_5\text{:Ce}$ phosphor exhibits blue-white emission with the peak maximum situated at 414 nm.

Y_2SiO_5 phosphor is usually used as luminescent material in fluorescent lamps, field emission display (FED) and projection television (PTV) because of its brightness, acceptable atmospheric stability and quantum efficiency [2,3].

Many methods such as solid state reaction, sol gel techniques, spray pyrolysis and combustion synthesis have been used to prepare silicate phosphors [4-6]. The analysis of the $\text{Y}_2\text{O}_3\text{-SiO}_2$ phase diagram shows the presence of various compounds such as: Y_2O_3 , SiO_2 , Y_2SiO_5 and $\text{Y}_2\text{Si}_2\text{O}_7$, depending on the synthesis temperature [7,8].

In correspondence to the 1:1 molar ratio, we can find two type of monoclinic Y_2SiO_5 ($\text{Y}_2\text{O}_3\cdot\text{SiO}_2$), known as X1- Y_2SiO_5 phase (crystallographic group P21/c) and X2- Y_2SiO_5 phase (crystallographic group B2/b) [9,10].The

^a Raluca Ripan Institute for Research in Chemistry, Babes Bolyai University, 400294, Cluj-Napoca, Romania, * laura_muresan2003@yahoo.com

^b National Institute for R & D of Isotopic and Molecular Technologies, 400295 Cluj-Napoca, Romania

second compound in the system is $Y_2Si_2O_7$ ($Y_2O_3 \cdot 2SiO_2$), which shows an even more complex polymorphism, since six $Y_2Si_2O_7$ different structures are reported for it [11].

In practical applications the chemical reaction between rare earth oxides and silicon dioxide at elevated temperatures should be considered as a possible cause of drastic modification of both structure and luminescent properties of yttrium silicate-based powders.

In this paper yttrium silicate phosphor samples were prepared by solid state reaction using different molar ratios between SiO_2 and Y_2O_3 . The effect of chemical composition and structure on optical properties of Ce^{3+} activated yttrium based silicates were investigated and discussed. Samples were characterised by infrared absorption spectroscopy (FT-IR), X-ray diffraction (XRD), and photoluminescence spectroscopy, i.e. emission (PL) and excitation (PLE) spectra.

RESULTS AND DISCUSSION

The Y_2O_3 - SiO_2 phase diagram is currently explored with a variety of synthesis techniques especially in the 1:1 and 1:2 molar ratio domains because of the optical properties that can be induced by dispersion of rare-earth elements such as Eu^{3+} , Tb^{3+} and Ce^{3+} into the matrix. According to the diagram phase [8] several compounds can be detected depending on the Y_2O_3 - SiO_2 molar ratio.

In order to study the influence of the powders composition on the structure and luminescent properties, yttrium silicate based materials were prepared by solid state reaction route at $1400^\circ C$ using different $SiO_2:Y_2O_3$ molar ratios ($MR_{Si:Y}$) namely: 1:4 (sample code YSO25); 1:1 (sample code YSO26); 1:0.5 (sample code YSO27) and 1:0.25 (sample code YSO28). The photoluminescence of the samples YSO29, YSO30, YSO31 and YSO32 was induced by adding 3% mol $Ce/(Y+Ce)$ in the mixture of silicon dioxide and yttrium oxide.

The crystalline structure and structural homogeneity of the powders were put in evidence by XRD measurements (Figure 1).

The XRD patterns indicate that all the powders contain mainly crystalline phases. Also, the XRD patterns confirm the structural changes that occur due to the addition of various amounts of SiO_2 in the synthesis mixture. Different compounds such as: X1- Y_2SiO_5 (low temperature phase); X2- Y_2SiO_5 (high temperature phase) and monoclinic $Y_2Si_2O_7$ together with unreacted Y_2O_3 and SiO_2 can be identified. It can be also observed that the increase of SiO_2 amount in the synthesis mixture determines changes in both, the composition and structure.

Based on the XRD patterns, the unit cell parameters and the quantitative phase composition were determined through Rietveld refinement using the PowderCell software. The amount (volume percentage) of the various phases in the silicate based powders was calculated [12].

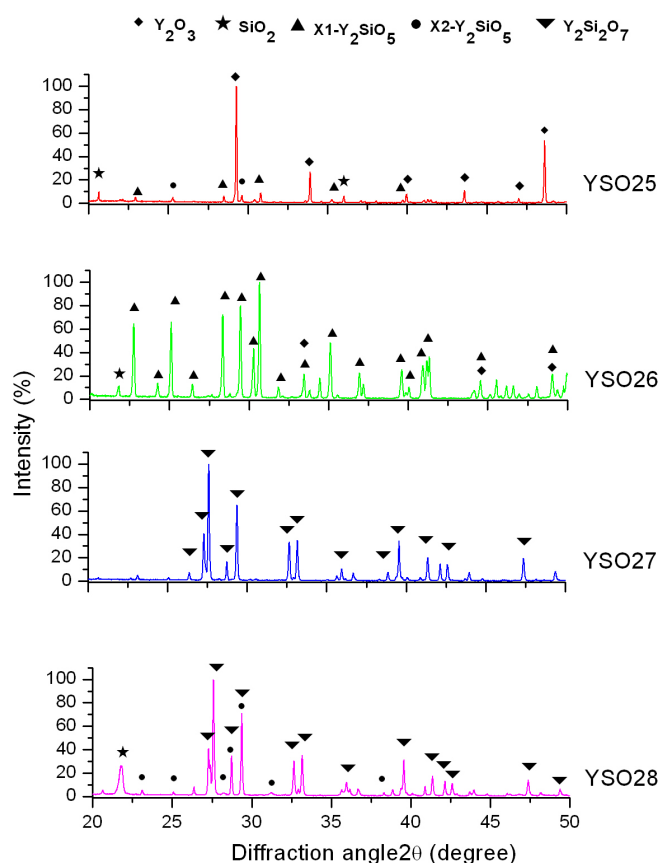


Figure 1. The X-ray diffraction patterns ($\lambda_{\text{Cu}}=1.540598\text{\AA}$) of samples prepared with different $\text{MR}_{\text{Si:Y}}$

Composition of the starting synthesis mixtures together with some microstructural parameters are presented in Table 1.

When yttrium oxide is used in excess (the case of $\text{MR}_{\text{Si:Y}}=1:4$, sample YSO25), the synthesis mixture contains mainly un-reacted crystalline cubic yttrium oxide phase in proportion of 89.4 vol.% together with 2 vol.% of unreacted tetragonal silicon dioxide and 8.6 vol.% X1, X2 yttrium silicate. When stoichiometric amounts of yttrium oxide and silica oxide were used in

sample YSO26, the phase X2-Y₂SiO₅ becomes the dominant (81.7 vol.%). Excess of silica dioxide (MR_{Si:Y} = 1:0.5) in the synthesis mixture leads to the formation of one phase powder that consists only in monoclinic yttrium disilicate- Y₂Si₂O₇.

The results are in agreement with the literature data namely: Y₂O₃ -cubic phase (PDF 43-1036); SiO₂ tetragonal phase (PDF 39-1425); X1-Y₂SiO₅ monoclinic phase, (PDF 41-0004); X2-Y₂SiO₅ monoclinic phase (PDF 21-1458) and Y₂Si₂O₇ monoclinic phase (PDF 38-0440).

Table 1. Microstructural parameters for SiO₂ - Y₂O₃ based phosphors

Sample	MR _{Si:Y}	Microstructural parameters					V[Å ³]
		Phase	a[Å]	b[Å]	c[Å]	Beta	
YSO25	1:4	Y ₂ O ₃ -cubic(89.4%)	10.616	10.616	10.616	90.0	1189.0
		X1-Y ₂ SiO ₅ (8.4%)	8.400	6.841	6.383	103.0	357.5
		X2-Y ₂ SiO ₅ (0.2%)	10.317	6.623	12.583	103.7	835.1
		SiO ₂ tetragonal (2 %)	4.973	4.973	6.923	90.0	171.2
YSO26	1:1	Y ₂ O ₃ -cubic (8.3%)	10.507	10.507	10.507	90.0	1159.9
		X2-Y ₂ SiO ₅ (81.7 %)	10.420	6.726	12.499	102.6	854.9
YSO27	1:0.5	SiO ₂ tetragonal (10.0%)	4.973	4.973	6.923	90.0	171.2
		Y ₂ Si ₂ O ₇ -monoclinic 100%	6.871	8.968	4.718	101.7	284.7
YSO28	1:0.25	Y ₂ Si ₂ O ₇ (78.8%)	6.871	8.969	4.719	101.7	284.8
		X2-Y ₂ SiO ₅ (6.2%)	10.453	6.732	12.444	103.0	854.0
		SiO ₂ tetragonal (15.0%)	4.973	4.973	6.923	90.0	171.2

FT-IR spectra for yttrium silicate based samples are presented in Figure 2. Significant changes are observed as the amount of SiO₂ increases from 20 mol.% to 80 mol.%, in the synthesis mixture.

The vibrational bands in FT-IR spectra in 400-1400 cm⁻¹ domain can be grouped in three main regions namely:

- 1070 -1200cm⁻¹ domain for stretching vibrations of silicon atoms against oxygen atoms in Si-O-Si bonds in β-Y₂Si₂O₇ phase [13];
- 850 -1000cm⁻¹ domain corresponds to Si-O stretching vibration involving non-bridging oxygen. The band situated at around 849 cm⁻¹ is ascribed to multiple Si-O stretching in which all oxygen and silicon atoms of silicate groups participate in the vibration [13];
- 400- 600 cm⁻¹ domain consist in lower vibrational bands more difficult to characterize, because single Y-O and Si-O vibrations coexist in similar spectral ranges. It can be stated that the vibrations situated in the range 600 to 500 cm⁻¹ are mainly due to Y-O stretching, and those from 500 to 400 cm⁻¹ are vibrations with a large component of Si-O bending [14,15].

It can be seen that as the SiO_2 amount decreases, the specific vibration for Si-O-Si bond in $\text{Y}_2\text{Si}_2\text{O}_7$ phase disappears (sample YSO27, YSO28) and bands from asymmetric stretching vibration in SiO_4^{2-} groups arise and become more structured (sample YSO25, YSO26).

Photoluminescence of $\text{Y}_2\text{SiO}_5\text{:Ce}$ phosphor samples was evaluated on the basis of excitation (PLE) and emission (PL) spectra and compared with an internal standard where the $\text{MR}_{\text{Si:Y}} = 1:1$. The internal standard was prepared by wet chemical synthesis route, using the SimAdd technique [16-18]. The intensity of the internal standard (YSO1.1) was considered to possess 100% photoluminescence [18].

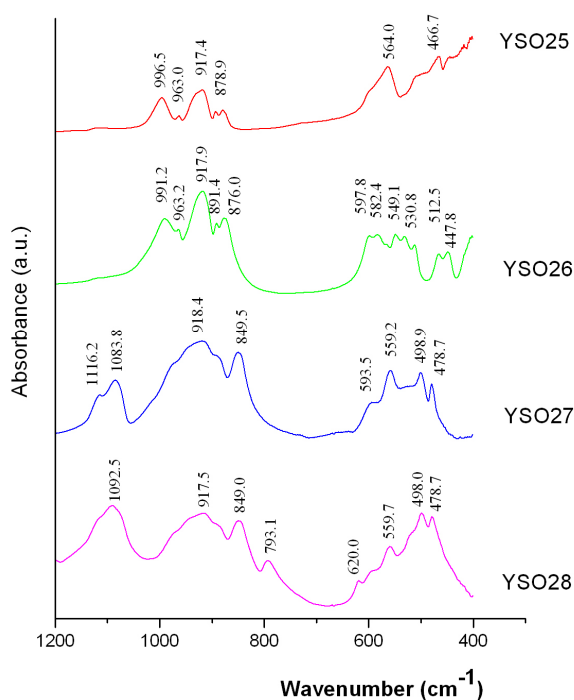


Figure 2. The FT-IR spectra of samples prepared with different $\text{RM}_{\text{Si:Y}}$

Figure 3 and Figure 4 show the PLE and PL spectra of Ce^{3+} activated Y_2SiO_5 samples synthesized by solid state reaction with different $\text{SiO}_2\text{:Y}_2\text{O}_3$ molar ratio.

The excitation spectra can give also information on the nature of the luminescent centres.

In this respect, the excitation spectra taken in the range of 220–400 nm present three wide bands (Figure 3). These bands (designated with I, II, III) are associated with the crystal field split of Ce^{3+} 5d electronic levels.

The excitation peaks of the internal standard (sample YSO 1.1) are situated at 265 nm, 300 nm and 356 nm, respectively.

The intensity and the position of excitation peaks of the yttrium silicate samples are variable and depend on the $SiO_2:Y_2O_3$ molar ratio. For samples YSO30 and YSO32, the peaks I and III present a shift from 265 nm to 246 nm and from 356 nm to 349 nm, respectively.

The excitation spectra for samples prepared with excess of SiO_2 namely YSO30 ($MR_{Si:Y}=1:0.25$) and YSO32 ($MR_{Si:Y}=1:0.5$) present a similar behaviour. Thus, the peak II with maximum situated at 301 nm for samples YSO30, YSO32 is more broad compared to the corresponding one situated at 299 nm for sample YSO29 and 300 nm for standard.

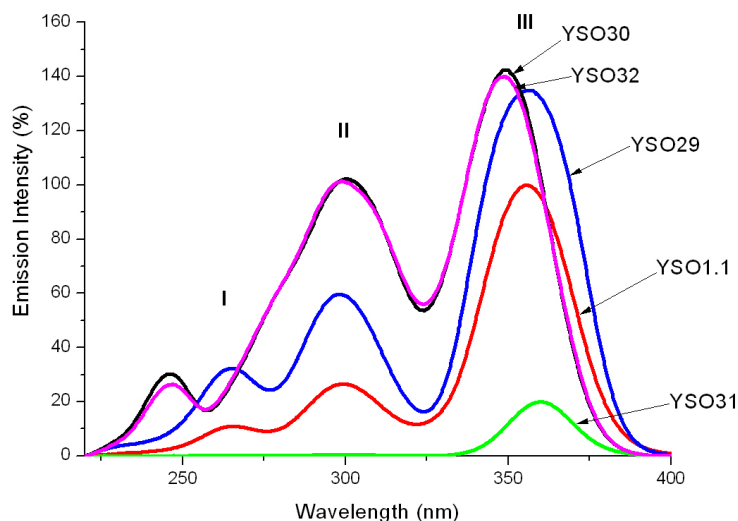


Figure 3. Excitation spectra of some YSO samples ($\lambda_{em}=420nm$)

The photoluminescent characteristics correlated with XRD and FT-IR data, lead to the conclusion that depending on the molar ratio, different luminescent centres are formed. In samples YSO30 and YSO32, the Ce^{3+} surrounding is given by the presence of the $Y_2Si_2O_7$ as host lattice, meanwhile in sample YSO 29 the luminescent centers are formed in an Y_2SiO_5 host lattice.

Excitation spectrum of the sample YSO31, prepared with SiO_2 : Y_2O_3 molar ratio of 1:4, presents only one broad band with low intensity with a maximum situated at 361 nm. The reduced excitability of YSO31 sample can be also explained in correlation with XRD data. Due to the formation of a non-homogeneous powder that consists mainly in a mixture of unreacted Y_2O_3 and SiO_2 together with Y_2SiO_5 in relative small proportion, the incorporation degree of cerium is reduced.

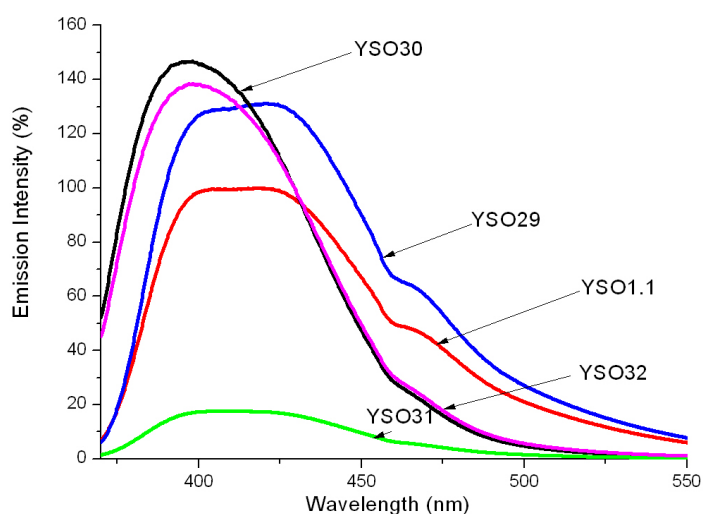


Figure 4. Emission spectra of some YSO samples ($\lambda_{\text{ex}}=356\text{nm}$)

Under UV light (365 nm) all YSO samples exhibit a luminescent emission situated in the blue domain of visible spectra. The emission spectra present a wide band with a maximum situated at around 400 nm as a result of the 4f energy levels splitting into $4f_{5/2}$ and $4f_{7/2}$ in cerium activator (Figure 4).

The Ce^{3+} activator ($r_{\text{Ce}^{3+}} = 0.106 \text{ nm}$) can easily substitute Y^{3+} from the oxide host lattice ($r_{\text{Y}^{3+}} = 0.104 \text{ nm}$) and populate two crystallographic sites in $\text{X1-Y}_2\text{SiO}_5$ and $\text{X2-Y}_2\text{SiO}_5$. If there is an excess of SiO_2 , the chemical surrounding of the Ce^{3+} becomes more complicated due to the formation of $\text{Y}_2\text{Si}_2\text{O}_7$ with different structures [11].

A double broad emission band with peaks situated at around 402 nm and 423 nm respectively, due to the splitting of the $4f^1$ ground configuration of the cerium ions into $^2F_{5/2}$ and $^2F_{7/2}$ can be observed for both YSO1.1 (standard) and YSO29 sample.

Considering the XRD information for $MR_{Si:Y}=1:1$ we can assume that the luminescent centres in sample YSO29 are given mainly by the presence of Ce^{3+} activators in $X2-Y_2SiO_5$ host lattice.

The emission intensity and the peak positions are modified as the composition of the silicate based samples is changed. Sample prepared with excess of silicon dioxide posses similar emission curves as can be observed for samples YSO 30 and YSO32 in which the main component is $Y_2Si_2O_7$. This samples have high photoluminescence ($I_{em} = 147\%$ and $I_{em} = 137\%$) with the maximum situated at 398 nm

Another tendency easily observed in the emission spectra is the large emission tail which extends toward the red region of the visible spectrum (from 450 to 550 nm) as well as the shoulder situated at 465 nm. This behaviour is associated with $5d-4f$ transitions and the formation of Y_2SiO_5 phase [19].

CONCLUSIONS

Yttrium silicate based materials were prepared by solid state reaction with different $SiO_2:Y_2O_3$ molar ratios in order to study the influence of the synthesis mixture composition on the structural and luminescent properties. It was revealed that $MR_{Si:Y}$ influences the structural and luminescent characteristics of samples.

The XRD patterns and FT-IR spectra put in evidence that the phosphor samples are formed from a mixture of unreacted Y_2O_3 and SiO_2 together with monoclinic $X1-Y_2SiO_5$, $X2-Y_2SiO_5$ and $Y_2Si_2O_7$ phases in various proportions depending on the molar ratio.

The photoluminescent investigations put in evidence that under UV light all yttrium silicate based samples exhibit more or less intense blue emission. The excitation spectra have three broad bands which present a shift toward shorter wavelengths as the content of the SiO_2 increase. The excess of Y_2O_3 leads to samples with small excitability and low emission intensity. This suggests that an insufficient amount of SiO_2 can not assure the formation of the proper host lattice surroundings for Ce^{3+} . An excess of SiO_2 in the synthesis mixture generates the formation of monoclinic yttrium disilicate phase with a high luminescent emission.

EXPERIMENTAL SECTION

Two samples series of yttrium based silicate powders were prepared by solid-state reaction method. In this respect, homogeneous synthesis mixtures containing Y_2O_3 (Sigma Aldrich) and SiO_2 (Sigma Aldrich) as generator of host-lattice and $Ce(NO_3)_3 \cdot 5H_2O$ (Sigma Aldrich) as activator supplier were fired at high temperature ($1400^{\circ}C$) for 4 hours, in air, using alumina crucibles. The yttrium silicate based powders were carefully washed, dried and sieved.

The first sample series is formed from samples: YSO25, YSO26, YSO27 and YSO28 which are prepared using different SiO₂:Y₂O₃ molar ratios namely: 1:4, 1:1, 1:0.5 and 1:0.25 respectively.

Second set of samples consist of samples: YSO29, YSO30 YSO31, YSO32 which are prepared using different SiO₂:Y₂O₃ molar ratios namely: 1:1, 1:0.25, 1:4, 1:0.5 and are prepared using 3% mol Ce/(Y+Ce) in the synthesis mixture in order to generate photoluminescent properties. The internal standard (YSO1.1) was prepared by SimAdd method using ammonium oxalate (Merck 99.9%), yttrium oxide (Aldrich 99.99%), cerium nitrate (Merck, extra pure) and silicagel powder (Alfa Aesar) as starting materials [16-18]. The synthesis consist in the thermal treatment at 1600^oC in nitrogen for 4 hrs of the precursor prepared by precipitation of yttrium-cerium nitrate solution, with ammonium oxalate solutions and silica suspension at pH=6 [18]. The post-precipitation stage consisted of 24 h aging, centrifuge separation, water wash and drying.

Samples were characterised by photoluminescence spectroscopy, X-ray diffraction (XRD), infrared absorption spectroscopy (FT-IR). The emission (PL) and excitation (PLE) spectra were registered with JASCO FP-6500 Spectrofluorimeter Wavel (Farbglasfilter WG 320/ Reichmann Feinoptik-Ger). X-ray diffraction patterns were obtained with BRUKER X8 ADVANCE X-Ray Diffractometer (CuK α λ =1.540598Å radiation). The infrared absorption spectra were measured with a NICOLET 6700 Spectrometer (KBr pellets technique).

ACKNOWLEDGMENTS

Financial support for this study was provided by the Romanian Ministry of Education, Research and Innovation (Project 71-122).

REFERENCES

1. W.M. Yen, S.Shionoya, H. Yamamoto, "Practical application of phosphors", CRC press, Taylor & Francis Grup, Boca Roton-London-New York, **2007**.
2. R.Y. Lee, F.I. Zhang, *J. Vac. Sci. Technol.*, **1998**, B16, 1013.
3. M. Leskelaa, *J. Alloys Compd.*, **1998**, 275-277, 702.
4. H. Jiao, X. Wang, S. Ye, *J. Lumin.*, **2007**, 122-123, 113.
5. X. Qin, Y. Ju, S. Bernhard, Nan Yao, *Mater. Res. Bul.*, **2007**, 42, 1440.
6. H. Jiao, L. Wei, N. Zhang, M. Zhong, X. Jing, *J. Eur. Ceramic Soc.*, **2007**, 27, 185.

7. E.M. Levin, C.R. Robbins, H.F. McMurdie, Phase Diagram for Ceramists, Fig. 2388, in M.K. Reser (Ed.), American Ceramic Society, Columbus, OH USA, **1969**.
8. Q.Y. Zhang, K. Pita, *J. Phys. D. Appl. Phys.*, **2002**, *35*, 3085.
9. C. Michel, G. Buisson, E.F. Bertaut, *C.R. Acad. Sci. B*, **1967**, *264*, 397.
10. N. I. Leonyuk, E. L. Belokoneva, G. Bocelli, L. Righi, E. V. Shvanskii, R. V. Henrykhson, N. V. Kulman, D. E. Kozhbakhteeva, *Cryst. Res. Technol.*, **1999**, *34*, 1175.
11. J. Felsche, *Struct. Bond.*, **1973**, *13*, 99.
12. W. Kraus, G. Nolze, *J. Appl. Crystallogr.*, **1996**, *29*, 301.
13. M. Di'az, C. Pecharrorna'n, *Chem. Mater.*, **2005**, *17*, 1774.
14. Y. Repelin, C. Proust, E. Husson, J. M. Beny, *J. Solid State Chem.*, **1995**, *118*, 163.
15. A. M. Hofmeister, A. Chopelas, *Phys. Chem. Miner.*, **1991**, *17*, 503.
16. E.J. Popovici, L. Muresan, A. Hristea, E. Indrea, M. Vasilescu, *J. Alloys Compd.*, **2007**, *434-435*, 809.
17. L. Muresan, E.J. Popovici, R. Grecu and L. Barbu Tudoran, *J. Alloys Compd.*, **2009**, *471*, 421.
18. L. Muresan, M. Stefan, E. Bica, M. Morar, E. Indrea, E.J. Popovici, *J. Optoelectron. Adv. M. - Symposia*, **2010**, *2*, 131.
19. J.A. Gonzalez-Ortega, E.M. Tejada, N. Perea, *Opt. Mater.*, **2005**, *27*, 1221.

Dedicated to the memory of Prof. dr. Ioan Silaghi-Dumitrescu marking 60 years from his birth

STUDIES ON THE SYNTHESIS OF MANGANESE DOPED ZINC SULPHIDE NANOCRYSTALLINE POWDERS

ADRIAN-IONUŢ CADIŞ^{a,b}, ELISABETH-JEANNE POPOVICI^a,
ECATERINA BICA^{a,b}, LUCIAN BARBU-TUDORAN^c

ABSTRACT. New synthesis precipitation technique to prepare nanoparticles of Mn-doped zinc sulphide ZnS:Mn²⁺ have been attempted. Various capping agents have been used to control the morphostructural properties of ZnS:Mn²⁺ particles. Infrared absorption spectroscopy (FT-IR), photoluminescence spectroscopy (PL), scanning (SEM) and transmission electron microscopy (TEM) were used to characterise the powder samples. Strong luminescent ZnS:Mn²⁺ nanocrystalline powders could be precipitated at room temperature, from sodium sulphide and zinc-manganese acetate solutions, using the reagent simultaneous addition technique-SimAdd and methacrylic acid or sodium dodecyl sulphate as passivating agent.

Keywords: ZnS nanoparticles, Mn-doped nanoparticles, photoluminescence.

INTRODUCTION

In recent times, there have been extensive studies on luminescent semiconductor nanocrystals because of their potential applications in future optoelectronic devices. In undoped II–VI semiconductors (e.g., CdS, CdSe, and ZnS), the bandgap is engineered by control of the crystal size that leads to tunable band-edge emission [1–6]. Following the report of Bhargava and Gallagher [7], doped semiconductor nanocrystals have been regarded as a new class of luminescent material. Among them, ZnS nanoparticles doped with Mn²⁺ exhibit high luminescence quantum efficiency and short luminescence lifetime.

These materials, because they can be obtained in the form of thin films [8], powders and sols [9], have wide range of applications in sensors, displays, electronic devices, laser devices, and nonlinear optical devices, etc. [6–7].

^a "Raluca Ripan" Institute for Research in Chemistry, "Babes-Bolyai" University, Fântânele 30, 400294 Cluj-Napoca, Romania, * cadisadi@chem.ubbcluj.ro

^b Faculty of Chemistry and Chemical Engineering, "Babes-Bolyai" University, 11, Arany Janos, 400028 Cluj-Napoca, Romania

^c Electronic Microscopy Centre, "Babes-Bolyai" University, Clinicilor 5-7, 400006 Cluj-Napoca, Romania

Having applications in various fields such as optoelectronics, photocatalysis, solar energy conversion, fluorescence microscopy, synthesis of un-doped or Mn-doped ZnS 1D nanostructure have also been reported recently by many researchers [10–13].

The increasing interest in un-doped or doped ZnS nanoparticles has lead to the development of a variety of chemical routes to prepare nanoparticles, including ultrasound [14] and microwave irradiation [15], sol–gel method [16], solid-state reaction [17] and chemical precipitation [18].

The morphostructural and luminescent properties of ZnS powders strongly depend on the specific preparation method and the experimental conditions.

The precipitation of zinc sulphide using the reagent sequential addition technique - *SeqAdd* is the most popular method due to some advantages such as the use of cheap raw materials, easy handling and large-scale-production potential [6].

The present paper reports our attempts to obtain ZnS:Mn nanoparticles by chemical precipitation, using a new wet-chemical synthesis route based on the reagent simultaneous addition technique - *SimAdd*, that was developed for the manufacture of microcrystalline phosphors [19]. In order to control the particle morphology and size, methacrylic acid and sodium dodecyl sulphate were used as passivating/capping agents. The influence of surfactants on the photoluminescence and morphostructural properties of ZnS:Mn²⁺ powders prepared by SimAdd was investigated, using scanning (SEM) and transmission (TEM) electron microscopy, infrared absorption (FTIR) and photoluminescence emission (PL) and excitation (PLE) spectroscopy.

RESULTS AND DISCUSSION

The preparation of ZnS:Mn²⁺ powder was based on the reaction, at room temperature, between zinc acetate and manganese acetate, as metal sources, and sodium sulphide, as chalcogen supplier. When using SimAdd technique, the reagents are simultaneously added into diluted zinc acetate solution containing no additives (C79 sample), sodium dodecyl sulphate – SDS (C80 sample) or methacrylic acid – MA (C81sample) as particle size regulating agent.

The main chemical process for the preparation of ZnS:Mn²⁺ powder i.e. for the formation of zinc-manganese double sulphide is described by the following equation:



Under UV excitation, the as prepared ZnS:Mn²⁺ powders show the characteristic Mn²⁺ emission. Photoluminescence emission (PL) and excitation (PLE) spectra are depicted in Figure 1. Sample C79 prepared with no additive was used as internal standard ($I_{600\text{nm}}=100\%$; $I_{340\text{nm}}=100\%$).

Photoluminescence emission (PL) spectra consist of two broad emission bands namely, a strong orange one at about 600 nm and a very weak blue one at 400–480 nm.

The characteristic orange emission band can be attributed to the electronic transition between ⁴T₁ and ⁶A₁ energy levels of the Mn²⁺ 3d states. Mn²⁺ d-electron states act as efficient luminescent centres while interacting strongly with s–p electronic states of the ZnS host into which an external electronic excitation is normally directed. The blue emission is characteristic to zinc sulphide and it is usually influenced by many factors e.g. particles size, crystallinity, doping level, surface states of particles etc. Since a large portion of the atoms in nanocrystals is located on or near the surface, the surface properties should have significant effect on their optical properties.

Photoluminescence properties of ZnS:Mn²⁺ powders are influenced by the presence of the passivating agents into the precipitation medium. The use of the sodium dodecyl sulphate increases the orange emission intensity with 25% while the presence of methacrylic acid improves it with only 7%. On the other hand, the intensification of the blue emission is insignificant in the presence of sodium dodecyl sulphate (~0.5%) or methacrylic acid (~0.2%).

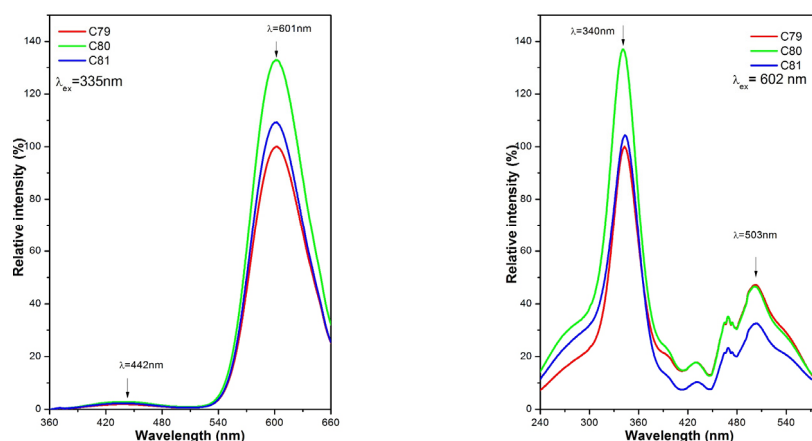


Figure 1. PL (left) and PLE (right) spectra of ZnS:Mn²⁺ powders prepared with no additive (C79), SDS (C80) and MA (C81)

Photoluminescence excitation spectra were registered by monitoring the characteristic orange emission (~ 600 nm) of Mn^{2+} under excitation with variable UV radiation. The highest PLE peak centred at about 340 nm can be attributed to the ZnS host lattice excitation whereas the multiple peaks in the 375-575 nm range can be related to Mn^{2+} presence.

In doped semiconductors, the possible paths for the luminescence excitation of the impurity ions include indirect excitation of the host lattice and direct excitation of impurity ions. This strong excitation absorption peak should arise from the direct excitation transitions of Mn^{2+} . According to the literature [20], the PLE peaks observed around 390, 430, 465, 500, and 535 nm can be attributed to the transitions between the ${}^6\text{A}_1({}^6\text{S})$ ground state and the excited states of ${}^4\text{E}({}^4\text{D})$, ${}^4\text{T}_2({}^4\text{D})$, ${}^4\text{A}_1({}^4\text{G})$ and ${}^4\text{E}({}^4\text{G})$, ${}^4\text{T}_2({}^4\text{G})$, ${}^4\text{T}_1({}^4\text{G})$ within the $\text{Mn}^{2+} 3\text{d}^5$ configuration, respectively.

The influence of the passivating agents on photoluminescence properties is also evident in PLE spectra. The strong excitation peak related with the ZnS host (~ 340 nm) is increased with about 37 % in sample with SDS and only with 4 % in sample with MA. SDS seems to do not influence the excitation peaks associated with Mn^{2+} while MA addition decrease them with about 30%, comparative with $\text{ZnS}:\text{Mn}^{2+}$ without surfactant.

Particle dimensions of $\text{ZnS}:\text{Mn}^{2+}$ powders were evaluated by electron microscopy.

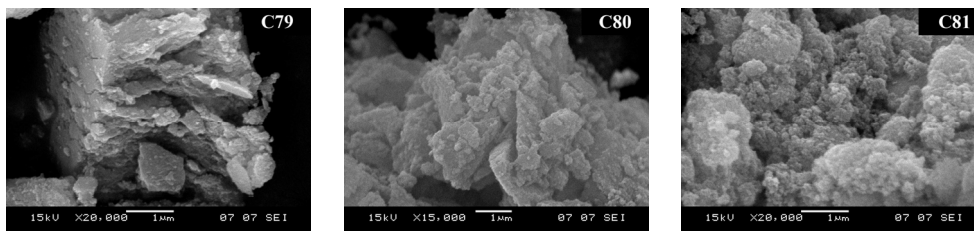


Figure 2. SEM images of different $\text{ZnS}:\text{Mn}^{2+}$ samples obtained in various experimental conditions.

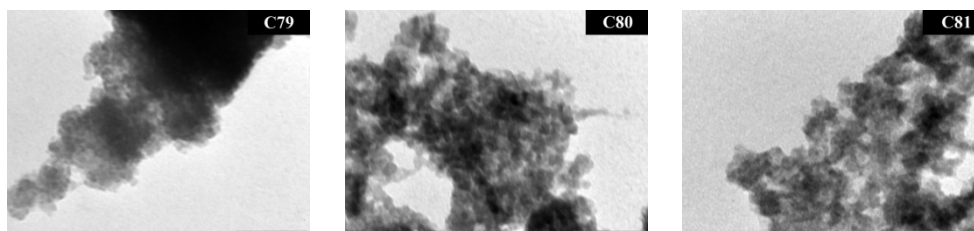


Figure 3. TEM images of different $\text{ZnS}:\text{Mn}^{2+}$ samples obtained in various experimental conditions (scale bar=50 nm).

SEM investigation of samples prepared with and without surfactants i.e. C80-SDS, C81-MA and C79, shows that ZnS:Mn²⁺ powders consist in large conglomerates formed from tightly packed under-micron particles (Figure 2).

TEM images of samples C79-no surfactant, C80-SDS and C81-MA illustrate the nanocrystalline state of ZnS:Mn²⁺ all powders (Figure 3). The average diameter of nanoparticles is evaluated at 6-10 nm.

The nanopowders obtained by SimAdd technique have a high surface area and energy that account for the strong tendency of particles toward agglomeration. SDS and MA additives seem to increase the powder dispersability; no effect on the particles dimension could be noticed.

The as prepared ZnS nanopowders show a high capacity to absorb impurities and regulating agent from the precipitation medium, as illustrated by the infrared absorption spectra depicted in Figure 4. FTIR spectrum of C80-SDS contains the characteristic absorption bands of sodium dodecyl sulphate i.e. O–H stretching (3800–3200 cm⁻¹) and bending (1700–1600 cm⁻¹), C–H stretching of CH₃ and CH₂ groups (3000–2800 cm⁻¹), C=O asymmetric and symmetric stretching (1600 and 1400 cm⁻¹), C–O stretching (1025 cm⁻¹) and SO₂ stretching (1300–1100 cm⁻¹) vibrations [21].

FTIR spectroscopy illustrates that, in spite of the fact that the precipitate was thoroughly washed, ZnS:Mn²⁺ powders with large surface area contain residual CH₃COO⁻, dodecyl sulphate and methacrylate ions.

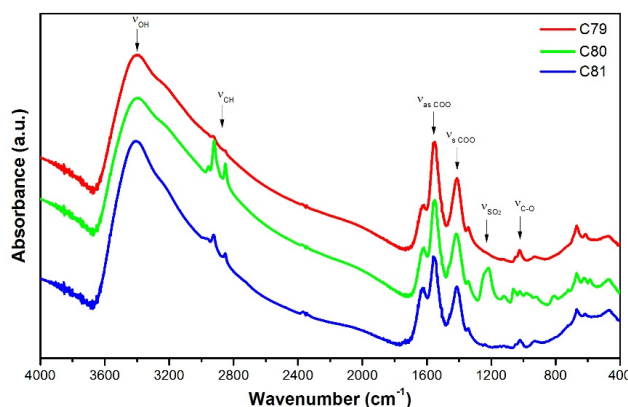


Figure 4. FT-IR spectra of ZnS:Mn²⁺ powders prepared with no additive (C79), SDS (C80) and MA (C81)

CONCLUSIONS

Luminescent manganese doped zinc sulphide (ZnS:Mn²⁺) nanopowders could be obtained by precipitation, using the simultaneous reagent addition technique-*SimAdd*, with or without sodium dodecyl sulphate or methacrylic acid as particle size regulating agents.

The photoluminescence measurements show that ZnS:Mn²⁺ powders show strong orange luminescence ($\lambda_{pk} \sim 600$ nm) characteristic to Mn²⁺. The strong PL of the un-annealed ZnS:Mn²⁺ powders could be associated with the particle nano-dimension. The strongest photoluminescent powder was obtained in the presence of sodium dodecyl sulphate.

Although ZnS:Mn²⁺ powders are formed from nanosized crystallites (6-10 nm), they are tightly packed into larger and irregular shaped particles. The large surface area explains the high absorption capacity of the ZnS powder, as illustrated by FTIR investigations.

EXPERIMENTAL SECTION

Manganese doped zinc sulphide powders were prepared by precipitation, using the reagent simultaneous addition technique-*SimAdd*, from Zn-Mn acetate and sodium sulphide in aqueous medium, at room temperature. In this respect, equal volumes of 1M aqueous solution of zinc -manganese acetate (8 % mol Mn/(Zn+Mn) and 1M aqueous solution of sodium sulphide were added, under stirring, in water, with or without surfactant addition, sodium dodecyl sulphate and methacrylic acid. The white-pink ZnS powder was separated through centrifugation, washed with isopropyl alcohol and dried at 80°C.

Infrared absorption spectra (FTIR) were registered on a NICOLET 6700 Spectrophotometer (KBr pellets technique). Photoluminescence emission (PL) and excitation (PLE) spectra were taken with JASCO FP-6500 Spectrofluorimeter (Farbglasfilter WG 320-ReichmannFeinoptik; Sample C79 prepared with no surfactant addition was used as internal standard $I_{em}=100\%$). The transmission electron microscopy (TEM) was performed with JEM JEOL 1010 microscope and the scanning electron microscopy (SEM) images were obtained with a JEOL-JSM 5510LV instrument, using Au-coated samples.

ACKNOWLEDGMENTS

The Romanian Ministry of Education, Research and Innovation (Contract ID-2488/710) supported this research project.

REFERENCES

1. K. Sooklal, B. S. Cullum, S. M. Angel, C. J. Murphy, *Journal of Physical Chemistry*, **1996**, 100(11), 4551.
2. N. Murase, R. Jagannathar, Y. Kanematsu, M. Watanable, A. Kurita, K. Hirata, T. Yazawa, T. Kushida, *Journal of Physical Chemistry B*, **1999**, 103(5), 754.

3. W. Chen, V. F. Aguekian, N. Vassiliev, A. Y. Serov, N. G. Filosofov, *Journal of Chemical Physics*, **2005**, 123(12), 124707.
4. Z. Quan, Z. Wang, P. Yang, J. Lin, J. Fang, *Inorganic Chemistry*, **2007**, 46(4), 1354.
5. B. Y. Geng, L. D. Zhang, G. Z. Wang, T. Xie, Y. G. Zhang, G. W. Meng, *Applied Physics Letters*, **2004**, 84(12), 2157.
6. Z. L. Wang, Y. Liu, Z. Zhang, "Handbook of Nanophase and Nanostructured Materials Synthesis", Tsinghua University Press and Kluwer Academic Plenum Publishers, New York, **2002**.
7. R. N. Bhargava, D. Gallagher, X. Hong, A. Nurmikko, *Physical Review Letters*, **1994**, 72(3), 416.
8. M. Stefan, I. Baldea, R. Grecu, E. Indrea, E.J. Popovici, *Studia Universitatis Babes-Bolyai, Chemia*, **2009**, 54(3), 203.
9. A. I. Cadis, A. R. Tomsa, M. Stefan, R. Grecu, L. Barbu-Tudoran, L. Silaghi-Dumitrescu, E. J. Popovici, *Journal of Optoelectronics and Advanced Materials – Symposia*, **2010**, 2(1), 111.
10. F. Piret, C. Bouvy, W. Marine, B. L. Su, *Chemical Physics Letters*, **2007**, 441(1-3), 83.
11. X. J. Zheng, Y. Q. Chen, T. Zhang, C. B. Jiang, B. Yang, B. Yuan, S. X. Mao, W. Li, *Scripta Materialia*, **2010**, 62(7), 520.
12. C. Unni, D. Philip, K. G. Gopchandran, *Optical Materials*, **2009**, 32(1), 169.
13. J. S. Jang, C. J. Yu, S. H. Choi, S. M. Ji, E. S. Kim, J. S. Lee, *Journal of Catalysis*, **2008**, 254(1), 144.
14. A. R. Tomsa, E. J. Popovici, A. I. Cadis, M. Stefan, L. Barbu-Tudoran, S. Astilean, *Journal of Optoelectronics and Advanced Materials*, **2008**, 10(9), 2342.
15. J. Q. Sun, X. P. Shen, K. M. Chen, Q. Liu, W. Liu, *Solid State Communications*, **2008**, 147(11–12), 501.
16. M. M. Biggs, O. M. Ntwaeaborwa, J. J. Terblans, H. C. Swart, *Physica B: Condensed Matter*, **2009**, 404(22), 4470.
17. L. P. Wang, X. D. Xu, X. Yuan, *Journal of Luminescence*, **2010**, 130(1), 137.
18. A. I. Cadis, A. R. Tomsa, E. Bica, L. Barbu-Tudoran, L. Silaghi-Dumitrescu, E. J. Popovici, *Studia Universitatis Babes-Bolyai, Chemia*, **2009**, 54(3), 23.
19. E. J. Popovici, M. Stefan, F. I. Lucaci, L. Muresan, E. Bica, M. Morar, E. Indrea, L. Barbu-Tudoran, *Physics Procedia*, **2009**, 2(2), 603.
20. W. Q. Peng, S. C. Qu, G. W. Cong, X. Q. Zhang, Z. G. Wang, *Journal of Crystal Growth*, **2005**, 282(1-2), 179.
21. B.H. Stuart, "Infrared Spectroscopy: Fundamentals and Applications", John Wiley & Sons Ltd., Chichester, **2004**.

Dedicated to the memory of Prof. dr. Ioan Silaghi-Dumitrescu marking 60 years from his birth

RAMAN IMAGING OF IN VIVO DAMAGED SKIN TISSUES FROM MICE SPECIMENS

ALEXANDRA FALAMAS^a, SIMONA CINTA PINZARU^{a,*},
CRISTINA A. DEHELEAN^b, MONICA M. VENTER^c

ABSTRACT Autopsy skin tissues collected from mice specimens exposed to UVB irradiation and 7,12-dimethylbenz(a)anthracene were immersed in formalin solution mixed with colloidal silver nanoparticles and analyzed using Raman imaging. The aim of this study was probe the SERS technique applied to tissue analysis, to detect the main molecular components present in the investigated organs and to search for a new way of acquiring enhanced Raman signal from these tissues for early diagnostic. The analysis of the collected spectra indicated chemisorption of the nanoparticles into the tissue and the possibility to record high quality SERS signal.

Keywords: *Raman imaging, tissue SERS, skin cancer, mouse model, silver nanoparticles*

INTRODUCTION

Raman spectroscopy has currently become a powerful vibrational technique largely used to probe the molecular composition of biological tissues [1-5]. Raman spectra provide information on molecular vibrations leading thus to the possibility of highly specific fingerprinting of the molecular structure and biochemical composition of cells and tissues. In the past two decades there has been a renewed interest in Raman techniques due to the discovery of surface-enhanced Raman scattering (SERS) effect [6-9]. Briefly, the usually weak Raman signals can be greatly enhanced when Raman scattering takes place on molecules at the surface or in very close vicinity to gold or silver nanoparticles. The SERS effect is mainly employed for the investigation of the

^a Babes Bolyai University, Dept. of Physics, Kogalniceanu 1, RO 400084, Cluj-Napoca, România

^b Victor Babeș University of Medicine and Pharmacy, Faculty of Pharmacy, Eftimie Murgu Square 2, RO- 300041, Timișoara, România

^c Babes Bolyai University, Faculty of Chemistry and Chemical Engineering Arany Janos 11, 400028 Cluj-Napoca, Romania

molecular species adsorbed on noble metal nanoparticles. Recently, SERS was applied in the study of biological cells and tissue [10-12]. Two effects are responsible for this enhancement: the first mechanism is related to resonances between the surface plasmons of the metal nanostructures and the excitation and scattered fields during the Raman process giving rise to enhanced local excitation fields. The second enhancement mechanism is based on the adsorption of the molecules at certain surface sites, creating a charge-transfer state between the metal and the adsorbed scatterer.

SERS in conjunction with Raman imaging technique was applied in this study for the investigation of the damaged skin tissues from mice models exposed to UV-B radiation and chemical cancer promoters. The main attraction of the Raman imaging technique is the possibility to obtain a „complete picture” the chemical species distribution in the very complex sample. Each Raman spectrum at a particular x-y coordinate contains a wealth of information about the chemical composition and molecular structure. For thin, dried tissue sections this technique is a powerful molecular imaging tool for detailed pathological assessment of the tissue. These images contain information about the molecular components and different components can be visualized by post-processing of data, because of the possibility of plotting the concentration (i.e. fingerprint band intensity) of various biochemicals as a function of position.

The aim of the Raman imaging was also to investigate whether the SERS effect can be applied to study tissue samples and further to probe the technique as a very sensitive tool for early cancer diagnostic. Tissue SERS was expected due to the colloidal silver nanoparticles in which the autopsy samples were immersed. Analyzing the samples using Raman spectroscopy, by acquiring single Raman spectra, we obtained either typical Raman signal characteristic for skin tissue supported by the literature, or different spectra with sharp bands, characteristic for SERS effect. One possible explanation for this could be the fact that the spectra were collected from regions where no silver nanoparticles penetrated the tissues. This is likely since the nanoparticles could not have been homogeneously distributed within the tissue sample. As a general characteristic in the field of tissue SERS, the amide I band is less representative but in the Raman spectra it has significant intensity. This is first confirmation whether the spectra collected are Raman or SERS, along with the presence or absence of the huge Ag-molecule mode observed around 220 cm^{-1} [10-12]. When medium intensity contribution is observed, that would be a suggestion that pure Raman signal is also collected nearby the SERS from the microscope objective collection cone. This could have been possible because of inhomogeneity distribution of the Ag nanoparticles inside the tissue. Due to this, the spot of the laser may have encompassed the margins of a “hot spot”, meaning that the SERS enhancement conditions varied more in the distance and location of the target molecule relative to the enhancing silver nanoparticles.

RESULTS AND DISCUSSION

The first results after two weeks of the skin exposure to the UVB radiation (295 nm) and the chemical carcinogen (7,12-dimethylbenz(a)anthracene, DMBA) application indicated by skin redness, lesions and after one month of exposure the visual aspects pointed towards important skin damages like photo aging and first steps to skin carcinoma. To get a better insight on the nature of the damage and to detect the main molecular components in the samples, the histopathology results of the thin tissue sections were correlated with the spectroscopic data.

A specific area of 180x180 μm was chosen from the skin sample collected from the NMRI specimen. In Fig.1 the Raman image collected from the sample can be observed along with the microscopic picture of the entire sample and the area used for investigation (left). This region was selected based on the density of the tissue. The Raman image shown in the middle displays the distribution of the amide I band in the investigated tissue. The last image in Fig.1 represents the HCA result and the distribution of the three clusters obtained after the analysis. The black pixels represent spectra with negative Quality Test results, which were removed from the analysis. The spectra shown in the figure are color coded averaged spectra each corresponding to one of the three clusters.

The selected area was divided after the HCA analysis into three clusters. The green one, corresponding to the main part of the tissue, the red one which could be assigned to the margins of the tissue and the blue one which is observed only in a few scattered points on the image. Each of the spectra presented in Fig.1 are shown with the same color as the corresponding cluster. The spectra look rather similar, presenting the same main features, such as the 1447 cm^{-1} band assigned to CH_2 bending in proteins and lipids, 1343 and 1315 cm^{-1} bands specific for DNA, as well as collagen, in the case of the later, 1131 cm^{-1} band attributed to C-C stretching vibrations of lipids and C-N stretching vibrations of proteins, 1003 cm^{-1} characteristic to phenylalanine and the 854 cm^{-1} assigned to ring breathing of tyrosine and C-C stretching of hydroxyproline ring specific to collagen [16-18].

Though, at a closer look, slight differences between them can be seen. For example the two bottom spectra present the amide I band of collagen around 1670 cm^{-1} , absent in the upper one. On the other hand, spectrum number 1 corresponding to the blue cluster presents an intense band at 1577 cm^{-1} assigned to tryptophan protein and guanine and adenine nucleic acids. In the 1180-1340 cm^{-1} spectral range, the spectra present the same bands, though differently amplified. The most contributions seen here are proteins, amide III bands (1252, 1225 cm^{-1}), phenylalanine and tryptophan (1209 cm^{-1}), nucleic acids (1181 cm^{-1}) and collagen (1316 cm^{-1}) [16-18]. Another

difference lies in the band seen at 477 cm^{-1} , which has a very weak intensity in the green spectrum compared to the other two. Also, the 322 cm^{-1} seen more amplified in the bottom spectrum is assigned to the substrate of CaF_2 on which the thin tissue sections were placed.

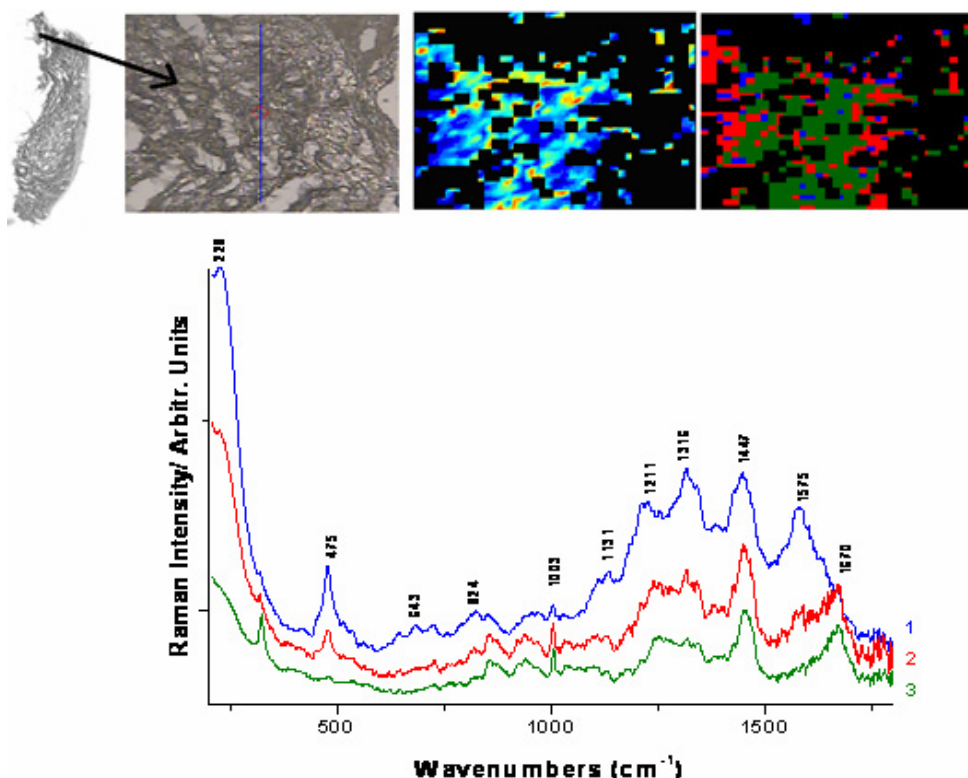


Figure 1. Microscopic image of the NMRI skin sample and the image of the area selected for investigation, the Raman map and the three clusters resulted after HCA analysis. In the below image the averaged-clustered spectra are presented, each corresponding to one cluster

One important observation is the appearance of the band at 228 cm^{-1} in the upper spectrum. This band can be seen in the middle one as well, though it seems as if it is not complete. The band could indicate the formation of Ag-O bond, meaning that the silver nanoparticles have penetrated the tissue and attached to the target molecules (SERS fingerprint). This could suggest that the upper spectrum is a SERS one, implying the method used in this study for acquiring SERS signal from biological tissues by inoculating them into colloidal nanoparticles, succeeded.

Keeping this in mind, an obvious conclusion would be that the only true SERS spectrum is the upper one assigned to the blue scattered cluster in the HCA image. The middle spectrum assigned to the red cluster has both Raman and SERS contributions and could be a result of the fact that the focus of the laser could have encompassed the margins of a “hot spot”, meaning that the SERS enhancement conditions varied more in the distance and location of the target molecule relative to the enhancing silver nanoparticles. Another aspect that needs to be pointed out is the fact that the Ag nanoparticles are not distributed homogenously inside the tissue. The lower spectrum assigned to the main part of the tissue, the green cluster, is a Raman spectrum being very similar to the single Raman spectra acquired from the same sample (not shown here).

Analyzing the entire Raman image, SERS variability became evident in many ways. The intensity of the acquired signals varied from one point of acquisition to another and the resulted signals showed differences in peak locations. To understand what happened inside the tissue with the Ag colloidal nanoparticles, in Fig. 2 are presented three spectra found in the Raman image acquired from three consecutive points.

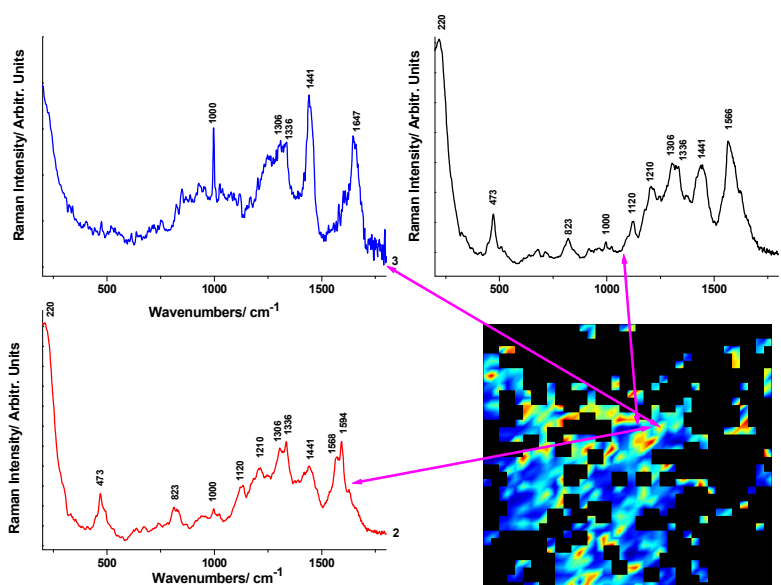


Figure 2. SERS spectra (1 and 2) in comparison to a Raman spectrum (3) acquired from three consecutive points from the Raman image.

Spectra 1 and 2 are SERS spectra, while the third is a Raman one. The differences between the Raman and the SERS spectra can easily be noticed, such as the absence of the amide I band at 1647 cm^{-1} from the SERS spectra, or the sharp intense phenylalanine band at 1000 cm^{-1} seen in the Raman spectrum.

On the other hand both SERS spectra present the 1568 cm^{-1} band assigned to tryptophan and nucleic acids [14], the 1210 cm^{-1} band assigned to phenylalanine and tryptophan [12], the 1120 cm^{-1} attributed to C-N stretching of proteins and C-C stretching of lipids and the 820 cm^{-1} band assigned to out of plane ring breathing of tyrosine and O-P-O stretching vibrations of DNA [12]. Although the main bands can be seen at the same wavenumbers, they are differently amplified and other weaker signals can be spotted as well. One possible explanation for the observed differences in the SERS spectra could be the fact that certain frequencies of scattering are more sensitive to the enhancement than others. Additionally, different portions of the tissue could have been subjected to the enhancement during the measurement. Depending on how many adsorbed molecules on the Ag nanoparticles, does the spot of the laser encompass, the spectra can present lots of fluctuations in signal intensities and frequencies. However, the epithelial layer would be more suitable for such SERS sensitive characterization and consequently, the method support further optimizations concerning the Ag nanoparticles incubation in order to perform routine applications in skin tissue monitoring.

For the present study we employed the damaged skin tissue only. Obviously, further SERS studies are required in order to investigate the molecular spectral response from normal tissue specimens for establishing an appropriate differentiation algorithm for early diagnostic.

CONCLUSIONS

In this study we have applied Raman imaging technique in conjunction with the SERS effect for the investigation of in vivo damaged biological skin tissues from mice specimens. The imaging display was obtained using the amide I band from proteins characteristic for tissue. SERS effect was evidenced for the studied skin sample. By inoculating Ag colloidal nanoparticles in biological tissues, we have proved here the possibility of recording SERS spectra which can be used to investigate the nature of the molecular components of carcinogenic skin tissue samples. To the best of our knowledge this is the first time when SERS effect was detected from skin tissues prepared in this manner.

EXPERIMENTAL SECTION

Sample Preparation and Animals Protocol: Female mice (NMRI specimens, 8 weeks old) were purchased from Charles River. The UMFT Bioethical Committee agrees the protocol and institutional guidelines were followed in the handling and care the animals. For the present study 2 animals from a group of 10 mice that were treated for skin carcinoma development were chose. The animals were accommodated to UMFT Biobase and they have been maintained in optimal conditions. The food was standard and was administrated as the water *ad libitum*. The day/night cycle was 12/12 hours and the humidity over 55%.

Tumor induction protocol has been largely described elsewhere [13,14]. For this study, NMRI mice specimens were exposed daily to UV radiation (295 nm) and orally in one dose completed by locally treated with 7,12-dimethylbenz(a)anthracene (DMBA) solution, a synthetic polycyclic aromatic hydrocarbon known to induce cancer in different organs. The skin carcinoma experimental model has been investigated after 10 weeks of photo-chemical damage evolution. Tissue samples were collected from the sacrificed mouse by CO₂ inhalation. For the skin biopsy only they were anesthiesied with xylazine and ketamine. Samples from the skin were detached and immersed in 10% formalin solution mixed with colloidal silver nanoparticles prepared according to the Lee Meisel method. From these samples, thin tissue sections were prepared using a LEICA CM3050S cryostat and placed on CaF₂. The samples were not submitted to any preparation, like “freezing shock” in liquid nitrogen or washing.

Instrumentation: The Raman maps were collected using a Raman microscope coupled to a 785 nm diode laser (Kaiser Optical Systems). Each map had a dimension of 19 x 19 =361 spectra with a step size of 10 μm, exposure time 2 s per spectrum, number of acquisitions 2 and dwell time between 10-30 s. The laser power was set to 200 mW.

Data analysis: The resulting Raman images were processed using the CytoSpec [15] software package. The data sets were normalized resulting in a linear correction of the complete spectrum, removing all negative intensities, background subtraction, polynomial baseline correction and filtering. Low-intensity spectra were removed from the data sets because they corresponded to positions outside the tissue, near holes, near fissures or near margins. The intensity of the amide I band at 1656 cm⁻¹ was used to determine whether some regions of the sample were too thin for the spectra to be included in the subsequent data analysis. In the end clustering analysis was performed on the data sets.

Cluster analysis identifies regions of the sample that have similar spectral response by clustering the spectra into groups or clusters such that differences in the intra-cluster spectral responses are minimized while simultaneously maximizing the inter-cluster differences between spectral responses. The hierarchical cluster analysis (HCA) algorithm calculates the symmetric distance matrix (size $n \times n$) between all considered spectra (number n) as a measure of their pair wise similarity. The algorithm then searches for the minimum distance, collects the two most similar spectra into a first cluster and recalculates spectral distances between all remaining spectra and the first cluster. In the next step the algorithm performs a new search for the most similar objects, which now can be spectra or clusters. The two most similar objects are clustered again and the distance values of the newly formed cluster are recalculated. This iterative procedure is repeated $n-1$ times until all spectra have been merged into one cluster.

ACKNOWLEDGMENTS

This work was supported by CNCSIS-UEFISCSU grants (PNII-IDEI code 2284/2008 and 1257/2007). A. Falamas thanks to Dr. Christoph Krafft and Professor Jürgen Popp ("Friedrich Schiller" University of Jena, Germany) for useful discussions and access to laboratory facilities.

REFERENCES

1. C. Kendall, M. Isabelle, F. Bayabt&Hegemark, J. Hutchings, L. Orr, J. Babrah, R. Baker, N. Stone, *Analyst*, **2009**, *134*, 1029.
2. Ch. Krafft, B. Dietyek, J. Popp, *Analyst*, **2009**, *134*, 1046.
3. Ch. Krafft, M. Kirsch, C. Beleites, G. Schackert, R. Salzer, *Anal. Bioanal. Chem.*, **2007**, *389*, 1133.
4. M. Schmitt, J. Popp, *J. Raman Spectrosc.*, **2006**, *37*, 20.
5. K. Hering, D. Cialla, D. Ackermann, K. Doerfer, T. Meolleer, R.H. Scheidewind, R. Mattheis, W.R. Fritysche, P. Roesch, J. Popp, *Anal. Bioanal. Chem.*, **2008**, *390(1)*, 113.
6. M. Fleischmann, P.J. Hendra, A.J. Mcquillian, *Chem. Phys. Lett.*, **1974**, *26*, 123.
7. D.L. Jeanmarie, R.P. Van Duyne, *J. Electroanal. Chem.*, **1977**, *84*, 1.
8. M.G. Albrecht, J.A. Creighton, *J. Electroanal. Chem.*, **1977**, *99(15)*, 5215.
9. M. Moskovits, , *Rev. Mod. Phys.*, **1985**, *57(3)*, 783.
10. S. Cinta Pinzaru, L.M. Andronie, I. Domsa, O. Cozar, S. Astilean, *J. Raman Spectrosc.*, **2008**, *39*, 331.

RAMAN IMAGING OF IN VIVO DAMAGED SKIN TISSUES FROM MICE SPECIMENS

11. X. Qian, X.H. Peng, D.O. Ansari, Q. Yina-Goen, G.Z. Chen, D.M. Shin, L. Yang, A.N. Young, D. May, M.D. Wang, S. Nie, *Nat. Biotechnol.*, **2008**, 26, 83.
12. S. Fendel, B. Schrader, *Fresenius J. Anal. Chem.*, **1998**, 360, 609.
13. C. Dwivedi, E.R. Maydew, J.J. Hora, D.M. Ramaeker, X. Guan, *Eur. J. Cancer Prev.*, **2005**, 14(5), 473.
14. L.H. Kligman, R. Elenitsas, *Melanoma Res.*, **2001**, 11, 319.
15. *CytoSpec - Application for FT-IR spectroscopy imaging*, www.cytospec.com.
16. R.E. Kast, G.K. Serhatkulu, A. Cao, A.K. Pandya, H. Dai, J.S. Thakur, V.M. Naik, R. Naik, M.D. Klein, G.W. Aunner, R. Rabah, *Biopolym. (Biospectrosc.)*, **2008**, 89(3), 235.
17. M.V.P. Chowdary, K.K. Kumar, S. Mathew, L. Rao, C.M. Krishna, J. Kurien, *Biopolym. (Biospectrosc.)*, **2009**, 91(7), 539.
18. I. Nottingher, S. Verrier, S. Haque, J.M. Polak, L. Hench, *Biopolym. (Biospectrosc.)*, **2003**, 72, 230.

Dedicated to the memory of Prof. dr. Ioan Silaghi-Dumitrescu marking 60 years from his birth

KINETIC STUDY OF FLUE GAS DESULPHURIZATION WITH SODIUM CARBONATE AT LOW TEMPERATURE

SIMION DRĂGAN^{a,*}, ADINA GHIRIȘAN^a

ABSTRACT. This paper presents the kinetic study of the dry desulphurization process at low temperature using solid adsorbents by thermogravimetric analysis technique. Experiments are performed in isothermal conditions, at three temperatures (373 K, 473 K and 573 K) with diameters of sodium carbonate granules of 31.5 μm and 900 μm and sulfur dioxide concentration of 0.5 % and 1.0 %. The particle size, temperature and gas flow rate show a dominant influence on the variation of carbonate conversion. The obtained activation energy values are in the range from 4.234 KJ/mol to 12.275 KJ/mol showing that the diffusion through the solid product layer is the determinate rate step of the process. The experimental results confirm that the shrinking Unreacted Core Model can be used to describe the sulfation of sodium carbonate at low temperature.

Keywords: *flue gas desulphurization, kinetic study, activation energy, sodium carbonate, unreacted core model, effective diffusion coefficient.*

INTRODUCTION

Problems concerning environmental protection are today very important, taking into consideration the big quantities of emissions (for example SO_2 , SO_3 , HF and HCl) evacuated in atmosphere [1, 2]. A particular case consists of the sulfur dioxide emissions. Sulfur dioxide is a harmful gas resulted in large quantities by fuel combustion with air excess, which in the atmosphere transforms itself into sulfuric acid – a major component of acidic rain, sulfuric acid being extremely soluble in water.

There are many processes used for the reduction of such emissions. The use of solid adsorbents to reduce SO_2 emissions from coal fired power plants has been investigated during the last twenty years [3-6]. The adsorption phenomenon of sulfur dioxide on solid adsorbents can be: a physico-sorption process, characterized by weak bonds (on zeolites for example) or/and chemo-sorption characterized by strong bonds.

^a *Babeș-Bolyai University, Faculty of Chemistry and Chemical Engineering, 11. Arany Janos, RO-400028 Cluj-Napoca, Romania; * sdragan@chem.ubbcluj.ro*

Adsorption of SO₂ on the sodium carbonate is a chemo-sorption process in accordance with reaction scheme (1):



In the worldwide there are plants at pilot and industrial scale, which are using adsorption of sulfur dioxide on calcium oxide and soda ash or sodium carbonate with a smaller than 50 % adsorption degree [3, 4]. The investigations are oriented towards to the discovery of influence of some parameters such as: initial porosity of solid particles, their geometrical size, reaction temperature, concentration of sulfur dioxide in the gas mixture, as well as the contact time over the reaction [5].

The aim of the present study is the kinetic study of the desulphurization process at low temperature using sodium carbonate as solid adsorbent by thermogravimetric analysis.

RESULTS AND DISCUSSION

The primary thermogravimetric measurements have been converted into kinetic curves considering the transformation degree of sodium carbonate, as Equation 2 shows:

$$\eta_{\text{Na}_2\text{CO}_3} = \frac{53}{63} \cdot \frac{\Delta m_s}{\bar{x}_{\text{Na}_2\text{CO}_3}^0 \cdot m_s^0} \quad (2)$$

and presented in Figure 1.

The experimental data presented in Figure 1 and Figure 2 show a significant influence of temperature and granule size on the conversion of sodium carbonate. Thus, it can be observed a positive effect on sodium carbonate conversion obtained by increasing the temperature and a negative effect by increasing the particle size.

As Figure 2 shows, for granule size of 900 μm, it can be achieved only a conversion lower than 30 % after a reaction times of 60 minutes, probably due to the strong influence of the SO₂ diffusion through the solid product layer.

The influence of the gas concentration and gas flow rate on the conversion of solid particles is less important, as it can be seen in Figure 3 and Figure 4.

The lower influence of the gas flow rate may be the qualitative confirmation for a kinetic mass transfer regime. A more accurate and quantitatively interpretation of the experimental results is not possible without kinetic modeling.

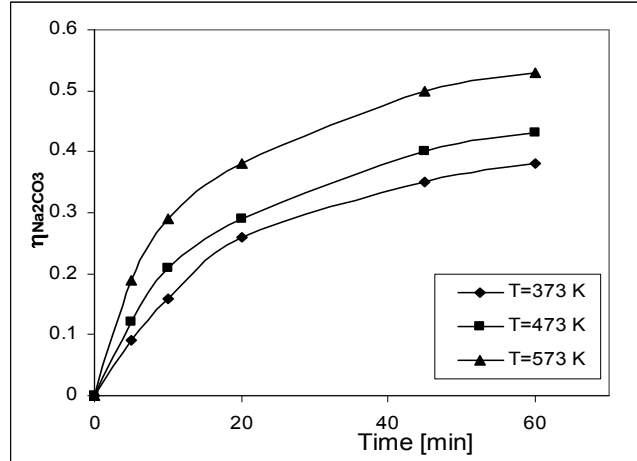


Figure 1. Kinetic curves conversion vs. time for $d_{\text{Na}_2\text{CO}_3} = 31.5 \mu\text{m}$, $C_{\text{SO}_2} = 0.5\%$, $G_v = 1.55 \times 10^{-4} \text{ m}^3/\text{s}$ at different temperature.

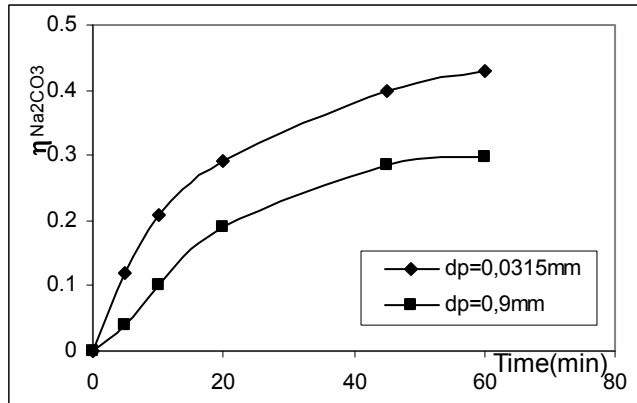


Figure 2. Kinetic curves conversion vs. time for different Na_2CO_3 diameters at $C_{\text{SO}_2}=0.5\%$, $T=473 \text{ K}$ and $G_v=1.55 \times 10^{-4} \text{ m}^3/\text{s}$.

To establish the mechanism of the desulphurization process the kinetic data presented in Figure 1 are processed using the *horizontal section method*. In accordance with this method for a constant conversion, the relative constant rate of the process k can be written as Equation (3) shows:

$$\bar{k} = \frac{1}{\tau} \quad (3)$$

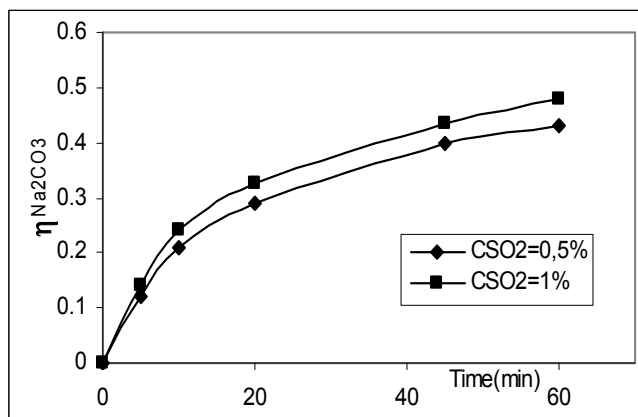


Figure 3. Kinetic curves conversion vs. time for $d_{\text{Na}_2\text{CO}_3} = 31.5 \mu\text{m}$ at $T=473 \text{ K}$, $G_v=1.55 \times 10^{-4} \text{ m}^3/\text{s}$ and different SO_2 concentrations.

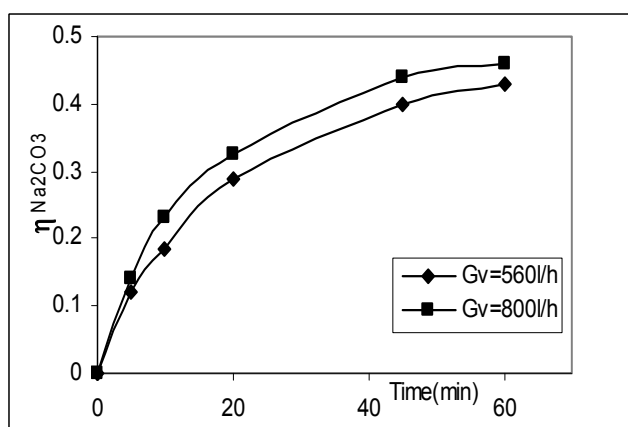


Figure 4. Kinetic curves conversion vs. time for $d_{\text{Na}_2\text{CO}_3} = 31.5 \mu\text{m}$ at $T=473 \text{ K}$, $c_{\text{SO}_2}=0.5\%$ and different gas flow rates.

Considering the influence of the temperature on the constant rate k (Arrhenius Equation 4), and processing the kinetic curves in $\ln k - 1/T$ coordinates, a linear Arrhenius dependence at different sulfation degree can be obtained (Figure 5). From the slope ($-E_a/R$), the activation energy E_a can be determined:

$$k = k_0 \cdot e^{-\frac{E_a}{RT}} \quad (4)$$

$$\ln k = \ln k_0 - \frac{E_a}{R} \cdot \frac{1}{T} \quad (5)$$

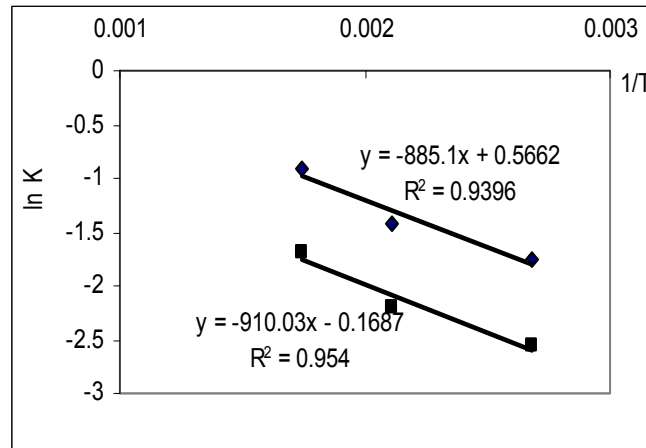


Figure 5. Determination of activation energy for particles of 31.5 μm at $C_{\text{SO}_2}=0.5\%$, $G_v=1.55 \times 10^{-4} \text{ m}^3/\text{s}$ at $\eta_{\text{Na}_2\text{CO}_3}=0.1$ and $\eta_{\text{Na}_2\text{CO}_3}=0.2$.

The activation energy values are in the range from 4.234 KJ/mol to 12.275 KJ/mol. These values indicate that mass transfer phenomena influenced the rate of the overall process, the diffusion through the solid product layer being the rate determining step [7].

Table 1. Activation energy values

d_p (mm)	w (m/s)	$\eta_{\text{Na}_2\text{CO}_3}$	E_a (KJ/mol)	$C_{\text{SO}_2} \cdot 10^4$ (mol/l)
0.0315	0.5	0.1	7.325	2.23
		0.2	7.531	
	0.71	0.1	5.440	
		0.2	7.729	
0.0315	0.5	0.1	4.734	4.46
		0.2	5.616	
	0.71	0.1	6.565	
		0.2	12.275	
0.9	0.5	0.1	7.729	2.23
		0.2	8.974	
	0.71	0.1	5.082	
		0.2	7.169	
0.9	0.5	0.1	4.234	4.46
		0.2	8.676	
	0.71	0.1	4.346	
		0.2	5.178	

The kinetic equation which describes the sulfation process can be written as Equation 6 shows:

$$\frac{dn_{SO_2}}{S \cdot d\tau} = -D_{ef_{SO_2}} \cdot \frac{dc_{SO_2}}{dr} \quad (6)$$

where S is the unreacted core surface of radius r:

$$S = 4\pi \cdot r^2 \quad (7)$$

The apparent activation energies are centralized in Table 1.

Considering sodium carbonate to be of spherical and homogeneous solid particles, the shrinking unreacted core model may be applied for the kinetic modeling of desulphurization process.

Combining Equation (6) and (7), as Equation (8) shows, and integrating in two steps, on the grain model theory:

$$\frac{-dn_{SO_2}}{d\tau} = -4\pi r^2 \cdot D_{ef_{SO_2}} \cdot \frac{dc_{SO_2}}{dr} \quad (8)$$

$$\frac{-dn_{SO_2}}{d\tau} \left(\frac{1}{r} - \frac{1}{R} \right) = 4\pi D_{ef_{SO_2}} \cdot c_{SO_2} \quad (9)$$

$$dn_{SO_2} = \frac{\rho_{[s]} \cdot \bar{X}_{Na_2CO_3}}{M_{Na_2CO_3}} \cdot 4\pi r^2 dr \quad (10)$$

$$dn_{SO_2} = \rho^* \cdot 4\pi r^2 dr \quad (11)$$

Equation (9) becomes:

$$-\rho^* \left(\frac{1}{r} - \frac{1}{R} \right) \cdot r^2 \cdot \frac{dr}{d\tau} = D_{ef_{SO_2}} \cdot c_{SO_2} \quad (12)$$

or as function of Na₂CO₃-conversion ($\eta_{Na_2CO_3}$):

$$\left[\frac{1}{(1-\eta_{Na_2CO_3})^{1/3}} - 1 \right] \frac{d\eta_{Na_2CO_3}}{d\tau} = 3 \cdot \frac{D_{ef_{SO_2}}}{\rho^* \cdot R^2} \cdot c_{SO_2} \quad (12')$$

The integration of Equation (12) at constant concentration of SO₂, Equation (13) is obtained:

$$\tau = \frac{1}{6} \cdot \frac{\rho^* \cdot R^2}{D_{ef_{SO_2}} \cdot c_{SO_2}} \left[1 - 3 \left(\frac{r}{R} \right)^2 + 2 \left(\frac{r}{R} \right)^3 \right] \quad (13)$$

or as function of Na₂CO₃-conversion ($\eta_{Na_2CO_3}$):

$$\tau = \frac{1}{6} \frac{\rho^* \cdot R^2}{D_{efSO_2} \cdot c_{SO_2}} \left[1 - 3(1 - \eta_{Na_2CO_3})^{2/3} + 2(1 - \eta_{Na_2CO_3}) \right] = \frac{1}{6} \frac{\rho^* \cdot R^2}{D_{efSO_2} \cdot c_{SO_2}} F(\eta_{Na_2CO_3}) \quad (13')$$

Equation (13') represents the mathematical model equation for sulfur dioxide diffusion through product layer.

For the validation of the proposed model the function $\tau = F(\eta)$ is shown for $d_p=31.5 \mu\text{m}$ and $C_{SO_2}=0.5 \%$ in Figure 6.

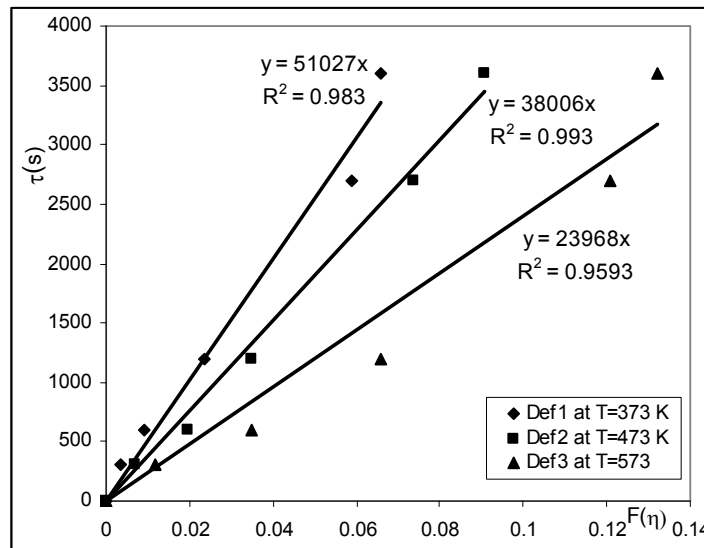


Figure 6. Dependence $\tau - F(\eta)$.

Table 2. D_{efSO_2} through the product layer in our work conditions

T (K)	R (m)	Def (m ² /s)	$C_{SO_2} \cdot 10^4$ (mol/l)	$\rho_{Na_2CO_3}^*$ (mol/l)
373	15.75×10^{-6}	2.73×10^{-11}	2.23	7.53
473		3.67×10^{-11}		
573		5.82×10^{-11}		
373	45×10^{-5}	7.0×10^{-10}	2.23	7.53
473		11×10^{-10}		
573		17×10^{-10}		
373	15.75×10^{-6}	1.42×10^{-11}	4.46	7.53
473		1.98×10^{-11}		
573		3.13×10^{-11}		
373	45×10^{-5}	3.0×10^{-10}	4.46	7.53
473		6×10^{-10}		
573		8×10^{-10}		

The obtained values of D_{efSO_2} in solid layer with the magnitude of 10^{-11} - 10^{-10} m²/s are comparable with those founded in the literature [5, 6].

With the obtained slope's lines, the effective diffusion coefficient of SO₂ can be calculated with Equation (14):

$$D_{\text{efSO}_2} = \frac{1}{6} \frac{\rho^* \cdot R^2}{c_{\text{SO}_2} \cdot \text{tg} \alpha} \quad (14)$$

The values of the effective diffusion coefficients are centralized in Table 2.

CONCLUSIONS

The kinetic study of the gas desulphurization process with sodium carbonate at low temperature has shown a significant influence of temperature and granule size. A positive effect on sodium carbonate conversion was obtained by increasing the temperature and decreasing the particle size.

The apparent activation energy values evaluated from experimental data are in the range from 4.234 KJ/mol to 12.275 KJ/mol and have shown that the sulphur dioxide diffusion through the solid product layer is rate determining step of the overall process.

The kinetic data were quantitatively analyzed on the basis of the unreacted core model integrated in the general form. The macro kinetic SO₂ diffusion through the solid product layer model was validated and the obtained values of the SO₂ effective diffusion coefficients are comparable with those founded in the literature.

EXPERIMENTAL SECTION

In order to determine the effect of the temperature, grain size and gas flow rate on desulphurization process, the isothermal gravimetric method was used. The experiments were carried out on experimental equipment presented in Figure 7.

The installation contains a hand-made thermo balance, having a 20 mm diameter tubular reactor placed in a tubular electric furnace, with possibilities to operate in temperature range of 373 - 1473 K. The solid reactant, sodium carbonate placed in thin layer on a ceramic nacelle, was introduced in the tubular reactor and the experiments were carried out isothermally at three temperatures (373, 473, 573 K), with diameter of sodium carbonate granules of 31.5 μm and 900 μm and SO₂ concentration of 0.5 % and 1.0 %. The size distribution of solid particles was obtained by sieving of sodium carbonate on a Retzsch set of sieves, mesh between 0 - 1000 μm. Each sample was sulfated in a gas-air mixture containing 0.5 % and 1.0 % (vol.) SO₂, at constant flow rate of $G_v = 560$ l/h and $G_v = 800$ l/h.

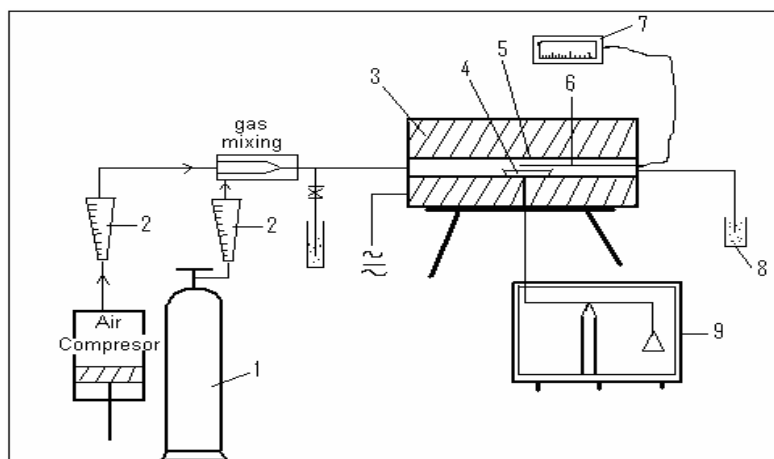


Figure 7. Experimental equipment.

1 - Gas cylinder with SO₂; 2 - Gas flow meter; 3 - Electric Furnace; 4 - Nacelle with solid sample; 5 - Tubular reactor; 6 - Thermocouple; 7 - Temperature controller; 8 - Absorbing vessel for gas; 9 - Thermo balance.

REFERENCES

1. H. Menig, „Emissionsminderung und Recycling – Grundlagen und Technologien”, Ecomed Verlag, **1996**, chapter 5.
2. J.C. Mycock, McKenna and L. Theodore, “Handbook of Air Pollution Control Engineering and Technology”, CRC Press, Inc, Boca Raton, **1995**.
3. S. Drăgan, *Rev. Chim. Buc.*, **1997**, 48(7), 755.
4. S. Drăgan, I. Siminiceanu, *Rev. Chim. Buc.*, **2004**, 55(11), 857.
5. T.C. Keener, W.T. Davis, *JAPCA*, **1984**, 34(6), 123.
6. T. Kopac, G. Dogu, T. Dogu, *Chem. Eng. Sci.*, **1996**, 51(10), 2201.
7. L. Ifrim, C. Calistru, “Procesul tip adsorbție-reactie-formare și creștere de germeni”, Ed. IPI Iasi, **1987**, chapter 4.

Dedicated to the memory of Prof. dr. Ioan Silaghi-Dumitrescu marking 60 years from his birth

CARBON NANOTUBES-GRAPHITE PASTE ELECTRODE MODIFIED WITH Cu(II)-EXCHANGED ZEOLITE FOR H₂O₂ DETECTION

**DELIA GLIGOR^a, CODRUȚA VARODI^b, ANDRADA MĂICĂNEANU^c,
LIANA MARIA MUREȘAN^{c,*}**

ABSTRACT. Modification of a natural zeolite from Macicas (Cluj County, Romania) with copper(II) (Z-Cu), followed by its incorporation in carbon paste, made of carbon nanotubes and graphite powder as conductive matrix (Z-Cu-G-CNT-CPEs), lead to a stable modified electrode. The Z-Cu-G-CNT-CPEs electrodes show significant electrocatalytic activity toward H₂O₂ reduction. The rate constant for catalytic H₂O₂ reduction, estimated from rotating disk electrode measurements, extrapolated to zero H₂O₂ concentration was found to be 74.4 M⁻¹ s⁻¹ (pH 7). The amperometric detection of H₂O₂, at -400 mV vs. Ag/AgCl/KCl_{sat} is characterized by the following electroanalytical parameters: sensitivity of 15.33 mA M⁻¹, detection limit of 0.24 mM and linear domain up to 10 mM H₂O₂.

Keywords: *carbon paste electrodes, zeolite, hydrogen peroxide, carbon nanotubes*

INTRODUCTION

Hydrogen peroxide is an important analyte in food, pharmaceutical, clinical, industrial and environmental analyses [1]. H₂O₂ can be determined using different analytical methods such as: chemiluminometry [2], spectrophotometry [3], titrimetry [4], enzymatic [5], acoustic emission [6] and electrochemical methods [7].

Among the new materials used for H₂O₂ electrochemical detection, zeolite-modified electrodes are of high interest, due to the fact that zeolites offer the most complete range of interesting properties required at an electrochemical interface [8]. These properties can be greatly improved by metal ions incorporation, as zeolites are versatile cation-exchangers [9].

^a *Facultatea de Știința Mediului, Universitatea Babeș-Bolyai, Str. M. Kogălniceanu Nr. 1, RO-400084 Cluj-Napoca, România*

^b *Institutul Național de Cercetare Dezvoltare pentru Tehnologie Izotopică și Moleculară, Str. Donath Nr. 65-103, RO-400293 Cluj-Napoca, România*

^c *Facultatea de Chimie și Inginerie Chimică, Universitatea Babeș-Bolyai, Str. Kogălniceanu Nr. 1, RO-400084 Cluj-Napoca, România, * limur@chem.ubbcluj.ro*

In last years, modified electrodes based on carbon nanotubes received considerable attention for determination of H_2O_2 , due to the possibility to obtain a good detection limit and a wide linear range [10-13].

The aim of this work was to explore the possibility of using Cu(II)-exchanged zeolitic volcanic tuff (Z-Cu) from Macicas (Cluj County, Romania) containing 70-80% clinoptilolite [14], for preparation of an amperometric sensor for H_2O_2 detection. The electrochemical reduction of H_2O_2 was investigated using a carbon paste electrode based on Cu-modified natural zeolite, incorporated in carbon nanotube-graphite paste conductive matrix. The electrochemical behavior of the modified electrode has been characterized by using cyclic voltammetry at different scan rates and pH values. The electrocatalytic efficiency toward H_2O_2 reduction was estimated, using amperometry and rotating disk electrode measurements.

RESULTS AND DISCUSSION

Electrode material characterization

According to compositional investigations, performed previously, the zeolitic volcanic tuff sample, Macicas (Cluj County), contains 70-80% clinoptilolite, present as tabular crystals. The zeolitic volcanic tuff sample shows a remarkable homogeneity in its mineralogical and chemical composition and has specific surface area of $35 \text{ m}^2/\text{g}$ [14-16].

Using ESEM technique we were able to analyze the surface morphology (figure 1A) and also to determine surface composition of the zeolitic volcanic tuff sample (figure 1B). Mass percent composition for the elements present is as follows: O-57.08%, Na-0.90%, Al-5.23%, Si-28.96%, K-1.91%, Ca-2.33%; Fe-3.60%. The elements distribution maps (results not shown) indicate a uniform distribution on the solid surface sample.

TEM images of the copper modified zeolite (figure 1C) show darker regions on the surface of the solid samples, which could be attributed to the presence of the metal on the surface. Due to the high concentration of the copper solution used during the modification treatment, part of the metal ions were deposited on the surface and probably transformed in copper oxide during the calcination process. On the TEM images of the electrode material Z-Cu-G-CNT (figure 1D), it is easy to observe the carbon nanotubes as fine lines and the graphite used as a conductive material as black dots on the investigated surface.

As can be observed from figure 2, the electrochemical behavior of Z-Cu-G-CNT-CPEs modified electrodes show a well shaped voltammetric response. In a first attempt, the redox peaks pair (E^0 of -165 mV vs. Ag/AgCl/ KCl_{sat}) for obtained modified electrodes was attributed to copper ions, immobilized on the natural zeolite.

CARBON NANOTUBES-GRAPHITE PASTE ELECTRODE MODIFIED WITH Cu(II)-EXCHANGED ZEOLITE

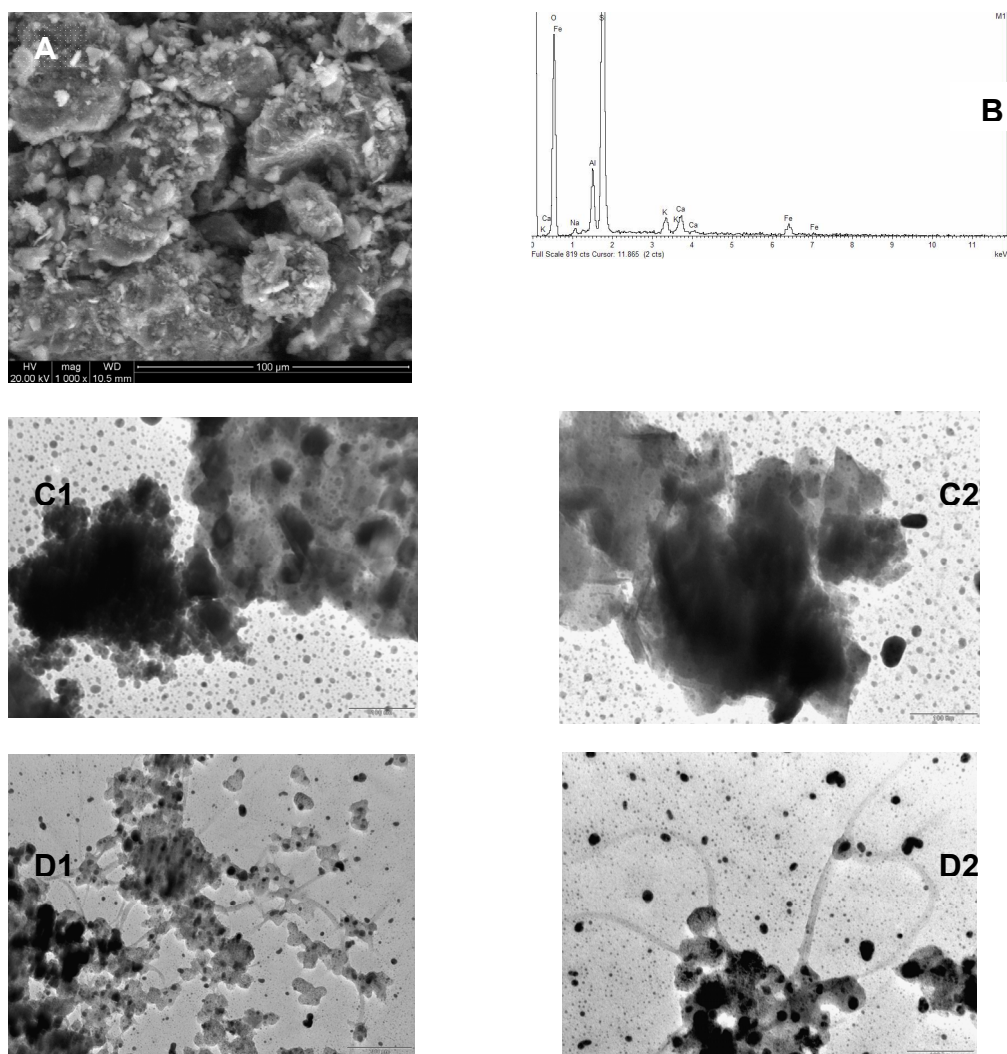


Figure 1. Electron microscopy images of zeolitic volcanic tuff (A), copper(II) modified zeolite (C1, C2) and electrode material (D1, D2). Note: (A) ESEM images; (B) ESEM spectra; (C) TEM images of different regions on copper(II) modified zeolite; (D) TEM images of the same region on Z-Cu-G-CNT material.

The redox response of the Z-Cu-G-CNT-CPEs was affected by pH (results not shown). Indeed, the formal standard potential, $E^{0'}$ (estimated as the average of the cathodic and the anodic peak potentials, recorded in the pH range from 3 to 9), changes with pH. This behavior suggests that the voltammetric response is a combined one, involving oxygen and Cu redox couples.

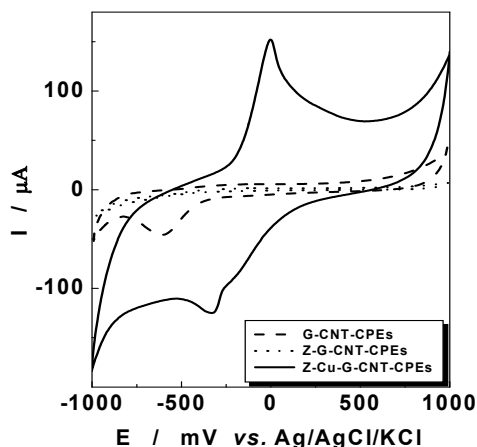


Figure 2. Cyclic voltammograms corresponding to obtained modified electrodes. Experimental conditions: starting potential, -1000 mV vs. Ag/AgCl/KCl_{sat}; potential scan rate, 10 mV s⁻¹; supporting electrolyte, 0.1 M phosphate buffer, pH 7.

Cyclic voltammetric measurements were performed in a wide range of potential scan rate (from 10 mV s⁻¹ to 2 V s⁻¹), when the Z-Cu-G-CNT-CPEs electrodes were in contact with phosphate buffer solutions of different pH values (from 3 to 9). The slopes of the log–log peak current vs. potential scan rate dependence were close to 0.5 (Table 1), indicating the existence of a diffusion process of ions from zeolite to electrode surface, combined with the diffusion of counterions from solution, in order to maintain the electroneutrality.

Table 1. Parameters of the log-log linear regression corresponding to the peak current dependence on the potential scan rate for Z-Cu-G-CNT-CPEs. Experimental conditions: as in figure 2.

pH	Slope		R/N	
	oxidation	reduction	oxidation	reduction
3	0.61 ± 0.005	0.67 ± 0.02	0.999 / 12	0.993 / 12
5	0.75 ± 0.01	0.71 ± 0.01	0.999 / 7	0.999 / 7
7	0.44 ± 0.01	0.77 ± 0.03	0.997 / 11	0.994 / 9
9	0.67 ± 0.04	0.89 ± 0.29	0.984 / 7	0.833 / 6

From the dependence of the peak potentials on the potential scan rate (results not shown), the heterogeneous electron-transfer rate constant (k_s , s⁻¹), for the redox process corresponding to Z-Cu-G-CNT-CPEs electrode was estimated to be 0.31 s⁻¹ at pH 7 (figure 3A) using the Laviron treatment [17].

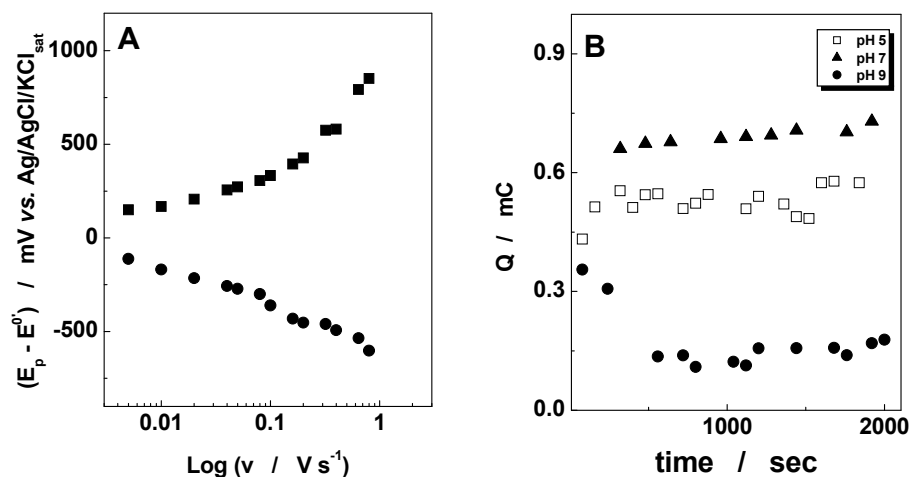


Figure 3. Experimental dependence of $(E_p - E^0)$ vs. logarithm of the scan rate (A) and time dependence of the charge amount (B) for Z-Cu-G-CNT-CPEs. Experimental conditions: scan rate, 50 mV s^{-1} ; potential range, -1000 to $1000 \text{ mV vs. Ag/AgCl/KCl}_{\text{sat}}$.

The stability of the Z-Cu-G-CNT-CPEs electrodes was examined by continuous cycling of the electrode potential within the range covering the Z-Cu-G-CNT-CPEs redox activity, at different pH values of the surrounding solution, and the corresponding cyclic voltammograms were recorded. During such experiments, the charge amount (Q) involved in the redox process slightly decreases (figure 3B), while the shape of the voltammograms remained invariant (results not shown), except when the supporting electrolyte was pH 9. The best electrochemical stability was obtained at pH 7, which is the most used pH value for amperometric sensors for H_2O_2 detection. Considering that the decrease of the charge amount obeys zero order kinetics, the deactivation rate constant of the electrode response was estimated at pH 7 ($3.50 \cdot 10^{-8} \text{ C s}^{-1}$). This very low value proves at the same time, that copper is strongly retained in the zeolite framework and it has high electrochemical stability.

Comparing the cyclic voltammograms recorded in phosphate buffer (pH 7) for a Z-Cu-G-CNT-CPEs electrode, in the absence and in the presence of 5 mM and 10 mM H_2O_2 (figure 4A), a good electrocatalytic activity for H_2O_2 reduction is shown. The Z-Cu-G-CNT-CPEs electrodes exhibit significant electrocatalytic efficiency, characterized by: (i) the decrease in overpotential for H_2O_2 reduction ($\sim 200 \text{ mV}$, estimated as the difference between the cathodic peak potentials observed on the Z-Cu-G-CNT-CPEs electrode and on Z-G-CNT-CPEs electrode); (ii) the electrocatalytic efficiency is improved when Cu-exchanged zeolite is used (63.2 for the Z-Cu-G-CNT-CPEs and 34.7 for

Z-G-CNT-CPEs, estimated as the ratio $((I_{\text{peak}})_{[\text{H}_2\text{O}_2]=5\text{mM}} - (I_{\text{peak}})_{[\text{H}_2\text{O}_2]=0}) / (I_{\text{peak}})_{[\text{H}_2\text{O}_2]=0}$, at an applied potential of $-400\text{ mV vs. Ag/AgCl/KCl}_{\text{sat}}$. This good electrocatalytic activity is due to the presence of a high quantity of copper in the zeolite structure ($1.9515\text{ mg Cu}^{2+}/\text{g zeolite}$), knowing that copper is an efficient mediator for H_2O_2 reduction.

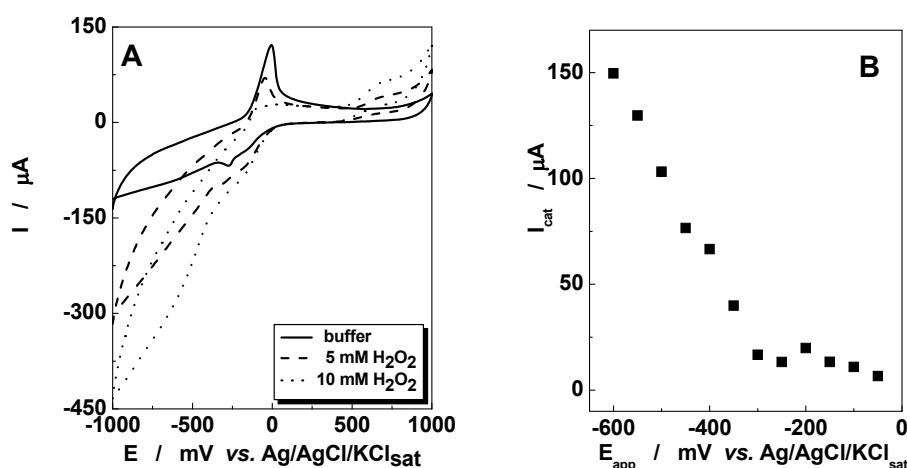


Figure 4. (A) Electrocatalytic activity of Z-Cu-G-CNT-CPEs electrode for H_2O_2 reduction, in absence and in presence of H_2O_2 . Experimental conditions: starting potential, $-1000\text{ mV vs. Ag/AgCl/KCl}_{\text{sat}}$; scan rate, 10 mVs^{-1} ; supporting electrolyte, $0.1\text{ M phosphate buffer (pH 7.0)}$.

(B) Effect of the applied potential on the electrocatalytic current recorded at Z-Cu-G-CNT-CPEs electrode, in presence of $5\text{ mM H}_2\text{O}_2$. Experimental conditions: supporting electrolyte, $0.1\text{ M phosphate buffer (pH 7.0)}$; rotation speed, 800 rpm .

Rotating disk electrode measurements were employed to investigate the kinetics of the electrocatalytic reduction of H_2O_2 on the Z-Cu-G-CNT-CPEs electrodes. First, in order to find the optimal applied potential, its effect on the reduction electrocatalytic current was examined (figure 4B). Consequently, for all further measurements, the applied potential selected was $-400\text{ mV vs. Ag/AgCl/KCl}_{\text{sat}}$.

Using the Koutecky–Levich treatment, applied for H_2O_2 reduction kinetics, the observed rate constants for H_2O_2 electrocatalytic reduction (k_{obs}) were evaluated at different H_2O_2 concentrations, at pH 7. The linear dependence between $1/I_{\text{cat}}$ and $1/\omega^{1/2}$ allowed calculation of k_{obs} values at different H_2O_2 concentrations. Supposing that the reduction reaction of H_2O_2 at the Z-Cu-G-CNT-CPEs obeys Michaelis–Menten kinetics, a plot of the reciprocal value of the observed rate constant vs. H_2O_2 concentration,

results in a straight line (results not shown). From the slope and the intercept of this straight line, the extrapolated values of k_{obs} to zero H_2O_2 concentration ($k_{\text{obs}, [\text{H}_2\text{O}_2] = 0} = 74.4 \text{ M}^{-1} \text{ s}^{-1}$, for $\Gamma = 2.5 \cdot 10^{-7} \text{ mol cm}^{-2}$), the apparent Michaelis–Menten constant ($K_M = 1.1 \text{ mM}$) and the turnover number for the electrocatalytic reaction ($k_{+2} = 0.08 \text{ s}^{-1}$) were estimated.

Finally, using amperometric measurements, performed in the optimal experimental conditions mentioned above, the amperometric response of Z-Cu-G-CNT-CPEs to increasing concentrations of H_2O_2 was recorded. By plotting the steady-state current values vs. H_2O_2 concentration, two calibration curves were obtained at -400 and $-150 \text{ mV vs. Ag/AgCl/KCl}_{\text{sat}}$ (figure 5).

As can be seen from figure 5, the kinetic parameters are better when the applied potential was $-400 \text{ mV vs. Ag/AgCl/KCl}_{\text{sat}}$. By fitting the amperometric calibration curve to Michaelis–Menten equation, the following kinetic parameters were found: $K_M = 60.51 \text{ mM}$ and $I_{\text{max}} = 920 \mu\text{A}$. At the same time, the electroanalytical parameters of Z-Cu-G-CNT-CPEs electrodes for H_2O_2 determination were estimated: the sensitivity (calculated as I_{max}/K_M ratio) was 15.33 mA M^{-1} ; the linear range was up to 10 mM ; the detection limit was 0.24 mM (signal to noise ratio of 3); the response time was less than 10 s . It can be observed that this detection limit is improved by using copper in comparison with other modified electrodes that used carbon nanotubes [13].

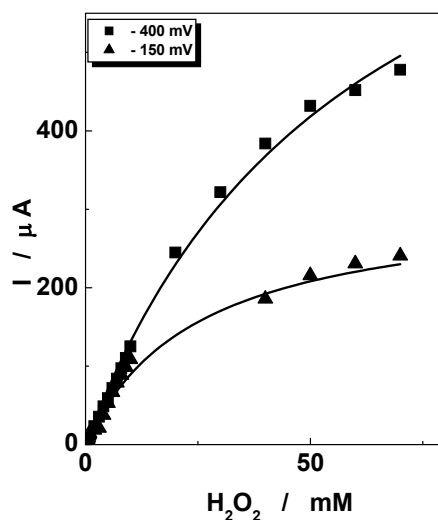


Figure 5. Calibration curves for H_2O_2 of Z-Cu-G-CNT-CPEs electrodes. Experimental conditions: applied potential, -400 mV and $-150 \text{ mV vs. Ag/AgCl/KCl}_{\text{sat}}$; supporting electrolyte, 0.1 M phosphate buffer ($\text{pH } 7.0$); rotation speed, 800 rpm .

CONCLUSIONS

A new electrocatalytic system for mediated reduction of H_2O_2 based on carbon paste electrodes modified with a Cu-exchanged zeolite, using carbon nanotubes and graphite powder is proposed and investigated from physical-chemical, electrochemical and electrocatalytic point of view. Under operation in optimal conditions, the Z-Cu-G-CNT-CPEs electrodes exhibit a good electrochemical stability at pH 7 and electrocatalytic efficiency towards H_2O_2 reduction.

EXPERIMENTAL SECTION

Chemicals

Single-walled carbon nanotubes (CNT) were obtained from Sigma (St. Louis, MO, USA), graphite powder and paraffin oil from Fluka (Buchs, Switzerland) and hydrogen peroxide, $\text{K}_2\text{HPO}_4 \cdot 2\text{H}_2\text{O}$ and $\text{KH}_2\text{PO}_4 \cdot \text{H}_2\text{O}$ from Merck (Darmstadt, Germany). NaCl, $\text{Cu}(\text{SO}_4)_2 \cdot 5\text{H}_2\text{O}$, ammonium solution 25% were purchased from Reactivul Bucharest.

All reagents were of analytical grade and used as received. The supporting electrolyte was 0.1 M phosphate buffer solution, obtained by mixing appropriate solutions of $\text{K}_2\text{HPO}_4 \cdot 2\text{H}_2\text{O}$ and $\text{KH}_2\text{PO}_4 \cdot \text{H}_2\text{O}$.

Preparation of modified zeolite

A zeolitic volcanic tuff sample from Macicás (Cluj County), Z, granulation $d < 0.2$ mm, brought in –Na form was contacted with a solution containing copper in order to obtain the required modification.

Certain stages were involved in the zeolitic volcanic tuff preparation. First, solid samples were subjected to a mechanical treatment consisting of crushing, grinding and size separation. Next, samples were washed with distilled water and dried. A chemical treatment consisting of a contact with an alkaline solution, NaCl, pH 10, followed. After this last treatment, the zeolitic volcanic tuff sample was washed again with distilled water, until chlorine ions were no more detected in the washing water, and dried. [15] The zeolitic volcanic tuff sample is now prepared for the next stage, the ionic exchange with the desired metallic ion, in our case copper. The established quantity of zeolitic volcanic tuff prepared as described above, was brought in Z-Cu form using a $\text{CuSO}_4 \cdot 5\text{H}_2\text{O}$ 0.5N solution. The ionic exchange process (Na^+ ions from the zeolite structure were replaced with Cu^{2+} ions from aqueous solution) was realised in a batch reactor with solid and liquid phases as immobile phases, using a solid: liquid ratio of 1:10. Solid and solution were kept in contact for 24 hours. After this time interval, the copper modified zeolitic volcanic

tuff sample was separated by filtration, dried for 6 hours at 105°C and then roasted at 400°C for 4 hours. In this way was obtained the M-Cu modified zeolitic volcanic tuff, containing 1.9515 mg Cu²⁺/g zeolite. The initial and final concentrations of copper ions in solution, used to establish the quantity of copper retained in the zeolitic volcanic tuff sample, were determined using a JENWAY 6305 spectrophotometer, 25% ammonium solution at $\lambda = 440$ nm.

Electrode Preparation

The modified electrodes, Z-G-CNT-CPEs and Z-Cu-G-CNT-CPEs were prepared by hand mixing the unmodified or modified zeolites with CNTs, graphite powder (2:1:1, w/w) and paraffin oil. The resulting pastes were packed into a cavity at the end of a Teflon tube. Electrical contact was established *via* a copper wire connected to the paste. The electrode surface was smoothed by rubbing on a filter paper just prior to use.

Physical-chemical and electrochemical measurements

Zeolitic volcanic tuff samples morphology was investigated using environmental scanning electron microscopy (ESEM, INCAx-sight 6427 Oxford Instruments) and transmission electron microscopy (TEM, Jeol JEM1010 with a MegaViewIII CCD camera - SIS-Olympus). Using ESEM techniques we also could determine the superficial composition of the zeolitic volcanic tuff sample.

Electrochemical experiments were carried out using a typical three-electrode electrochemical cell. The modified carbon paste electrode was used as working electrode, a platinum ring as counter electrode and an Ag/AgCl/KCl_{sat} as reference electrode. Cyclic voltammetry experiments were performed on a PC-controlled electrochemical analyzer (Autolab-PGSTAT 10, EcoChemie, Utrecht, The Netherlands).

Steady state amperometric measurements at different rotating speeds of the working electrode were performed using an EG&G rotator (Radiometer) and the same carbon paste as disk material. The current-time data were collected using the above-mentioned electrochemical analyzer.

Batch amperometric measurements at different H₂O₂ concentrations were carried out at an applied potential of -400 mV vs. Ag/AgCl/KCl_{sat}, under magnetic stirring, using 0.1 M phosphate buffer solution as supporting electrolyte. The current-time data were collected using the above-mentioned electrochemical analyzer.

The pH of the phosphate buffer solutions was adjusted using NaOH or H₃PO₄ and a pH-meter (HI255, Hanna Instruments, Romania), with a combined glass electrode.

The experimental results are the average of at least three identically prepared electrodes, if not otherwise mentioned.

ACKNOWLEDGMENTS

This work was supported by CNCSIS –UEFISCSU, project number PNII – IDEI 512/2007.

REFERENCES

1. C.-L. Wang, A. Mulchandani, *Analytical Chemistry*, **1995**, 67, 1109.
2. S. Hanaoka, J.M. Lin, M. Yamada, *Analytica Chimica Acta*, **2001**, 426, 57.
3. J.M. Fernandez-Romero, M.D. Luque de Castro, *Analytical Chemistry*, **1993**, 65, 3048.
4. E.C Hurdis, J. Hendrik Romeyn, *Analytical Chemistry*, **1954**, 26, 320.
5. C. Ruan, R. Yang, X. Chen, J. Deng, *Journal of Electroanalytical Chemistry*, **1998**, 455, 121.
6. P.D. Wentzell, S.J. Vanslyke, K.P. Bateman, *Analytica Chimica Acta*, **1991**, 246, 43.
7. Y. Yang, S. Mu, *Biosensors & Bioelectronics*, **2005**, 21, 74.
8. A Walcarius, *Analytica Chimica Acta*, **1999**, 388, 79.
9. A. Walcarius, *Analytica Chimica Acta*, **1999**, 384, 1.
10. V. Vamvakaki, N. A. Chaniotakis, *Sensors and Actuators B*, **2007**, 126, 193.
11. Q. Zhao, Z. Gan, Q. Zhuang, *Electroanalysis*, **2002**, 14, 1609.
12. J. Li, J.-D. Qiu, J.-J. Xu, H.-Y. Chen, X.-H. Xia, *Advanced Functional Materials*, **2007**, 17, 1574.
13. J. Kruusma, V. Sammelselg, C. E. Banks, *Electrochemistry Communications*, **2008**, 10, 1872.
14. H. Bedeleian, A. Măicăneanu, S. Burcă, M. Stanca, *Studia Universitatis Babeș-Bolyai, Geologia*, **2010**, 55, 9.
15. H. Bedeleian, M. Stanca, A. Măicăneanu, S. Burcă, *Studia Universitatis Babeș-Bolyai, Geologia*, **2006**, 51, 43.
16. A. Măicăneanu, H. Bedeleian, M. Stanca, "Zeoliții naturali. Caracterizare și aplicații în protecția mediului", Editura Presa Universitară Clujeană, Cluj-Napoca, **2008**, chapter 3.
17. E. Laviron, *Journal of Electroanalytical Chemistry*, **1979**, 101, 19.

Dedicated to the memory of Prof. dr. Ioan Silaghi-Dumitrescu marking 60 years from his birth

BEHAVIOR OF MIXED DMPC-CHOLESTEROL MONOLAYERS AT THE AIR/WATER INTERFACE

AURORA MOCANU^{*}, ROXANA-DIANA PAȘCA, OSSY HOROVITZ,
MARIA TOMOAI-A-COTISEL

ABSTRACT. The phase behaviour of cholesterol (CHO) and dimyristoyl phosphatidyl choline (DMPC) monolayers at the air/water interface was investigated by surface pressure measurements using Langmuir technique. Compression isotherms and isobars as functions of composition were represented, and the surface compressibility modulus was calculated, in order to characterize the physical states of the monolayers. At a constant lateral surface pressure, the monolayers were transferred by Langmuir-Blodgett technique (LBT) from air-water interface on solid supports and further studied by atomic force microscopy (AFM). This study shows that the strong interactions between DMPC and CHO lead to well defined two-dimensional nanostructures, which can have practical applications for biosensors fabrication. Also, this type of nanostructures seems plausible to occur in natural membranes and thus, can influence the protein distribution and protein function *in vivo*.

Keywords: *cholesterol, DMPC, monolayers, Langmuir-Blodgett technique, atomic force microscopy*

INTRODUCTION

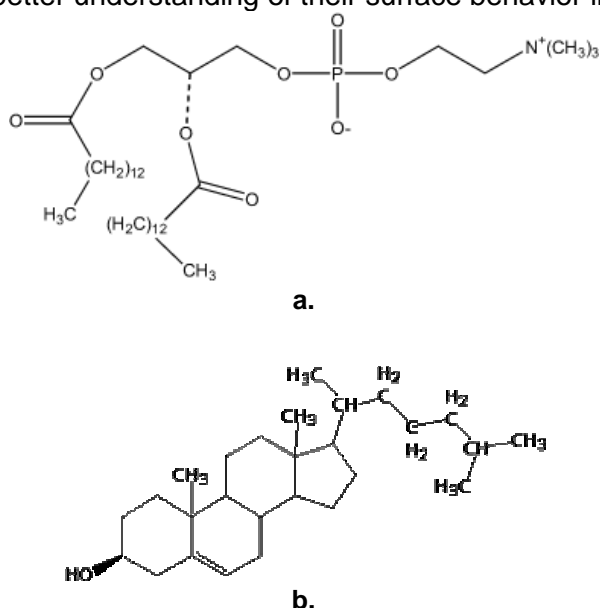
Phospholipids and cholesterol are the primary constituents of vertebrate cell membranes [1, 2] and their interaction is important for the membrane organization and properties [3-5]. Possible interactions are hydrogen bonds between the cholesterol OH-group and carbonylic oxygen atoms of the phospholipid DMPC (Scheme 1) and van der Waals forces [6].

An approach to the understanding of these interactions is the investigation of the organization of such biomolecules at the air/aqueous solution interfaces in the two-dimensional monomolecular layers, at controlled lateral surface pressures. These monolayers are realized by spreading and compressing the biomolecules at the air/water interface [7-9]. Dimyristoyl

^{*} *Babeș-Bolyai University, Faculty of Chemistry and Chemical Engineering, Arany Janos 11, 400028 Cluj-Napoca, Romania, mcotisel@chem.ubbcluj.ro*

phosphatidyl choline (DMPC) is a typical biomolecule forming highly ordered monolayers [10-12]. The DMPC molecules can be spread, compressed and oriented at the air/water interface at various lateral surface pressures to form DMPC monolayers of close-packed polar groups within the interfacial water having the hydrocarbon chains oriented into the air phase. The interaction of phospholipids with sterols was studied both in films at the air/water interface [5, 6, 13-16] and on solid support, by AFM techniques [17, 18].

In the present paper, we have chosen cholesterol (CHO) and DMPC (Scheme 1) to be investigated in monolayers, which are considered as membrane models, for a better understanding of their surface behavior in mixed films.



Scheme 1. Chemical structures of DMPC (a) and cholesterol (b).

RESULTS AND DISCUSSION

The *compression isotherms* measured for DMPC, cholesterol and their mixtures at different ratios are represented as surface pressure, π , versus area per molecule, A (Fig. 1). Surface pressure is defined as the difference between the surface tension at the air/water interface, σ_0 , and the surface tension, σ , at the same interface in the presence of the investigated monolayer:

$$\pi = \sigma_0 - \sigma \quad (1)$$

The mole fractions of cholesterol (x_{CHO}) in the mixed monolayers varied from 0.1 to 0.9 (step value 0.1). It is evident that all compression isotherms are shifted towards left (smaller areas per molecule) with increasing x_{CHO} values, *i.e.* a condensing effect of cholesterol is manifested.

BEHAVIOR OF MIXED DMPC-CHOLESTEROL MONOLAYERS AT THE AIR/WATER INTERFACE

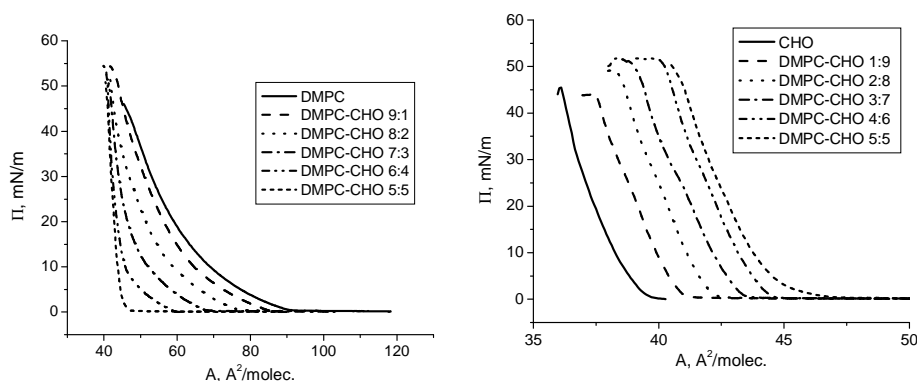


Figure 1. Representative compression isotherms for DMPC and DMPC-CHO mixed monolayers with $x_{\text{CHO}} \leq 0.5$ (a), and for CHO and DMPC-CHO mixed monolayers with $x_{\text{CHO}} \geq 0.5$ (b).

The differences in the collapse pressures (the highest lateral surface pressure for monolayer stability) for the various monolayers are also visible in these isotherms. While for the pure DMPC and CHO the values are the lowest (about 46 mN/m for DMPC, respectively 42 mN/m for CHO), the mixed monolayers present higher collapse pressures.

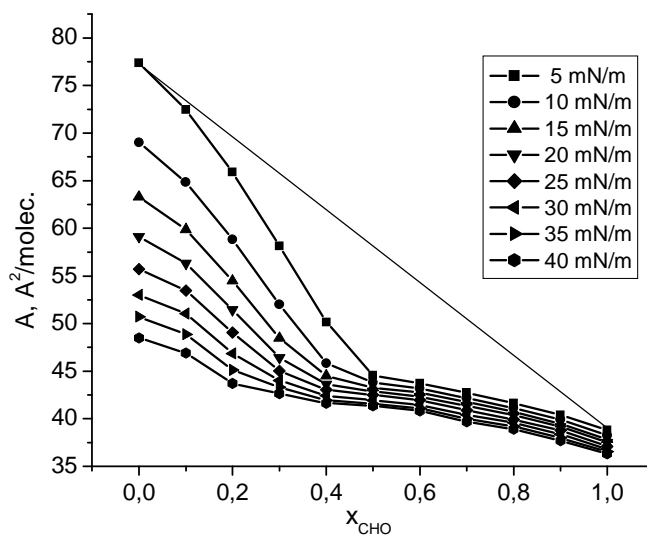


Figure 2. Mean molecular areas vs. cholesterol mole fractions in DMPC-CHO mixed monolayers at the surface pressures given in the inset.

A proof for the condensing effect of cholesterol in the mixed monolayers is given by the representation of mean areas per molecule, A , against the mixture composition, x_{CHO} , at constant values of the surface pressure, π . Such *isobars* are given in Fig. 2 for π -values from 5 up to 40 mN/m. This condensing effect, i.e. negative deviations from the mixing rule, represented by a straight line connecting the points for pure components (as the solid line given in Fig. 2 for $\pi = 5$ mN/m), is most pronounced for small values of the surface pressure, and it is maintained even with the highest lateral surface pressures.

This condensing effect of cholesterol, and therefore the higher packing density of mixed DMPC-CHO monolayers, can be ascribed to the attracting van der Waals forces and the hydrogen bondings between the phospholipids and cholesterol, stabilizing these mixed structures [13, 19-21] and inducing a chain ordering.

Isothermal compressibility of a monolayer is defined by:

$$C_s = -\frac{1}{A} \left(\frac{\partial A}{\partial \pi} \right)_T \quad (2)$$

Its reciprocal value, the surface compressibility modulus:

$$C_s^{-1} = -A \left(\frac{\partial \pi}{\partial A} \right)_T \quad (2a) \text{ the surface correspondent of the bulk modulus,}$$

$$K = -V \left(\frac{\partial p}{\partial V} \right)_T, \text{ is a measure of the interfacial elasticity and a characteristic}$$

for the variations in the physical state of the monolayers. The isothermal compressibility was calculated from the compression isotherms $\pi = f(A)_T$ in Fig. 1, by graphical derivation. Representations of surface pressures against C_s^{-1} values are given in Fig. 3.

In each case, the values of C_s^{-1} are roughly growing with increasing surface pressure, and reach a maximum for a surface pressure corresponding to the high packing in the monolayers before collapse. DMPC and mixed DMPC-CHO monolayers for $x_{\text{CHO}} \leq 0.2$ present the lowest and cholesterol (at least for high π -values) the highest C_s^{-1} values for the same surface pressure, while mixed monolayers show intermediate values. For cholesterol mole fractions above 0.5 the differences between mixed layers and pure cholesterol are diminished.

This surface compressibility modulus C_s^{-1} , is considered to be an indicator for the physical state of the monomolecular film [22]. When these values pass beyond 100 mN/m, the layer should attain the liquid-condensed (LC) state, whereas values above 250 mN/m suggest the presence of the solid state, implying a close packing of the hydrocarbon chains [6]. Applying

this criterion, all the mixed DMPC-CHO monolayers can pass by compression in the LC state, and even in the solid state, for various compositions with a higher cholesterol content ($x_{\text{CHO}} \geq 0.4$).

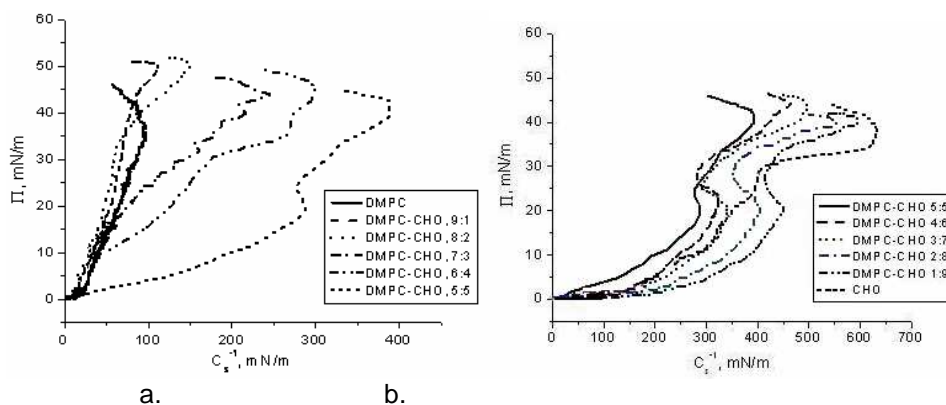


Figure 3. Surface pressure *versus* reciprocal isothermal compressibility for DMPC and DMPC-CHO mixed monolayers with $x_{\text{CHO}} \leq 0.5$ (a), and for CHO and DMPC-CHO mixed monolayers with $x_{\text{CHO}} \geq 0.5$ (b).

A representation of the surface pressures at which film collapse occurs, as seen in the compressibility isotherms (Fig. 1), against the cholesterol content of the DMPC-CHO mixtures (Fig. 4) shows a maximum for cholesterol mole fractions between 0.4 and 0.5, thus the most stable monolayers are obtained for these compositions.

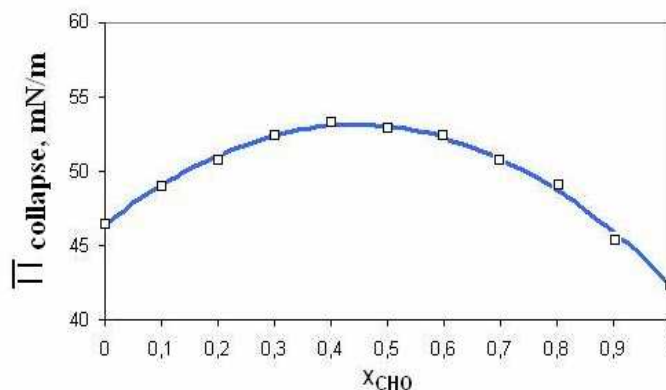


Figure 4. Surface pressures at film collapse *versus* cholesterol content in binary DMPC-CHO mixed monolayers.

AFM observations were used to complete the picture of DMPC, CHO and mixed DMPC-CHO layers near collapse pressure, transferred on glass surface. Representative AFM results are shown for pure DMPC film, (Fig. 5), pure cholesterol film (Fig. 6) and for one of the DMPC-CHO mixed monolayers, corresponding to a cholesterol mole fraction $x_{\text{CHO}} = 0.8$ (Fig. 7).

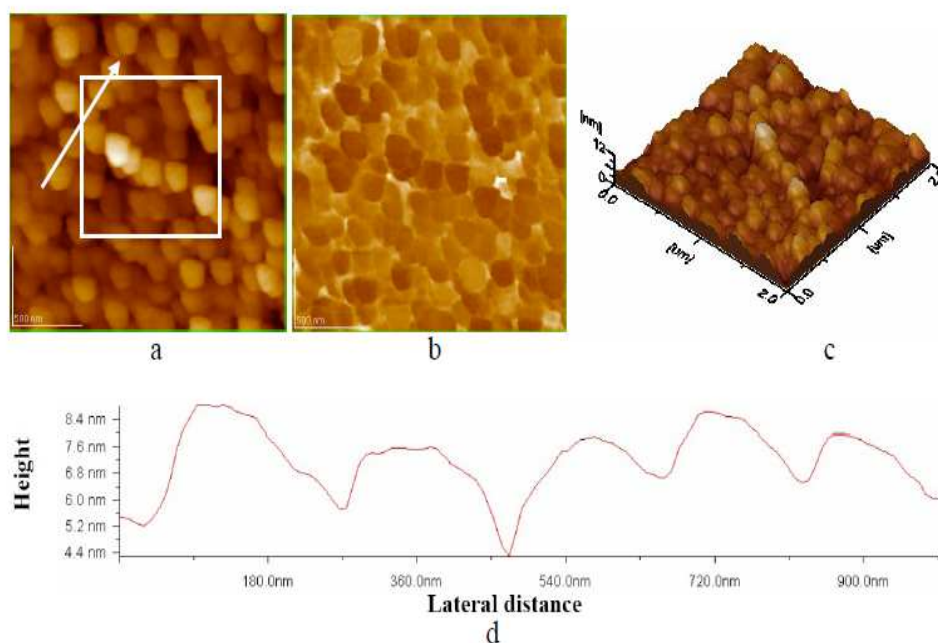


Figure 5. AFM images of DMPC film on optical polished glass near the collapse ($\pi_{\text{collapse}} = 46 \text{ mN/m}$). Scanned area $2 \mu\text{m} \times 2 \mu\text{m}$. a) 2D- topography; b) phase image; c) 3D-topography; d) profile of the cross-section along the arrow in panel a.

The 2D- and 3D-topography images (Fig. 5-7a and c) reveal nanostructures of high domains, up to 12 nm for DMPC (Fig. 5c) and the mixed layer (Fig. 7c) and to 10 nm for cholesterol (Fig. 6c). Most of these structures present an apparent height, as seen in the profiles of cross-sections, of about 8 or 9 nm for pure DMPC (Fig. 5 d) and the mixed film (Fig. 7d) and 5 – 6 nm for the cholesterol film (Fig. 6d). The phase (Fig. 5b, 6b) and the amplitude (Fig. 7b) images appear to be complementary to the topographic ones, showing the structural features of the monolayers. The size of the domains appears to be up to about 200 nm (Figs. 5d-7d).

BEHAVIOR OF MIXED DMPC-CHOLESTEROL MONOLAYERS AT THE AIR/WATER INTERFACE

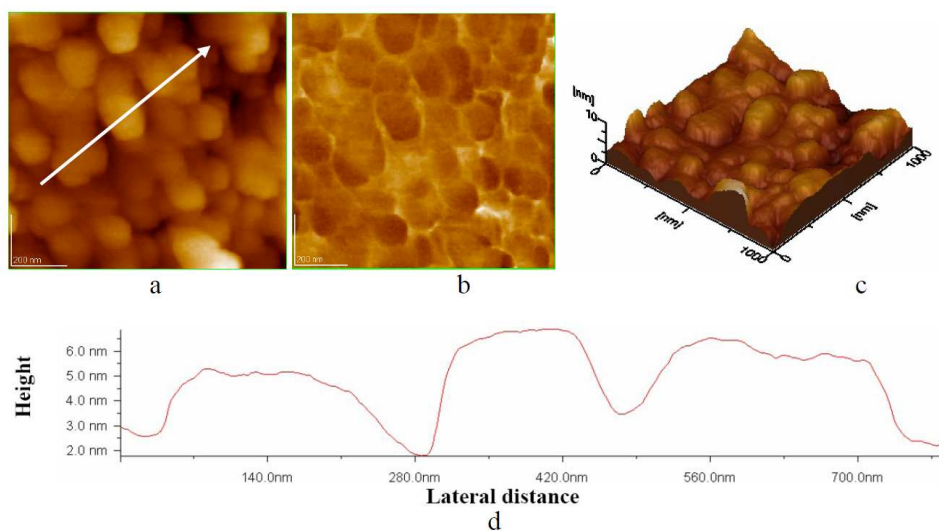


Figure 6. AFM images of cholesterol film on optical polished glass at collapse ($\pi_{\text{collapse}} = 42 \text{ mN/m}$). Scanned area $1 \mu\text{m} \times 1 \mu\text{m}$. a) 2D- topography; b) phase image; c) 3D-topography; d) profile of the cross-section along the arrow in panel a.

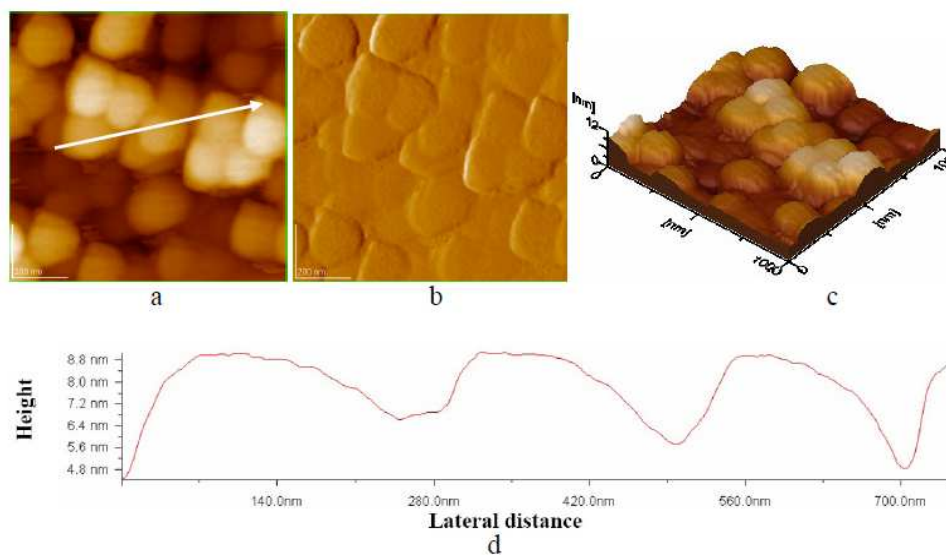


Figure 7. AFM images of a mixed DMPC-cholesterol film ($x_{\text{CHO}} = 0.8$) transferred on optical polished glass at $\pi_{\text{collapse}} = 50 \text{ mN/m}$. Scanned area $1 \mu\text{m} \times 1 \mu\text{m}$. a) 2D- topography; b) amplitude image; c) 3D-topography; d) profile of the cross-section along the arrow in panel a.

CONCLUSIONS

Cholesterol, DMPC and their mixtures containing the two biomolecules in ratios from 9:1 to 1:9 were studied as monolayers at the air/water interface and as Langmuir-Blodgett films transferred on solid glass support. These films are important as membrane models, and their investigation is a step towards the understanding of membrane structure and properties.

From the measured compression isotherms (surface pressure vs. molecular area) and isobars (molecular area vs. composition at constant surface pressure), the condensing effect of cholesterol in the mixed films with DMPC is clearly evidenced. It results from the chain ordering and the stabilization of the mixed structures, due to hydrogen bonds and van der Waals attractions between cholesterol and DMPC molecules, resulting in a higher packing density. The increased stability for DMPC-CHO mixed films at nearly equimolar ratio is also evidenced by regularities found in the collapse pressure of these films.

From the surface compressibility module of the monolayers, obtained by derivation of the compression isotherms, the physical states of the films (liquid-condensed state and solid state) could be assigned

AFM images of the films transferred on solid surface near their collapse pressure revealed the formation of characteristic nanostructured domains.

EXPERIMENTAL SECTION

1,2-Dimyristoyl-*sn*-glycero-3-phosphocholine (DMPC) and β -cholesterol (CHO) were purchased from Sigma (Saint Louis, USA) and used without further purification. Benzene (>99.8%) was a product of Lach-Ner (Czech Republic), hexane (>99%) and ethanol (>99.5%) were purchased from Merck (Germany). All organic solvents used were analytical grade reagents. Ultra pure water with a resistivity greater than 18 M Ω cm, obtained from an Elga apparatus was used in all experiments. Its pH was 5.5 and its surface tension was superior to 71.8 mN/m at 25°C. All glass ware was cleaned with sulfochromic mixture and then abundantly rinsed with the distilled water. Optically polished glass was used as solid support in the deposition process, after cleaning with sulfochromic mixture followed by rinsing with deionized water.

Surface pressure vs. area per molecule isotherms were recorded using KSV LB Standard Trough (KSV Ltd., Finland) controlled by KSV-5000 software and equipped with two movable barriers, a Wilhelmy balance, and a dipper for monolayers transfer from air/water interface to solid support. A Teflon trough with effective area of 765 cm² was used in all experiments; the volume of the subphase was 1500 cm³. Deionized highly purified water was used as the subphase. Before each measurement, the subphase surface was cleaned by sweeping and suction processes.

The spreading solutions used were made in benzene (CHO, ca. 1 mg/ml), ethanol/hexane mixture (2:98, v/v) for DMPC, and by mixing DMPC and CHO at different molar ratios (concentration of mixed solutions of about 1 $\mu\text{mol/ml}$). The organic solutions were spread with a Hamilton syringe. After spreading, the solution was left for 10 min for solvent evaporation. The compression of the monolayer was performed at a rate of 15 mm/min for CHO monolayer, 10 mm/min for DMPC monolayer and 15 mm/min for DMPC:CHO mixtures. All isotherms were recorded upon symmetric compression of the monolayer. For each monolayer composition, measurements were repeated at least three times.

AFM measurements were made on Langmuir-Blodgett (LB) films of DMPC in the absence and in the presence of CHO and on CHO pure films on optically polished glass supports. The vertical LB deposition method was used, at constant lateral surface pressures, near the collapse pressure of the individual monolayer. The measurements were conducted in tapping mode on the scanning probe microscope (AFM–JEOL 4210, Japan). The calibration of the AFM scanner was checked by imaging freshly cleaved highly oriented pyrolytic graphite (HOPG) and muscovite mica samples. Non-contact conical shaped tips of silicon nitride coated with aluminum were used. The tip was on a cantilever with a resonant frequency in the range of 200 - 300 kHz and with a spring constant of 17.5 N/m. We used low scan rates of 1 Hz and high scan rates in the range of 20-30 Hz to detect noise artefacts. The scan angle was also changed in different directions to observe real images from those corresponding to noise. AFM observations are repeated on different areas from 10 μm x 10 μm to 0.5 μm x 0.5 μm of the same LB film. The AFM images were obtained from at least three macroscopically separated areas on each LB film. All images were processed using the standard procedures for AFM. The widths and the thickness variations of the domains were estimated from AFM topographic images and cross-section profiles. AFM images consist of multiple scans displaced laterally from each other in y direction with 256 x 256 pixels. Low pass filtering was performed to remove the statistical noise without to lose the features of the sample. All AFM experiments were carried out under ambient laboratory conditions (about 20°C) as previously reported [23-26].

ACKNOWLEDGMENTS

One of us (Roxana-Diana Pașca) has received financial support for this study from the *Babes-Bolyai University of Cluj-Napoca, Romania* (Programme No. 32/2009).

REFERENCES

1. W. R. Nes, *Lipids*, **1974**, *9*, 596.
2. J. Henriksen, A. C. Rowat, E. Brief, Y. W. Hsueh, J. L. Thewalt, M. J. Zuckermann, J. H. Ipsen, *Biophysical Journal*, **2006**, *90*, 1639.
3. J. Pencer, M. P. Nieh, T. A. Harroun, S. Krueger, C. Adams, J. Katsaras, *Biochimica Biophysica Acta*, **2005**, *1720*, 84.
4. J. Henriksen, J., A. C. Rowat, J. H. Ipsen, *European Biophysics Journal*, **2004**, *33*, 732.
5. M. D Ali, K. H. Cheng, J. Huang, *Proceedings of the Natural Academy of Sciences USA*, **2007**, *104*, 5372.
6. K. Sabatini, J.-P. Mattila, P. K. J. Kinnunen, *Biophysical Journal*, **2008**, *95*, 2340.
7. O. Albrecht, H. Gruler, E. Sackmann, *Journal of Colloid and Interface Science*, **1981**, *79*, 319.
8. V. Vogel, D. Mobius, *Journal of Colloid and Interface Science*, **1988**, *126*, 408.9.
M. Tomoaia-Cotisel, Gh. Tomoaia, V. D. Pop, A. Mocanu, O. Cozar, N. Apetroaei, Gh. Popa, *Revue Roumaine de Chimie*, **2005**, *50*, 471.
10. L. Berthelot, V. Rosilio, M. L. Costa, S. Chierici, G. Albrecht, P. Boullanger, A. Baszkin, *Colloids and Surfaces B: Biointerfaces*, **1998**, *11*, 239.
11. C. A. S. Andrade, N. S. Santos-Magalhães, C. P. de Melo, *Journal of Colloid and Interface Science*, **2006**, *298*, 145.
12. D. Matyszevska, R. Bilewicz, *Colloids and Surfaces A: Physicochemical and Engineering Aspects*, **2008**, *321*, 11.
13. P. Dynarowicz-Latka, K. Hac-Wydro, *Colloid Surfaces B: Biointerfaces*, **2004**, *37*, 21.
14. Y. Tagami, T. Narita, H. Ikigai, Y. Oishi, *Colloids and Surfaces A: Physicochemical and Engineering Aspects*, **2009**, *347*, 225.
15. B. Korchowiec, M. Paluch, Y. Corvis, E. Rogalska, *Chemistry and Physics of Lipids*, **2006**, *144*, 127.
16. Y. Su, Q. Li, L. Chen, Z. Yu, *Colloids and Surfaces A: Physicochemical and Engineering Aspects*, **2007**, *293*, 123.
17. Y. Tagami, H. Ikigai, Y. Oishi, *Colloids and Surfaces A: Physicochemical and Engineering Aspects*, **2006**, *284*, 475.
18. C. Yuan, L. J. Johnston, *Biophysical Journal*, **2001**, *81*, 1059.
19. Yeagle, P. L., *Biochimica et Biophysica Acta*, **1985**, *822*, 267.
20. E. E. Berring, K. Borrenpohl, S. J. Fliesler, A. Barnoski Serfis, *Chemistry and Physics of Lipids*, **2005**, *136*, 1.
21. K. Kim, C. Kim, Y. Byun, *Langmuir*, **2001**, *17*, 5066.
22. J. T. Davies, E. K. Rideal, "Interfacial Phenomena", 2nd ed., Academic Press, New York, **1963**.
23. M. Tomoaia-Cotisel, A. Tomoaia-Cotisel, T. Yupsanis, G. Tomoaia, I. Balea, A. Mocanu, C. Racz, *Revue Roumaine de Chimie*, **2006**, *51*, 1181.
24. O. Horovitz, G. Tomoaia, A. Mocanu, T. Yupsanis, M. Tomoaia-Cotisel, *Gold Bulletin*, **2007**, *40*, 213.
25. M. Tomoaia-Cotisel, A. Mocanu, *Revista de Chimie (Bucharest)*, **2008**, *59*, 1230.
26. A. Mocanu, I. Cernica, G. Tomoaia, L. D. Bobos, O. Horovitz, M. Tomoaia-Cotisel, *Colloids and Surfaces A: Physicochemical and Engineering Aspects*, **2009**, *338*, 93.

Dedicated to the memory of Prof. dr. Ioan Silaghi-Dumitrescu marking 60 years from his birth

STRUCTURE OF STARCH GRANULES REVEALED BY ATOMIC FORCE MICROSCOPY

MARIA TOMOAI-COTISEL^{a,*}, NICOLAE CIOICA^b, CONSTANTIN COTA^b,
CSABA RACZ^a, IOAN PETEAN^a, LIVIU DOREL BOBOS^a,
AURORA MOCANU^a, OSSY HOROVITZ^a

ABSTRACT. Atomic force microscopy (AFM) was used to reveal the micro and nanostructure of maize starch granules from Romanian cultivar. The size, shape and surface morphology of the native maize starch granules are shown by AFM observations. Numerous structures, protrusions (particles), pores or depressions and cracks were found on the surface of maize starch granules and they have a broad range of sizes. The occurrence of small spherical protrusions might be related with the highly branched amylopectin molecules in substantial agreement with the amylopectin blocklets model. The larger particles were also visualized, representing different associations of amylopectin and amylose and other granule surface components as previously discussed. The existence of rather smooth regions with low surface roughness and rougher zones on the starch granules is confirmed.

Keywords: *native maize starch, granule surface, supramolecular structuring, atomic force microscopy (AFM)*

INTRODUCTION

Currently, starch is widely used in its native form or after various modifications for plastics and food industry [1], as well as for pharmaceutical products [2, 3] and for orthopaedic implants [4]. The numerous applications of starch intensify the studies on starch granule structure due to the large variability of starch origins [1]. It is known that a differentiation in the starch granule structure and, consequently, in starch properties is related to the starch cultivar. The potential starch source in Romania might be the native maize starch, which is available in large quantities.

^a Babeș-Bolyai University of Cluj-Napoca, Faculty of Chemistry and Chemical Engineering, Department of Physical Chemistry, 11 Arany Janos Str., 400028 Cluj-Napoca, Romania; * mcotisel@chem.ubbcluj.ro

^b INMA, 59 Al. Vaida-Voievod Str., 400436 Cluj-Napoca, Romania

The surface morphology of granules is important for the characterization of the maize starch used as raw material for various applications, including the manufacturing of biodegradable plastics. In this respect, it is already understood that the starch processing involves many interfacial modifications and the rate of such changes is controlled mainly by the surface structure of granules. The data on the surface properties of Romanian maize starch granules is unavailable yet.

Starch granules are made of polysaccharides, consisting of D-glucose units, linked together into two different macromolecules, namely amylose and amylopectin [5]. Amylose contains an almost linear chain based on α -1,4 linked glucose residues. Its chain configuration is that of single helices. Amylopectin is a highly branched carbohydrate based on both α -1,4 and α -1,6 linkages [6-8]. Amylopectin has crystalline or amorphous structure and amylose is rather amorphous [9].

The amylose/amylopectin ratio in starch granules varies according to the source, the starch from most cereals containing about 20-30% amylose, but there are starches with up to 98% amylopectin, and also high amylose starch with 60-80% amylose [10]. The starch granules from different plants have different dimensions and various shapes, such as spherical, oval, disk, polygonal or rods [11, 12]. In the starch granule, amylose and amylopectin molecules seem to be structured in growth rings [9], while at the surface of the starch granule, a tightly associated amylose and amylopectin network is formed [13, 14]. Therefore, the size, shape and surface morphology of the starch granules are important data to be known for the different practical applications of starches [15-24].

Among the imaging techniques, the atomic force microscopy (AFM) provides an important tool for probing starch granule structure at molecular level. AFM studies have been performed on starch granules for starches from different botanical sources [18, 21, 22, 25-36]. However, the ultrastructure of the starch granules is not completely understood. The advantages of the AFM technique are related to the sample preparation, the ability to image under ambient air conditions, under almost normal structural conditions for the starch granules. The images are obtained as 2D- and 3D-topographies, phase and amplitude (error signals) images. In addition, the atomic force microscopy (AFM) can go to molecular or even atomic resolution (1-2 Å vertical resolution and less than 1 nm lateral resolution) [37-41].

In the present work we provide the micro- and nanostructure data by AFM imaging, such as size, shape and surface morphology, for native maize starch powder spread out in thin films or compacted into tablets.

RESULTS AND DISCUSSION

Size, shape and surface morphology of the starch granules

AFM images of the starch granule surface are obtained, in tapping mode of AFM operation, as two dimensional (2D) and three dimensional (3D) topographies, as amplitude (errors signal) images and phase images. The contrast in the AFM phase imaging makes possible the detection of variations in properties (such as: phase composition, stiffness, elasticity) of the granule surface (periphery).

A selection of AFM images for maize starch granules compacted into a tablet is given in Figures 1-3.

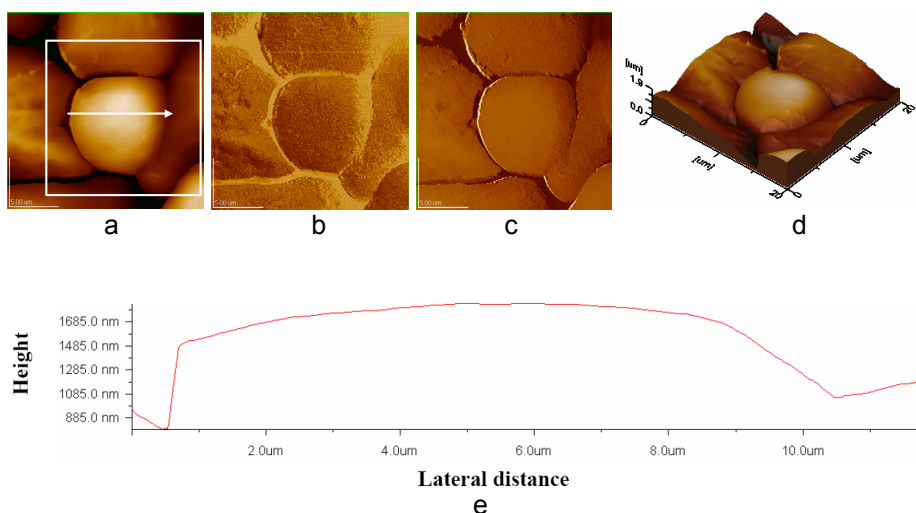


Figure 1. AFM images of maize starch compacted as a tablet. Scanned area: 20 μm x 20 μm . a) 2D – topography; b) phase image; c) amplitude image; d) 3D-topography; e) profile of the cross-section along the arrow given in panel a.

Figure 1 shows a group of several starch granules with rather sharp granule contours. The granules of maize starch have mainly round and oval shapes (Figs 1 and 2). The central granule (see marked area) in Figure 1 is re-scanned in Figure 2, and it has a deformed spherical shape, with the diameter fluctuating between 9.0 μm and 9.5 μm . The height difference is between 1250 and 1300 nm (Figure 1e and 2e). Frequently, on the tablet surface, oval granules are found and their larger axis ranges from 5 to 16 μm .

By accurate imaging analysis, several depressions and pores of undefined oval shape are clearly observed in Figure 1 (a, b), particularly on the granule surface on the right of 2D-topography and phase images, and

they are generally below 1 μm in size. The surface structures are detected on the profile (which is slightly undulated) of the cross-section (Figure 2e) along the arrow on the granule in Figure 2a.

Furthermore, the surface structures are clearly observed in the marked area, given in Figure 2a, at an enlargement corresponding to a re-scanning area of 1 μm x 1 μm , as shown in Figure 3.

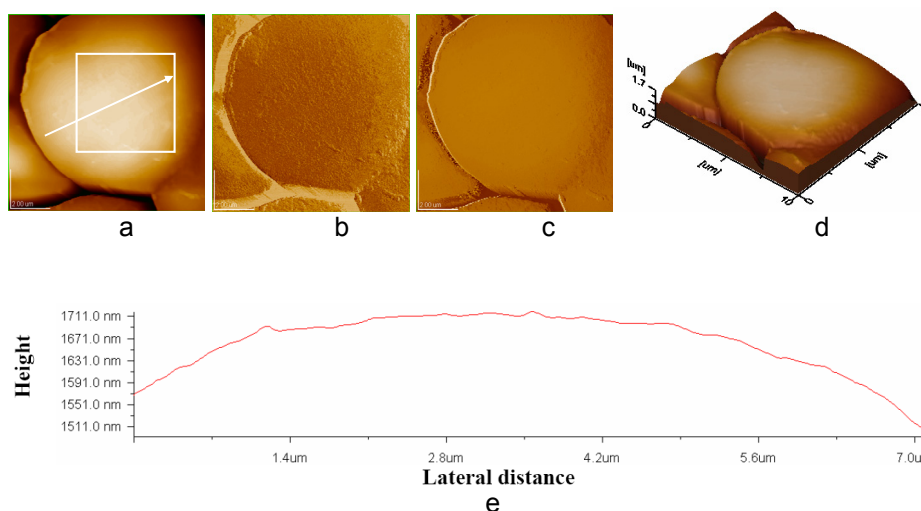


Figure 2. AFM images of compacted maize starch powder (tablet). Scanned area: 10 μm x 10 μm . a) 2D – topography; b) phase image; c) amplitude image; d) 3D-topography; e) profile of the cross section along the arrow in panel a.

Figure 4-7 display the structure of outermost layer of maize starch powder spread out in thin film for several different magnifications (selected scanning areas), in order to prove the microstructure and the surface features of starch granule surface.

Figure 4 presents an oval shaped starch granule, which shows a rather regular contour (Figure 4a-c), with the long axis of about 5.6 μm (Figure 4d and the arrow in Figure 4a) and the difference in height of about 2000 nm (Figure 4d). Figure 5 shows a starch granule with irregular contour (Figure 5a-c), although it resembles to a rather oval shape (Figure 5d) with short axis of about 6 μm , estimated from the cross-section profile (Figure 5e) along the arrow given in Figure 5a. Its long axis, determined from Figure 5a, is about 8 μm . On the 3D-topography (Figure 5d) the structure of the granule surface is rather visible and it is significantly enhanced at higher magnifications, respectively at smaller scanned areas.

STRUCTURE OF STARCH GRANULES REVEALED BY ATOMIC FORCE MICROSCOPY

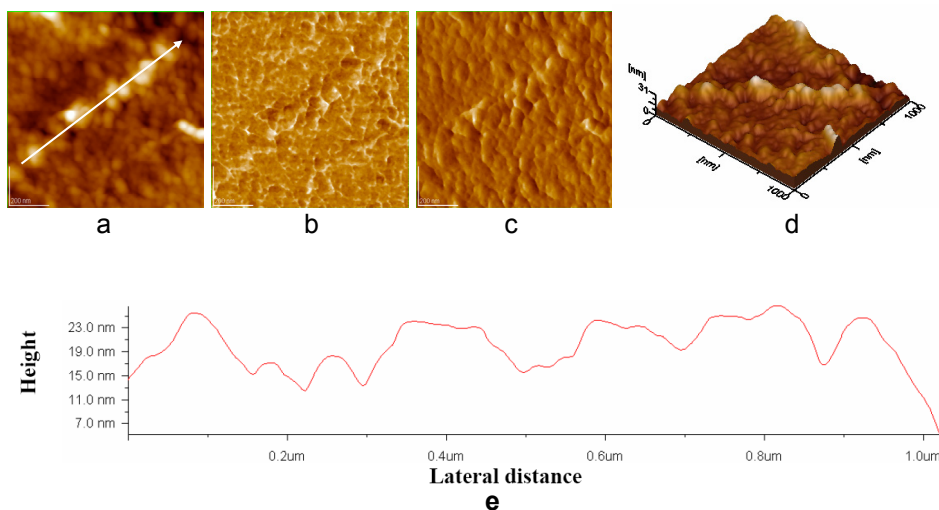


Figure 3. AFM images of the compacted maize starch powder (tablet). Scanned area: $1\ \mu\text{m} \times 1\ \mu\text{m}$. a) 2D – topography; b) phase image; c) amplitude image; d) 3D-topography; e) profile of the cross section along the arrow in panel a.

For example, Figure 6 and 7 display clearly the nanostructure on the starch granule surface at two different areas scanned on the oval maize starch granule from Figure 4.

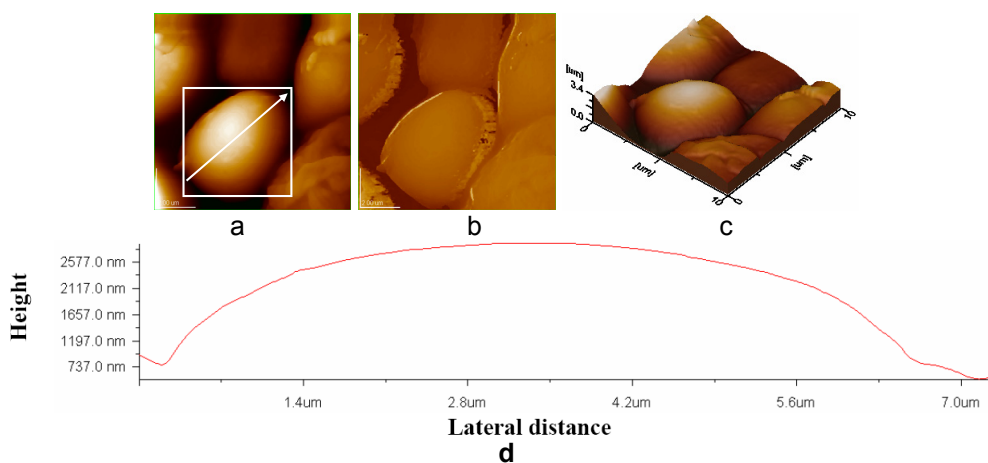


Figure 4. AFM images of the maize starch powder spread out in thin film. Scanned area: $10\ \mu\text{m} \times 10\ \mu\text{m}$. a) 2D – topography; b) amplitude image; c) 3D-topography; d) profile of the cross section along the arrow given in panel a.

From Figures 1, 2, 4 and 5, it is to be observed that almost all granules are well defined with rather sharp granule contours independently of sample preparation method. The granules of maize starch have mainly round and oval shapes, both in tablets and in thin films of powder spread out on adhesive tape. Occasionally, polygonal shapes of starch granules were also observed.

These data suggest that in the tablets obtained by compression of the maize starch powder, the starch granules are quite well packed and consequently, the granules show a rather good compactibility and compressibility. They also indicate a low surface fragility of granules surface in substantial agreement with the compaction behaviour reported on other starch samples [2, 3]. The compaction and the fragility behaviour of the starch powder is important in various applications such as in plastics production and for drug delivery systems. Undoubtedly, these observations might have implications in the formulation of poorly compactable drugs, starch powder being an important component [3] in such systems.

According to the AFM images, the granules of maize starch present a variety of forms, such as regular shapes from rather spherical (Figure 1 and 2) or elliptical and oval (Figure 4) to irregular oval form (Figure 5) or polygonal shape with rather smooth or rough surfaces with depressions or irregular holes of undefined shape. The surface roughness determined as root mean square (RMS) is given in Table 1.

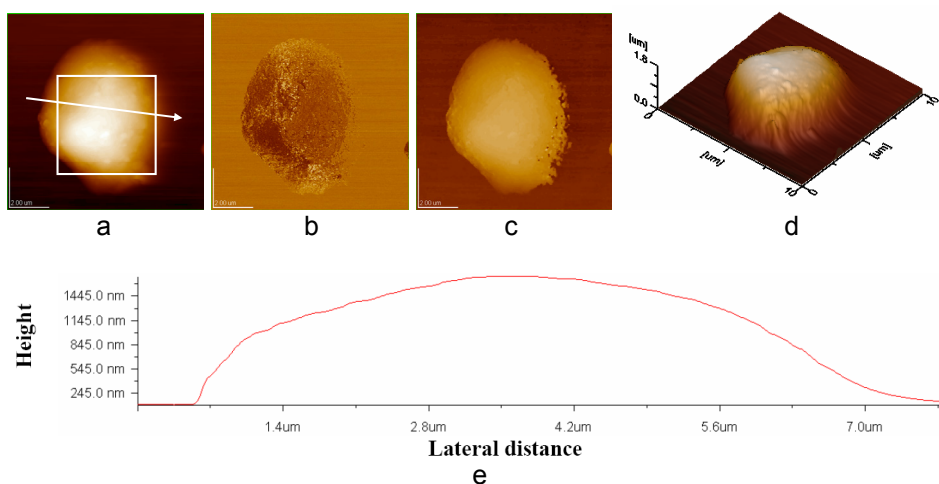


Figure 5. AFM images of the maize starch powder spread out in thin film. Scanned area: 10 μm x 10 μm . a) 2D – topography; b) phase image; c) amplitude image; d) 3D-topography; e) profile of the cross-section along the arrow in panel a.

STRUCTURE OF STARCH GRANULES REVEALED BY ATOMIC FORCE MICROSCOPY

Table 1. Surface roughness given as root mean square (RMS) for maize starch powders.

Figures	Scanned area, μm^2	RMS on tablet profile, nm	RMS on thin film profile, nm
Fig. 1	20 x 20	298	-
Fig. 2	10 x 10	55.3	-
Fig. 3	1 x 1	5.11	-
Fig. 4	10 x 10	-	568
Fig. 5	10 x 10	-	555
Fig. 6	2 x 2	-	12.4
Fig. 7	1 x 1	-	6.17

The granule size distribution is not deduced by AFM imaging, because a very large number of granules must be scanned for that purpose. The size distribution for the maize starch granules is obtained by scanning electron microscopy (SEM) measurements (unpublished results). The average size of the starch granules is about $9.3 \mu\text{m}$ with a standard deviation of $2.9 \mu\text{m}$ and with extreme values between 2 and $25 \mu\text{m}$.

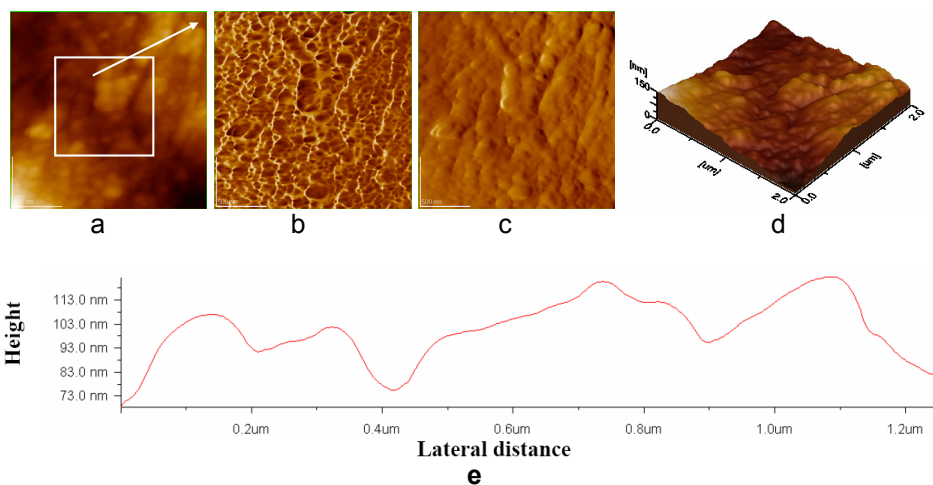


Figure 6. AFM images of maize starch powder spread as a thin film. Scanned area: $2 \mu\text{m} \times 2 \mu\text{m}$. a) 2D – topography; b) phase image; c) amplitude image; d) 3D-topography; e) profile of the cross-section along the arrow in panel a.

Referring to the surface morphology, narrow pores or rather large depressions were observed at microstructural level on some parts of the surface of starch granules. These results suggest that structural differences exist even on the same granule surface, in good agreement with recently reported data on potato starch [42].

The fine structure of starch granule surface

Figure 3, 6 and 7 display numerous surface features of maize starch granules, which are rather pronounced for these magnifications.

By comparing the AFM images in Figure 3, given for the starch granules packed into a tablet, with the corresponding ones in Figure 6 and 7, for starch powder spread out in thin films, a certain morphological resemblance is clearly observed for the surfaces of maize starch granules. These data show that not only the microstructure of the starch granules is similar, but also the ultrastructure of the granule surface is comparable and practically independent of sample preparation method. This situation could reflect a strong interaction between the starch macromolecules, resulting in similar particle shapes at granule surface (periphery).

From the AFM images, 2D topographies (Figure 3a, 6a and 7a), and 3D topographies (Figure 3d, 6d and 7d), as well as phase images (Figure 3b, 6b and 7b) and amplitude images (Figure 3c, 6c and 7c), one can observe the surface structuration on the starch granules, primarily the presence of surface protrusions (small rounded and elongated nodules or particles).

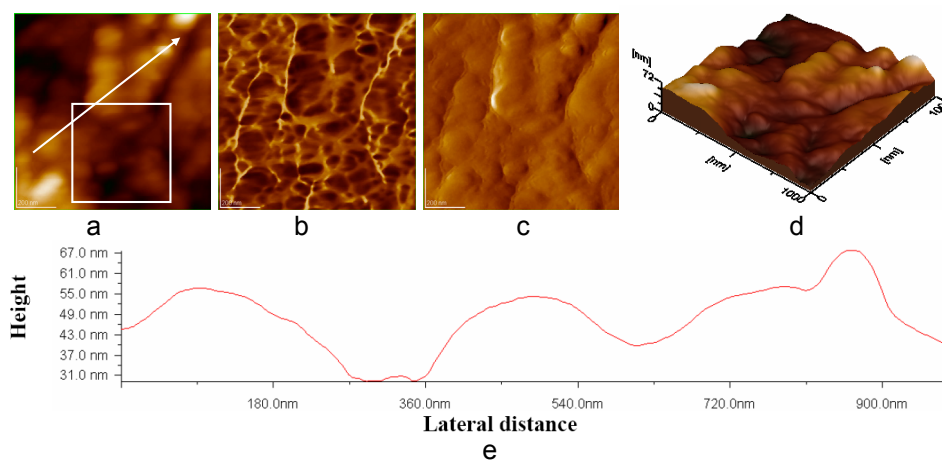


Figure 7. AFM images of the maize starch powder spread as a thin film. Scanned area: 1 μm x 1 μm . a) 2D – topography; b) phase image; c) amplitude image; d) 3D-topography; e) profile of the cross section along the arrow in panel a.

These particles are evidenced at small scanning areas, as given in Figure 3, 6 and 7 for the maize starch. In the profile of the cross-sections (Figure 3e, 6e and 7e) one can see the local nanostructure of the granule surface (see, arrows in Figure 3a, 6a and 7a) with nodules (nanoparticles) which protrude from the surface, generally between about 50 and 80 nm (Figure 3e and 7e) for the maize starch.

The apparent diameter of the smallest found features (about 30 nm) was comparable with the radius of curvature of the AFM probe tip (15-20 nm), so the images are expected to be subjected to tip convolution effects.

Anyway, the observed nanoparticles, named also protrusions, subparticles or nodules, are surface features and generally present rather round or elongated shapes on the granule surface of the maize starch granules. In addition, it is to be noted that particles in roughly the same range (about 20 to 50 nm size) were reported to be formed by precipitation with ethanol from suspensions of gelatinized potato starch [35]. They were also detected at the surface of wheat or oat starch granules [35].

The observed sizes are also in substantial agreement with the fine structure of granules of different types of starches found within the granule [27-29, 31] and on the surface [18, 22, 25, 33-35]. For instance, small particles of about 30 nm in diameter were also found in the internal structure of rice [27, 28], corn [29] and pea starches granules. On the granule surface of potato and wheat starches the fine particles more or less spherical of about 25 nm were also identified [18], which were observed both within and at the surface of starch granules degraded by alpha-amylase.

These nanoparticles on the granules surface could correspond to clusters built from amylopectin side chains bundled into blocklet structures [43], evidenced earlier both on the granule surface and in lamellar structures within the starch granule [44], in agreement with the proposed cluster model [18, 35]. They can be bundled further on into larger blocklets organized within the starch granule or on the surface of granule.

In other words, the small protrusions identified in this work, composed mainly of about 30 to 50 nm size nanoparticles might represent the ends of amylopectin side-chain clusters at the granule surface [18].

Therefore, our results support the blocklets model of the starch granule structure [43-45], independent of the starch botanical resources. According to the blocklets concept, the amylopectin forms nanoparticles on the granule surface of native maize starch. Furthermore, a complex surface network (arrangement) might be assembled among the different components bound on granule surface of the native maize starch.

Closer examination of the AFM images revealed a few quite large protrusions on granules surface of maize starch of roughly 120 nm in diameter placed above (Figure 3 and Figure 7) the flatter surface containing the 30 to 50 nm size nanostructures mentioned above.

On the other hand, the surface of the maize starch granules also possesses several larger protrusions of about 150 to 200 nm (low magnification, Figure 5).

Undoubtedly, the AFM images on the granules surface have demonstrated that the maize starch powder possesses substantially similar surface structures on different granules at nanostructural level for both tablet and thin films.

Even more, on the same granule surface, some zones are detected with a rather high roughness, and quite smooth zones with low roughness are also observed. The roughness, measured by the root mean square (RMS), is given in Table 1 for several selected scanned surfaces.

The surface roughness is apparently higher for the outermost layer of the thin film than for the corresponding value for the tablet surface (Table 1). This is a somehow expected situation due to the compressibility of the granules within the tablet.

There are exceptions, for very small scanned areas, when the roughness appears to be almost identical for both maize starch tablet and thin film (Table 1).

Due to the existence of various protrusions of different size, it appears rational to suggest that the amylopectin blocklets (the smallest identified particles) are probably enlarged either by their self assemblies and/or by their attachment to other granule surface components [46-48], such as amylose, granule proteins and phospholipids. Thus, the starch carbohydrate components will possibly build a highly complex network involving the proteins or lipids attached (or bound) to the starch granule surface. Such complex surface organisation supports the existence of a highly structured surface (periphery) of starch granules according to [49] and its role in maintaining the integrity of the starch granule. The effect of starch granule surface can be also evidenced in the starch gelatinization process, where chemical modifications of the granule surface take place.

CONCLUSIONS

We can conclude that the AFM technique is an appropriate tool for the observation of granules surface of the native maize starch. AFM allows a good visualization of the starch granules, revealing their shapes, surfaces morphology and sizes. The surface structures evidenced by AFM imaging, such as protruding nodules on the surface of the starch granules have various sizes, in a large range of values, from 30 nm to 80 nm. Frequently, fine particles were found to self assemble on the granule surface into rather straight arrangements forming rows (Figure 3 and 7).

The surface organization of the starch granule is probably consisting of blocklets as structural elements that have already been proposed for the association and clustering of amylopectin helices within the starch granule and on the granule surface. We suggest that the observed smallest fine particles might also correspond to the individual clusters of amylopectin in substantial agreement with the proposed cluster model and blocklets concept.

In future investigations we intend to deepen the understanding of the nanostructure of native maize starch with the aim to characterize and control the raw starch material, both native and in different processing stages, such as in gelatinization process, in manufacturing of thermoplastic starch products.

EXPERIMENTAL SECTION

A commercially available maize starch from Romanian cultivar was purchased from Nordic Invest, Cluj-Napoca, Romania. The humidity of the starch samples was about 12%, by the manufacturer analysis. The native maize starch powder was used as supplied.

AFM images were recorded using a AFM-JEOL 4210 (JEOL Ltd. Tokyo, Japan) operated in the tapping mode, thus allowing for the simultaneously topography, phase and amplitude images for each starch sample.

Starch samples were prepared by two methods, namely the starch powder was compacted into tablets or directly spread out in thin films on an adhesive tape. The starch tablets were prepared as follows: the starch powder (around 1g) is compressed in a hydraulic press in vacuum, without any binding agent. Starch powder was also spread on a double adhesive band, on which the starch granules are holding in place as a thin film. Then, each starch sample, tablet or thin film, was independently affixed to the AFM sample support. The outermost layer of starch tablet or of the thin film of starch granules was imaged in air with a scanner (30 μm x 30 μm maximum scan size) under normal air conditions, at room temperature (about 22 $^{\circ}\text{C}$) and at atmospheric pressure.

All images were recorded in tapping mode using commercially available sharpened silicon nitride (Si_3N_4) probes (Mikromasch, Estonia). The conical shaped tips were on cantilevers with a resonant frequency in the range of 200 - 300 kHz and with a spring constant of 48 N/m.

Both a low scanning rate, 1 Hz, and a higher rate, in the range 2-6 Hz were used, in order to detect possible scanning artefacts or those resulting from the sample preparation method. The scanning angle was also modified on different directions, in order to distinguish between real images and those corresponding to artefacts. The AFM images consist of multiple scans displaced laterally from each other in y direction with 256 x 256 pixels. All AFM experiments were carried out under ambient laboratory temperature conditions as previously reported [37, 38].

AFM observations were repeated on different areas on the scanned surface (i.e. for different magnifications), resulting in scanned areas from 20 μm x 20 μm to 1 μm x 1 μm or scaled down even more (0.5 μm x 0.5 μm) for the same sample. The AFM images were obtained from at least six macroscopic zones separately identified on each sample. All the images were processed according to standard AFM proceeding, as described for example in [39-41].

In particular, on each sample of starch granules, AFM images were recorded at least at six macroscopically different locations on the surface, with each of the locations separated by at least 2 or 3 μm . All imaging data were analyzed using JEOL standard software.

ACKNOWLEDGMENTS

This research was financially supported by the project 31-039 from the 2nd National Program.

REFERENCES

1. J. Ubbink, A. Burbidge, R. Mezzenga, *Soft Matter*, **2008**, *4*, 1569.
2. C. K. Chang, F. A. Alvarez–Nunez, J. V. Rinella Jr., L.-E. Magnusson, K. Sueda, *AAPS PharmSciTech.*, **2008**, *9*, 597.
3. S. Edge, D. F. Steele, J. N. Staniforth, A. Chen, P. M. Woodcock, *Drug Development and Industrial Pharmacy*, **2002**, *28*, 989.
4. I.B. Leonor, A. Ito, K. Onuma, N. Kanzaki, R.L. Reis, *Biomaterials*, **2003**, *24*, 579.
5. J. M. V. Blanshard, "Starch: Properties and Potential", John Wiley and Sons, Brisbane, **1987**, p. 16-54.
6. H. F. Zobel, *Starch/Stärke*, **1988**, *40* (2), 44.
7. D. J. Gallant, B. Bouchet, A. Buleon, S. Perez, *European Journal of Clinical Nutrition*, **1992**, *46*, Suppl. 2, S3.
8. S. You, J. Jane, *Carbohydrate Polymers*, **2002**, *49* (3), 307.
9. J. Jane, *Journal of Applied Glycoscience*, **2006**, *53*, 205.
10. N. Singh, J. Singh, L. Kaur, N. S. Sodhi, B. S. Gill, *Food Chemistry*, **2003**, *81*, 219.
11. D. French, in "Starch: Chemistry and Technology", R. L. Whistler, J. N. Bemiller, E. F. Paschall, Eds., Academic Press, London, **1984**, p. 183-247.
12. J. Jane, T. Kasemsuwan, S. Leas, H. Zobel, J. F. Róbyt, *Starch/Stärke*, **1994**, *46* (4), 121.
13. J. Jane, J. J. Shen, *Carbohydrate Research*, **1993**, *247*, 279.
14. D. D. Pan, J. Jane, *Biomacromolecules*, **2000**, *1*, 126.
15. H. Fuwa, Y. Sugimoto, T. Takaya, Z. Nikuni, *Carbohydrate Research*, **1979**, *70*, 233.
16. M. R. Sandhya Rani, K. R. Bhattacharya, *Starch/Stärke*, **1995**, *47* (9), 334.
17. P. M. Baldwin, J. Adler, M. C. Davies, C. D. Melia, *Starch/Stärke*, **1994**, *46* (9), 341.
18. P.M. Baldwin, M. C. Davies, C. D. Melia, *International Journal of Biological Macromolecules*, **1997**, *21*, 103.
19. R. S. Policegoudra, S. M. Aradhya, *Food Hydrocolloids*, **2008**, *22*, 513.

20. S. Wang, J. L. Yu, O. Zhu, J. Yu, F. Jin, *Food Hydrocolloids*, **2009**, 23, 426.
21. J. Szymonska, M. Targosz-Korecka, F. Krok, *Journal of Physics: Conference Series*, **2009**, 146, 012027.
22. M. Sujka, J. Jamroz, *LWT – Food Science and Technology*, **2009**, 42, 1219.
23. F. H. Cisneros, R. Zevillanos, L. Cisneros-Zevillanos, *Journal of Agricultural and Food Chemistry*, **2009**, 57, 7363.
24. H. Yan, G. U. Zhengbiao, *Food Research. International*, **2010**, 43, 767.
25. N. H. Thomson, M. J. Miles, S. G. Ring, P. R. Shewry, A. S. Tatham, *Journal of Vacuum Science and Technology B*, **1994**, 12, 1565.
26. P. R. Shewry, M. J. Miles, N. H. Thomson, A. S. Tatham, *Cereal Chemistry*, **1997**, 74, 193.
27. T. Ohtani, T. Yoshino, T. Ushiki, S. Hagiwara, T. Maekawa, *Journal of Electron Microscopy*, **2000**, 49, 487.
28. T. Ohtani, T. Yoshino, S. Hagiwara, T. Maekawa, *Starch/Stärke*, **2000**, 52 (5), 150.
29. A. A. Baker, M. J. Miles, W. Herbert, *Carbohydrate Research*, **2001**, 330, 249.
30. M. J. Ridout, A. P. Gunning, M. L. Parker, R. H. Wilson, V. J. Morris, *Carbohydrate Polymers*, **2002**, 50 (2), 123.
31. M. J. Ridout, M. L. Parker, C. L. Hedley, T. Y. Bogracheva, V. J. Morris, *Carbohydrate Research*, **2003**, 338, 2135.
32. Z. Liu, C. Chen, Z. Ouyang, Y. Guo, J. Hu, M. Li, *Journal of Vacuum Science and Technology B*, **2001**, 19, 111.
33. L. Juszczak, T. Fortuna, F. Krok, *Starch/Stärke*, **2003**, 55 (1), 1.
34. L. Juszczak, T. Fortuna, F. Krok, *Starch/Stärke*, **2003**, 55 (1), 8.
35. J. Szymonska, F. Krok, *International Journal of Biological Macromolecules*, **2003**, 33, 1.
36. J. Cabálková, J. Přebyl, P. Skládal, P. Kulich, J. Chmelík, *Tree Physiology*, **2008**, 28, 1593.
37. M. Tomoaia-Cotisel, in “Convergence of Micro-Nano-Biotechnologies” Vol. 9, Eds. M. Zaharescu, E. Burzo, L. Dumitru, I. Kleps, D. Dascalu, Romanian Acad. Press, Bucharest, **2006**, p. 147 - 161.
38. M. Tomoaia-Cotisel, A. Tomoaia-Cotisel, T. Yupsanis, G. Tomoaia, I. Balea, A. Mocanu, C. Racz, *Revue Roumaine de Chimie*, **2006**, 51, 1181.
39. O. Horovitz, G. Tomoaia, A. Mocanu, T. Yupsanis, M. Tomoaia-Cotisel, *Gold Bulletin*, **2007**, 40, 213.
40. M. Tomoaia-Cotisel, A. Mocanu, *Revista de Chimie (Bucharest)*, **2008**, 59, 1230.
41. A. Mocanu, I. Cernica, G. Tomoaia, L. D. Bobos, O. Horovitz, M. Tomoaia-Cotisel, *Colloids and Surfaces, A*, **2009**, 338, 93.
42. J. Huang, P. Zhang, Z. Chen, H. Li, *Carbohydrate Polymers*, **2010**, 80 (1), 215.
43. D. J. Gallant, B. Bouchet, P. M. Baldwin, *Carbohydrate Polymers*, **1997**, 32 (3-4), 177.
44. P. M. Baldwin, J. Adler, M. C. Davies, C. D. Melia, *Journal of Cereal Science*, **1998**, 27 (3), 255.

M. T.-COTISEL, N. CIOICA, C. COTA, CS. RACZ, I. PETEAN, L. D. BOBOS, A. MOCANU, O. HOROVITZ

45. P. Laity, A. Cassidy, J. Skepper, B. Jones, R. Cameron, *European Journal of Pharmaceutics and Biopharmaceutics*, **2010**, *74*, 377.
46. P. L. Russell, B. M. Gough, P. Greenwell, A. Fowler, H. S. Munro, *Journal of Cereal Science*, **1987**, *5*, 83.
47. P. M. Baldwin, C. D. Melia, M. C. Davies, *Journal of Cereal Science*, *26*, 329.
48. A. Rindlav-Westling, P. Gatenholm, *Biomacromolecules*, **2003**, *4*, 166.
49. J. Yu, P. R. Chang, X. Ma, X., *Carbohydrate Polymers*, **2010**, *79* (2), 296.

Dedicated to the memory of Prof. dr. Ioan Silaghi-Dumitrescu marking 60 years from his birth

SYNTHESIS AND SPECTROSCOPIC INVESTIGATIONS OF NEW UO_2^{2+} – POLYOXOMETALATE COMPLEXES

DAN RUSU^a, OANA BABAN^b, SIMINA DREVE^c, MIRCEA PUIA^d,
MARIANA RUSU^b

ABSTRACT. The $\text{Na}_{10}[(\text{UO}_2)_2(\text{H}_2\text{O})_2\text{X}_2\text{W}_{20}\text{O}_{70}] \cdot n\text{H}_2\text{O}$ heteropolyoxo-metalates ($\text{Na}_{10}1$: $\text{X} = \text{Sb}^{\text{III}}$, $n = 28$; $\text{Na}_{10}2$: $\text{X} = \text{Bi}^{\text{III}}$, $n = 34$) were synthesized and investigated by chemical and thermal analysis, FT-IR, Raman, UV-Vis and fluorescence emission spectroscopies for determining subsequently the behavior of the encapsulated uranyl cations, their coordination by the tungstoantimonate(III) or tungstobismutate(III) fragments, and the corresponding pentagonal-bipyramidal local symmetry. Polyoxoanions $[(\text{UO}_2)_2(\text{H}_2\text{O})_2\text{X}_2\text{W}_{20}\text{O}_{70}]^{10-}$ are structural similarly and consist from two $\beta\text{-B-[XW}_9\text{O}_{33}]^9$ ($\text{X} = \text{Sb}^{\text{III}}, \text{Bi}^{\text{III}}$) framework which are linked by an equatorial belt of two $\text{UO}_2(\text{H}_2\text{O})_2^{2+}$ units and two WO_2 groups.

Keywords: Uranium (VI); Heteropolyoxotungstates; IR, Raman, UV, Vis and fluorescence emission spectroscopies.

INTRODUCTION

The current research in polyoxometallate (POM) chemistry is characterized by the perception and the achievement of their applications in different areas, especially in the field of nanomaterials, catalysis, image reactive, as potential agents for nuclear waste sequestration and storage, magnetic chemistry and medicine [1]. At the same time, it must be pointed out that the polyoxometallate chemistry has a tradition in studying the formation and stability of heteropolyoxotungstates containing heteroatoms of lanthanides and actinides [2-15]. The structure of these polyoxotungstate species was first reported by Weakley [16], and it can be described as a 1:2 sandwich type structure of $\text{Ln}^{3+/4+}$ or An^{4+} ions with monolacunary polyoxoanions

^a Universitatea de Medicină și Farmacie Iuliu Hațieganu, Facultatea de Farmacie, Str. E. Isac Nr. 13, RO-400023, Cluj-Napoca, Romania

^b Universitatea Babeș-Bolyai, Facultatea de Chimie și Inginerie Chimică, Str. M. Kogalniceanu Nr. 1, RO-400084 Cluj-Napoca, Romania, mrusu@chem.ubbcluj.ro

^c Institutul Național pentru Izotopi și Tehnologie Moleculară, Str. Donath Nr. 63, RO-400293 Cluj-Napoca, Romania

^d Universitatea Babeș Bolyai, Facultatea de Fizică, Str. M. Kogalniceanu Nr. 1, RO-400084 Cluj-Napoca, Romania

“ligands”, such as $[\text{Ln}^{\text{III}}(\text{PW}_{11}\text{O}_{39})_2]^{11-}$, in which the metallic cations occupy a anti-phrysmatic coordinative position. Sometimes, although U^{IV} can be stabilized in these complexes, the chemistry of the aqueous solutions of the first actinides is dominated by trans-dioxin cations, from which the most familiar is UO_2^{2+} . Pope [17] reports the example of the heteropolyoxotungstate which incorporates the UO_2^{2+} , linear steric, as expected. Subsequently, other uranyl polyoxometallate complexes were reported. [18-27]

Since 1970 [28-30], a number of articles have been published regarding the $\{\text{XW}_{11}\}$, with $(\text{X}=\text{Sb}^{\text{III}}, \text{Bi}^{\text{III}})$, type of monolacunary polyoxocations and their complexes with a ratio of 1:1 with the di- and trivalent cations of transitional metals. Recently, these species have been revealed as dimmers on the basis of the structure determined on the Krebs salts $[\text{Sb}_2\text{W}_{22}\text{O}_{74}(\text{OH})_2]^{12-}$, $[\text{Sb}_2\text{W}_{20}\text{Fe}^{\text{III}}_2\text{O}_{70}(\text{H}_2\text{O})_6]^{8-}$, $[\text{Sb}_2\text{W}_{20}\text{Co}^{\text{II}}_2\text{O}_{70}(\text{H}_2\text{O})_6]^{10-}$ and $[\text{Bi}_2\text{W}_{20}\text{Fe}^{\text{III}}_2\text{O}_{70}(\text{H}_2\text{O})_6]^{6-}$ [31, 32]. The polyoxotungstate anion structure consists of two trilacunary groups $\{\text{B}-\beta\text{-XW}_9\}$, bonded by two additional tungsten atoms and other two additional tungsten centers with a weaker bond, which can be replaced with $\text{M}^{\text{II/III}}$ cations in the substituted polyoxoanions.

The Krebs $[\text{X}_2\text{W}_{22}\text{O}_{74}(\text{OH})_2]^{12-}$ polyoxoanion type belongs to the clusters that incorporate different lacunary trivacante polyoxometallic fragments with the formula $\text{B}-\beta [\text{XW}_9\text{O}_{33}]^{9-}$ where $\text{X} = \text{Sb}^{\text{III}}, \text{Bi}^{\text{III}}$.

The aim of the present paper is to report the new sodium salts of the di-substituted Krebs tungstoantimonate and tungstobismutate $[(\text{UO}_2)_2(\text{H}_2\text{O})_2\text{X}_2\text{W}_{20}\text{O}_{70}]^{10-}$, $\text{X} = \text{Sb}^{\text{III}}, \text{Bi}^{\text{III}}$. The 2:1 complexes corresponding to the formula $\text{Na}_{10}[(\text{UO}_2)_2(\text{H}_2\text{O})_2\text{X}_2\text{W}_{20}\text{O}_{70}]$, $\text{X} = \text{Sb}^{\text{III}}, \text{Bi}^{\text{III}}$ were obtained according to the following reaction:



In order to establish the behavior of UO_2^{2+} cations encapsulated in heteropolyoxometalates, the coordination pattern of the metallic ions to the Keggin fragments and the local symmetry around them, the new complexes were investigated by means of spectroscopic (FT-IR, Raman, UV, Vis and fluorescence emission) methods.

RESULTS AND DISCUSSIONS

Chemical and thermal analysis

The following abbreviations will be used: i) for the anions: L_1 for $[\text{Sb}_2\text{W}_{22}\text{O}_{74}(\text{OH})_2]^{12-}$, $\mathbf{1}$ for $[(\text{UO}_2)_2(\text{H}_2\text{O})_4\text{Sb}_2\text{W}_{20}\text{O}_{70}]^{10-}$, L_2 for $[\text{Bi}_2\text{W}_{22}\text{O}_{74}(\text{OH})_2]^{12-}$, $\mathbf{2}$ for $[(\text{UO}_2)_2(\text{H}_2\text{O})_4\text{Bi}_2\text{W}_{20}\text{O}_{70}]^{10-}$ ii) for the salts: Na_{12}L_1 for $\text{Na}_{12}[\text{Sb}_2\text{W}_{22}\text{O}_{74}(\text{OH})_2] \cdot 42\text{H}_2\text{O}$, $\text{Na}_{10}\mathbf{1}$ for $\text{Na}_{10}[(\text{UO}_2)_2(\text{H}_2\text{O})_4\text{Sb}_2\text{W}_{20}\text{O}_{70}] \cdot 28\text{H}_2\text{O}$, Na_{12}L_2 for $\text{Na}_{12}[\text{Bi}_2\text{W}_{22}\text{O}_{74}(\text{OH})_2] \cdot 44\text{H}_2\text{O}$, $\text{Na}_{10}\mathbf{2}$ for $\text{Na}_{10}[(\text{UO}_2)_2(\text{H}_2\text{O})_4\text{Bi}_2\text{W}_{20}\text{O}_{70}] \cdot 34\text{H}_2\text{O}$.

The chemical reaction of UO_2^{2+} with $[\text{X}_2\text{W}_{22}\text{O}_{74}(\text{OH})_2]^{12-}$ ($\text{X}=\text{Sb}^{\text{III}}, \text{Bi}^{\text{III}}$) in water can be described by eqn. (1). The isolation of the final products as sodium salt, and their recrystallization from hot water, resulted in relatively good yields of the $\text{Na}_{10}\mathbf{1}$ and $\text{Na}_{10}\mathbf{2}$. The analytical data are presented in table 1.

Table 1. Analytical data of the $\text{Na}_{10}\mathbf{1}$ and $\text{Na}_{10}\mathbf{2}$ polyoxometalate complexes

Complex	Yield (g / %)	Colour	Found (calc.) (%)				
			Na	X	W	U	H ₂ O
$\text{Na}_{10}\mathbf{1}$	4.15 / 65	Yellow-Orange	3.72 (3.60)	3.86 (3.81)	57.70 (57.57)	7.48 (7.45)	8.98 (9.02)
$\text{Na}_{10}\mathbf{2}$	4.73 / 71	Yellow-Orange	3.54 (3.45)	6.28 (6.27)	55.60 (55.15)	7.18 (7.14)	10.22 (10.26)

Due to the fact that the $[\text{X}_2\text{W}_{22}\text{O}_{74}(\text{OH})_2]^{12-}$ species -where $\text{X}=\text{Sb}^{\text{III}}, \text{Bi}^{\text{III}}$ - were not stable in aqueous solutions, the reaction was led by adding solid sodium salt of the ligands to the $\text{UO}_2(\text{NO}_3)_2$ aqueous solution. The polyoxoanion complexes obtained were stable only in the presence of an excess of sodium ions. The complexes were crystallized, with a good yield, after a few days, from solution kept at 5 °C.

The suggested formula for $\text{Na}_{10}[(\text{UO}_2)_2(\text{H}_2\text{O})_4\text{Sb}_2\text{W}_{20}\text{O}_{70}].28\text{H}_2\text{O}$ and $\text{Na}_{10}[(\text{UO}_2)_2(\text{H}_2\text{O})_4\text{Bi}_2\text{W}_{20}\text{O}_{70}].34\text{H}_2\text{O}$ complexes are consistent with results of the analyses of the final products (Table 1).

The thermo-gravimetric analysis shows that between 35-325 °C the mass loss was 1.3491 mg (8.98 %) and 1.5039 mg (10.22 %) for ($\text{Na}_{10}\mathbf{1}$) and ($\text{Na}_{10}\mathbf{2}$) complexes respectively. The water loss process took place in two successive phases: the first between 35-120 °C which corresponds to 28 ($\text{Na}_{10}\mathbf{1}$) and 34 ($\text{Na}_{10}\mathbf{2}$) crystallization water molecules respectively, and the second between 120-325 °C, corresponding to 4 coordinating water molecules for both complexes.

The DTA curves indicate two endothermic and two exothermic effects. The endothermic effects with a maximum temperature of ≈ 120 °C and ≈ 325 °C corresponds to the water loss processes. The exothermic effect with a maximum at ≈ 430 °C correspond to the crystallization process of the oxides from the mixture, and the exothermic effect with a maximum temperature at ≈ 500 °C corresponds to the phase transformation from the oxides structures in the mixture [33].

Vibrational spectra

FT – IR spectra

By comparing the FT-IR spectra of the uranyl complexes with those for the corresponding ligands and their shifts toward higher or lower frequencies, we obtained information regarding the UO_2^{2+} ions coordination to the lacunary

polyoxometallates units, the symmetry and the bond strength. The FT-IR spectra of the polyoxometallates generally exhibit contributions of the polyoxoanion frameworks. The characteristic IR vibration bands of Na₁₀**1** and Na₁₀**2** complexes, as compared to those of the Na₁₂L₁ and Na₁₂L₂ ligands, are shown in Table 2.

Table 2. Main vibration bands observed in the FT-IR spectra (cm⁻¹)

Vibration	Na ₁₂ L ₁	Na ₁₂ L ₂	Na ₁₀ 1	Na ₁₀ 2
$\nu_{as}(W=O_t)$	939	948	940	948
$\nu_{as}(W-O_c-W)$	879	875	889 870	880 868
$W-O-UO_2^{2+}$			836	836
$\nu_{as}(W-O_e-W)$	798 762	790 735	775 720	795 720

In the 1000-700 cm⁻¹ range, we observed characteristic bands, which we assigned to the asymmetric stretching vibrations of the bridges W-O_{c,e}-W, W-O_i and of the terminal bonds W=O_t.

All anti-symmetric frequency bands involving tungsten ions are shifted towards higher or lower frequencies (by 1 – 39 cm⁻¹) in the complex spectra, compared to the ligands.

The tiny shift of the $\nu_{as}(W=O_t)$ vibration indicates that terminal O_t atoms are not involved in the coordination of UO₂²⁺ ions.

The $\nu_{as}(W-O_c-W)$ vibration band of the tricentric W-O_c-W bond of the corner sharing WO₆ octahedra is split in both complexes, being shifted in the complexes spectra toward higher frequencies in comparison with the ligands. This is consistent with an increase in the anion cohesion, when the co-ordination of the uranyl ions in the polyoxometalates frameworks takes place.

The $\nu_{as}(W-O_e-W)$ vibration band of the tricentric W-O_e-W bond of the edge sharing WO₆ octahedra is split in both complexes, being shifted in the complexes spectra toward lower frequencies for Na₁₀**1** or higher for Na₁₀**2** in comparison with the ligands. This is consistent with a decrease or increase of the anions cohesion, when coordination of the uranyl ions in the polyoxometalates frameworks takes place.

The shift of $\nu_{as}(W-O_{c,e}-W)$ vibration bands is due to the uranyl ions coordination with the lacunary polyoxometalate ligands by O_c and O_e atoms.

In addition, the IR spectra of the uranyl polyoxometalate complexes exhibit at ~ 836 cm⁻¹ a band which is assigned to the stretching vibrations of the $\nu_{as}(UO_2^{2+})$.

The $\nu_{as}(UO_2^{2+})$ bands are shifted in polyoxotungstate complexes to lower frequencies, in comparison with the corresponding band from the

$\text{UO}_2(\text{NO}_3)_2 \cdot 4\text{H}_2\text{O}$ (965 cm^{-1}) [34], because the polyoxometalate ligands form strong bonds with uranium by lowering the order of the $\text{U}=\text{O}$ band and consistently lowering the $\nu_{\text{as}}(\text{O}=\text{U}=\text{O})$ frequency.

Raman spectra

The Raman spectra of the complexes $\text{Na}_{10}\mathbf{1}$ and $\text{Na}_{10}\mathbf{2}$ (Figure 1) also show vibration bands which are characteristic to the polyoxometalate framework. The strongest bands occurring at 958 and 956 cm^{-1} , respectively, can be assigned to $\nu_s(\text{W}-\text{O}_i)$ vibrations. The less intense bands appearing in the $900\text{--}700 \text{ cm}^{-1}$ range are assigned to the stretching of the $\text{W}-\text{O}_{\text{c,e}}-\text{W}$ bridges, and the band appearing at 214 cm^{-1} is assigned to $\nu_s(\text{W}-\text{O}_i)$ vibration, where O_i is an internal oxygen atom which links Sb or Bi and W atoms. In comparison to the related lacunary ligands $\text{Na}_{12}\mathbf{L}_1$ and $\text{Na}_{12}\mathbf{L}_2$, a shift of these bands towards higher or lower energies is observed, indicating an increase in stability for the $\text{Na}_{12}\mathbf{L}_1$ and a decrease in stability for the $\text{Na}_{12}\mathbf{L}_2$ complexes of the polyoxoanion framework, upon coordination of the uranyl ions [35].

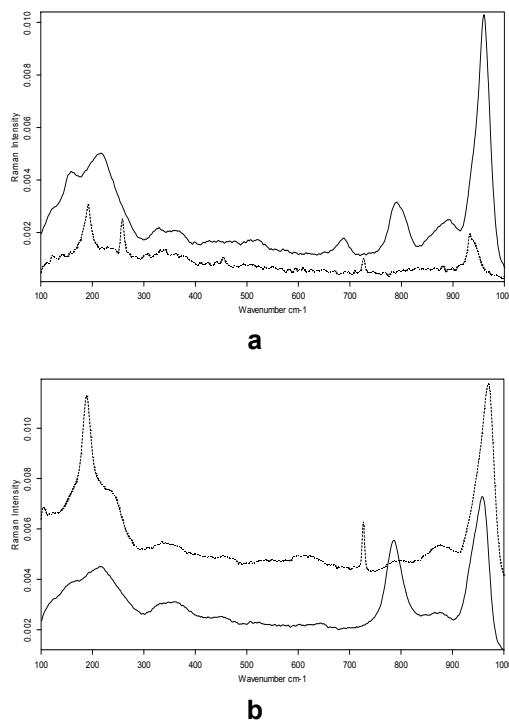


Figure 1. Raman spectra of the polyoxometalate complexes (solid line) a) $\text{Na}_{10}\mathbf{1}$ and b) $\text{Na}_{10}\mathbf{2}$, and of the related ligands (dotted line) a) $\text{Na}_{12}\mathbf{L}_1$ and b) $\text{Na}_{12}\mathbf{L}_2$.

Electronic spectra

UV-spectra

The complexes' spectra are similar to the ones of the ligands. Each spectrum presents two bands assigned to the $p_{\pi} \rightarrow d_{\pi}$ ligand-to-metal charge transfer transition in the $W=O_t$ bonds and $d_{\pi} - p_{\pi} - d_{\pi}$ electronic transitions between the energy levels of the $W-O_{c,e}-W$ bonds (Table 3).

The higher energy band (ν_1), due to the $d_{\pi} - p_{\pi}$ proper transitions from the $W=O_t$ bonds, with an absorption maximum at ~ 210 nm, are insignificantly shifted in the complexes compared to the ligands, which can be associated with the lack of involvement of the terminal oxygen atoms in the coordination of the cations of uranyl.

The lower energy band (ν_2) corresponding to the $d_{\pi} - p_{\pi} - d_{\pi}$ electronic transitions from the tri-centric $W-O_{c,e}-W$ bonds, displays an expected absorption maximum in the range of 250-300 nm, for all polyoxotungstate complexes, shifted towards lower energies compared to the ligands, which is associated with the involvement of the oxygen atoms of these bonds in the coordination of the uranyl cations [36, 37].

Table 3. Charge transfer bands observed in the UV absorption spectra (cm^{-1}/nm)

Bands	Na ₁₂ L ₁	Na ₁₂ L ₂	Na ₁₀ 1	Na ₁₀ 2
ν_2 : $d_{\pi} \rightarrow p_{\pi} \rightarrow d_{\pi}$ ($W-O_b-W$)	39682/252	39525/253	39215/255 36200/276	39062/256 35840/279
ν_1 : $p_{\pi} \rightarrow d_{\pi}$ ($W=O_t$)	47169/212	47169/212	46728/214	46728/214

Visible-spectra

Visible spectra of the Na₁₀1 and Na₁₀2 complexes are similar and present six bands. The transition assignments were made in accordance with [18], and were presented in Figure 2.

The visible electronic spectra of uranyl complexes exhibit two charge transfer bands at ~ 420 nm and ~ 430 nm respectively, which can be attributed to internal $O=U=O$ transitions and four charge transfer bands at ~ 440 , ~ 468 , ~ 480 and ~ 500 nm which can be assigned to ligand – uranyl electronic transitions [17-21].

As resulting from the specialty literature, as well as from the present report, when it comes to the polyoxometalate-uranyl complexes, we observe a trend, namely that the U(VI) always adopts its favored seven-coordinate pentagonal-bipyramidal geometry but with a certain degree of distortion, in order to accommodate the positions of the unsaturated oxygen donor atoms of the polyoxoanion [20,21].

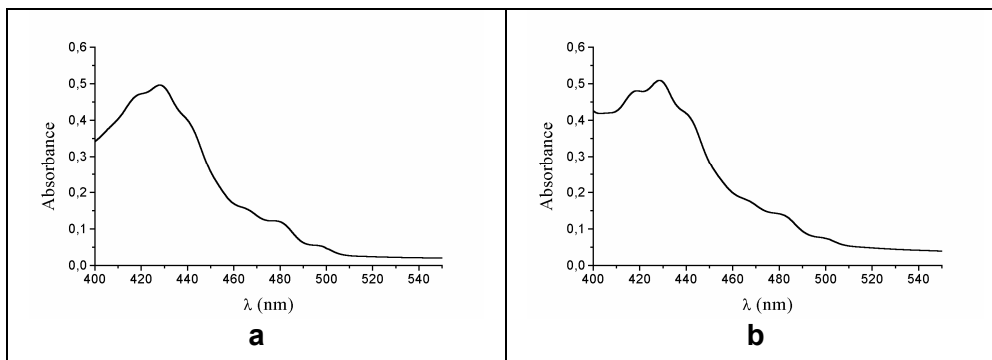


Figure 2. The electronic visible spectra of the polyoxometalate complexes: a) $\text{Na}_{10}\mathbf{1}$; b) $\text{Na}_{10}\mathbf{2}$.

Fluorescence emission spectra

The spectrofluorimetric analysis reveals a strong fluorescence emission in the range of 470–580 nm, corresponding to the excitation of the 300 nm band and a sharp emission at 824 nm for an excitation of the 550 nm band.

When comparing the values with some literature data, we can assume that the sharp emission band at 824 nm, presented in both uranyl systems, can be the fluorimetric signal of the uranyl ion in both systems [38–40].

The accuracy of the determinations and the shape of bands suggest that no important quenching phenomenon occurs, confirming the high purity of the $\text{Na}_{10}\mathbf{1}$, and $\text{Na}_{10}\mathbf{2}$ complexes, respectively.

CONCLUSIONS

In this work, we have synthesized two new polyoxometalate complexes with uranyl ions of $[(\text{UO}_2)_2(\text{H}_2\text{O})_4(\text{X}_2\text{W}_{20}\text{O}_{70})]^{10-}$, $\text{X} = \text{Sb}^{\text{III}}, \text{Bi}^{\text{III}}$ type.

The UV and FT-IR spectra indicate the coordination of each uranyl ion to oxygen atoms from the corner-sharing and edge-sharing octahedra of the trilaacurary Keggin anions.

Visible electronic spectra indicate the coordination of the uranyl cations in the $[(\text{UO}_2)_2(\text{H}_2\text{O})_2(\text{X}_2\text{W}_{20}\text{O}_{70})]^{10-}$ complexes, too.

The fluorescence emission spectra reveal the presence of the uranyl ions in both studied compounds and suggest that no important quenching phenomenon occurs, confirming the high purity of $\text{Na}_{10}\mathbf{1}$ and $\text{Na}_{10}\mathbf{2}$ respectively.

According to our studies, we recommend for the uranyl polyoxometalate complexes a “sandwich” kind of structure, which consist of two $\text{B}-\beta-\text{XW}_9\text{O}_{33}$ Keggin frameworks which are linked by two uranyl ions and two WO_2 fragments (Figure 3). Each uranium atom adopts the pentagonal- bi-pyramidal coordination, forming two equatorial bonds with the terminal oxygen atoms of one pair of

two WO_6 octahedra bonded by common edges, which belong to one of the $B-\beta-XW_9O_{33}$ fragments and a bond with the terminal oxygen of one of the WO_6 octahedra belonging to the other $B-\beta-XW_9O_{33}$ fragment, the other two equatorial coordinating points of the uranyl cation being satisfied by two molecules of water.

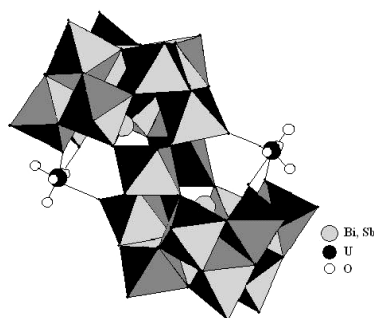


Figure 3. Proposed structure of the $Na_{10}1$ and $Na_{10}2$ polyoxometallate complexes.

EXPERIMENTAL SECTION

Materials

We have used reagent grade chemicals and all syntheses and studies were carried out in distilled water.

Both the sodium salt of the polyoxometallate ligand $Na_{12}[Sb_2W_{22}O_{74}(OH)_2] \cdot 42H_2O$ ($Na_{12}L_1$), and the sodium salt of the polyoxometallate ligand $Na_{12}[Bi_2W_{22}O_{74}(OH)_2] \cdot 44H_2O$ ($Na_{12}L_2$) were prepared as previously reported [31] and [32] respectively.

Synthesis of $Na_{10}[(UO_2)_2(H_2O)_4Sb_2W_{20}O_{70}] \cdot 28H_2O$ ($Na_{10}1$) and $Na_{10}[(UO_2)_2(H_2O)_4Bi_2W_{20}O_{70}] \cdot 34H_2O$ ($Na_{10}2$) complexes

To a solution of $UO_2(NO_3)_2 \cdot 4H_2O$ (0.47 g, 2 mmol) in distilled water (50 ml) we added solid sodium salts of the ligand $Na_{12}[X_2W_{22}O_{74}(OH)_2]$ ($X=Sb^{III}, Bi^{III}$) (6.27 g $Na_{12}L_1$ or 6.75 g $Na_{12}L_2$, respectively, 1 mmol). The slightly turbid yellow-orange final solution was strongly stirred at $70^\circ C$ for 30 minutes, its pH was adjusted to the value of 4.5 with 1M HCl and filtered under suction. It was then cooled to room temperature and 10 g of NaCl was added. An orange-yellow precipitate appeared, which was recrystallized from hot water, having a pH value of 4.5. The orange translucent crystals of $Na_{10}[(UO_2)_2(H_2O)_4Sb_2W_{20}O_{70}] \cdot 28H_2O$ or $Na_{10}[(UO_2)_2(H_2O)_4Bi_2W_{20}O_{70}] \cdot 34H_2O$ respectively, were obtained within a few days from a solution kept at $5^\circ C$. The yield was: 4.15 g (65%) and 4.73 g (71%), respectively.

Methods and instrumentation

We used inductively Coupled Plasma spectroscopy (I.C.P.) for the elemental analysis of uranium, antimony, bismuth and tungsten and flamephotometry for sodium. The water content was thermogravimetrically determined, by means of a METTLER-TGA/SDTA 851^e device, with a balance sensibility of 1 mg, using a SOFT:STAR^e Software program. The working parameters are as follows: the working mass, $m_{\text{sample}}=15.1280$ mg for $\text{Na}_{10}[(\text{UO}_2)_2(\text{H}_2\text{O})_4\text{Sb}_2\text{W}_{20}\text{O}_{70}]$ compound and $m_{\text{sample}}=14.8256$ mg for $\text{Na}_{10}[(\text{UO}_2)_2(\text{H}_2\text{O})_4\text{Bi}_2\text{W}_{20}\text{O}_{70}]$ compound (temperature range, $T=20-800$ °C, the heating rate, $dT/dt=10$ °C, the balance sensibility, $S=1$ µg).

The FT-IR spectra were recorded with an Equinox 55 Bruker spectrophotometer on KBr pellets, in the $4000-400$ cm^{-1} range. Raman spectra were recorded on solid powders, at room temperature, with a DILOR OMARS 89 Raman spectrophotometer. Electronic spectra were obtained in aqueous solutions within a range of $\lambda =200-800$ nm using a JASCO 530 spectrophotometer.

The fluorescence emission spectra were obtained using a ABLE & JASCO FP-6500 spectrofluorometer with 150W xenon lamp, solid sample sealed holder, with a PC acquisition system running on Microsoft Windows. The measurements were made by exposing the samples directly in the sealed solid holder, using an excitation degree of 300 nm and 550 nm respectively, at room temperature.

REFERENCES

1. M. T. Pope, A. Müller, "Polyoxometalates. From Platonic Solids to Anti-Retroviral Activity", Kluwer Academic Publishers, Dordrecht, The Netherlands, **1994**, pp.1.
2. B.H. Myasoedov, *Sov. Radiochem.*, **1990**, 32, 361.
3. Gh. Marcu, M. Rusu, A.V. Botar, *Rev. Roum. Chim.*, **1974**, 19, 827.
4. Gh. Marcu, M. Rusu, *Rev. Roum. Chim.*, **1976**, 21, 385.
5. Gh. Marcu, M. Rusu, *Rev. Roum. Chim.*, **1977**, 22, 227.
6. Gh. Marcu, M. Rusu, L. Ochesel, *Rev. Roum. Chim.*, **1977**, 22, 849.
7. M. Rusu, Gh. Marcu, E. Perte, *Rev. Roum. Chim.*, **1978**, 23, 1403.
8. M. Rusu, Gh. Marcu, *Rev. Roum. Chim.*, **1979**, 24, 351.
9. Gh. Marcu, M. Rusu, E. Perțe, *Rev. Roum. Chim.*, **1979**, 24, 159.
10. Gh. Marcu, A. Botar, M. Rusu, *Rev. Roum. Chim.*, **1979**, 24, 1465.
11. M. Rusu, A. Curticăpean, A. V. Botar, *Rev. Roum. Chim.*, **1995**, 41, 687.
12. M. Rusu, D. Rusu, Gh. Marcu, *J. Radioanalyt. Nucl. Chem.*, **1999**, 242, 119.

13. M. Rusu, D. Rusu, C. Roşu, A.R. Tomşa, Gh. Marcu, *J. Radioanalyt. Nucl. Chem.*, **1999**, 242, 467.
14. M. Rusu, *J. Radioanalyt. Nucl. Chem.*, **2000**, 245, 353.
15. M. Rusu, D. Rusu, C. Roşu, C. Crăciun, L. David, A.R. Tomşa, Gh. Marcu, *J. Radioanalyt. Nucl. Chem.*, **2000**, 245/2, 363.
16. R.D. Peacock, T.J.R. Weakley, *J. Chem. Soc. A.*, **1971**, 1836.
17. K.C. Kim, M. T. Pope, *J. Am. Chem. Soc.*, **1999**, 121, 8512.
18. K.C. Kim, M. T. Pope, *J. Chem. Soc. Dalton Trans.*, **2001**, 986.
19. C. Rosu, M. Rusu, C. Ciocan, *Rev. Chim. (Bucuresti)*, **2002**, 53, 57.
20. K. C. Kim, A.J. Gaunt, M. T. Pope, *Journal of Cluster Science*, **2002**, 13, 423.
21. A.J. Gaunt, I. May, R. Copping, I. Bhatt, D. Collison, O.D. Fox, K.T. Holman, M.T. Pope, *J. Chem. Soc. Dalton Trans.*, **2003**, 3009.
22. C. Craciun, D. Rusu, L. Pop-Fanea, M. Hossu, M. Rusu, L. David, *Journal of Radioanal. and Nucl. Chem*, **2005**, 264(3), 589.
23. R. Khoshnavazi, H. Eshtiagh-hossieni, M.H. Alizadeh, M.T. Pope, *Polyhedron*, **2006**, 25, 1921.
24. R. Copping, I. May, D. Collison, C.J. Jones, C.A. Sharrad, M.J. Sarsfield, *Royal Society of Chemistry*, **2006**, 305.
25. R. Tan, X. Wang, F. Chai, Y. Ian, Z. Su, *Inorg. Chem. Commun.*, **2006**, 1331.
26. R. Khoshnavazi, H. Eshtiagh-hossieni, M.H. Alizadeh, M.T. Pope, *Inorg. Chim. Acta*, **2007**, 360, 686.
27. M.H. Alizadeh, M. Mohadeszadeh, *Journal of Clust. Sci.*, **2008**, 19(2), 435.
28. P. Souchay, M. Leray, G. Hervè, *C. R. Acad. Sci. Ser. C*, **1970**, 271, 1337.
29. M. Michelon, P. Souchay, R. Massart, G. Hervè, *C. R. Acad. Sci., Ser. C*, **1971**, 273, 1117.
30. M. Michelon, G. Hervè, *C. R. Acad. Sci., Ser. C*, **1972**, 273, 209.
31. M. Bösing, I. Loose, H. Pohlmann, B. Krebs, *Chem. Eur. J.*, **1997**, 3, 1232.
32. I. Loose, E. Droste, M. Bosing, H. Pohlmann, M.H. Dickman, C. Rosu, M.T. Pope, B. Krebs, *Inorg. Chem.*, **1999**, 38, 2688.
33. M. Pospisil, *J. Thermal Analysis*, **1995**, 44, 133.
34. W. M. Hosny, *Synth. React. Inorg. Met.-Org. Chem.*, **1998**, 28, 1029.
35. F. Rocchiccioli-Deltcheff, M. Fournier, R. Franck, R. Thouvenot, *Inorg. Chem.*, **1983**, 22, 46.
36. G. M. Varga, E. Papaconstantinou, M.T. Pope, *Inorg. Chem.*, **1970**, 9, 662.
37. H. So, M.T. Pope, *Inorg. Chem.*, **1972**, 11, 1441.
38. S. Amayri, T. Arnold, T. Reich, H. Foerstendorf, G. Geipel, G. Bernhard and A. Massanek, *Environ. Sci. Technol.*, **2004**, 38, 6032.
39. C. Jacopin, M. Sawicki, G. Plancque, D. Doizi, F. Taran, E. Ansoborlo, B. Amekraz C. Moulin, *Inorg. Chem.* **2003**, 42, 5015.
40. X. Kong, Y. Ren, L. Long, R. Huang, L. Zheng, *Inorg. Chem. Comm.*, **2007**, 894.

Dedicated to the memory of Prof. dr. Ioan Silaghi-Dumitrescu marking 60 years from his birth

THE THERMODYNAMICS AND KINETICS OF SATURATED HYDROCARBON SEPARATION ON A DB-1 COLUMN

LÉNÁRD-ISTVÁN CSEPEI^a, CSABA BOLLA^b

ABSTRACT. Results concerning the thermodynamics and kinetics of separation of some saturated hydrocarbons on a DB-1 non-polar capillary chromatographic column are presented. The effect of temperature on the retention time at constant carrier gas flow was studied in order to determine the adsorption enthalpy and adsorption entropy of the compounds on the poly-dimethyl-siloxane stationary phase. The dependence of the height equivalent to theoretical plate on the carrier gas linear velocities at constant temperature was also determined in order to have access to the optimal linear velocity, the longitudinal diffusion (B) and resistance to mass transfer (C) coefficients. These terms can be determined from the Golay equation. The linearization of the Golay equation is also presented.

Keywords: *gas chromatography, DB-1 capillary column, hydrocarbon isomer separation, adsorption enthalpy, adsorption entropy, Golay equation, longitudinal diffusion coefficient, resistance to mass transfer coefficient.*

INTRODUCTION

The efficiency of the gas chromatographic separation depends on many variables. These variables can be divided in two groups: design- and operational parameters. The design parameters are given by the construction of the chromatographic setup and include the following: the length, the diameter and the polarity of the chromatographic column, the stationary phase film thickness and the carrier gas viscosity. For the separation of a multi-component mixture using a chromatographic system with given design parameters one can vary the operational parameters, i.e the temperature of the column and the carrier gas flow rate. Both can be ramped with a desired rate [1-4].

^a *Fritz Haber Institute der Max Planck Gesellschaft, Faradayweg 4-6, 14195 Berlin, Deutschland, cslenard@gmail.com*

^b *Universitatea Babeș-Bolyai, Facultatea de Chimie și Inginerie Chimică, Str. Kogălniceanu Nr. 1, RO-400084 Cluj-Napoca, Romania, csbolla@chem.ubbcluj.ro*

The separation of mixtures containing a few components can be made relatively easily by careful and consistent-with-reason variation of the operational parameters. However for the separation of a complex mixture the trial-and-error method might be very time consuming. Numerous examples of difficult-to-separate mixtures can be listed from various fields of chemistry:

- food control and research (separation of carbohydrates, fats, chiral flavor and aroma compounds) [5]
- pharmaceutical and toxicological analysis (screening for drugs and their metabolites in human blood) [6]
- forensic chemistry, analysis of controlled substances (drug profiling, the separation of derivatized amphetamines, opiates from impurities, adulterants and diluents) [7]
- environmental analysis (separation of polychlorinated biphenyls, heterocyclic amines, nitro-polyaromatic hydrocarbon isomers, tetra- and pentachloro-dibenzo-p-dioxin isomers, nitrogen and phosphorous containing pesticides [8], separation of PAHs and PCBs) [9]
- heterogeneous catalysis research (separation of alkane isomers formed in isomerisation/hydroisomerisation and catalytic cracking reactions [10-12], separation of alkane from olefin and water formed in oxidative dehydrogenation and partial oxidation reactions, separation of various partial oxidation products from different substrates) [13].

However a critical reader can identify a few shortcomings in some of the above mentioned literature. In most of the cases the authors report only the retention times, or the chromatogram is shown. The resolution is given very rarely. In several cases it is evident from the chromatograms that the peaks are partly overlapped [9-11]. The use of such a method for quantitative determinations lacks analytical rigor, especially when the authors claim the validation of a new chromatographic method for analytical purposes. It also can be noted that in most of the cases there is no description about the way how the chromatographic method was developed. Seemingly the temperature ramps, holding times and the carrier gas flow rate are set empirically/arbitrarily. In general, the optimization of the chromatographic method with respect to resolution and analysis time is seldom reported. In the following we present through three examples in more detail the above mentioned deficiencies.

Kim and Vane claimed the successful development of a chromatographic method for the simultaneous separation and identification of a mixture containing 40 PAH and PCB compounds [9]. The temperature program and carrier gas flow rate was given. The resolution was given only for the benzo[b]fluoranthene and benzo[k]fluoranthene peak-pair. These were found to be "80% resolved by 2 seconds". However this is confusing, because the unit of the resolution is not percentage and seconds, but it is a dimensionless number. Some other peaks were characterized only qualitatively by shape and width. No comparison was given between the combined method developed by the authors and the existing method for the individual determination of PAHs and PCBs.

Claude et al. studied the hydro-isomerisation of n-C₁₀-n-C₂₄ alkanes [10]. The products were analyzed by on-line gas-chromatography. The temperature program was the following: 10 °C for 5 minutes than a ramp of 5 °C/min to 120 °C followed by the second ramp of 2 °C/min to 200 °C and finally the third ramp of 0,1 °C/min up to 205 °C. The mono- and multi-branched products eluted in two groups. Although the resolution is not given for the peak-pairs, from the chromatogram one can see that there are partly or totally overlapped peaks. The analysis time was 115-120 minutes, but apparently nothing elutes from the columns before 80 minutes. This means that only about 32% of the chromatogram contains information. The choice of the temperature program is strange because in gas chromatography the use of sub-ambient starting temperature is uncustomary for two reasons. The first reason is that after the completion of a measurement, the GC oven needs to be cooled down from 205 °C to 10 °C for the starting another analysis. The cooling is time consuming; therefore the sampling rate is lower than 1 injection/120 minutes. Moreover at that low starting temperature the long chain alkanes are condensing in the column inlet and possibly also in the injector port or valve system and vaporizing when the temperature becomes high enough.

Huybrechts et al. developed a high throughput reactor system for long-chain n-alkane hydroconversion combined with a fast analytical system [11]. They employed a multi-capillary column with poly-dimethylsiloxane stationary phase for the separation of the C₁-C₁₀ products. The N₂ carrier gas flow rate was set to 67 ml/min. The temperature was ramped from 40 to 75 °C by 15 °C/min. The analysis time was only 3,2 minutes instead of 45 minutes for a conventional 50 m long capillary column. However the authors admitted that there were overlapped peaks, like 2,5-dimethyl-octane and 3,5-dimethyl-octane, 3,4-dimethyl-octane and 3-ethyl-4-methyl-heptane, 4-propyl-heptane and 4,5-dimethyl-octane, 4-ethyl-octane and 2,3-dimethyl-octane, 5-methyl-nonane and 4-methyl-nonane, 3-ethyl-octane and 3-methyl-nonane and 2-methyl-nonane, respectively. Because of the insufficient peak resolution the product selectivities are questionable. Apparently no attempt was undertaken to improve the resolution of peaks. Therefore it can be concluded that the analytical accuracy was sacrificed for fast data acquisition.

Whenever there is a need to separate a complex mixture it is recommended to develop and optimize the chromatographic method based on a rational way. For this purpose the knowledge of the thermodynamic and kinetic parameters of the separation is needed [1-4, 14, 15]. Possibly because of their apparent simplicity, computer programs and expert systems are becoming more and more extensively used for the method development. However these are based on a large number of retention time data determined under various conditions. Thus, the method development is possible only for those compounds for which retention data already exists in the databases

and libraries of these programs [4, 16]. Some gas chromatography companies claim that their software enables the user to develop a separation method from a single isothermal run.

The most important thermodynamic quantity of the separation is the adsorption enthalpy (heat of adsorption). This quantity gives information about the interaction between the adsorbent and adsorbate. Based on the strength of interaction the adsorption can be divided into three groups: physical, reversible chemical and irreversible chemical adsorption. The threshold value for the adsorption enthalpy between physical and chemical adsorption is 62,8 kJ/mol (or 15 kcal/mol) [2-4]. The adsorption entropy is connected to the loss of degrees of freedom upon adsorption of the molecules on the surface of the column material. Hence the adsorption entropy has a negative value [4]. From the rate theory one can determine the longitudinal diffusion coefficient and the resistance to mass transfer coefficient.

Besides the fact that all these quantities are indispensable for a rational development of the separation method, they are useful in understanding of the retention mechanism [1-4]. These information could also be explored in the Qualitative Structure Retention Relationship (QSRR) studies, i.e. the knowledge of thermodynamic and kinetic quantities gives a hint of which molecular variable (descriptor) has the greatest effect in the separation. Therefore this approach in QSRR would offer the possibility to reduce the number of variables in a rational way, to those which do have physical meaning in terms of the phenomena implied by the separation. It was already shown that a properly chosen equation involving 2-3 parameters among the physical variables (boiling point, molar refraction, molar volume, van der Waals volume, number of carbon atoms, dipole moment) and topological indices (connectivity index and general index of molecular complexity) gives a good correlation [17].

In this work we proposed to study the separation of some saturated hydrocarbons (n-hexane, 2-methyl-hexane, 3-methyl-hexane, 2,2-dimethyl-butane, 2,2-dimethyl-pentane, methyl-cyclopentane and cyclohexane) on a DB-1 capillary column. In the literature the Kováts retention indices of these compounds are available on DB-1 [18-21] and on various other capillary columns, determined mostly at 60°C. A very good inter-laboratory reproducibility of the retention index on the same column can be observed. Moreover the intra-laboratory reproducibility of the Kováts retention index on three different columns, DB-1, squalene and SE-30 was also shown [21]. However, up to our best knowledge, the thermodynamic and kinetic parameters of the separation of these compounds on the poly-dimethyl-siloxane stationary phase are still missing. Therefore we aimed to determine these quantities. Since some of these hydrocarbons are the products of n-hexane isomerisation reaction, we also proposed to develop a separation method for a mixture of isomers.

RESULTS AND DISCUSSION

For the determination of the adsorption enthalpy and entropy of the analytes, isothermal chromatographic runs were performed in the temperature interval between 60 and 120°C, at 2,0 ml/min constant carrier gas flow rate. The plot of retention time of the compounds at different temperatures is shown in Figure 1. The retention times seem to decrease exponentially with the temperature. The curves do not cross each other; therefore the elution order does not change in the studied temperature interval.

At the first glance it can be seen that the peaks are well resolved in the 60-90°C interval. At higher temperature the difference of retention times of the adjacent peaks becomes closer to each other, suggesting the decrease of the resolution.

The elution order is the following: 2,2-dimethyl-butane; 2-methyl-pentane; 3-methyl-pentane; n-hexane; 2,2-dimethyl-pentane; methyl-cyclopentane; cyclohexane. This is in agreement with the literature. The Kováts retention indices corresponding to the compounds listed according to the elution order are the following: 538,0; 569,7; 584,4; 600; 625,7; 630,4; 664,2 [18-21]. The first four members of this elution order show that the retention time decreases with the branching of the carbon chain.

The retention factor (k) for each compound was calculated from the retention time (t_R) and gas holdup time (t_M), respectively, according to the equation (1). The gas holdup time was determined by measuring the retention time of air, which is neither retained nor separated to oxygen and nitrogen by the DB-1 column. The adjusted retention time ($t'_R = t_R - t_M$) is equal with the time the analyte spends on the stationary phase. Therefore the retention factor is the ratio between the times the analyte spends on the stationary phase and in the mobile phase, respectively.

The separation factor (α) has been calculated for the successively eluting peaks, according to the equation 2 and represented in function of temperature. The lower the separation factor, the more difficult to separate the peaks and vice versa. When two peaks are overlapped (partly or totally co-eluting), the separation factor becomes very close to or equal to 1.

$$k = \frac{t_R - t_M}{t_M} = \frac{t'_R}{t_M} \quad (1)$$

$$\alpha = \frac{k_{i+1}}{k_i} = \frac{t'_{R,i+1}}{t'_{R,i}} \quad (2)$$

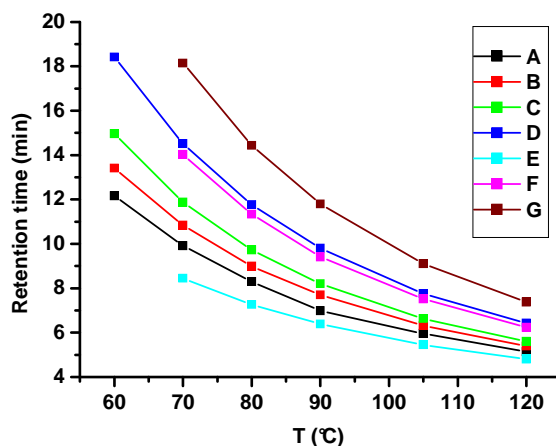


Figure 1. The effect of the temperature on the retention time of the analytes. A: 2-methyl-pentane, B: 3-methyl-pentane, C: n-hexane, D: methyl-cyclopentane, E: 2,2-dimethyl-butane, F: 2,2-dimethyl-pentane, G: cyclohexane.

It can be seen from Figure 2 (a) that the most difficult to separate peak-pair is methyl-cyclopentane and 2,2-dimethyl pentane. Surprisingly, the methyl-cyclopentane and cyclohexane peak-pair is the easiest to separate. The separation of the chain isomers of n-hexane is relatively easy. This separation is the most important from the point of view of n-hexane isomerisation reaction. For kinetic studies the reaction is carried out at low n-hexane conversion. In this case mostly 2-methyl-pentane and 3-methyl-pentane isomers are formed.

The resolution of the adjacent peaks has been calculated (equation 3). A resolution larger than 1,5 means baseline resolution of the adjacent peaks. The shapes of the resolution versus temperature curves are very similar to the retention factor versus temperature curves. Based on these figures it can be seen that an isothermal chromatographic method operating in the temperature interval between 80-105°C is good with respect to the resolution of the peaks and the analysis time. The analysis time in case of an isothermal method at 80°C would be roughly of 15 minutes. However the optimal method among the studied ones is the isothermal run at 105°C. In this case the analysis time is reduced to about 10 minutes. The analysis time might be reduced further by developing a temperature programmed chromatographic method.

$$R_s = \frac{2 \cdot (t_{R,i+1} - t_{R,i})}{w_{i+1} + w_i} = \frac{2 \cdot (t'_{R,i+1} - t'_{R,i})}{w_{i+1} + w_i} \quad (3)$$

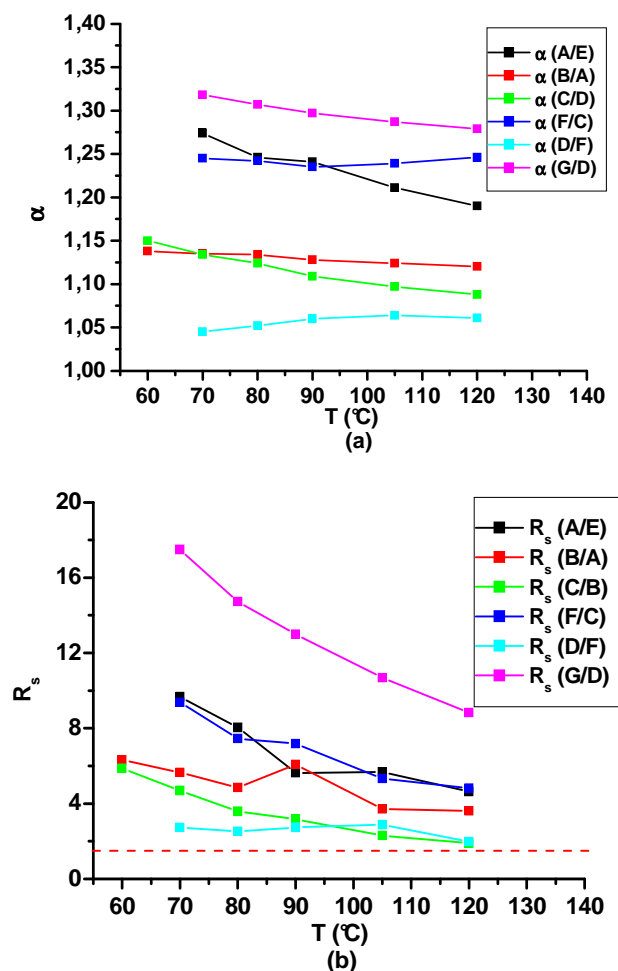


Figure 2. (a) The effect of the temperature on separation factor (α) of the successively eluting analytes. (b) The effect of the temperature on retention factor (R_s) of the successively eluting analytes. The dotted horizontal line at $R_s=1,5$ stands for the limit of baseline separation. The compounds in both figures are: A: 2-methyl-pentane, B: 3-methyl-pentane, C: n-hexane, D: methyl-cyclopentane, E: 2,2-dimethyl-butane, F: 2,2-dimethyl-pentane, G: cyclohexane

The temperature programmed method can be developed experimentally, by trying different heating rates, starting- and end temperatures. The hold times at starting and end temperature can also be varied, but then the parameter space will be very large. Therefore a large number of experiments need to be done.

The other approach in method development is the modeling of the retention times under temperature programmed conditions. This is possible once the adsorption enthalpy and entropy is extracted from the isothermal runs [1-4, 14, 15].

For the determination of the thermodynamic quantities, the specific retention volume (V_g) was calculated (equation 4) at different column temperatures (T).

$$V_g = \frac{F_c \cdot j \cdot (t_R - t_M) \cdot 273}{m_{sp} \cdot T} \quad (4)$$

For the calculation of V_g , the adjusted retention time was determined and normalized with the mass of the stationary phase (m_{sp}). The flow rate of the carrier gas (F_c) should be constant for the measurements at different temperatures (i.e. the GC was operated in constant flow mode). Because the inlet and outlet pressure (p_i and p_o , respectively) is different at different column temperatures, the pressure drop along the column also changes significantly with the variation of the temperature. Therefore the requirement for isothermal and isobaric operation mode is apparently infringed. To overcome this, the retention volume data should be corrected with the James-Martin correction factor (equation 5) [1-4].

$$j = \frac{3}{2} \cdot \frac{\left[\left(\frac{p_i}{p_o} \right)^2 - 1 \right]}{\left[\left(\frac{p_i}{p_o} \right)^3 - 1 \right]} \quad (5)$$

We show here the simplification of the above equation for calculation of the James-Martin correction factor for large difference between the inlet and outlet pressure. When the relative pressure is higher than 6, the 2nd and 3rd power of the relative pressure is so high that the -1 term may be omitted from both the numerator and denominator of the above formula. Then it may be simplified further by canceling the power and the equation 6 will be equivalent with equation 5. The equivalence of these equations with the condition of $p_i/p_o > 6$ is demonstrated by the Figure 3.

$$j = \frac{3}{2} \cdot \left(\frac{p_i}{p_o} \right)^{-1} \quad (6)$$

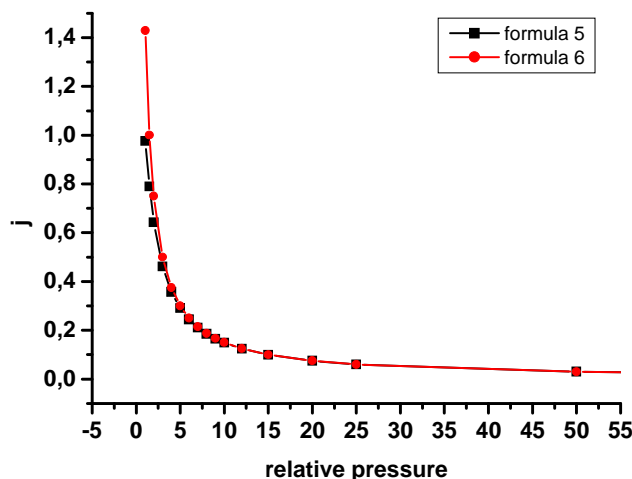


Figure 3. The James-Martin factor at different relative pressures.

Since the chromatographic experiments were done in a GC-MS setup, the end of the column is placed in the chamber of the mass spectrometer, where the pressure (p_0) is in the order of 10^{-8} bar. The inlet pressure (p_i) is slightly higher than the atmospheric pressure. Therefore the relative pressure (p_i/p_0) is in the order of 10^8 . Because the above mentioned condition concerning the relative pressure is fulfilled, we used the simple equation (6) to calculate the James-Martin correction factor.

The logarithm of the specific retention volume was represented in function of the reciprocal temperature (Figure 4). The adsorption enthalpy was calculated from the slope of the straight line; while the adsorption entropy was calculated from the intercept, based on the equation (7) [1-4, 14]. The older literature [1] might be misleading with respect of the adsorption enthalpy. There the adsorption enthalpy is considered to be identical with the evaporation heat of the solute from a solution. However from the energetic point of view the adsorption-desorption equilibrium is not identical with the condensation-evaporation equilibrium.

The adsorption-desorption equilibrium involved by gas chromatography implies only adsorbate-adsorbent interactions at low adsorbate concentration (infinite dilution). In this case it is possible to determine the adsorption enthalpy of the adsorbate (analyte) on the adsorbent (stationary phase).

At higher adsorbate concentration the adsorbate-adsorbate interactions will have a contribution besides the adsorbate-adsorbent interaction. Therefore the apparent enthalpy will be a combination of the adsorption and condensation enthalpy.

$$\ln(V_g) = -\frac{\Delta H_{ads}}{R \cdot T} + \frac{\Delta S_{ads}}{R} \quad (7)$$

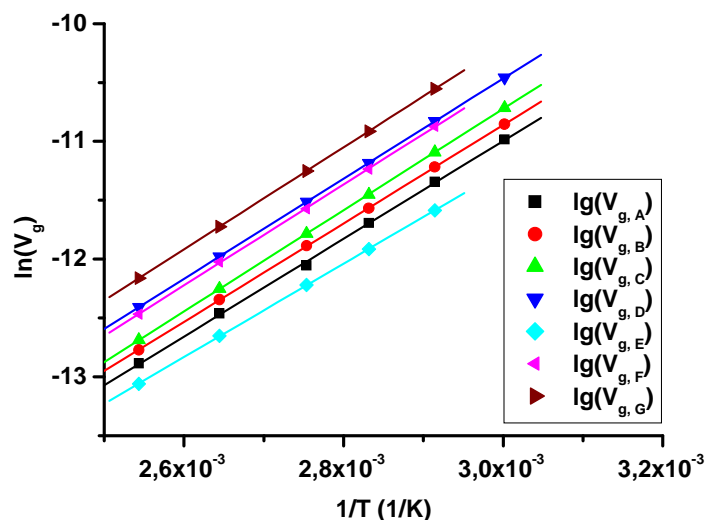


Figure 4. Plot of the logarithm of the specific retention volume (V_g) in function of the reciprocal temperature. A: 2-methyl-pentane, B: 3-methyl-pentane, C: n-hexane, D: methyl-cyclopentane, E: 2,2-dimethyl-butane, F: 2,2-dimethyl-pentane, G: cyclohexane.

In order to show that the thermodynamics of the adsorption and condensation is different, in the Table 1 we compiled the phase change thermodynamic quantities amongst the determined adsorption enthalpy and entropy. For comparison, we also determined the adsorption thermodynamic quantities for polar compounds like water, methanol and acetonitrile.

The magnitude of the adsorption enthalpy indicates physical adsorption of all the studied compounds on the stationary phase. The numerical values of adsorption enthalpy are close to each other regardless of the polarity of the analyte. This is not unexpected since the stationary phase is not polar. It can also be seen that the adsorption enthalpy of all the hydrocarbons are 3 up to 4,5 kJ/mol more negative than the enthalpy of condensation. In case of the water and methanol the case was observed, however for the acetonitrile the adsorption enthalpy and condensation enthalpy are found to be equal within experimental errors.

The adsorption entropy determined from the Figure 3 has a significant negative value. This means that upon adsorption the degrees of freedom of the molecules are significantly reduced. The adsorption entropy of the hydrocarbons is almost the same. Compared to them the adsorption entropy of water, methanol and acetonitrile is more negative.

The condensation entropy is not readily available. However the vaporization entropy can be calculated based on the equation 8 [22]. The data needed for the calculation of the vaporization entropy are available. The enthalpy of vaporization is numerically equal to the absolute value of the condensation enthalpy (equation 9). Therefore the absolute value of the condensation entropy is equal with the vaporization entropy (equation 10). The values are close to 87-89 J/mol·K predicted by the Trouton's rule. However the water and methanol is a well known exception from the Trouton's rule due to hydrogen bonding.

It can be noted that the adsorption entropy is roughly 2,3 times more negative than the condensation entropy of the compounds. This also indicates that the thermodynamic parameters of adsorption and condensation are very different.

$$\Delta S_{vap} = \frac{\Delta H_{vap}}{T_{boil}} \quad (8)$$

$$\Delta H_{vap} = -\Delta H_{con} \quad (9)$$

$$\Delta S_{vap} = -\Delta S_{con} \quad (10)$$

When the average linear velocity of the carrier gas is increased the retention times and peak widths are decreasing and vice versa. For the optimization of the average linear velocity (u), and the determination of the kinetic parameters the Golay equation was used [1-4]. The Golay equation is similar to the van Deemter equation which is applicable in case of the packed columns. However in the capillary columns there is no eddy diffusion, therefore the Golay equation does not contain the first term of the van Deemter equation.

The height equivalent of the plate theory (H) was determined at different carrier gas flow rates. On plot (5) one can see that the minimum of the curves correspond roughly to the optimal average linear velocity of 23 cm/s (or 0,8 ml/min carrier gas flow rate). However, if the resolution at higher carrier gas flow rate is satisfactory as it was shown above, one may apply higher flow rate to shorten the analysis time [3].

Table 1. The thermodynamic parameters of the adsorption of the compounds on polydimethyl-siloxane stationary phase. ΔH_{ads} – adsorption enthalpy, ΔS_{ads} – adsorption entropy, ΔH_{con} – enthalpy of condensation [22, 23], T_{boil} – boiling point at atmospheric pressure [23], ΔS_{con} – the condensation entropy, $\Delta H_{\text{con}} - \Delta H_{\text{ads}}$ – the absolute difference between the enthalpy of condensation and the adsorption enthalpy. A: 2-methyl-pentane, B: 3-methyl-pentane, C: n-hexane, D: methyl-cyclopentane, E: 2,2-dimethyl-butane, F: 2,2-dimethyl-pentane, G: cyclohexane, H: water, I: methanol, J: acetonitrile.

Compound	$-\Delta H_{\text{ads}}$ (kJ/mol)	$-\Delta S_{\text{ads}}$ (J/molK)	$-\Delta H_{\text{con}}$ (kJ/mol)	T_{boil} (K)	$-\Delta S_{\text{con}}$ (J/molK)	$\Delta H_{\text{con}} - \Delta H_{\text{ads}}$ (kJ/mol)
A	34,5±0,4	214,1±2,7	30,0±0,1	334,0±0,1	89,9±0,3	4,5±0,4
B	34,8±0,1	213,7±0,5	30,3±0,1	336,4±0,4	90,1±2,7	4,5±0,9
C	35,8±0,1	215,6±0,3	31,1±0,9	341,9±0,3	91,0±0,3	4,7±0,1
D	36,6±0,8	212,3±0,2	31,7±0,1	345,0±0,2	91,9±0,3	3,7±0,1
E	33,0±0,1	211,6±0,6	27,8±0,1	322,9±0,1	86,1±0,3	5,2±0,1
F	35,6±0,2	213,3±1,3	32,5±0,1	352,3±0,3	92,3±0,3	3,1±0,2
G	36,0±0,1	211,9±0,4	33,0±2,0	353,9±0,2	93,2±5,7	3,0±2,0
H	34,7±0,8	237,2±4,9	40,7	373,2±0,4	109,1	-6,0
I	31,2±1,0	223,9±3,4	37,0±2,0	337,8±0,3	109,5±5,9	-5,8±2,2
J	33,6±0,2	219,2±1,4	33,3±0,3	354,8±0,4	93,9±0,9	0,2±0,4

For the determination of the longitudinal diffusion term (B) and resistance to mass transport term, one can perform a nonlinear fitting procedure according to the Golay equation 11.

$$H = \frac{B}{u} + C \cdot u \quad (11)$$

Here we present the linearization of the Golay-equation. Both sides of the equation 11 were multiplied by the average linear velocity of the carrier gas (u). The resulted equation 12 is still nonlinear, but after performing $H \cdot u = Y$ and $u^2 = X$ variable changes, it can be transformed into the linear equation 13. Then the B and C parameters can be determined according to the conventional linear fitting procedure (Figure 6).

$$H \cdot u = B + C \cdot u^2 \quad (12)$$

$$Y = B + C \cdot X \quad (13)$$

The value of the longitudinal diffusion coefficient (B) is high and the resistance to mass transfer (A) is small. This is a known feature for a GC-MS system, because there is a very large pressure drop along the column [3,4]. The variation of B and C values with the structure of the compounds is difficult to interpret. However the numerical values of the longitudinal diffusion coefficient are statistically close to each other.

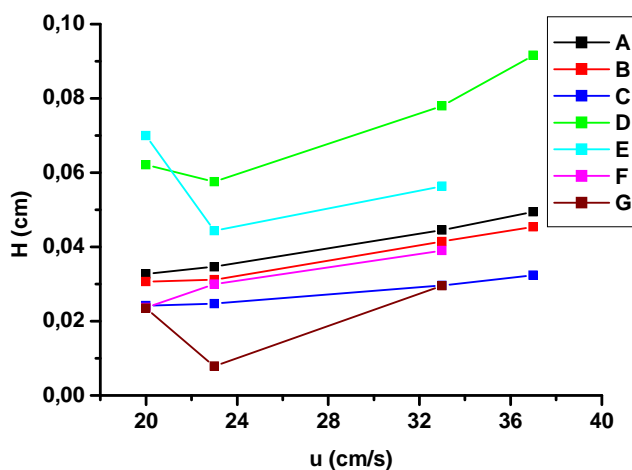


Figure 5. The effect of the carrier gas linear velocity on the height equivalent of the plate theory. A: 2-methyl-pentane, B: 3-methyl-pentane, C: n-hexane, D: methyl-cyclopentane, E: 2,2-dimethyl-butane, F: 2,2-dimethyl-pentane, G: cyclohexane.

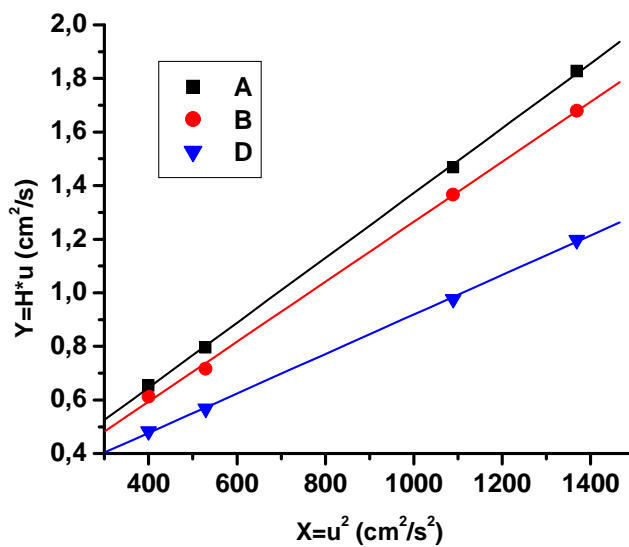


Figure 6. Fitting the linearized Golay equation. 2-methyl-pentane, B: 3-methyl-pentane, D: methyl-cyclopentane, the other compounds were omitted for clarity reasons.

Table 2. The longitudinal diffusion coefficient and resistance to mass transport of the compounds. (a) - because hexane was the solvent, and its peak was not symmetric (tailing) and much broader and compared to the other peaks, the data were omitted from this table.

Compound name	B (cm ² /s)	C (s)
2-methyl-pentane	1,62 ± 0,15	1,21 ± 0,02
3- methyl-pentane	1,46 ± 0,24	1,12 ± 0,03
n-hexane	(a)	(a)
methyl-ciklopentane	1,82 ± 0,11	0,74 ± 0,01
2,2-dimethyl-butane	1,41 ± 0,27	1,15 ± 0,06
2,2-dimethyl-pentane	1,73 ± 0,30	1,02 ± 0,04
ciklohexane	2,26 ± 0,35	0,99 ± 0,06

CONCLUSIONS

Jennings et al. pointed out in the preface of their textbook [3] that although chromatography is a very powerful analytical technique, many researchers are using it only as a means to an end and sometimes the better understanding of the chromatographic principles is lacking. However, due to the fact that it is such a powerful technique, even with little knowledge it is still possible to generate useful data. For the improvement of the data quality and quantity, the scientists who employ chromatography are encouraged for a more comprehensive understanding of their specific separation problem.

In this paper we proposed to follow these recommendations for the rational development of the separation method for some saturated hydrocarbons. In the first approach isothermal chromatographic runs were performed. An optimal chromatographic method was chosen with respect of resolution and analysis time. We also reported the thermodynamic and kinetic parameters of the separation process. These data will be used for the estimation of the retention times under temperature programmed conditions.

EXPERIMENTAL SECTION

The chromatographic measurements were performed on a GC-MS (Agilent 6890 GC coupled with Agilent 5975B MSD) setup. Two solutions have been prepared:

- (a) 2-methyl-pentane and 3-methyl-pentane in n-hexane, and
- (b) 2,2-dimethyl-butane, 2,2-dimethyl-pentane and cyclohexane in n-hexane as solvent. The concentration of all the compounds was approximately 1,0 vol%.

The sampling was performed via an automatic liquid sampler equipped with a 10 μl syringe. A volume of 1,0 μl solution has been injected in the liner heated up to 150°C. The split ratio was set to 1:15 for all the measurements. Helium was used for the split-flow.

DB-1 type non-polar column chromatographic column was used, which is suitable for general separation purposes. The length of the column was 60 m, the diameter was 320 μm , the thickness of the stationary phase was 5,0 μm . The stationary phase consists of 100% poly-dimethyl-siloxane. The characteristics of this stationary phase are the following: dispersion index=9, dipole index=0, acid-base index=0 [3]. Helium was used as carrier gas.

The first series of measurements consisted of isothermal runs at 60, 70, 80, 90, 105 and 120°C, and at constant carrier gas flow rate of 2,0 ml/min, respectively. In the second experiment series the carrier gas flow rate was set to 2,0; 1,6; 0,8 and 0,6 ml/min, respectively, while the column temperature was kept constant at 60°C. The average linear velocity of the carrier gas corresponding to the above flow rates were 37, 33, 23 and 20 cm/s, respectively. The variation of average linear velocities in a wider interval was not possible because of technical reasons. Flow rates lower than 0,6 ml/min could not be achieved because the pressure at the inlet of the column would be below the threshold level of 0,1 bar. However the upper limit of carrier gas flow rate of 2,0 ml/min was determined by the pumping capacity of the turbo-molecular pump of the MS detector.

REFERENCES

1. J. Tranchant, Principles and retention values, Isothermal-isobaric chromatography in J. Tranchant (ed.), Practical Manual of Gas Chromatography, Elsevier Publishing Company, Amsterdam, **1969**, 1.
2. H. Purnell, Gas Chromatography, Wiley, New York, **1962**, 75.
3. W. Jennings, E. Mittelfehldt, P. Stremple, Analytical Gas Chromatography, Academic Press, **1997**, 114.
4. R. L. Grob, E. F. Barry, Modern Practice of Gas Chromatography, Wiley, New York, **2004**, 615.
5. O. Fröhlich, G. Takeoka, K. H. Engel, Analysis of Food Ingredients, Chapter II. 73-171, in R. Wittkowsky, R. Matisek (eds.), Technomic Publishing Company Inc., **1990**, ISBN 1-56676-006-2.
6. M. E. Sharp, *J. Anal. Toxicol*, **1987**, 11, 8.
7. M. D. Cole, The Analysis of Controlled Substances, Wiley, **2003**, ISBN 0-471-49252-1, 1.

8. T. Shibamoto (ed.), *Chromatographic Analysis of Environmental and Food Toxicants*, Marcel Dekker Inc., **1998**, ISBN 0-8247-0145-3, 1-93, 169.
9. A. Kim, Ch. Vane, *Simultaneous Determination of PAHs and PCBs by GCMS Analysis*, British Geological Survey, BGS Laboratory Technique Development, Internal Report IR/07/045, **2007**, free access under: <http://nora.nerc.ac.uk/7569/1/IR07045.pdf>
10. M. C. Claude, J. A. Martens, *J. Catal.*, **2000**, *190*, 39.
11. W. Huybrechts, J. Mijoin, P. A. Jacobs, J. A. Martens, *Appl. Catal. A: General*, **2003**, *243*, 1.
12. R. C. Striebich, *Fast Gas Chromatography* in J. Cazes (ed.) *Encyclopedia of Chromatography*, Marcel Dekker Inc., DOI 10.1081/E-Echr120004560, **2002**.
13. E. Yu. Yakovleva, O. V. Skrypnik, *J. Anal. Chem.*, **2008**, *63*, 5, 455.
14. R. P. W. Scott, *Programmed Temperature Gas Chromatography*, J. Cazes (ed.) *Encyclopedia of Chromatography*, Marcel Dekker Inc., DOI 10.1081/E-Echr120004560, **2002**.
15. V. Bartu, S. Wicar, *Anal. Chim. Acta*, **1983**, *150*, 245.
16. A. Braithwaite, F. J. Smith, *Chromatographic Methods*, 5th Edition, Kluwer Academic Publishers, **1999**, 417.
17. K. Héberger, *Anal. Chim. Acta*, **1989**, *223*, 161, and references therein.
18. E. Kováts, *Helv. Chim. Acta*, **1958**, *41*, 1915.
19. J. Krupčík, I. Skačáni, E. Benická, Pat Sandra, *Collect. Czech. Chem. Commun.*, **1994**, *59*, 2390.
20. A. J. Lubeck, D. L. Sutton, *J. Hi. Res. Chromatogr. and Chromatogr. Comm.*, **1983**, *6*, 328.
21. D. Estrel, M. Mohnke, F. Biermans, H. Rotzsche, *J. Hi. Resol. Chromatogr.*, **1995**, *18*, 403.
22. P. Atkins, J. de Paula, *Atkins' Physical Chemistry*, Oxford University Press, 8th Ed., **2006**, 87.
23. www.nist.webbook.org/chemistry

Dedicated to the memory of Prof. dr. Ioan Silaghi-Dumitrescu marking 60 years from his birth

THE STUDY OF POLYPHENOLS FROM *TRIFOLIUM PRATENSE* L. AND *MEDICAGO SATIVA* L. HYDROALCOHOLIC EXTRACTS BY HPLC-UV-MS

NELI-KINGA OLAH^a, DANIELA HANGANU^b,
LAURIAN VLASE^c, CODRUTA COBZAC^d

ABSTRACT. The polyphenols are widespread compounds from plants having important pharmacological activities. *Trifolium pratense* L. and *Medicago sativa* L. are important cultivated medicinal plants mostly for their content in polyphenols and especially in isoflavons that are also polyphenolic compounds. The identification and quantitative determination of polyphenols from *Trifolium pratense* and *Medicago sativa* hydroalcoholic extracts was performed by a rapid HPLC-UV-MS methods by that can be identified a wide range of polyphenols. There were evaluated the native hydroalcoholic extracts and also the hydrolyzed extracts. There were found in *Trifolium pratense* hyperoside, isoquercitrine – glycosides having as aglykon quercetol, p-coumaric, ferulic, genistic and chlorogenic. In *Medicago sativa* were identified apigenine, p-coumaric, ferulic and genistic acids.

Keywords: *Trifolium pratense*, *Medicago sativa*, polyphenols, HPLC-UV-MS

INTRODUCTION

The polyphenols are important active compounds that are present in many plants. The flavonoids, including isoflavons, the polyphenyl carboxylic acids, the tannins, the coumarins take part from polyphenols family.

The polyphenols has important pharmacological properties, one of them being the antioxidant activity. They are important for maintain the health and also as therapeutic compounds in different diseases [1,2].

^a "Vasile Goldis" West University of Arad, Faculty of Pharmacy, Department of Pharmaceutical Industry, 1 Feleacului Street, 300041, Romania and SC PlantExtrakt SRL, 407059 Radaia, Jud. Cluj, Romania, olahdr@aol.com

^b "Iuliu Hațieganu" University of Medicine and Pharmacy, Faculty of Pharmacy, Department of Pharmacognosy, Cluj-Napoca, 15 I. Creangă Street, Romania, handa_1964@yahoo.com

^c "Iuliu Hațieganu" University of Medicine and Pharmacy, Faculty of Pharmacy, Department of Pharmaceutical Technology and Biopharmaceutics, Cluj-Napoca, 15 I. Creangă Street, Romania

^d "Babes-Bolyai" University, Faculty of Chemistry and Chemical Engineering, Department of Analytical Chemistry, Arany Janos str. 11, Cluj-Napoca, Romania

Trifolium pratense is a cultivated plant being known for its content in isoflavons as daidzein, genistein and formononetin, but contains also other polyphenols as flavonoids, coumarins and also other compounds like essential oil, cyanogenetic glycosides, etc. [2,3,4,5,6].

Medicago sativa is also a cultivated plant. It contains saponins, carotenoids, and polyphenols including isoflavons like genistein, daidzein and cumestans [2,3,7,8].

The total polyphenols can be evaluated by spectrophotometric methods using Folin-Ciocalteu [9] or Arnow [10] reagent. The individual polyphenols can be identified and quantitatively determined just by chromatographic methods: TLC [11] and more exactly by HPLC coupled with UV-Vis spectrophotometric detector and mass-spectrometric detector [5,6,12,13,14,15,16,17].

This paper present the evaluation of polyphenolic profile from *Trifolium pratense* and *Medicago sativa* hydroalcoholic extracts using a HPLC-UV-MS method that provides the possibility of identification of a wide range of polyphenols.

RESULTS AND DISCUSSION

The table 1 presents the retention times found for 16 polyphenol standards respectively the equations for calibration curves obtained for each of 16 standards. In figure 1 can be seen the obtained chromatogram for the standards.

Table 1. The retention time and calibration curves equation for polyphenol standards

Peak no.	Name of standard	Retention time, min, $r_t \pm SD$	Calibration curves equation A = peak area, c = concentration
1	Gentisic acid *	2.15+ 0.07	A = -0,335 + 14,261c
3	Chlorogenic acid *	5.62+ 0.05	A = -1,324 + 26,492c
5	p-coumaric acid	8.70+ 0.08	A = -0,326 + 33,230c
6	Ferulic acid	12.20 ± 0.10	A = -1,017 + 39,558c
7	Sinapic acid	14.30 ± 0.10	A = -0,237 + 37,103c
8	Hyperoside	18.60 ± 0.12	A = 0,107 + 19,294c
9	Izoquercitrin	19.60 ± 0.10	A = -0,273 + 12,978c
10	Rutoside	20.20 ± 0.15	A = 0,227 + 13,473c
11	Myricetin	20.70 ± 0.06	A = 0,270 + 26,150c
12	Fisetin	22.60 ± 0.15	A = 0,292 + 17,190c
13	Quercitrin	23.00 ± 0.13	A = 0,048 + 10,698c
14	Quercetol	26.80 ± 0.15	A = -1,152 + 36,327c
15	Patuletine	28.70 ± 0.12	A = -0,430 + 31,450c
16	Luteolin	29.10 ± 0.19	A = -0,761 + 28,927c
17	Kaempferol	31.60 ± 0.17	A = -1,271 + 30,152c
18	Apigenin	33.10 ± 0.15	A = -0,909 + 20,403c

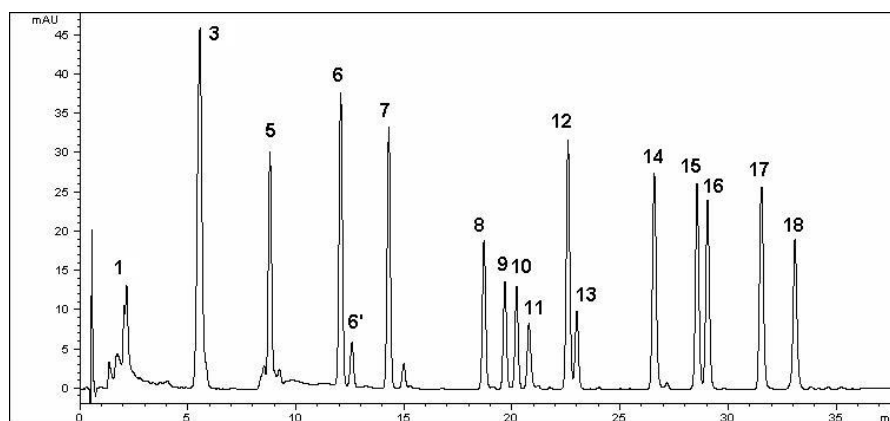


Figure 1. The chromatogram of polyphenol standards

In figures 2 and 3 can be seen the HPLC-UV chromatograms for the native hydroalcoholic and hydrolyzed *Trifolium pratense* extract. It can be identify in native extract the hyperoside and isoquercitrin from flavonoids group respectively in small amount, the free p-coumaric and ferulic acids. The identification of flavonoids was made based on comparison of retention time and MS spectra with those of the studied standards. These compounds can be also quantified by HPLC-UV. The small amount from p-coumaric and ferulic acids were identified based on them MS spectra. Because of small amount these compounds can not be exactly quantified by HPLC-UV.

The hyperoside and isoquercitrin free during the hydrolysis quercetol, they aglykon. These could be demonstrated by HPLC-UV-MS evaluation of hydrolyzed extract in that there were identified quercetin, p-coumaric, ferulic, chlorogenic and genistic acids. The higher amounts from p-coumaric and ferulic acids respectively the presence of other acids that can not be identified in the native extract, can be explained by the hydrolysis of the compounds in that they are naturally bounded. The quercetol, p-coumaric and ferulic acids were identified based on the comparison of retention times and MS spectra with those of the studied standards.

The chromatogram of native *Trifolium pratense* hydroalcoholic extract shows a main peak X at 21-22 minute that can not be identified as being one of the studied standards. The evaluation of MS spectra (figures 4 and 5) show that this compound has the molecular weight 448 (= 447 + 1 – the signal is for deprotonated molecule) and has a main fragment with molecular weight 286 (= 284 + 1 + 1 – the signal is for deprotonated fragment having a radical to a phenol position). The kaempferol and luteolin, both being flavonoid aglykons, has the molecular weight 286. This indicates that the unidentified can be glycosides of kaempferol or luteolin.

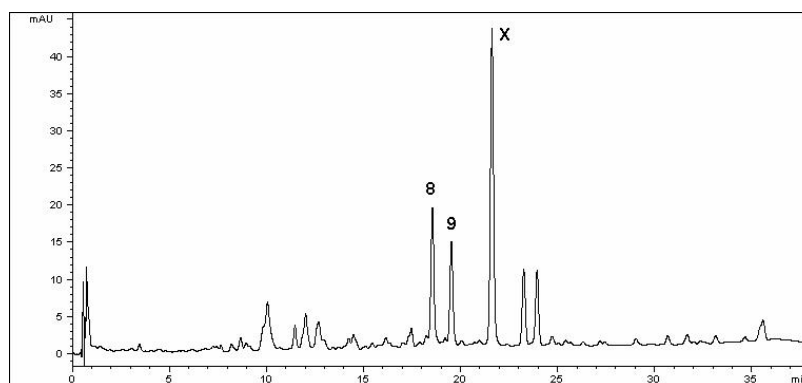


Figure 2. The chromatogram of native *Trifolium pratense* hydroalcoholic extracts

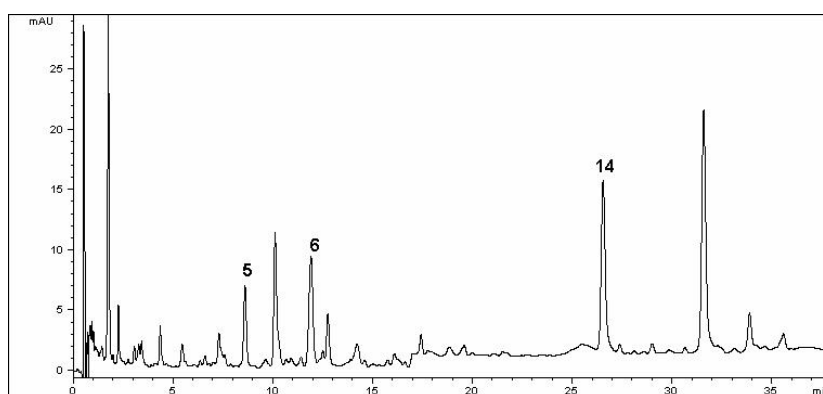


Figure 3. The chromatogram of hydrolyzed *Trifolium pratense* hydroalcoholic extracts

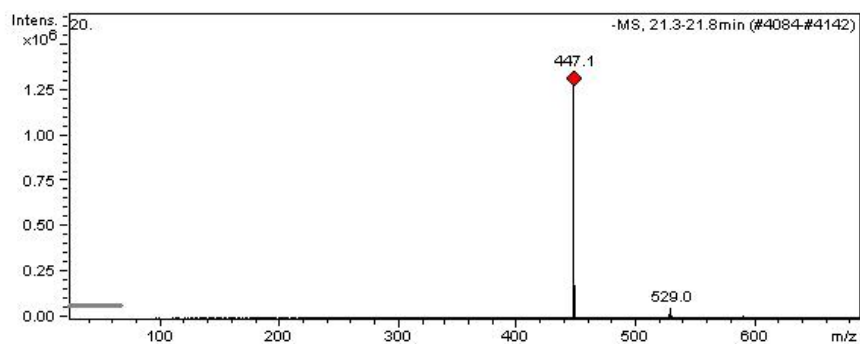


Figure 4. The MS spectra for compound X with molecular signal

In figures 6 and 7 can be observed the HPLC-UV chromatograms for native respectively hydrolyzed *Medicago sativa* hydroalcoholic extract. It can be identify in native extract the apigenin based on comparison of retention time and MS spectra with those of standard apigenin respectively the p-coumaric acid based on MS spectra. This result shows that the apigenin can be found in *Medicago sativa* also as free aglykon, in significant amount to be quantified. The p-coumaric acid is present in small amount as free acid in native extract.

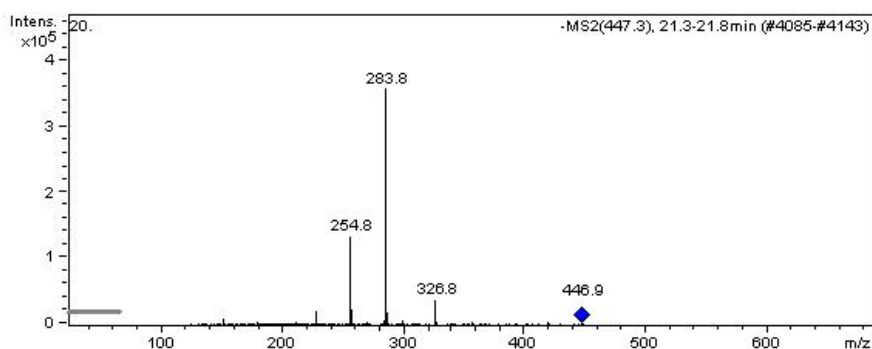


Figure 5. The MS spectra for compound X with fragmentation

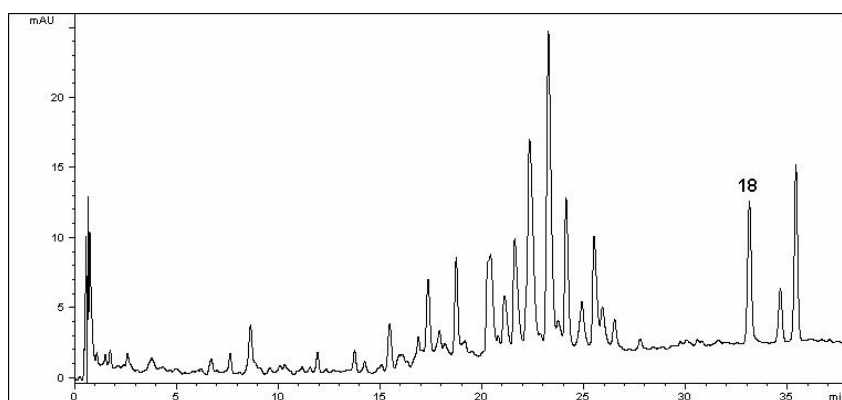


Figure 6. The chromatogram of native *Medicago sativa* hydroalcoholic extracts

The chromatograms show also a lot of significant compounds separated at 15-27 minute that can not be identified as being one of the studied standard compounds. After hydrolysis the chromatogram shows a lower level for apigenin and the unidentified compounds from 15-27 minutes. That indicated that also the unidentified compounds can be flavonoids, probably C-glycosides. The

lower level of these compounds and of apigenin can be explained by the degradation of some flavonoidic compounds like apigenin in the hydrolysis condition.

In the hydrolyzed extract can be identified based on retention time and MS spectra in comparison with those of standards the following polyphenols: apigenin, ferulic and p-coumaric acids respectively based just on MS spectra the genistic acid. These results show that the polyphenolic acids are present in *Medicago sativa* mostly in bounded form. The apigenin, p-coumaric and ferulic acids can be quantified.

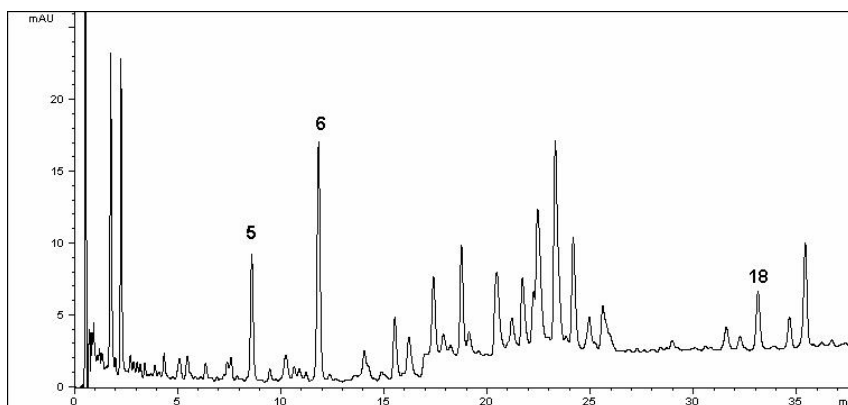


Figure 7. The chromatogram of hydrolyzed *Medicago sativa* hydroalcoholic extracts

In table 2 can be observed the retention times and MS spectra data of identified compounds that can be compared with those of the standards.

In table 3 are presented the results of quantitative determination on the identified compounds. It can be seen that the *Trifolium pratense* extract contains mostly flavonoids – hyperoside and isoquercitrin and smaller amount of bounded acids: p-coumaric acid and ferulic acid. The *Medicago sativa* extract contains apigenin in higher amount and in smaller amount bounded p-coumaric acid and ferulic acid.

The quercetol identified in this paper in the *Trifolium pratense* extract was found also by Booth in different commercial *Trifolium pratense* products. The result of quantitative determination for quercetol (5,581 $\mu\text{g/ml}$ extract meaning 1,86 % reported to the dry plant) shows a higher value that found by Booth (1 %). Booth identified in *Trifolium pratense* also the kaempferol (0,07 %) and fisetin (0,02 %), in small amounts [4]. The kaempferol glycoside can not be certainly identified in the studied Romanian *Trifolium pratense*, neither the kaempferol in the hydrolyzed sample.

Table 2. The retention time and MS spectra data for identified compounds

Name of sample	Name of identified compound	Retention time, min, r_t	MS spectra data for identified compounds / standards
<i>Trifolium pratense</i> native extract	Hyperoside	18,6	463> 254.9, 270.9, 300.7 463> 254.9, 270.9, 300.7
	Isoquercetin	19,6	463> 254.9, 270.9, 300.7, 342.8 463> 254.9, 270.9, 300.7, 342.8
	p-coumaric acid	8,7	163> 118.7 163> 118.7
	Ferulic acid	12,2	193.2> 133.7, 148.7, 177.6 193.2> 133.7, 148.7, 177.6
<i>Trifolium pratense</i> hydrolyzed extract	Quercetol	26,8	301> 150.6, 178.6, 272.7 301> 150.6, 178.6, 272.7
	p-coumaric acid	8,7	163> 118.7 163> 118.7
	Ferulic acid	12,2	193.2> 133.7, 148.7, 177.6 193.2> 133.7, 148.7, 177.6
	Chlorogenic acid	5,62	353.5>178.7, 190.7 353.5>178.7, 190.7
	Genistic acid	2,15	153>108.7 153>108.7
<i>Medicago sativa</i> native extract	Apigenin	33,1	269.2>148.6, 150.6, 224.7, 226.7 269.2>148.6, 150.6, 224.7, 226.7
	p-coumaric acid	8,7	163> 118.7 163> 118.7
<i>Medicago sativa</i> hydrolyzed extract	Apigenin	33,1	269.2>148.6, 150.6, 224.7, 226.7 269.2>148.6, 150.6, 224.7, 226.7
	p-coumaric acid	8,7	163> 118.7 163> 118.7
	Ferulic acid	12,2	193.2> 133.7, 148.7, 177.6 193.2> 133.7, 148.7, 177.6
	Genistic acid	2,15	153>108.7 153>108.7

Table 3. The results of quantitative determination of identified compounds

Sample	Compound	Concentration, μ g/ml
<i>Trifolium pratense</i> native extract	Hyperoside	9,766
	Isoquercetin	11,206
<i>Trifolium pratense</i> hydrolyzed extract	Quercetol	5,581
	p-coumaric acid	1,900
	Ferulic acid	3,074
<i>Medicago sativa</i> native extract	Apigenin	11,206
<i>Medicago sativa</i> hydrolyzed extract	Apigenin	2,667
	p-coumaric acid	2,387
	Ferulic acid	4,424

The apigenin identified and quantified in the *Medicago sativa* extract was found in this plant by Stochmal also [8].

The results presented in this paper show that near isoflavons both plants contain also other flavonoids and polyphenolic acids. The polyphenolic acids (p-coumaric, genistic, chlorogenic and ferulic acids) from *Trifolium pratense* and *Medicago sativa* were studied in detail for first time in this paper.

CONCLUSIONS

Using the proposed HPLC method it can be separated a wide range of polyphenols from complex samples as the plant extracts. Using UV and MS detection can be identify also the compounds in small amounts due by the high sensitivity and more precise data that can be obtain with the MS detector.

In the studied plant extracts can be identified the main flavonoidic compounds and polyphenolic acids, both in free and bounded forms. Those existing in significant amounts could be also quantified by HPLC-UV. The present study confirm the presence of some flavonoids in both plants, compounds identified also by other researchers, but the detailed qualitative and quantitative study of polyphenolic acids in these plants is made for first time in this paper.

The identification and quantification of polyphenols from *Trifolium pratense* and *Medicago sativa* extracts is important for the study of therapeutically active compounds from these plants.

EXPERIMENTAL SECTION

There were used the aerial part of fresh plant from *Trifolium pratense* and *Medicago sativa*, both harvested from organic culture near Cluj, in 2008. The plants were botanical identified to PlantExtrakt, Radaia.

The hydroalcoholic extracts were obtained from fresh plant (70% moisture) using 90 % vol. ethanol (pharmaceutical grade) by cold maceration at room temperature, in 10 days. After 10 days of maceration by repetitive mixing the extracts were decanted and the plant residue was pressed. The extracts obtained from decantation and pressing were mixed and filtered. The fresh plant-extract ratio was 1:1 for both extracts.

The hydrolysis of extracts was made using 2N hydrochloric acid (Merck, Germany), 1 ml to 1 ml extract. The hydrolysis was performed at boiling temperature in 40 minutes.

There were used HPLC grade methanol (Merck, Germany) and analytical grade acetic acid (Merck, Germany) to perform the HPLC analysis. As standards were used genistic acid, chlorogenic acid, p-coumaric acid, ferulic acid, sinapic acid, hyperoside, isoquercitrin, rutoside, myricetin, fisetin, quercitrin, quercetol, patuletine, luteolin, kaempferol and apigenin purchased from Merck, Fluka, Sigma or LGC.

The experiment was carried out using an Agilent 1100 HPLC Series system (Agilent, USA) equipped with degasser, binary gradient pump, column thermostat, autosampler and UV detector. The HPLC system was coupled with an Agilent 1100 mass spectrometer (LC/MSD Ion Trap VL). For separation purpose, a reverse-phase analytical column was employed (Zorbax SB-C18 100 x 3.0 mm i.d., 3.5 μm particle); the working temperature was 48 °C. The detection of the compounds was performed on both UV and MS mode. The UV detector was set at 330 nm until 17.5 min, then at 370 nm. The MS system operated using an electrospray ion source in negative mode. The chromatographic data were processed using ChemStation and DataAnalysis software from Agilent, USA.

The mobile phase was a binary gradient prepared from methanol and solution of acetic acid 0.1% (v/v). The elution started with a linear gradient, beginning with 5% methanol and ending at 42% methanol, for 35 minutes; isocratic elution followed for the next 3 minutes with 42% methanol. The flow rate was 1 ml min⁻¹ and the injection volume was 5 μl .

The MS signal was used only for qualitative analysis based on specific mass spectra of each compound. The MS spectra obtained from a standard solution of compounds were integrated in a mass spectra library. Later, the MS traces/spectra of the analysed samples were compared to spectra from library, which allows positive identification of compounds, based on spectral match. The UV trace was used for quantification of identified compounds from MS detection. Using the chromatographic conditions described above, the polyphenols eluted in less than 35 minutes. The acids were identified by MRM mode and the other polyphenols by AUTO MS mode. The detection limits were calculated as minimal concentration producing a reproducible peak with a signal-to-noise ratio greater than three. Quantitative determinations were performed using an external standard method. Calibration curves in the 0.5–50 $\mu\text{g ml}^{-1}$ range with good linearity ($R^2 > 0.999$) for a five point plot were used to determine the concentration of polyphenols in plant samples.

REFERENCES

1. R. Hansel, O. Sticher, "Pharmakognosie. Phytopharmazie", Springer Verlag, Berlin-Heidelberg-New York, **2004**, 735.
2. I. Ciulei, E. Grigorescu, U. Stanescu, „Plante medicinale. Fitochimie si fitoterapie“, Ed. Medicala, Bucuresti, **1993**, 729, 677.
3. D. Heber, „PDR for Herbal Medicines“, 3rd edition, Thomson, USA, 679, 11.
4. N.L. Booth et al., *Journal of Complementary Medicine*, **2006**, 12 (2), 133.

5. J. Polasek, E.F. Queiroz, K. Hostettmann, *Phytochem Anal.*, **2007**, *18*(1), 13.
6. Q. Wu, M. Wang, J.E. Simon, *J Chromatogr A.*, **2003**, *1016*(2), 195.
7. R.M. Feingold, *Archive of Intern Medicine*, **1990**, *159* (13), 338.
8. A. Stochmal, S. Piacente, C. Pizza, F. De Riccardis, R. Leitz, W. Oleszek, *J. Agric. Food Chem.*, **2001**, *49* (2), 753.
9. *** Farmacopeea Romana, ed. X, Editura Medicala, Bucuresti, **1993**.
10. *** Farmacopeea Romana, ed. IX, Editura Medicala, Bucuresti, **1976**.
11. H. Wagner, S. Bladt, "Plant Drug Analysis", Springer Verlag, Berlin-Heidelberg, **1996**.
12. S. Leucuta, L. Vlase, S. Gocan, L. Radu, C. Fodorea, *Journal of Liquid Chromatography & Related Technologies*, **2005**, *28* (19), 3109.
13. L. Bucur, L. Vlase, C. Fodorea, V. Istudor, *Revista de Chimie*, **2006**, *57* (2), 189.
14. C.A. Dehelean, L. Vlase, C. Peev, D. Antal, C. Soica, *Revista de chimie*, **2006**, *57* (8), 826.
15. G. Crisan, B. Kiss, L. Vlase, G. Balica, M. Tamas, *Chemistry of Natural Compounds*, **2009**, *45*(6), 885.
16. M.J. Simirgiotis, G. Schmeda-Hirschmann, *J Chromatogr A.*, **2010**, *1217*(4), 443.
17. P. Dugo, P. Donato, F. Cacciola, M.P. Germanò, A. Rapisarda, L. Mondello, *J. Sep. Sci.*, **2009**, *32*(21), 3627.

Dedicated to the memory of Prof. dr. Ioan Silaghi-Dumitrescu marking 60 years from his birth

KINETIC STUDIES OF SORPTION OF COPPER(II) IONS ONTO DIFFERENT CALCIUM-HYDROXYAPATITE MATERIALS

ERZSÉBET-SÁRA BOGYA*, IOAN BÂLDEA, RÉKA BARABÁS,
ALEXANDRA CSAVDÁRI, GRAZIELLA TURDEAN,
VALENTINA-ROXANA DEJEU

ABSTRACT. A study on the removal of copper ions from aqueous solutions by synthetic hydroxyapatite and structurally modified apatite has been carried on under batch conditions. The influence of different sorption parameters, such as heat treatment of the material, particle size, initial metal ion concentration and temperature has been studied and discussed. Maximum adsorption capacity and efficiency were determined. The results showed that the removal efficiency of Cu(II) by hydroxyapatite containing silica (HAP-Si) could reach 99.7%, when the initial Cu(II) concentration was 5 mM. The mechanism of the sorption process was studied, by employing pseudo-first, pseudo-second-order kinetic models and intraparticle diffusion model. Activation energy for hydroxyapatite and 10%_{wf} silica doped hydroxyapatite was obtained, considering pseudo-second-order kinetics model.

Keywords: *hydroxyapatite, modified hydroxyapatite, copper removal, kinetics, diffusion, activation energy*

INTRODUCTION

Hydroxyapatite (HAP) is a mineral, from the group of apatites, having the chemical formula $\text{Ca}_{10}(\text{PO}_4)_6(\text{OH})_2$. Among the different calcium phosphates, hydroxyapatite is the most important bioceramic used in dentistry and orthopedic surgery [1-3]. One way to enhance the bioactive behavior of hydroxyapatite is to obtain substituted apatite, which resemble the chemical composition and structure of the mineral phase in bones. These ionic substitutions can affect the surface structure and charge of hydroxyapatite, which could have an influence on the material in biological environment. In this sense, an interesting way to improve the bioactivity of hydroxyapatite is the addition of silicon to the apatite structure, taking into account the influence

* Babeș-Bolyai University, Faculty of Chemistry and Chemical Engineering, 11 Arany János Str., RO-400084 Cluj-Napoca, Romania, bogyaes@ubbcluj.ro

of this element on the bioactivity of bioactive glasses and glass-ceramics [4,5]. In addition, several studies have revealed the considerable importance of silicon on bone formation and growth under *in vitro* and *in vivo* conditions [6].

Apatite can be used for remediation of soil and water from industrial and nuclear wastes due to their ability to retain a variety of ionic species, especially actinides and heavy metals [7,8]. The mechanisms of the metal cations retention are different and include: ion exchange, adsorption, dissolution/precipitation, and formation of surface complexes [9].

The sorption of pollutants from aqueous solution plays an important role in wastewater treatment because it avoids the process of sludge elimination. Well-designed sorption processes have good efficiency and high quality of effluent after treatment. Sorption material can also be recycled. It is therefore understandable that the study of sorption kinetics in wastewater treatment is interesting as it provides insights into the reaction pathways and into the mechanism of sorption reactions. In addition, the kinetics allows the evaluation of the solute uptake rate which in turn controls the residence time of sorbate uptake at the solid–solution interface. Therefore, it is important to predict the rate at which pollutant is removed from aqueous solutions in order to design appropriate sorption treatment plants. To control the sorption kinetics, knowledge of the rate law describing the sorption system is required. The rate law is determined experimentally.

This paper aims to study the sorption of copper(II) ions onto structurally modified apatite, comparing it to normal hydroxyapatite, and establishing the best kinetic model and mechanism.

RESULTS AND DISCUSSION

As described by Sposito (1986) [10], sorption is the loss of a chemical species from an aqueous solution to a contiguous solid phase. Two of the principle mechanisms of sorption include adsorption, the two-dimensional accumulation of matter at the mineral-water interface; and precipitation, the three-dimensional growth of a solid phase. The study of the nature of copper sorption onto apatites represents the aim of this paper.

As mentioned in the experimental section, copper(II) sorption measurements were carried out with five types of material of two different particle sizes ($> 90 \mu\text{m}$ and $< 45 \mu\text{m}$) and with calcined and non-calcined samples for each material at four different copper concentrations (10^{-4} M, 5×10^{-4} M, 10^{-3} M, 5×10^{-3} M).

For all non-calcined materials at the 10^{-3} M copper concentration, the sorption capacity was almost identical, meaning that the η (efficiency) was around 99.7 %, the difference between them consisting in the saturation time. For the calcined samples, the efficiency was about 60-70 % [11, 12].

The sorption efficiency is defined as $\eta = (c_0 - c_i) / c_0$; c_0 being the initial copper concentration, c_i the actual copper concentration at a specific time, and the sorption capacity given as $q_t = c_{ads} / m$; c_{ads} being the adsorbed amount of copper at a specific time in moles, and m the quantity of the material on which it was adsorbed in grams. The effect of the initial concentration of copper ions was also studied. Its efficiency was calculated for each material at four copper nitrate concentrations as presented in the legend of figure 1 ($c_1 = 5 \text{ mM}$, $c_2 = 1 \text{ mM}$, $c_3 = 0.5 \text{ mM}$ and $c_4 = 0.1 \text{ mM}$).

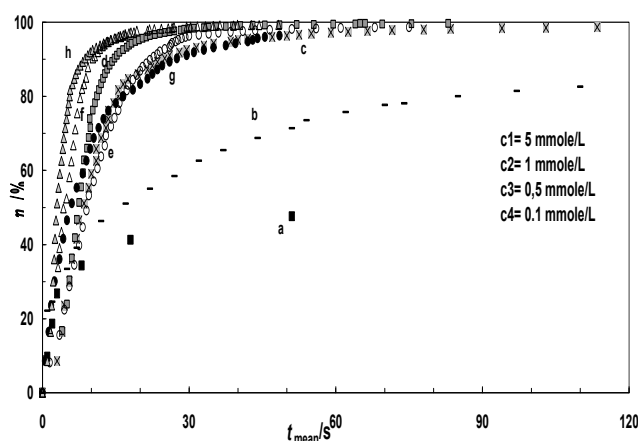


Figure 1. Sorption efficiency for different concentrations and materials as a function of time. of: nCHAP < 45 μm , c_1 (a); nCHAP-Si 10%_{wt} Si < 45 μm , c_1 (b); nCHAP < 45 μm , c_2 (c); nCHAP-Si 10%_{wt} Si < 45 μm , c_2 (d); nCHAP < 45 μm , c_3 (e); nCHAP-Si 10%_{wt} Si < 45 μm , c_3 (f); nCHAP < 45 μm , c_4 (g); nCHAP-Si 10%_{wt} Si < 45 μm , c_4 (h).

At the concentration of 5 mM the copper ions sorption efficiency for nCHAP was about 60%, comparable to HAP-Si with 10%_{wt} silica that reaches the efficiency of above 99.6 %, and has the sorption capacity of 20.54 mg/g. CHAP does not sorbs copper ions at such high concentrations and HAP-Si 10%_{wt} Si retains the amount of 50 %. At concentrations lower than 5 mM, sorption takes place at the 99.8 % efficiency for non-calcined materials, and also for calcined materials at concentrations equal or lower than 0.1 mM.

These results show that, for a rapid and complete sorption, the most suitable material is non-calcined silica hydroxyapatite with 10%_{wt} of silica [11, 12].

The increase of temperature enhances the copper sorption for all the studied materials. At higher temperature the end time of the sorption for nCHAP-Si 10%_{wt} silica >45 μm and 10^{-3} mol/L copper(II) concentration decreases below one minute.

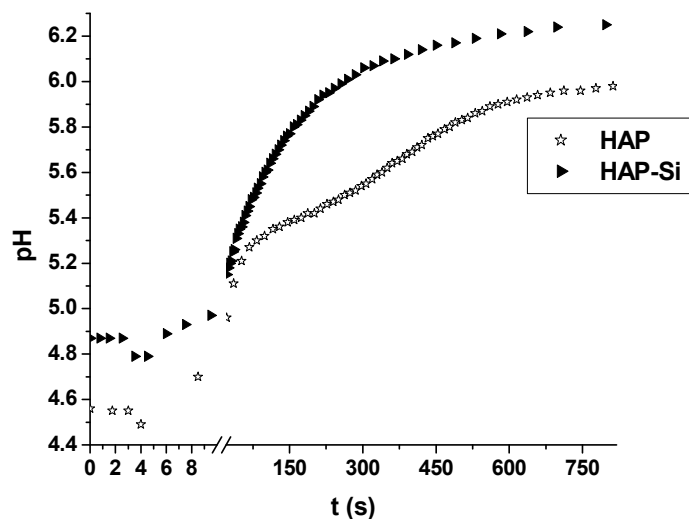


Figure 2. pH variation during the reaction of ncHAP and ncHAP-Si 10%_{wt} $\Phi > 90 \mu\text{m}$ with copper ions ($[\text{Cu}^{2+}] = 10^{-3} \text{ mol/L}$)

Table 1. Initial and final pH in the case of copper nitrate reaction with apatites at 10^{-3} mol/L copper (II) concentration and $T = 293 \text{ K}$

Material	pH _i	pH _f
ncHAP $>90 \mu\text{m}$	5.16	5.75
ncHAP $<45 \mu\text{m}$	5.25	6.08
ncHAP-Si 5% _{wt} Si $>90 \mu\text{m}$	5.2	6.08
ncHAP-Si 5% _{wt} Si $<45 \mu\text{m}$	5.08	6.11
ncHAP-Si 5% _{wt} Si $>90 \mu\text{m}$	5.12	6.46
ncHAP-Si 5% _{wt} Si $<45 \mu\text{m}$	5.11	6.41
ncHAP-Si 10% _{wt} Si $>90 \mu\text{m}$	5.19	6.75
ncHAP-Si 10% _{wt} Si $<45 \mu\text{m}$	5.31	6.52
ncHAP-Si 15% _{wt} Si $>90 \mu\text{m}$	5.11	5.91
ncHAP-Si 15% _{wt} Si $<45 \mu\text{m}$	5.1	5.89

The pH of solution modifies between 4.7 and 6.2 (see figure 2), for $10^{-3} \text{ M Cu}^{2+}$ concentration. Within the initial period of the process, it can be noticed a slight decrease of the pH in the case of materials with higher granulometry. This phenomenon can be caused by ionic exchange between the copper and protons on the superficial $-\text{OH}$ sites. Later increase of pH values is due to the dissolution of the material in the acidic media and base hydrolysis. Table 1 compares the initial and final pH values for all the materials. The highest variation was observed at ncHAP-Si 10%_{wt} Si.

The release of calcium ions during copper(II) sorption was registered with a calcium selective electrode. It was observed that within a very short period calcium concentration increases due to the dissolution of the hydroxyapatite and then decreased significantly. After this initial stage, the calcium release is much slower than the copper sorption and therefore hydrogen ions should be released to maintain the balance of charge. This leads to the conclusion that copper-calcium ion exchange does not control the Cu^{2+} sorption.

Kinetic studies

In order to determine the rate constants, the two mostly used kinetic models in sorption processes, namely pseudo-first and pseudo-second order model, have been checked with our experimental data. Generally, the reaction rate is defined as the change of reactants or products per unit of time. In the case of first-order kinetics the reaction rate is represented as $r = k_1 c_A$, or in terms of sorption efficiency

$$\frac{d\eta}{dt} = k_1(1 - \eta) \quad (1.)$$

where, k_1 is the first order rate coefficient (s^{-1}), c_A stands for the actual concentration of the reactant (mol/L), η the efficiency and t the time (s). The linear form, obtained by integration is

$$-\ln(1 - \eta) = k_1 t \quad (2.)$$

The data were treated based on the supposition that the process can be described by two consecutive first order steps. According to literature [13], the first step represents a rapid complexation on the specific sites of the HAP surface. The second step is attributed either to ion diffusion into the HA structure or to formation of hydroxyapatite containing this heavy metal instead of calcium. Based on this supposition equation (2.) has been plotted with the data for all the non-calcined materials (see figure 3). The slope of the linear part of the curve gives the first order rate constants for the two consecutive steps. The rate constant values and the regression coefficients are presented in table 2. The rate coefficients have higher values for the first step and at lower particle size. The higher calcium concentration of nHAP-Si 5%_{wt} Si as compared to nHAP-Si 5%_{wt} Si does not influence positively the reaction rate. It indicates that the ionic exchange is not the rate determining step. The highest values of the apparent rate constants were calculated for nHAP-Si 10%_{wt} $\Phi < 45 \mu\text{m}$, that is in concordance with the fastest reaction time.

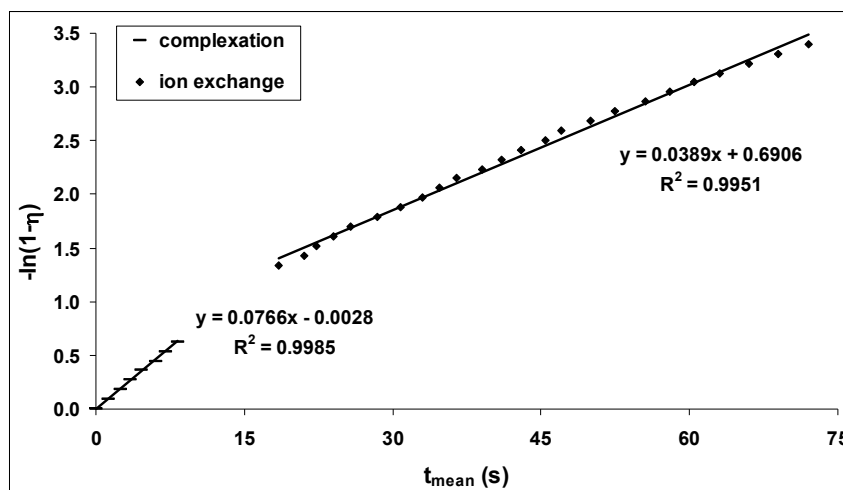


Figure 3. First order kinetics representation for nHAP-Si 10 %wt Si Φ , 45 μm $[\text{Cu}^{2+}] = 1 \text{ mM}$. T=279 K

The pseudo-second order rate model, based on sorbent capacity [14], can be expressed as a differential equation:

$$\frac{dq_t}{dt} = k_2(q_e - q_t)^2 \quad (3.)$$

By integrating this within the same boundary conditions and rearranged, the following linear form is obtained:

$$\frac{1}{q_t} = \frac{1}{k_2 q_e^2} + \frac{1}{q_e} t \quad (4)$$

Here q_t and q_e is amount of solute sorbed on the surface at a time t and at the equilibrium state. A plot of t/q_t versus t should give a straight line with a slope of $1/q_e$ and the intercept of $1/k_2 q_e^2$ (see figure 4). Furthermore, the initial sorption rate h (mmol/g s), when $t \rightarrow 0$, can also be calculated as follows: $h = k_2 q_e^2$ [15,16]. The experimental points lay on the unique straight line over a large period of time. As it can be seen in table 2 the amount of copper ions at equilibrium (mmol/g) is approximately constant for all the materials at the same initial copper (II) concentration. The correlation coefficients for the linear plots for the pseudo-second order rate law are better (>0.995) as compared to the values obtained with the first-order model. This suggests that the system does not obey first-order kinetics, but a pseudo-second order one. According Y. S. Ho and G. McKay [16] in systems described by pseudo-second order model the rate-limiting step may involve some strong interaction (valence forces) between sorbate species and active sites of adsorbent. This model provides the best correlation of the data.

Table 2. Comparison between experimental and calculated amounts of Cu(II) sorbed at equilibrium (q_e), sorption rate constants (k_1 , k_1' and k_2) and corresponding regression coefficients (R^2), for pseudo-first and pseudo-second order kinetic models, at 293 K and $[Cu^{2+}] = 10^{-3}$ M

pseudo-first order								pseudo second order					
$\Phi > 90 \mu m$				$\Phi < 45 \mu m$				$\Phi > 90 \mu m$			$\Phi < 45 \mu m$		
k_1	R^2	k_1'	R^2	k_1	R^2	k_1'	R^2	k_2	q_e	R^2	k_2	q_e	R^2
ncHAP													
0.051	0.997	0.011	0.996	0.118	0.987	0.06	0.995	0.249	0.21	1	1.634	0.206	1
ncHAP-Si 5%_{wt} Si													
0.021	0.996	0.008	0.998	0.097	0.97	0.086	0.994	0.065	0.234	0.999	1.236	0.210	0.999
ncHAP-Si 5%+_{wt} Si													
0.015	0.991	0.008	0.993	0.095	0.978	0.079	0.999	0.069	0.226	0.997	0.819	0.215	0.997
ncHAP-Si 10%_{wt} Si													
0.069	0.99	0.024	0.995	0.071	0.94	0.096	0.985	0.470	0.213	1	1.425	0.218	0.995
ncHAP-Si 15%_{wt} Si													
0.067	0.988	0.007	0.999	0.124	0.991	0.051	0.99	0.219	0.208	1	1.529	0.206	1

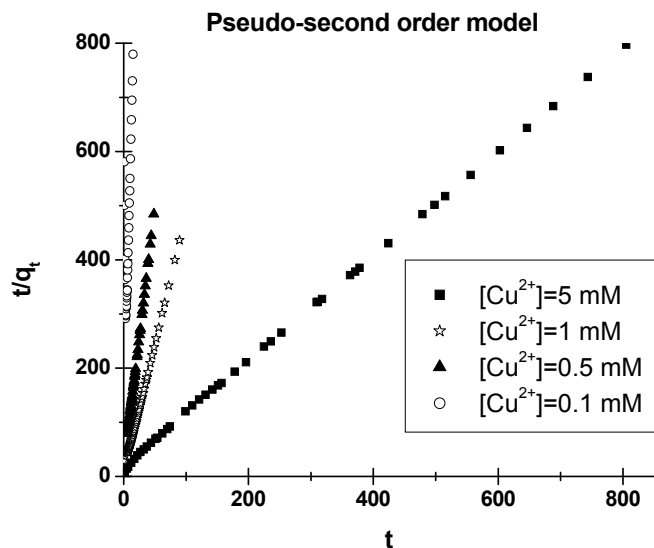


Figure 4. Pseudo-second order rate model for ncHAP-Si 10%_{wt} <45 μm at different initial copper ion concentrations

By using the values of the second order rate constants determined at different temperatures (279, 293, 303, 313, 323 K), the experimental Arrhenius activation energy were obtained for two different concentration and material. The activation energy values are summarized in **Table 3**.

Table 3. Activation energy calculate by Arrhenius type linearization based on pseudo second order rate coefficient values for ncHAP and ncHAP-Si 10%_{wt} Si

Material	Φ (μm)	10 ⁻³		5 10 ⁻⁴	
		Ea (kJ/mol)	R ²	Ea (kJ/mol)	R ²
ncHAP	>90	35.82	0.972	30.57	0.986
	<45	20.33	0.981	57.46	0.987
ncHAP-Si 10% _{wt} Si	>90	34.73	0.961	42.51	0.993
	<45	42.44	0.985	52.75	0.995

Their values are increased at higher granulometry and concentration, with the exception of ncHAP Φ>90 μm. The activation energies ranges within 20-60 kJ/mol, which indicates that the sorption of copper in not governed only by ion exchange mechanism. Based on literature data, energies between 8–16 kJ/mol are characteristic for the ion-exchange mechanisms [17].

Intraparticle diffusion

The mechanism of sorption is either film diffusion controlled or particle diffusion controlled. Before adsorption takes place, several diffusion processes known to affect the adsorption process takes place. The sorbate, will have to diffuse trough the bulk of the solution to the film surrounding the adsorbent and then into the micro pores and macro/ pores of the adsorbent. The first one is bulk diffusion resistance which of course is reduced if there is enough agitation to reduce the concentration gradient. The second is external mass transfer resistance and the third is intraparticle mass transfer resistance. When this last one is the rate limiting step, than sorption mechanism is controlled by intraparticle diffusion.

The model developed by Mackay and Poots [18] can be used to establish the mechanism of sorption.

$$q_t = K_{id} \cdot t^{1/2} + I \quad (5)$$

Where, q_t is the amount of copper ions sorbs at time t . The slope of the linear part of the curve (i.e., q_t Vs $t^{0.5}$) gives the initial rate of the sorption, controlled by intraparticle diffusion K_{id} (mg/g s^{0.5}). The extrapolation of the

straight lines to the time axis gives intercepts I , which are proportional to the boundary layer thickness. The kinetic constants and R^2 values for the intraparticle diffusion model are shown on **Table 4**.

The values of the regression coefficients (R^2) indicate that the model fits the experimental data quite well up to 55-70 % of the process, confirming the intraparticle diffusion in the sorption process. The boundary layer thickness is insignificant. Thus, the boundary layer acts as a viscous drag to the sorption [18].

Table 4. Kinetic constants and regression coefficients (R^2) for Mackay and Poots intraparticle diffusion equation and the efficiency value representative for the linear part of the curve for copper ion sorption on apatites

Material	K_{id}	I	R^2	η (%)
ncHAP $\Phi > 90 \mu\text{m}$	10^{-4}	$3 \cdot 10^{-5}$	0.968	71
ncHAP-Si 5% _{wt} Si $\Phi > 90 \mu\text{m}$	$6 \cdot 10^{-5}$	$4 \cdot 10^{-5}$	0.986	78
ncHAP-Si 10% _{wt} Si $\Phi > 90 \mu\text{m}$	$2 \cdot 10^{-4}$	$2 \cdot 10^{-5}$	0.982	68
ncHAP-Si 15% _{wt} Si $\Phi > 90 \mu\text{m}$	10^{-4}	10^{-4}	0.924	56

CONCLUSIONS

Hydroxyapatite modified with silica was synthesized by addition of sodium silicate to the reaction mixture. These materials were used in copper sorption experiments. The retaining capacity is influenced by calcination, silica content, particle size, initial copper concentration and temperature. Calcined materials show weak metal sorption properties and the silica containing materials have better sorption efficiency than unmodified hydroxyapatite. The 10%_{wt} silica containing hydroxyapatite has the highest copper sorption efficiency. The pseudo-second order model, exhibiting the highest regression coefficients, describes better the sorption of copper onto all the materials. This model agrees with the assumption that the rate-limiting step is chemical sorption or chemisorption involving valence forces between sorbent and sorbate. The activation energies calculated with the pseudo-second order model, in the range of 20-60 kJ/mol also indicate the involvement of chemical interactions. Intraparticle diffusion, irrespective of its mechanism, also plays an important role in this sorption process.

EXPERIMENTAL SECTION

Hydroxyapatite was prepared by the precipitation method described previously [11, 12], under continuous mechanical stirring. The used materials were: 0.5 mol/L solution of calcium nitrate, 0.3 mol/L solution of diammonium phosphate and 25 % ammonia solution (Merck, Germany). The diammonium

phosphate and the ammonium solution were slowly added to the calcium nitrate solution. The reaction mixture pH was adjusted with ammonia to maintain in the range of 9 and 9.5, and the reaction temperature was kept at 20 °C by means of a FALC FA-90 thermostat. The reaction mixture was stirred by FALC mechanical stirrer for 20 hours. For the structurally modified hydroxyapatite, sodium silicate together with the diammonium phosphate and ammonia solution was added to the preparation mixture.

The reaction pH was also adjusted to a value between 9 and 9.5, the temperature was 20 °C and the reaction time was 8 h. Four types of silica-hydroxyapatite (HAP-Si) were prepared: with 5 %, 5 %+, 10 % and 15 mass % of silica. The HAP-Si with 5 %+ of silica content contained by 10 mass % more calcium compared to the other materials. After the reaction was accomplished, the precipitate was washed and filtered. The filtered material was dried for 24 hours at 105 °C. Thermal treatment of the samples was carried out at 1000 °C for one hour, in a Barnstead 47900 furnace.

The characteristics of the materials were established by Infra Red spectroscopy, scanning electron microscopy (SEM), X-ray and BET measurement. The results were presented previously [11, 12].

The prepared materials were employed in kinetic studies of Cu (II) ion retention. Copper nitrate solution was used, in the concentration range between 10^{-4} mol/L and $5 \cdot 10^{-3}$ mol/L. A copper selective electrode (Tacussel PCU 2M) previously calibrated and a reference saturated K^+/KNO_3 electrode were used to monitor copper (II) concentration. A Digitronic DXP-2040 potentiometer was employed. The experiments were carried out in a double walled reactor, connected to a FALC FA-90 thermostat under continuous magnetic stirring, provided by a FALC FA-20 magnetic stirrer. Replicate runs were made and each time, values corresponding to the given potential were averaged.

The reagents were of analytical grade and twice-distilled water was used to prepare all solutions and suspensions. In order to reproduce conditions existing during the purification of waste water, no pH adjustment was made during the experiments. However, pH was monitored with a pH selective electrode during the experiments.

0.25 g sample and 50 mL of copper nitrate solution of different concentrations were used for each experiment. The decrease of electrode potential with time was measured and the data were recorded by a computer. The retained copper quantity, sorption efficiency, and capacity of the material were calculated using the Microsoft Excel and Origin 6.0 software. Analytical detection limit for Cu^{2+} was 5 μ mol/L. The increase calcium ion concentration was registered with a calcium selective electrode. The detection limit was established at $5 \cdot 10^{-7}$ mol/L.

REFERENCES

1. L. A. Landin, L. G. Danielsson, C Wattsgard, *Journal of Bone and Joint Surgery Br*, **1987**, 69-B, 234.
2. J. Zhang, M. Maeda, N. Kotobuki, M. Hirose, H. Ohgushi, D. Jiang, M. Iwasa, *Materials Chemistry and Physics*, **2006**, 99, 398.
3. V. P. Orlovskii, V. S. Komlev, S. M. Barinov, *Inorganic Materials*, **2002**, 38, 10, 973.
4. I. R. Gibson, S. M. Best, W. Bonfield, *Journal of Biomedical Materials Research*, **1999**, 44, 422.
5. M. Vallet-Regí, D. Arcos, *Journal of Materials Chemistry*, **2005**, 15, 1509.
6. F. Balas, J. Pérez-Pariente, M. Vallet-Regí, *Journal of Biomedical Materials Research Part A*, **2003**, 66A, 2, 364.
7. W. Zheng, X.-m. Li, Q. Yang, G.-m. Zeng, X.-x. Shen, Y. Zhang, J.-j. Liu, *Journal of Hazardous Materials*, **2007**, 147, 1-2, 534.
8. F. Fernane, M. O. Mecherri, P. Sharrock, M. Hadioui, H. Lounici, M. Fedoroff, *Materials Characterization*, **2008**, 59, 554.
9. S. McGrellis, J.-N. Serafini, J. JeanJean, J.-L. Pastol, M. Fedoroff, *Separation and Purification Technology*, **2001**, 24, 129.
10. S. K. Lower, P. A. Maurice, S. J. Traina, E. H. Carlson, *American Mineralogist*, **1998**, 83, 147.
11. E. S. Bogya, R. Barabás, A. Csavdári, V. Dejeu, I. Baldea, *Chemical Papers*, **2009**, 63, 5, 568.
12. E. S. Bogya, R. Barabás, L. Bizo, V.R. Dejeu, *Proceedings of the 11th ECERS Conference, Polish Ceramic Society, Krakow*, **2009**, 1109-1113, ISBN: 978-83-60958-54-4.
13. A. Corami, S. Mignardi, V. Ferrini, *Journal of Hazardous Materials*, **2007**, 146, 1-2, 164.
14. I. Smiciklas, A. Onjia, S. Raicević, D. Janačković, M. Mitrić, *Journal of Hazardous Materials*, **2008**, 152, 876.
15. M. Fedoroff, G. Lefevre, M. Duc, S. Milonjic, C. Neskovic, *Materials Science Forum*, **2004**, 453-454, 305.
16. Y.S. Ho, G. McKay, *Process Biochemistry*, **1999**, 34, 451.
17. S. S. Dimovic, I. Plecas, M. Mitric, *Water Research*, **2006**, 40, 2267.
18. J. C. Igwe, O. F. Mbonu, A. A. Abia, *Journal of Applied Science*, **2007**, 19, 2840.

Dedicated to the memory of Prof. dr. Ioan Silaghi-Dumitrescu marking 60 years from his birth

THE VALUES OF BIOCHEMICAL INDICATORS IN PEOPLE WHO PRACTICE 'MAINTENANCE' AEROBICS

AURICA CREȚU^a, DENISA-IOANA CREȚU^b

ABSTRACT. Physical effort affects by its stressful character the homeostatic level of the body, resulting in acceleration of biochemical reactions of aerobe and anaerobe nature. This article presents dynamics in the variation of some of the biochemical parameters of the blood in women who practice 'maintenance' aerobics.

Keywords: *effort, biochemical indicators, homeostasis*

INTRODUCTION

Biochemical parameters represent an area of investigation with various implications in terms of health control, quality of life as well as predisposition to certain pathological conditions arising from a labor that exceeds the effort capacity of the body. Studies conducted to date indicate that metabolic changes that occur during intense muscle activity largely depend on biochemical parameters and affect the efficiency of physical effort.

The aim of this study was to demonstrate that variations of certain biochemical indicators such as glucose, triglyceride levels, uric acid, magnesium and serum creatinine depend on the intensity of physical effort and they, in turn, act on the rate of achieving metabolic changes, disturbing the working capacity of the organism. The study of these parameters in women who have not practiced any sports before is of practical and public interest as more and more women turn to aerobics as a way to shape their body. When specific literature studies focus mainly on athletes or on items such as glucose and triglycerides, parameters like uric acid, magnesium and serum creatinine are vaguely raised. Therefore, our research intends to provide a complete, updated picture of the evolution of these five parameters in women aged 20-30 years old who practice aerobics.

^a *Universitatea Babeș-Bolyai, Facultatea de Educație Fizică și Sport, Extensia Bistrița, Str. Andrei Mureșanu Nr. 3-5, RO-420117 Bistrița, Romania, cretuaurica@yahoo.com*

^b *Universitatea de Medicină și Farmacie „Iuliu Hațieganu”, Facultatea de Medicină, Str. Victor Babeș Nr. 8, RO-400012, Cluj-Napoca, denysa_crt@yahoo.com*

RESULTS AND DISCUSSION

The statistical tests applied revealed the results shown in Table 1.

Table 1. P values obtained after applying Student t Test

	January -April	April- July	January- July
Glucose (mg%)	0,05	0,047	0,001
Triglycerides (mg%)	0,08	0,42	0,07
Uric Acid (mg%)	0,17	0,28	0,34
Creatinine (mg%)	0,2	0,07	0,03
Magnesium (mg%)	0,19	0,02	0,07

* $p \leq 0.05$ -significant

** $p \geq 0.05$ -insignificant

Glucose values have significantly diminished in the interval January-April and January- July 2009, as seen in Figure 1. Diminished blood glucose values were significantly lower than the ones presented in the reference range ($p = 0.001$), in a gradual decrease.

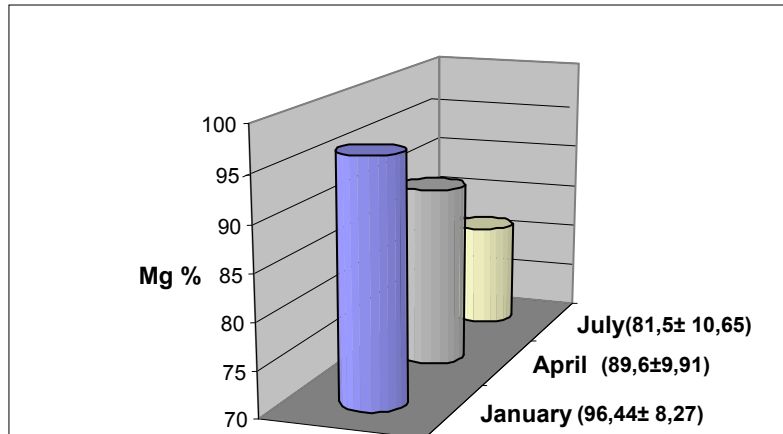


Figure 1. Glucose levels in January-July period (average \pm standard deviation)

In comparison with our study, similar results were obtained, but on obese, sedentary postmenopausal women who completed a 6-month (three times per week) program of aerobics.[1] Use of glucose during exercise and the amount of blood sugar metabolized per unit of insulin plasma as an indicator of insulin sensitivity increases only when weight loss is accompanied by exercise [1].

Although insignificant (statistically) changes were recorded, a decrease of triglycerides values suggests lipid mobilization after moderate physical exertion (Figure 2).

Studies performed on women aged between 30 and 50 after a single 60-minute aerobics session show an increase of free fatty acids during effort [2], as triglycerides stored in the fat tissue can be mobilized and sent in the form of free fatty acids used as an energy source and circulating lipids.

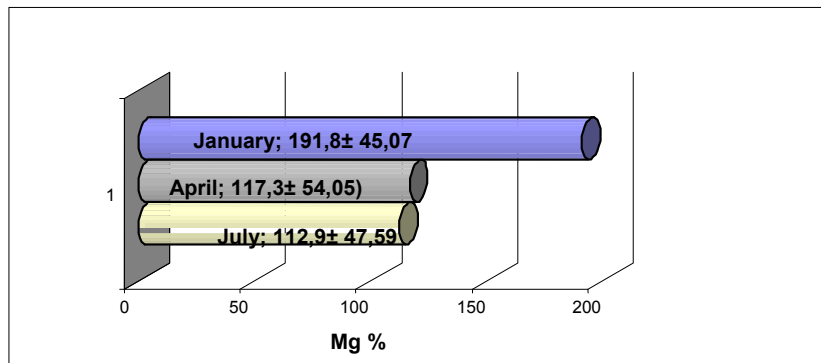


Figure 2. Mean values of triglycerides± standard deviation

Our study indicates that in the long-term effort uric acid presents an increase of the numerical values (Figure 3). Despite the fact that the variations had $p>0,05$, the mathematical increases of this indicator of free purines that were recorded are considered a sign of persistent metabolic fatigue or incomplete biochemical recovery.

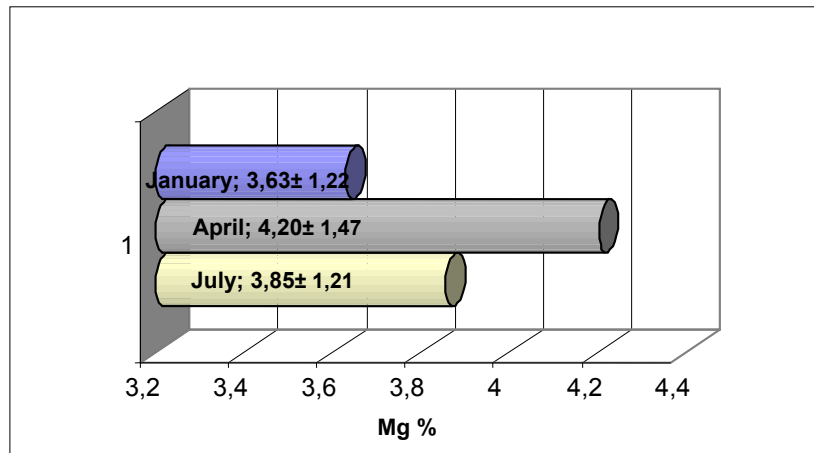


Figure 3. Uric acid-mean value changes (± standard deviation)

Specific literature contains limited knowledge concerning the evolution of uric acid during physical effort. Studies made on animals (horses subjected to a prolonged effort-endurance races) specify that uric acid can be used as a biochemical parameter in determining the metabolic activity during effort [3].

The hypomagnesaemia condition that was obtained in the first part of our study -January-April (although statistically insignificant) can be explained as a redistribution of magnesium in the body to accommodate the metabolic needs of our study participants-that were not prior engaged to any physical activity. However, a statistically significant numerical increase ($p = 0.02$) of magnesium in plasma in the April-July interval (after 6 months of prolonged effort, Figure 4), does not correlate with other findings concerning the conditions in which plasmatic Mg increases after physical exertion.

Magnesium is involved in many functions of the skeletal muscle. Other studies connect the inadequate intake of magnesium (in the form of pills or diet) with a deficiency status in athletes participating in sports requiring weight control. [4]

Specific literature explains hypomagnesaemia as stress caused by physical exercise or as the effect of lipolysis (since fatty acids are mobilized for muscle energy, lipolysis would cause a decrease in plasma Mg) whereas hypermagnesaemia occurs at athletes following short term high intensity exercise as the consequence of a decrease in plasma volume and a shift of cellular magnesium resulting from acidosis [5].

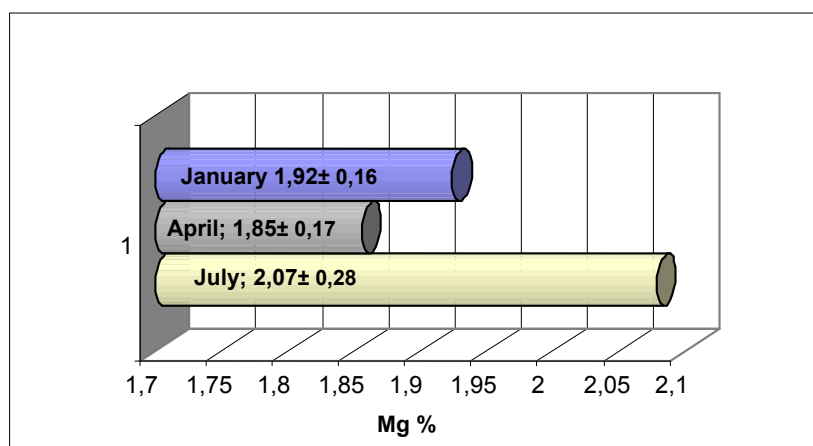


Figure 4. Changes of average values of magnesium (\pm standard deviation).

With regard to serum creatinine, this biochemical parameter increased significantly in July ($p = 0.03$) compared to the reference range-January (Figure 5).

In comparison with our study, other authors use the elevations of serum creatinine as an indicator of exertion-related muscle damage produced in healthy individuals that were subjected to a single session of 50 eccentric exercises.[6]

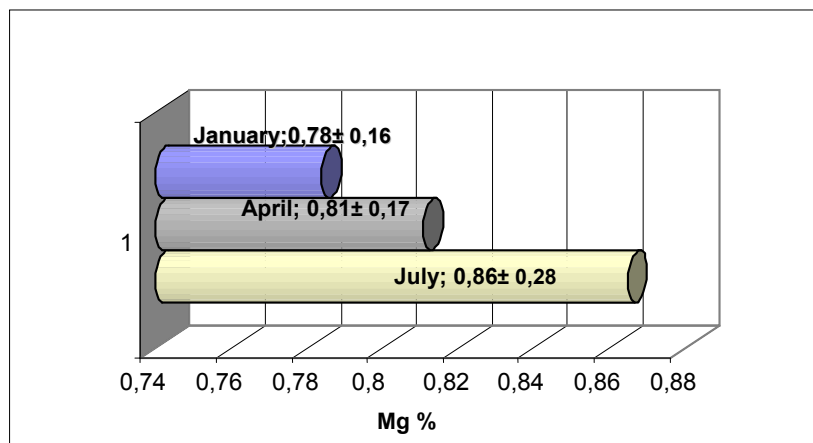


Figure 5. Serum creatinine changes during exercise and post-effort (mean values \pm standard deviation)

CONCLUSIONS

1. The significant decrease of glucose parameters indicates that the physical strain was intense enough to mobilize blood sugar reserves. Furthermore, the fact that the values of this parameter have been progressively decreasing during the experiment point toward the fact that the participants had a balanced diet.

2. A decline of triglycerides levels, although statistically insignificant, reveals that the effects of physical exertion on the body in terms of weight loss facilitates fat mobilization and allows the energy deficit to rely less on a hypocaloric diet. On the other hand, exercises performed at moderate levels of intensity counteract undesirable lipid changes that occur with age.

3. The increase of uric acid and decrease of magnesium during the period January –April is a sign of incomplete metabolic recovery. However, reversing this report in the April-July interval, with the decline of uric acid and an increase of magnesium, point toward a better correlation between the effort capacity and the intensity of physical effort.

4. A continuous numerical increase of serum creatinine levels indicates a sustained muscular effort of the subjects.

5. Our data are gain added relevance compared to other studies from the fact that the determinations are made in three different points (January-April-July), focusing on the evolution on the biochemical parameters in time.

6. This study complements the existing data in literature concerning glucose, triglycerides, and adds new, innovating information on the changes of uric acid, magnesium and serum creatinine with reference to the increasingly segment of the population represented by women who practice aerobic workouts.

7. The practical applicability is more than obvious because progressively more women turn to aerobics as a method of maintenance. Therefore, the need of a personal, customized training program arises, that adjusts to the possibilities and necessities of each person in order to prevent internal imbalances such as our study showed.

EXPERIMENTAL SECTION

Our study refers to a group of 20 female subjects, aged 20-30 years, who have performed workouts with an aerobe character during January-July 2009. The exercises were carried out with a frequency of 3 sessions per week, 60 minutes each session. For the gradual accommodation of the body during exercise, the focus was on the slow adaptation of the subjects through the execution of movements that were destined to the selective influence of the locomotor's apparatus.

The determination of biochemical parameters in the collected blood was carried out at a specialized laboratory.

During the study, changes of the biochemical indicators were monitored in the following ranges:

- Baseline (control data/before the training program began) - January 2009;
- Second determination - after 2 months - beginning of April, 2009;
- Last investigation - July, 2009.

Statistical analysis

Data were analyzed using the Statistical Analysis Toolpak. To calculate batch variations Fisher test was used and for comparing data obtained from investigations T test: Two Sample Assuming Equal Variances and T-Test: Two Sample Assuming Unequal Variances were used. $p < 0.05$ was considered significant. Correlation coefficients were calculated with the help of Correlation function-Data Analysis.

REFERENCES

1. A. S. Ryan, B. J. Nicklas, D. M. Berman, *Obesity (Silver Spring)*, **2006**, 14(6), 1064.
2. M. Charnas, B. H. Opaszowski, R. Charnas, D. Rózańska, E. Jówko, J. Sadowski, L. Dorofeyeva, *J. Strength. Cond. Res.*, **2009**, 23(3), 954.
3. F. Castejón, P. Trigo, A. Muñoz, C. Riber, *Equine Vet. J. Suppl.*, **2006**, (36), 70.
4. F. H. Nielsen, H. C. Lukaski, *Magnes Res.*, **2006**, 19(3), 180.
5. Y. Rayssiguier, C. Y. Guezennec, J. Durlach, *Magnes Res.*, **1990**, 3(2), 93.
6. P. M. Clarkson, A. K. Kearns, P. Rouzier, R. Rubin, P. D. Thompson, *Med. Sci. Sports Exerc.*, **2006**, 38(4), 623.

Dedicated to the memory of Prof. dr. Ioan Silaghi-Dumitrescu marking 60 years from his birth

INTERMOLECULAR INTERACTIONS OF 1- AND 2-BROMOPROPANE WITH SOLVENT MIXTURES STUDIED BY INFRARED SPECTROSCOPY

RODICA GRECU^a, VIRGINIA COMAN^a
AND ONUC COZAR^b

ABSTRACT. The parameters of a vibrational band are sensitive to the environment created by solvents. The effects of the two solvent mixtures cyclohexane/tetrahydrofuran and carbon tetrachloride/acetonitrile on the frequency and half bandwidth of $\nu(\text{C-Br})$ band of 1- and 2-bromopropane are investigated. The first mixture can be considered "ideal" and the frequency and half bandwidth of $\nu(\text{C-Br})$ bands varies linearly on the mole fraction of the polar solvent. In the case of carbon tetrachloride/acetonitrile mixture, a process of "preferential solvation" with the maximum effect at 2 : 1 volume ratio was evidenced.

Keywords: *infrared spectroscopy, 1-bromopropane, 2-bromopropane, intermolecular interactions, solvent mixtures, preferential solvation index Z*

INTRODUCTION

Vibrational spectroscopy provides an effective mean of examining intermolecular interactions in non-aqueous solutions. The spectral band profile includes all information about the interactions of a normal vibrational mode with neighboring medium (first of all the static structural perturbations associated to the distribution of local configurations of the solvent).

The interaction of 2-bromopropane and *trans* and *gauche* conformational isomers of 1-bromopropane (named bromopropanes) with solvents is non-specific and is dominated by the dielectric properties of the solvents [1-3]. The Onsager reaction field [4] in which the solvent is represented by a continuum dielectric medium characterized by bulk dielectric constant ϵ was a suitable model to describe the interaction of bromopropanes with neat solvents.

^a *Universitatea Babeș-Bolyai, Institutul de Cercetări în Chimie Raluca Ripan, Str. Fântânele 30, RO-400294 Cluj-Napoca, Romania, rodicagrecu2000@yahoo.com*

^b *Universitatea Babeș-Bolyai, Facultatea de Fizică, Str. Kogălniceanu 1, RO-400084 Cluj-Napoca, Romania*

Reported in this paper are the effects of two solvent mixtures prepared from solvents of different polarities cyclohexane/tetrahydrofuran (CH/THF) and carbon tetrachloride/acetonitrile (CCl₄/CH₃CN) on the frequency and half bandwidth of $\nu(\text{C-Br})$ band of 1- and 2-bromopropane.

RESULTS AND DISCUSSION

Dielectric properties of solvent mixtures

A mixture of two individual solvents is a medium that generally does not act additively according to its composition.

Theoretically, a binary solvent mixture is "ideal" when a parameter P_{mix} of the mixture is related with the parameters P_1 and P_2 of each solvent through the following relation:

$$P_{\text{mix}} = P_1x_1 + P_2x_2 \quad (1)$$

where x_1, x_2 are the mole fractions of the components.

Practically, because of the molecular interaction forces the total volume of the mixture is inferior to the sum of the individual volumes and is difficult to find an ideal mixture.

The solvent mixtures used in this study have been cyclohexane/tetrahydrofuran (CH/THF) and carbon tetrachloride/acetonitrile (CCl₄/CH₃CN). Every mixture contains a nonpolar solvent ($\mu = 0$) and a polar one. The dipolar moment of tetrahydrofurane is small ($\mu = 0.7$ D) while the molecule of acetonitrile is a very polar one ($\mu = 3.5$ D).

The mixture CH/THF is considered ideal. The values ϵ_{mix}^e of the dielectric constant experimentally determined for different solvent mixtures come near the values ϵ_{mix}^m calculated according to the relation (1) and vary linear with the mole fraction x_P of tetrahydrofuran.

Table 1. Values of the dielectric constants ϵ_{mix} for different solvent mixtures

Nonpolar/ polar solvent volume ratio	CH/THF mixture			CCl ₄ /CH ₃ CN mixture			
	x_P	ϵ_{mix}^m	ϵ_{mix}^v	x_P	ϵ_{mix}^m	ϵ_{mix}^v	ϵ_{mix}^e
1 : 0	0.000	2.024	2.024	0.000	2.234	2.234	2.234
30 : 1	0.042	2.255	2.200	0.058	4.233	3.337	3.004
20 : 1	0.062	2.365	2.282	0.084	5.129	3.854	3.381
10 : 1	0.116	2.662	2.524	0.155	7.576	5.370	4.502
5 : 1	0.208	3.167	2.936	0.269	11.505	7.955	6.617
2 : 1	0.397	4.206	3.854	0.479	18.743	13.711	11.797
1 : 1	0.568	5.145	4.822	0.648	24.568	19.467	17.576
1 : 2	0.725	6.008	5.684	0.786	29.324	25.188	23.727

Nonpolar/ polar solvent volume ratio	CH/THF mixture			CCl ₄ /CH ₃ CN mixture			
	X _P	ε ^m _{mix}	ε ^v _{mix}	X _P	ε ^m _{mix}	ε ^v _{mix}	ε ^e _{mix}
1 : 3	0.798	6.409	6.146	0.846	31.392	28.080	26.896
0 : 1	1.000	7.520	7.520	1.000	36.700	36.700	36.710

ε^e_{mix}: dielectric constants experimentally determined for different solvent mixtures

ε^m_{mix}: dielectric constants of solvent mixtures calculated according to relation (1)

ε^v_{mix}: dielectric constants calculated according to relation (2)

For a CCl₄ / CH₃CN mixture, an important deviation from linearity in the dependence of ε^e_{mix} on the mole fraction x_P of acetonitrile was noticed. The experimental dielectric constants of this system are better approximated by the ε^v_{mix} values calculated according to the empirical relation (2):

$$\varepsilon_{\text{mix}}^{\text{v}} = \varepsilon_{\text{N}}V_{\text{N}} + \varepsilon_{\text{P}}V_{\text{P}} \quad (2)$$

where V is the volume fraction of solvents and the indexes N and P indicate the nonpolar and respectively the polar solvent from the mixture.

From the thermodynamic point of view the dielectric Onsager functions calculated [5] using different dielectric constants ε_{mix} are not suitable to describe the effects of a mixture of solvents even if this is considered ideal. The mixture composition or the non-homogeneity of the mixture in the vicinity of solute can modify even the dielectric constant of the individual solvents.

Frequency shift of ν(C–Br) infrared bands of bromopropanes

If the solute sample does not disturb the solvent structure, the maximum of the infrared absorption band should be shifted linearly with the mole fraction of the polar solvent from the mixture. This kind of variation was observed for the bromopropanes solved in the mixture CH/THF considered ideal (see Figure 1).

The dependence of the maximum of ν(C–Br) bands on the mole fraction of acetonitrile is non-linear under the effect of CCl₄/CH₃CN mixture (Figure 1). The effect is more pronounced at smaller concentrations, proving the importance of local effects of the medium in the proximity of the solute.

Generally, a non-linear dependence of the frequency of the absorption band on the mole fraction x_P is considered as a proof for a specific association solute-solvent, for example hydrogen bonding, but also as a result of a “dielectric enrichment” of the solvent shell around the dipolar solute molecule. If the mixture contains solvents having very different polarities, a process of

“preferential solvation” occurs that disturbs their distribution into the electric field of a dipolar solute molecule. The composition of the solvent shell in the vicinity of solute could be different by the composition of the bulk mixture.

The process of “preferential solvation” in $\text{CCl}_4/\text{CH}_3\text{CN}$ mixtures can be characterized by the index Z that expresses [6] the relation between the mole ratios $X = x_N/x_P$ and $Y = y_N/y_P$:

$$Y = X e^{-Z}$$

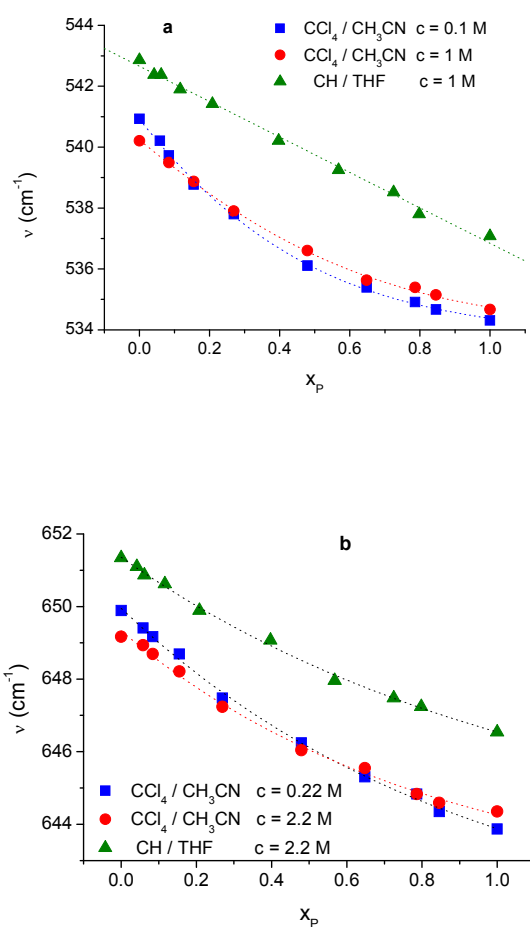


Figure 1. Dependence of $\nu(\text{C-Br})$ frequency of (a) 2-bromopropane and (b) *trans* 1-bromopropane on the mole fraction of the polar solvent in CH/THF and $\text{CCl}_4/\text{CH}_3\text{CN}$ mixtures (c is the molar concentration of the solute)

The mole fractions y_P of acetonitrile in the solvation shell of bromopropanes were calculated assuming a linear dependence of $\nu(\text{C-Br})$ frequency on it. Because of small differences between the $\nu(\text{C-Br})$ frequency values, the calculated index Z has an uncertainty of ± 0.1 .

Table 2. Mole fraction of polar solvent in the solvation shell y_P and index Z of "preferential solvation" of bromopropanes in $\text{CCl}_4/\text{CH}_3\text{CN}$ mixtures (c = molar concentration of solutes)

x_P	y_P					
	2-bromopropane		<i>gauche</i> 1-bromopropane		<i>trans</i> 1-bromopropane	
	$c=0.11\text{M}$	$c=1.00\text{M}$	$c=0.22\text{M}$	$c=2.20\text{M}$	$c=0.22\text{M}$	$c=2.20\text{M}$
0.058	0.149	0.120	0.125	0.097	0.106	0.090
0.084	0.208	0.169	0.176	0.138	0.150	0.129
0.155	0.344	0.289	0.300	0.243	0.260	0.228
0.269	0.512	0.450	0.461	0.392	0.414	0.372
0.479	0.724	0.671	0.691	0.617	0.639	0.597
0.648	0.840	0.804	0.811	0.763	0.780	0.748
0.786	0.913	0.891	0.895	0.866	0.876	0.856
0.846	0.940	0.924	0.927	0.906	0.913	0.898
1.000	1.000	1.000	1.000	1.000	1.000	1.000
Z	1.05	0.80	0.84	0.55	0.65	0.48

It can be noticed that Z value increases in the following order: *trans* 1-bromopropane < *gauche* 1-bromopropane < 2-bromopropane.

The decrease of solute concentration in CCl_4/ACN mixture determines also an increase of index Z . For all solutes, the difference $y_P - x_P$ has a maximum value for $\text{CCl}_4 : \text{CH}_3\text{CN}$ volume ratio of 2 : 1 ($x_P \sim 0.4$). At this concentration the maximum half bandwidth was also evidenced.

Half bandwidth of $\nu(\text{C-Br})$ infrared bands of bromopropanes

The changes observed in the parameter half bandwidth ($\Delta\nu_{1/2}$) of $\nu(\text{C-Br})$ bands are related with the complexity of solvent medium in the vicinity of solute molecule, more exactly the part of molecule implied in the studied vibrational mode.

According to Yoshino [6] the greatest modification of the half bandwidth of an absorption band is expected for a value 0.5 of the mole fraction of the polar solvent from a solvent mixture if the difference between the solvation energy of the solute in the individual components of the mixture is zero.

The parameter $\Delta\nu_{1/2}$ of C-Br stretching band increases monotonously with the mole fraction of polar solvent from the bulk CH/THF mixture which is considered ideal (Figure 2).

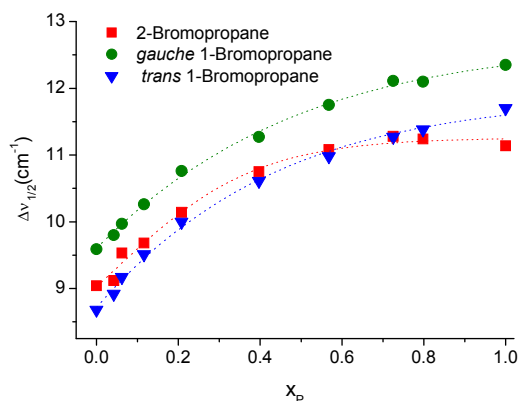


Figure 2. Dependence of the half bandwidth $\Delta\nu_{1/2}$ of $\nu(\text{C-Br})$ band of 2-bromopropane ($c=1.06$ M) and 1-bromopropane ($c=2.2$ M) on the mole fraction x_p of tetrahydrofuran from the CH/THF mixtures

A different behaviour is noticed under the effect of $\text{CCl}_4/\text{CH}_3\text{CN}$ mixture (Figure 3). A maximum half bandwidth for the mole fraction of acetonitrile ~ 0.4 is observed. This corresponds to a $\text{CCl}_4 : \text{CH}_3\text{CN}$ volume ratio of 2 : 1 where, in the conditions of preferential solvation, the difference $y_p - x_p$ is the greatest.

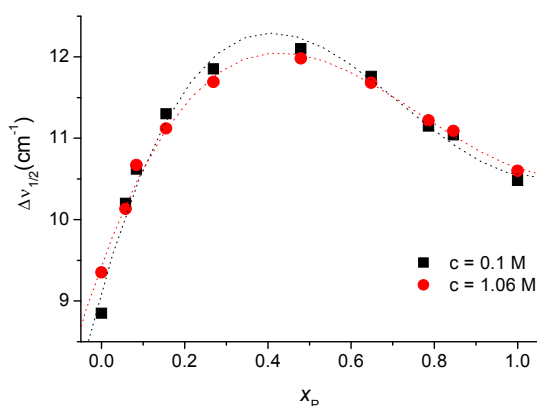


Figure 3. Dependence of the half bandwidth $\Delta\nu_{1/2}$ of 2-bromopropane $\nu(\text{C-Br})$ band on the mole fraction x_p of acetonitrile from the $\text{CCl}_4/\text{CH}_3\text{CN}$ mixtures (c is the molar concentration of solute)

In Figure 3 is presented the case of 2-bromopropane, but the graphs for the conformational isomers of 1-bromopropane are similar.

The maximum half bandwidth of $\nu(\text{C-Br})$ band observed for values of mole fraction of acetonitrile smaller than 0.5 indicate a difference between the solvation energies of bromopropanes in the individual components of the $\text{CCl}_4/\text{CH}_3\text{CN}$ mixture

CONCLUSIONS

The solutes 2-bromopropane and 1-bromopropane do not disturb the "ideal" CH / THF solvent mixture.

The deviation from linear dependence of $\nu(\text{C-Br})$ band frequency on mole fraction of acetonitrile observed under the effect of $\text{CCl}_4/\text{CH}_3\text{CN}$ mixture is determined by the local "dielectric enrichment" of the solvation shell. The process of "preferential solvation" in this mixture can be characterized by the index Z which increases in the following order: *trans* 1-bromopropane < *gauche* 1-bromopropane < 2-bromopropane.

The maximum half bandwidth of $\nu(\text{C-Br})$ band was observed for values of molar fraction of acetonitrile smaller than 0.5, indicating an increase of the difference between the solvation energy of bromopropanes in the individual components of the $\text{CCl}_4/\text{CH}_3\text{CN}$ mixture. More exactly, the maximum broadening of $\nu(\text{C-Br})$ band corresponds to the composition 2:1 of solvent mixture, for which the difference between mole fraction of acetonitrile in the bulk and in the vicinity of solute is the greatest.

EXPERIMENTAL SECTION

The analyzed spectra were collected using a JASCO 610 FTIR spectrometer, with a resolution of 0.5 cm^{-1} and sealed KBr cells of 0.012 and 0.062 cm path length. The spectra were obtained by subtracting the spectrum of pure solvent (multiplied with a proper factor which depends on the solute concentration) from that of the solution using the Spectra Analysis software of the spectrometer.

The frequency of $\nu(\text{C-Br})$ vibrational mode of bromopropane compounds studied as neat liquids is 538.3 cm^{-1} for 2-bromopropane, 563.1 cm^{-1} for *gauche* isomer and 647.5 cm^{-1} for *trans* isomer of 1-bromopropane respectively.

The solvent mixtures used in this study, cyclohexane/ tetrahydrofuran (CH/THF) and carbon tetrachloride/acetonitrile ($\text{CCl}_4/\text{CH}_3\text{CN}$), were prepared from spectral grade solvents.

The solute concentrations were of 1.06 M for 2-bromopropane and 2.2 M for 1-bromopropane in both solvent mixtures and of 0.1 M and 0.22 M respectively, in CCl₄/CH₃CN solvent mixture.

The concentrations of 2-bromopropane were 0.1 M and 1.06 M and of 1-bromopropane were 0.22 M and 2.2 M in both solvent mixtures (CH/TH and CCl₄/CH₃CN).

ACKNOWLEDGMENTS

This paper is dedicated to the memory of Prof.dr Ioan Silaghi-Dumitrescu who provided scientific support in performing the *ab initio* calculations from the Ph.D. thesis by RG - „Spectre de absorbtie la molecule poliatomice” (Absorption spectra of polyatomic molecules).

REFERENCES

1. R. Grecu, I. Bratu, O. Cozar, *Balkan Phys. Lett.*, **1997**, 5, 231.
2. R. Grecu, A. Kun, I. Silaghi-Dumitrescu, *XXVI European Congress on Molecular Spectroscopy*, Villeneuve d'Ascq (France), 1-6 Sept. **2002**, Book of Abstracts p.131.
3. R. Grecu, A. Kun, I. Silaghi-Dumitrescu, *J. Mol. Structure*, **2001**, 39, 565.
4. L. Onsager, *J. Am. Chem. Soc.*, **1936**, 58, 1486.
5. V. Bekárek, *Collect. Czech. Chem. Commun.*, **1989**, 54, 3162.
6. S. P. Van, G. S. Hammond, *J. Am. Chem. Soc.*, **1978**, 100, 3895.
7. T. Yoshino, *J. Chem. Phys.*, **1956**, 24, 76.

Dedicated to the memory of Prof. dr. Ioan Silaghi-Dumitrescu marking 60 years from his birth

ADHESIVE INFLUENCE ON DOUBLE-LAP BONDED-JOINTS ASSEMBLIES

OVIDIU NEMES*

ABSTRACT. This work presents the influence of the adhesive on the double-lap joint assemblies. The adhesive characteristics and the influence on the stress distribution in double-lap adhesive bonded-joints assemblies' configuration are also presented.

Keywords: *structural adhesives, adhesive properties, double-lap adhesive assemblies*

INTRODUCTION

Adhesively bonded method distributes the stresses over the whole joining surface and removes the concentrations of stresses at the boundary of holes generated by bolting or riveting assemblies. Consequently, it is essential to know the stress distribution, which, because of its complexity, makes prediction of fractures difficult. To study the stress distribution it is very important to know the adhesive characteristics.

There are several models which try to define the stress distributions in double-lap [1 – 12]. Complex studies about various analytical models are compared by da Silva et al. [13].

Mortensen and Thomsen [14, 15] developed an approach for the analysis and design of various joints adhesively bonded. They took into account the influence of the interface effects between the adherends and they modelled the adhesive layer by assimilating it to a spring.

Diaz Diaz et al. [16] assumed in their classical double lap model that the adhesive thickness is small compared to that of the adherends and the stresses to be uniform through the adhesive thickness. The model can be considered as a stacking of Reisner-Mindlin plates and the equations based on this model were applied to the geometry of a symmetrical adhesively bonded joint. The model was validated by comparing the model results with those of a finite element calculation

* *Universitatea Tehnică din Cluj-Napoca, Facultatea de Știința și Ingineria Materialelor, B-dul Muncii Nr. 103-105, RO-400641 Cluj-Napoca, Romania; ovidiu.nemes@sim.utcluj.ro*

Using a variational method and some simplifying assumptions, the author of this work developed and validated a new analytical model for a fast pre dimensioning of adhesive bonded assemblies [17-21]. The first stage consists in building a statically acceptable stress field, i.e. verifying the boundary conditions and the equilibrium equations. Then, the potential energy generated by such a stress field is calculated. In the third stage, the potential energy is minimized in order to determine the stress distributions. Finally, the analytical model proposed for double lap adhesive by bonded joints was validated using numerical and experimental methods.

In this paper, the adhesive influence on the stress distribution in double-lap adhesive bonded-joints assemblies' configuration was studied.

RESULTS AND DISCUSSION

A theoretical model of calculation of assemblies joined with adhesive, based on an energy method was developed by the author and coworkers [17-21]. After the determination of the cinematically acceptable field of stresses, according to the applied load, a variational calculus on the expression of elastic potential energy leads to the complete expression of the stress field in the whole assembly.

A first parametric analysis (geometrical and physicals parameters) is carried out on an assembly and makes it possible to deduce the optimal length and the thickness of the adhesive.

The performance of the adhesive bonded joints depends on the performance of the adhesive. The latest generations of adhesives, delivered in the form of film, make it possible to minimize the number of operations to make the join and greatly increase the mechanical resistance.

However, the design engineer must have at his disposal methods and/or reliable computer codes for predimensioning with known margins.

Using this energetical model, some analysis was carried out. The first step was to characterize the adhesive by tensile tests (plastic behavior of the adhesive was shows in experimental part).

Adhesive elastic modulus influence

The stresses in the adhesive are very important to predict the failure moment. For that it is primordial to have their distributions.

Figure 1 represents the influence of the elastic modulus of the adhesive on the shear stress distribution. The maximum peaks increase slightly when the elastic modulus increases.

Adhesive thickness influence

Another important parameter in double-lap adhesive bonded-joints assemblies' characterization is the thickness of the adhesive.

Figure 2 shows the influence of adhesive thickness on the adhesive shear stresses distribution. When the adhesive thickness increases, the maximum stresses in the adhesive decrease and the distribution tends to be uniform over the entire overlap length.

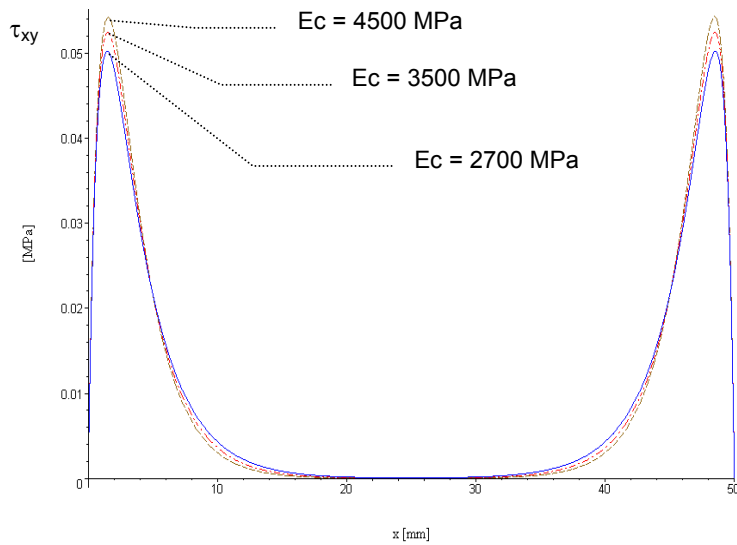


Figure 1. The influence of the elastic modulus of the adhesive on shear stress distribution in an AU 4G-AV 119-AU 4G assembly.

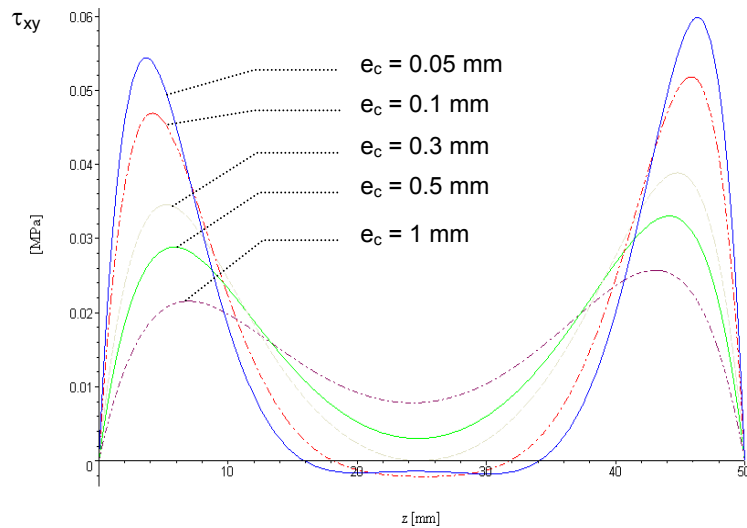


Figure 2. . The influence the of adhesive thickness on shear stress distribution in an AU 4G-AV 119-AU 4G assembly.
 $e_c = 0.05$ mm, $e_c = 0.1$ mm, $e_c = 0.3$ mm, $e_c = 0.5$ mm, $e_c = 1$ mm

The analytical model underestimated the stresses in the adhesive, leading to an over-estimate of the forces at rupture. However, this model is reliable and allows fast analysis of this type of assembly.

EXPERIMENTAL PART

To obtain mechanical properties of the adhesive we have we carried out a plate with 10 layers of Redux adhesive film. The characteristics of the adhesive film, given by the manufacturer, are presented in table 1.

After the polymerization of the plate we cut out a piece with the following dimensions: 200x20x1.98 mm for tensile testing.

The tensile tests were carried out using an INSTRON 8862 system. The load is applied with imposed displacement at the speed of 0,5 mm/min. On certain tests we performed rises in cyclic loads (4 to 5 cycles).

The stress, displacement and deformations acquisition is carried out by a NICOLET-GOULD acquisition system.

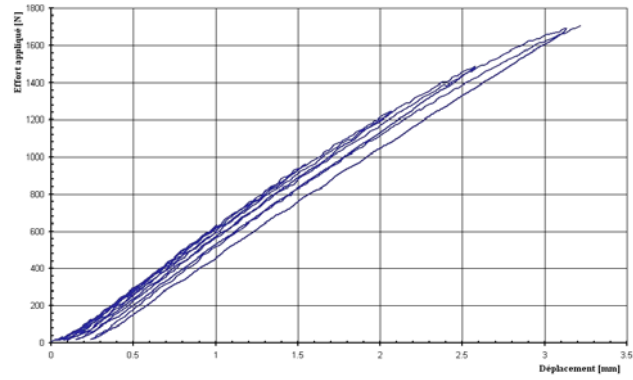
The mechanical characteristics obtained by the tests are given in table 2. The double-lap adhesive bonded assembly has the following elements: two aluminium substrates AU 2024 T3 and a layer of epoxy adhesive AV 119 from Huntsman.

Table 1. Adhesive film technical data*.

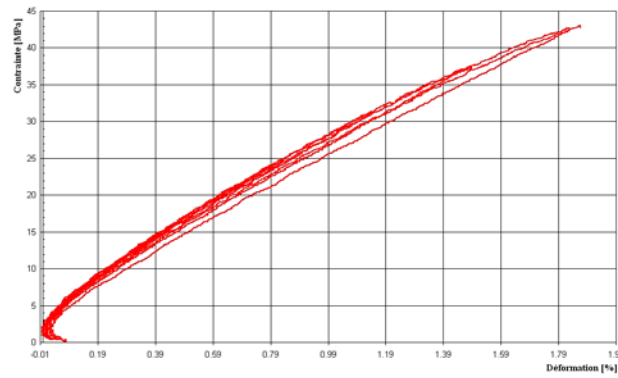
HEXCEL COMPOSITES Duxford Cambridge CB2 4QD, England	Product Type: Batch No.: Primes Type: Batch No.:	Redux 312/5 054917A Redux 112 V051196
<u>ADHESIVE TEST REPORT</u>		
Specification IFS 201-216	Test No.:	17845
<u>Lap shear strength (MPa)</u>		
	<u>22 °C</u>	<u>80 °C</u>
	37.9	29.4
	40.3	27.4
	38.6	29.5
	37.8	28.8
	39.5	
Mean	38.8 MPa	28.8 MPa
Min Ind.	37.8 MPa	27.4 MPa
Requirements – Mean	35.0 MPa	28.0 MPa
Min Ind.	32.0 MPa	25.0 MPa

*Hexcel Composites

Figure 3 shows the plastic behavior of the adhesive.



a)



b)

Figure 3. Adhesive tensile behaviour:
a) Applied load - displacement; b) Stress - deformation.

Table 2. Experimental results.

	$F_R^{(c)}$ [N]	$\sigma_{xx \text{ max}}^{(c)}$ [MPa]	E_c [MPa]
1.	1730.47514	43.2618786	2014.07580
2.	2642.60815	44.7899687	2648.54446
3.	1708.61762	43.1469095	2750.00250

CONCLUSIONS

Based on presented case study, we can draw the following conclusions: the intensities of the peaks in the adhesive stress distribution are influenced by the elastic modulus of the adhesive. The maximum peaks increase slightly when the elastic modulus of the adhesive increase. As the adhesive thickness increases, the stresses in the adhesive decrease and the stress distribution is more uniform.

ACKNOWLEDGEMENT

The Ministry of Education and Research, Bucharest (ID-1100, PN II project) is thanked for the financial support of this work.

REFERENCES

1. O. Volkersen, Die Luftfahrtforschung, **1938**, 15, 41.
2. M. Goland, N.Y. Buffalo, E. Reissner, Journal of Applied Mechanics, **1944**, 66, A17.
3. L.J. Hart-Smith, NASA-CR-112236, **1973**.
4. W.J. Renton, J.K. Vinson, Journal of Applied Mechanics, **1977**, 101.
5. I.U. Ojalvo, H.L. Eidinoff, AIAA Journal, **1978**, 16, 204.
6. D.A. Bigwood, A.D. Crocombe, International Journal of Adhesion & Adhesives, **1989**, 9, 229.
7. D.J. Allman, Journal of Mechanical Applied Mathematics, **1977**, 30, 415.
8. O. Volkersen, Construction métallique, **1965**, 4, 3.
9. Y. Gilibert, A. Rigolot, Mécanique des solides, **1979**, 288, 287.
10. Y. Gilibert, A. Rigolot, Matériaux et Constructions, **1985**, 18, 363.
11. Y. Gilibert, Matériaux et techniques, **1991**, 5.
12. L. Tong, International Journal of Solids Structures, **1994**, 31, 2919.
13. L.F.M. da Silva, P.J.C. das Neves, R.D. Adams, J.K. Spelt, Int. J. Adhes. Adhes. **2009**, 29, 319.
14. F. Mortensen, O.T. Thomsen, Composite Structures, **2002**, 56, 165.
15. F. Mortensen, O.T. Thomsen, Composite Science and Technology, **2002**, 62, 1011.
16. A. Diaz Diaz, R. Hadj-Ahmed, G. Foret, A. Ehrlacher, Int. J. Adhes. Adhes. **2009**, 29, 67.
17. O. Nemes, F. Lachaud, A. Mojtabi, Int. J. Adhes. Adhes. **2006**, 26, 474.
18. O. Nemes, Studia Universitatis Babes-Bolyai Chemia, **2007**, 52, 175.
19. O. Nemes, F. Lachaud, A. Mojtabi, M. Borzan and St. Grigoras, Materials, Mater. Plast. **2008**, 45, 390.
20. O. Nemes, F. Lachaud, J. Adhes. Sci. Technol. **2009**, 23, 1383.
21. O. Nemes, F. Lachaud, Int. J. Adhes. Adhes. **2010**, 30, 288.